TOWARDS STOCHASTIC FINITE ELEMENT ANALYSIS OF REINFORCED CONCRETE STRUCTURES

by

Mark David Hunter

A thesis submitted in conformity with the requirements
for the degree of Master of Applied Science

Graduate Department of Civil Engineering
University of Toronto

Towards Stochastic Finite Element Analysis of Reinforced Concrete Structures

Mark David Hunter

Master of Applied Science

Civil and Environmental Engineering
University of Toronto

2016

ABSTRACT

Stochastic simulation is used primarily as a basis for the resistance models in a reliability analysis and is often used to calibrate many structural concrete building codes. This thesis outlines the implementation of stochastic simulation techniques into VecTor2, a NLFEA program for the analysis of reinforced concrete. Stochastic simulation was conducted on a subset of beams from the Toronto size effect series. The simulation results form the basis of a reliability analysis that computes the reliability indices for the CSA A23.3-14 and the ACI 318-14 codes.

Additionally, an experimental program assessing spatial variability within monolithic concrete using nondestructive techniques is presented and discussed. Ultrasonic pulse velocity (UPV) measurements were taken on a grid for a large reinforced concrete specimen. Data were collected from cylinders to develop a regression model for strength versus UPV. Geospatial statistical methods were then employed to determine spatially variable material properties for a finite element model.

ACKNOWLEDGMENTS

Firstly, I would like to thank my supervisor Professor Frank J. Vecchio. His continual guidance helped me shape this thesis into a document that I can be proud of. I am lucky to have benefited from a supervisor with a formidable wealth of expertise in the analysis of reinforced concrete.

Next I would like to thank the faculty members who, often and without hesitation, agreed to discuss my work. Thank you to Professor Evan C. Bentz, Professor Oh-Sung Kwon, and Professor Daman Panesar, all of whom provided valuable insight to my project. I would like to thank Dr. Karl-Heinz Reineck for graciously providing an experimental database. I would also like to thank NSERC, Consultec Ltd., and Dr. Michael Simpson for their financial support and professional guidance.

Thank you to my fellow research group members and graduate students: Stamatina Chasioti, Anca Jurcut, Benard Isojeh, Andac Lulec, Vahid Sadeghian, Simon Liu, Giorgio Proestos, Allan Kuan, Edvard Bruun, Paola Miglietta, Saif Shaban, and Siavash Habibi. You all have made my time at the at the University of Toronto an academically rich and social environment. Graduate school is a war of attrition. I offer this chart as an illustration of how deadlines can sneak up on you, beat you down, and also motivate you. Good luck with your studies.

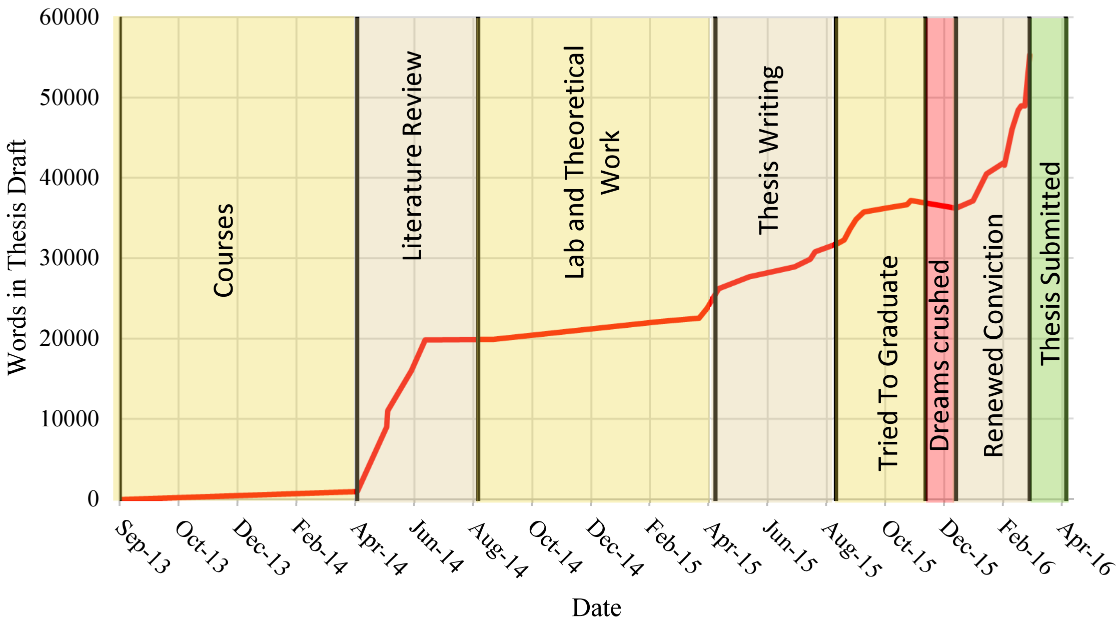

Lastly, thank you to all my friends and family who have supported me throughout this process. Especially thank you to Katelyn MacDonald, who’s advice, love, and support made this experience immeasurably better.

TABLE OF CONTENTS

LIST OF TABLES

LIST OF FIGURES

CHAPTER 1: INTRODUCTION

Stochastic simulation is perhaps best understood in comparison with deterministic simulation. In a deterministic simulation, the goal of the selected model is to replicate a physical system. In the case of reinforced concrete, the Disturbed Stress Field Model (Vecchio et al., 2000) is a deterministic model for the analysis of reinforced concrete elements. It aims to provide an accurate stress-strain response for reinforced concrete as an anisotropic smeared cracked material. What categorizes this simulation as deterministic is the need to define the input parameters. If the input parameters are known and the model is sufficient, the model will produce a good estimation of the physical behaviour. In a stochastic simulation, the goal is to infer statistical data about an output quantity based on statistical knowledge of the system inputs. In the context of this thesis, the inputs under consideration are the spatial and global variability of concrete and steel material properties.

Graham and Talay (2013) note that stochastic simulations are only useful for certain types of engineering problems. Consider a system where the physical experiment can be described by well-established models, but model parameters are difficult to calibrate. In the case of reinforced concrete, it is well known that the concrete material properties exhibit a large variability (Mirza et al., 1979; Bartlett and MacGregor, 1996; Unanwa and Mahan, 2014). When testing structures in a laboratory, material testing is done on each specimen to determine the exact material properties. This allows for good deterministic models to produce accurate and reliable simulation of the structural behaviour. However, an engineer making an assessment of a structure in the field may not have access to perfect information. It may be too costly to determine the material properties, or physical testing may be impractical.

As an example, consider the structural assessment of an existing foundation. The foundation in question is a large pile cap for a 15000 ton cement storage silo seen in Fig. 1.1. The original design for the foundation is based on the assumption that plane section remain plane and that sectional strength governs. However, the span to depth ratio of the foundation is less than 2.4, which means that sectional assumptions for shear are likely violated. Thus an engineer has been tasked with assessing the strength of the pile cap.

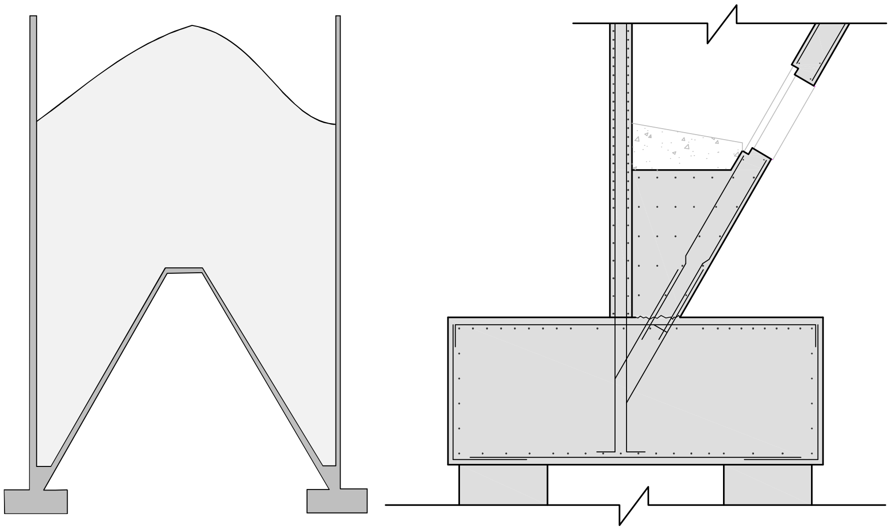

(a) (b)

Fig.1.1: 15000 Ton Cement Storage Silo. Images courtesy of Consultec Ltd.
(a) Elevation of Silo. (b) Foundation Detail.

To start, a deterministic strut and tie model is developed. The results of the strut and tie model indicate that the foundation is shear critical. This means that the strength of the foundation is heavily dependent on the behaviour of the concrete, and not the longitudinal reinforcing steel. In addition, it is noted the failure mode of the foundation (brittle shear or ductile yielding of longitudinal reinforcement) is very sensitive to the material properties and the assumed strut angle. Such a problem is ideally suited to more advanced analysis procedures. Thus the engineer may elect to use a nonlinear finite element program, perhaps VecTor2. Traditionally, the structure is assessed as safe by using the nominal material properties as inputs and achieving an acceptable factor of safety. However, due to the sensitivity of the material property inputs, additional information is required for the engineer to make a rational assessment of the structure. It may be too costly to excavate around the foundation to determine the actual material properties. Instead the problem can be approached in a stochastic framework. Information on the distribution of concrete and steel material properties can be used to produce information on the distribution of strength and the sensitivity to failure mode. A stochastic simulation could be carried out to determine the reliability index for this specific foundation. This reliability index can be compared against code recommended reliability indices to determine if the structure meets the safety requirements of the local building code. This is a practical example where stochastic simulation can aid engineers in their assessment of existing infrastructure.

The variability associated with existing infrastructure in general is not limited simply to the inherent material variability. There is a large degree of uncertainty associated with deteriorated infrastructure. The extent, location, and behaviour of reinforced concrete deterioration is a topic of significant research. Thus it is imperative that the ability to analyze deteriorated reinforced concrete is implemented into advanced analysis programs. If the above example had exhibited signs of reinforcing corrosion, the assessment of its reliability is further complicated. There is much work to be done on the development of analysis tools that can capture concrete deterioration in a reliability framework. The first step towards such tools is the focus of this thesis.

1.1 Scope of Stochastic Modelling Capabilities

The stochastic modelling capabilities implemented in this thesis include Monte Carlo sampling and Latin Hypercube sampling for uncorrelated uniform sampling, uniform sampling with correlated random variables, and spatial variation using random field generation. Monte Carlo sampling is recommended in the literature when the number of simulations can be very large. The advantage of Monte Carlo sampling is that it provides a completely unbiased sample of the input variables. However, due to computational limitations, generating greater than a few hundred simulations may be impractical. In this case, it is recommended that Latin Hypercube sampling be used as it provides a good estimate of the mean and standard deviation of the output parameters.

The implementation of random fields in this thesis is limited to Gaussian random fields. This assumes that the distributions are normal. However, for many of the selected models, a lognormal distribution is used for the concrete compressive strength. The inclusion of lognormal distributions for random fields is not yet implemented. This is addressed partially by coupling global uniform sampling with localized random field sampling. Additionally, the implemented software will not identify discontinuities in material properties and apply different random fields to each of the discontinuities. User specified material property scaling factors can be employed for any spatial variation that is outside of the scope of the implemented analysis types. Lastly, correlated random fields cannot be generated for different random variables. The implementation for random field analysis assumes that the tensile strength and modulus of elasticity are scaled directly from the compressive strength. The simulation of cross correlated random field was outside of the scope of this thesis. The simulation of independent random fields was considered not to represent reality and thus the direct scaling approach is preferred.

1.2 Thesis Outline

This section summarizes the components of this thesis and outlines the order in which they are presented. Each chapter is summarized briefly below. It is intended to help the reader understand the direction of this thesis.

Chapter 2 presents the relevant literature and background knowledge for this thesis. A review of basic statistics and an introduction into reliability analysis is discussed. Literature on several statistical models for concrete and steel strength are presented and discussed.

Chapter 3 presents the procedures, results, and analysis of the subsidiary experimental program. A large reinforced concrete slab strip was constructed and tested by Collins et al. (2015). Non-destructive testing data were collected on a large specimen to determine the spatial variability of the in-situ concrete strength for the purpose of assessing how spatial variability influences modelling of reinforced concrete beams.

Chapter 4 summarizes all of the various implementations for stochastic simulation tools in VecTor2. The theory behind each implementation is discussed and the verification of the implementation is presented.

Chapter 5 employs the implementations discussed in Chapter 4 to conduct a reliability study of beams without shear reinforcement. The CSA A23.3-14 and ACI 318-14 codes are compared through the lens of a reliability analysis.

Chapter 6 outlines the main conclusions and identifies areas where future research is required.

1.3 Research Significance

Stochastic simulation is used primarily as a basis for the resistance models in a reliability analysis. In the case of reinforced concrete, simplified reliability has been used to calibrate many building codes (Nowak and Szerszen, 2003; Razkozy and Nowak, 2014; Bartlett, 2006). The material resistance factors in the case of the Canadian code, and the member resistance factors in the case of the American code, are calibrated to achieve a code level reliability. However, as a recent prediction competition (Collins et al., 2015) has shown, prediction of the shear strength of concrete beams with no transverse reinforcement still remains a challenging task. With such uncertainty, the calibration of resistance factors and load factors for building codes requires software that can provide a good deterministic prediction of structural behaviour. VecTor2 represents a viable option for the simulation of reinforced concrete. It has the ability to analyze virtually any planar reinforced concrete structure, including disturbed regions. The addition of stochastic simulation tools to VecTor2 allow it to be used to create member resistance curves and thus be a useful tool in the assessment of safety and structural reliability for reinforced concrete members.

CHAPTER 2: LITERATURE REVIEW

This chapter provides an overview of the literature pertaining to stochastic simulation and the behaviour and analysis of corroded reinforced concrete. A review of basic statistics and reliability analysis is provided. Several statistical models for concrete and steel material properties are reviewed and discussed. A selected number of Monte Carlo simulations are presented and discussed. Lastly, relevant experimental results and existing models for the analysis of corroded reinforced concrete are presented.

2.1 Review of Basic Statistics

This section summarizes the basic statistics theory that is employed in this thesis. It is intended to refresh the reader on some of the terms and concepts that are required to interpret the inputs and results of a stochastic simulation. Note that this section is only a summary of statistics. For a complete review of statistical concepts, or for any further clarification on the concepts presented in this section, the reader is encouraged to consult the references provided.

2.1.1 Normal Distribution

The normal distribution, also referred to as the Gaussian distribution, is the most common form of distribution used for describing the statistics of a large sample. The distribution was developed independently by De Moivre in 1733 and Gauss approximately 100 years later (Montgomery and Runger, 2011). The distribution is characterized by its symmetry around the average of the sample. The shape of the normal distribution is governed by the standard deviation. A normal distribution is mathematically described by Equation 2.1.

$$f(x) = \frac{1}{\sqrt{2\pi}\sigma} exp\left[\frac{-(x-\mu)^2}{2\sigma^2}\right] \tag{2.1}$$

The expected value of a normal distribution is equal to the mean (μ) and the variance is equal to the square of the standard deviation (σ). The normal distribution is often standardized into a normal distribution with a mean of 0.0 and a standard deviation of 1.0. This is referred to as the Z statistic and is shown in Equation 2.2.

$$Z = \frac{X - \mu}{\sigma} \tag{2.2}$$

2.1.2 Lognormal Distribution

The lognormal distribution is used to represent random variables with exponential relationships. In the case of a lognormal distribution, a variable Y is related to a variable X through the relation $X = e^Y$. If Y has a mean of θ and a standard deviation of ω and the variable Y is normally distributed, we can represent the distribution of X by Equation 2.3.

$$f(x) = \frac{1}{x\omega\sqrt{2\pi}} exp\left[\frac{-(\ln(x) - \theta)^2}{2\omega^2}\right] \tag{2.3}$$

The mean and variance of X are described in Equation 2.4 and Equation 2.5 respectively.

$$E[X] = e^{\theta + \frac{\omega^2}{2}} \tag{2.4}$$

$$V[X] = e^{2\theta + \omega^2}(e^{\omega^2} - 1) \tag{2.5}$$

A lognormal distribution is often used on random variables that can obtain values close to zero but cannot be negative.

2.1.3 Beta Distribution

A beta distribution can be assumed to describe a continuous random variable that has a finite range. The parameters of the beta distribution allow it to take on multiple shapes. The beta distribution can be described with two parameters: α and β. Equation 2.6 describes the beta distribution.

$$f(x;\, \alpha, \beta) = \frac{1}{\mathrm{B}(\alpha, \beta)} x^{\alpha - 1}(1 - x)^{\beta - 1}, for\ 0 \le x \le 1 \tag{2.6}$$

where,

$$\alpha > 0 \tag{2.6a}$$

$$\beta > 0 \tag{2.6b}$$

$$\mathrm{B}(\alpha, \beta) = \int_{0}^{1} t^{\alpha-1}(1-t)^{\beta-1}dt \tag{2.6c}$$

Additionally, the beta distribution can be transformed to be bounded by values A, and B. This is done using the transformation described in Equation 2.7, where *A* is referred to as the lower bound and *(B-A)* is referred to as the range.

$$f(x;\ \alpha, \beta, A, B) = A + (B - A)f(x; \alpha, \beta) \tag{2.7}$$

2.1.4 Statistical Inference

There are many tools available for statistical inference, this section focuses on two tests that are used to evaluate the performance of the random variable generators (described later in Section 4.1) and the distributions inferred from the stochastic simulation results.

2.1.4.1 Chi-squared Goodness of Fit Test

The chi-squared goodness of fit test is a statistical tool used for the evaluation of a fit distribution when compared to a population of data. This test is widely employed to statistically determine the strength of a given fit to a set of experimental data. The chi-squared goodness of fit test determines if the aggregate difference between the observed frequency and the theoretical frequency is significant. The hypothesis is expressed as follows:

H_0: The data follow the selected distribution

H_1: The data do not follow the selected distribution.

The test statistic, X^2, is calculated using Equation 2.8, where O_i is the observed frequency, and E_i is the estimated frequency.

$$X^2 = \sum_{i=1}^{l} \frac{(O_i - E_i)^2}{E_i} \tag{2.8}$$

As the number of samples, i, approaches infinity, the test statistic approaches a chi-squared distribution. To evaluate the hypothesis, the test statistic is compared to a one-sided chi-squared distribution at a given confidence. If the calculated test statistic is greater than the chi-squared statistic, the null hypothesis is rejected and therefore the proposed distribution is rejected.

The chi-squared goodness of fit test can be a useful tool for the evaluation of a fit distribution, however, it requires the analyst to select the bin size. This can induce bias in the test and can result in accepting the hypothesis for one set of bin sizes, and rejecting it for another set.

2.1.4.2 Kolmogorov-Smirnov Test

The Kolmogorov-Smirnov (KS) test compares the calculated maximum difference between the empirical cumulative distribution and analytical cumulative distribution functions. This maximum absolute difference forms the test statistic which is compared to a tabulated value to determine if the data follow the distribution. The null and rejection hypotheses are defined as,

H_0: The data follow the selected distribution.

H_1: The distribution do not follow the distribution.

The empirical distribution is calculated as the number of values less than a given value in a set of ordered observations. Equation 2.9 is used to calculate the test statistic.

$$\widetilde{D} = \left|\hat{F}_{xi} - \hat{S}_{xi}\right| \tag{2.9a}$$

$$D = \left|\hat{F}_{xi} - \hat{S}_{xi-1}\right| \tag{2.9b}$$

$$Z = \sqrt{n}\max\left(\left|\widetilde{D}\right|, |D|\right) \tag{2.9c}$$

where $\hat{F}_{xi}$ is the analytical estimate for the standard CDF at each point xi, and $\hat{S}_{xi}$ is the observed or empirical CDF. This is then compared with a Smirnov formula (Corder and Foreman, 2014) which is computed using Equation 2.10. If the p-value calculated from the Smirnov formula is greater than the selected level of confidence, the distribution fits the analytical cumulative distribution.

$$if\ 0 \leq Z < 0.27, then\ p = 1 \tag{2.10a}$$

$$if\ 0.27 \leq Z < 1, then\ p = 1 - \frac{2.506628}{Z}(Q + Q^9 + Q^{25}) \tag{2.10b}$$

$$where\ Q = e^{-1.233701Z^{-2}} \tag{2.10c}$$

$$if\ 1 \leq Z < 3.1\ then\ p = 2(Q - Q^4 + Q^9 - Q^{16}) \tag{2.10d}$$

$$where\ Q = e^{-2Z^{-2}} \tag{2.10e}$$

$$if\ Z > 3.1, then\ p = 0 \tag{2.10f}$$

2.2 Basics of Reliability Analysis

The following section is intended to be an introduction to structural reliability as it pertains to the scope of this thesis. Multiple topics are introduced and discussed at a qualitative level. For derivations and additional information, the reader is referred to the references provided.

Reliability analysis is the mathematical basis for the limit state design method. In a limit state design, the load that will act on the structure is predicted and factored by a prescribed value. Additionally, the resistance of each structural element is factored by either material resistance factors (CSA A23.3) or member resistance factors (ACI-318). The derivation of these factors, both for loading and resistance, are the result of reliability methods. Adequate structural safety is determined by reducing the probability of failure of the structure. In the simplest definition of reliability, the load effect (denoted as S) and the resistance (denoted as R) are assumed to be random variables with a given distribution. A structure will fail if R ≤ S. So, it follows that the probability of failure for a structure can be defined as:

$$p_f = P(R \leq S) \tag{2.11a}$$

$$p_f = P(R - S \leq 0) \tag{2.11b}$$

$$p_f = P(G \leq 0) \tag{2.11c}$$

where G is defined as the limit state function, in this case G = R – S. If R and S are normally distributed, and independent random variables, the mean and standard deviation of G is calculated as,

$$\mu_G = \mu_R - \mu_S \tag{2.12a}$$

$$\sigma_G^2 = \sigma_R^2 - \sigma_S^2 \tag{2.12b}$$

where μ represents the mean value of G, R, and S, and σ^2 represents the variance for G, R and S. The probability of failure for the structural system is then defined as,

$$p_f = \Phi\left(\frac{0 - \mu_G}{\sigma_G}\right) = \Phi(-\beta) \tag{2.13}$$

where

$$\beta = \frac{\mu_G}{\sigma_G} \tag{2.14}$$

The term β is defined as the reliability index. The reliability index describes how far away the limit state function is away from zero (or failure). A higher reliability index means a lower probability of failure. Thus it is a useful metric in assessing the safety of a structure. This concept is illustrated in Fig. 2.1.

For a normal distribution, the reliability index can be calculated as:

$$\beta = \frac{\mu_R - \mu_S}{\sqrt{\sigma_R^2 - \sigma_S^2}} \tag{2.15}$$

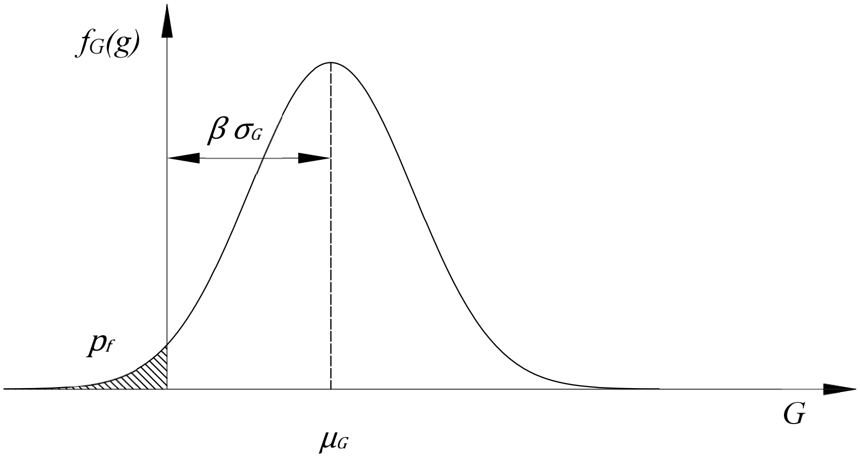

Fig. 2.1: Illustration of basic reliability function. Reproduced from Melchers (1999).

Similarly, for a lognormal distribution, the structural reliability can be calculated as:

$$\beta = \frac{\ln(\mu_R/\mu_S)}{\sqrt{\sigma_R^2 - \sigma_S^2}} \tag{2.16}$$

In general, the reliability functions for a structure can be more complicated than the simple case described above. To address complicated reliability functions, the second-moment assumption is used. The second-moment assumption uses only the first and second moments resulting from the method of maximum likelihood. The second-moment assumption was first published by Cornell (1969). As shown above, the reliability index can be directly calculated for a normal and lognormal distribution. However when the function deviates from normality, the variables are not independent, or the failure function is nonlinear, different methods to determine the reliability index are required.

One such method is the first order second-moment theory which employs the Hasofer-Lind transformation (Hasofer and Lind, 1974). Consider a failure function G(x) that is nonlinear. The failure function can be linearized through the use of a Taylor series expansion. The linearization of the failure function is called a first order method. Consider the joint probability of two random variables X_1 and X_2. There exists a nonlinear failure function G(x) that describes the failure of the structure. When determining the reliability factor, it is important that the reliability is an invariant. To obtain this, all variables of the failure function are transformed into a standard normalized space through the use of Equation 2.17.

$$Y_i = \left(\frac{X_i - \mu_X}{\sigma_X}\right) \tag{2.17}$$

This transformation is known as a transformation to y-space. Additionally, the same transformation must be applied to the failure function to create the y-space failure function, denoted $G_Y(y)$. Note that if any of the variables within X are correlated, additional steps are required. The invariant reliability index, β, is then determined as the minimum length line between the origin and the nonlinear failure function. This concept is illustrated in Fig. 2.2.

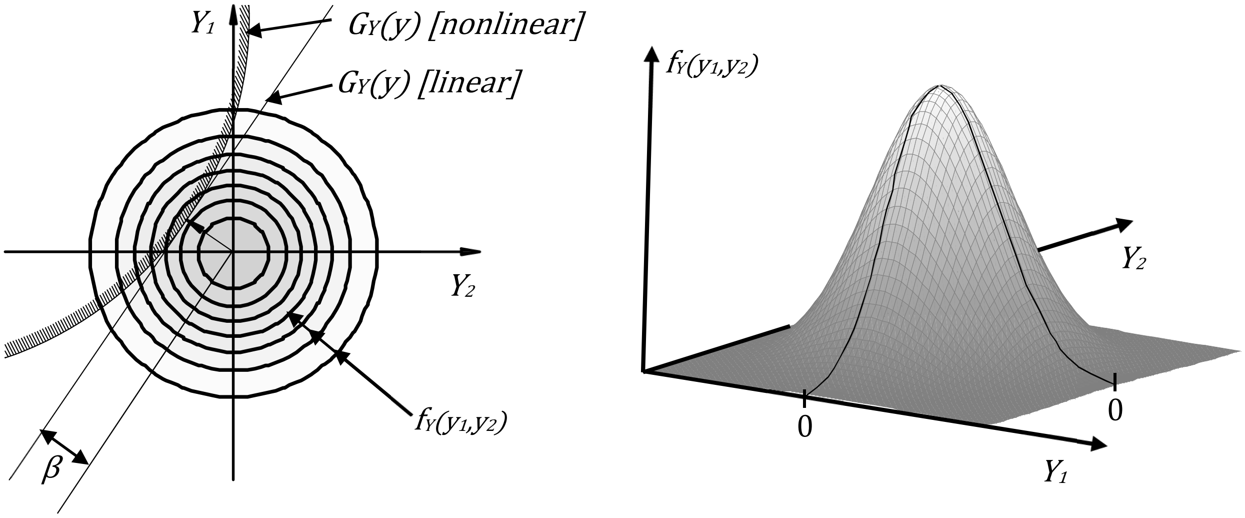

Fig. 2.2: Illustration of first order second-moment concept.

Reproduced from Melchers (1999).

If the random variables deviate from the normal distribution, the first order reliability methods must be used. For the purpose of this thesis, the structural reliability of a single structural element is most often considered. Thus a single resistance curve will be determined through stochastic simulation, and a single load effect curve will be assumed. Thus the equations 2.15 and 2.16 will be most readily employed in the reliability analysis.

2.3 Concrete Material Property Statistics

This section reviews the variability of concrete material properties as presented in the literature. The parameters reviewed include the concrete compressive strength, the tensile strength, and the modulus of elasticity.

2.3.1 Mirza et al. – 1979

In order to determine and calibrate the material resistance factors used in limit state design of concrete, the distribution and statistical parameters of material properties must be identified. Mirza et al. (1979) determined the statistical parameters for concrete compressive strength, tensile strength, and modulus of elasticity. Data were compiled from many published and unpublished studies to determine these parameters.

Concrete in compression exhibits large variability from multiple sources: material properties and proportions of the mix; variations in mixing, placing and curing; variations in test procedures; and variations between test specimens and in-situ data. Equation 2.18 is the relationship between the strength of concrete within structures and the specified strength assumed by Mirza et al. (1979).

$$f'_{c,is,R} = f'_c\left(r_{c,real} r_{in-situ} r_R\right) \tag{2.18}$$

where $r_{c,real}$ relates the cylinder strength to the specified design strength, $r_{in\text{-}situ}$ relates the in-situ compressive strength to the cylinder strength, and r_R considers the rate of loading. Using relationships described in the literature, Equation 2.19 and Equation 2.20 are proposed to determine the mean in-situ compressive strength for a loading rate of R.

$$f'_{c,is,R} = f'_{c,is}[0.89(1 + 0.08 logR)] \tag{2.19}$$

where

$$f'_{c,is} = 0.675 f'_c + 1100 \leq 1.15 f'_c \ \ (psi) \tag{2.20a}$$

$$f'_{c,is} = 0.675 f'_c + 7.584 \leq 1.15 f'_c \ \ (MPa) \tag{2.20b}$$

In addition, the coefficient of variation for a specified concrete strength ($V_{c,is,R}$) is calculated using Equation 2.21.

$$V^2_{c,is,R} = V^2_{c,cyl} + 0.0084 \tag{2.21}$$

The coefficient of variation for the cylinder strength ($V_{c,cyl}$) was determined from a literature review. It was reported that the coefficient of variation for field-cast laboratory-cured cylinders with strengths less than 4000 psi [28 MPa] can be taken as 0.10, 0.15, and 0.20 for excellent, average, and poor quality concrete. Above 4000 psi [28 MPa], the standard deviation remains constant at 400 psi [2.8 MPa], 600 psi [4.2 MPa], and 800 psi [5.6 MPa] for excellent, average, and poor quality concrete respectively (Mirza et al., 1979). It was recommended by Mirza et al. (1979) to assume a normal distribution for concrete compressive strength.

It is well established that a relation exists between the strength of concrete in tension and the concrete compressive strength. Several relations were established from regression analysis for the determination of concrete tensile strength as a function of the compressive strength. Data were collected for the splitting strength and modulus of rupture and regression was then conducted for each set of data. The tensile strength of concrete is effected by the size and type of aggregate, air entrainment, curing conditions, water to cement ratio, cement content, and the age of the specimen at loading. However it is most common and convenient to relate the compressive strength to the tensile strength.

The variability from the regression trends was modelled as a random variable described by Equation 2.22.

$$A = \frac{f_t(observed)}{a(f_c)^n} \tag{2.22}$$

where the coefficients *a*, and *n* are determined from regression analysis. The distributions of *A* for splitting strength and modulus of rupture are shown in Fig.2.3. The parameter *A* has a mean of 1.0 for both the splitting and modulus of rupture. The coefficients of variation for splitting and modulus of rupture are 0.13 and 0.20 respectively.

Mirza et al (1979) identified three main areas contributing to the variation of the tensile strength of concrete: the effect of volume, the speed of loading, and the effect of being in-situ. The effect of volume was considered insignificant to the work of Mirza et al. (1979) and thus neglected for the analysis. Insufficient data were available to capture the effect of in-situ versus controlled specimens and thus the in-situ mean compressive strength was used. Lastly, previously determined rate effects were incorporated to establish an expression for the mean tensile strength. Equation 2.23 represents the general form of the statistical relationship. Equation 2.24 and Equation 2.25

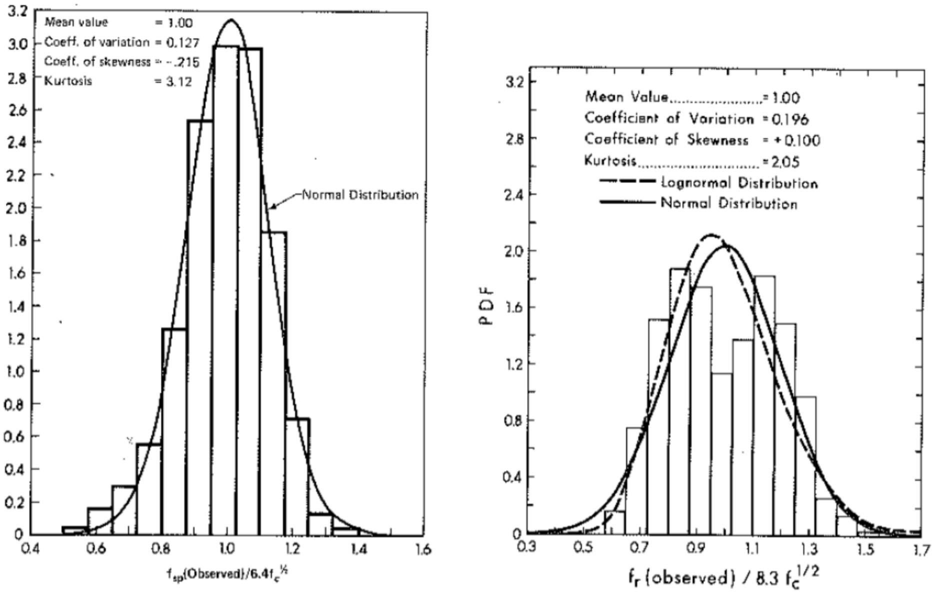

(a) (b)

Fig.2.3: Histogram and assumed distributions for (a) splitting strength and (b) modulus of rupture. Taken from Mirza et al. (1979)

are the forms derived from the data present in the study for splitting tests and modulus of rupture respectively.

$$f'_{t,is,R} = A\left(a\left(f'_{c,is}\right)^{n}\right)r_R \tag{2.23}$$

$$f'_{sp,is,R} = \left(6.4\left(f'_{c,is}\right)^{0.5}\right)[0.96(1 + 0.11logR)] \quad (psi) \tag{2.24a}$$

$$f'_{sp,is,R} = \left(0.5314\left(f'_{c,is}\right)^{0.5}\right)[0.96(1 + 0.11logR)] \quad (MPa) \tag{2.24b}$$

$$f'_{r,is,R} = \left(8.3\left(f'_{c,is}\right)^{0.5}\right)[0.96(1 + 0.11logR)] \quad (psi) \tag{2.25a}$$

$$f'_{r,is,R} = \left(0.6892\left(f'_{c,is}\right)^{0.5}\right)[0.96(1 + 0.11logR)] \quad (MPa) \tag{2.25b}$$

The coefficients of variation were derived for splitting strength and modulus of rupture. Equation 2.26 and Equation 2.27 represent the coefficients of variation for splitting strength and modulus of rupture respectively.

$$V_{sp,is,R}^2 = \frac{V_{c,cyl}^2}{4} + 0.019 \geq V_{c,is,R}^2 \tag{2.26}$$

$$V_{t,is,R}^2 = \frac{V_{c,cyl}^2}{4} + 0.0421 \geq V_{c,is,R}^2 \tag{2.27}$$

The statistical properties of the modulus of elasticity of concrete were also studied. A similar approach used to generate the tensile strength statistics was adopted for the modulus of elasticity. The regression analysis considered the initial tangent modulus, and the secant modulus. Regression of test data resulted in Equation 2.28, which is used to predict the mean tangent modulus. The compressive strength of cylinders in the study ranged from 6.9 MPa (1000 psi) to 48.3 MPa (7000 psi). Mirza et al. (1979) recommended a coefficient of variation for the initial tangent modulus of 0.08. It is noted that multiple regression relationships were conducted, however the square root is most widely used and thus presented.

$$\bar{E}_{c,i} = 60400\sqrt{f_c} \;\; (psi) \tag{2.28a}$$

$$\bar{E}_{c,i} = 5015.3\sqrt{f_c} \;\; (MPa) \tag{2.28b}$$

Similarly, for the secant modulus, Equation 2.29 was derived and a coefficient of variation of 0.12 was recommended (Mirza et al., 1979).

$$\bar{E}_{c,s} = 55400\sqrt{f_c} \;\; (psi) \tag{2.29a}$$

$$\bar{E}_{c,s} = 4600.1\sqrt{f_c} \;\; (MPa) \tag{2.29b}$$

Incorporating the effects of loading rate, Equation 2.30 was proposed to predict the mean initial tangent modulus of elasticity.

$$\bar{E}_{c,i} = 60400\sqrt{f_c}(1.16 - 0.08\log R) \;\; (psi) \tag{2.30a}$$

$$\bar{E}_{c,i} = 5015.3\sqrt{f_c}(1.16 - 0.08\log R) \;\; (MPa) \tag{2.30b}$$

It was noted by the authors, that the mean secant modulus could be predicted using Hognestad's parabola for pre-peak compressive strength. The coefficients of variation for the initial tangent modulus and the secant modulus can be calculated using Equation 2.31 and Equation 2.32 respectively.

$$V_{Eci,is,R}^2 = \frac{V_{c,cyl}^2}{4} + 0.0085 \tag{2.31}$$

$$V_{Ecs,is,R}^2 = \frac{V_{c,cyl}^2}{4} + 0.0165 \tag{2.32}$$

In summary, all of the parameters investigated by Mirza et al. (1979) were assumed to follow a normal distribution. In the case of tensile strength and modulus of elasticity, regression equations were presented to calculate the mean of the distribution. Lastly, the coefficient of variation for each parameter are calculated based on the coefficients of variation for the quality of concrete.

2.3.2 Nessim et al. – 1993

The work done by Nessim et al. (1993) was focused on verification of the material resistance factors for the CSA-S474 code for the design of offshore structures in Canadian waters. The material resistance factors for the code were taken directly from the CAN3-A23.3 code; however, the nature of offshore structures requires generally higher concrete strengths and larger bar sizes for steel reinforcement. The material resistance factors were thus investigated to determine if an adjustment was required.

The study focused on the difference in design procedures in three areas: the variability of concrete strength, the variability of steel yield strength, and the variability in loading. The approach adopted by the study was to design the structures based on the CSA Code, the Det norske Veritas (DnV) rules, and then determine the reliability of the structural elements and compare it with the accepted reliability in the CSA Code.

The variation of concrete strength was determined based on a review of the literature. The results of several studies were compiled and used to determine the relationship between specified concrete strength and actual concrete strength in the structure. The relationship between actual compressive strength and specified compressive strength is described by Equation 2.33.

$$f'_{c,is} = \alpha f'_c \tag{2.33}$$

The mean and variance of the above relation are described by Equation 2.34 and Equation 2.35 respectively.

$$\overline{f_{c,\imath s}} = \bar{\alpha}\overline{f_c} \tag{2.34}$$

$$V^2_{c,is} = V^2_\alpha + V^2_c + V^2_\alpha V^2_c \tag{2.35}$$

The CSA Code uses two expressions to relate the mean compressive strength to the specified compressive strength. These equations were used by Nessim et al (1993) to determine the specified compressive strength for the strength data obtained from the literature. The expressions from the CSA Code are shown in Equation 2.36 and Equation 2.37.

$$f'_c = \overline{f'_c} - 1.4\sigma_c \qquad \sigma_c < 3.5\ MPa \tag{2.36}$$

$$f'_c = \overline{f'_c} - 2.4\sigma_c + 3.5 \qquad \sigma_c > 3.5\ MPa \tag{2.37}$$

Regression analysis on the pairs of specified compressive strength and mean compressive strength yielded Equation 2.38. The regression analysis is presented in Fig. 2.4.

$$\overline{f_{c,\imath s}} = 6.1 + 0.82 f'_c \tag{2.38}$$

In addition to the compressive strength predictions, the coefficient of variation was examined. A scatter plot of coefficient of variation versus compressive strength reveals that there is no discernible relationship and thus the coefficient of variation was concluded to be independent of the compressive strength. Fig. 2.5 shows the scatter plot of coefficient of variation and mean cylinder strength.

2.3.3 Stephens et al. – 1995

Stephens et al. (1995) conducted a reliability assessment for CANDU concrete containment

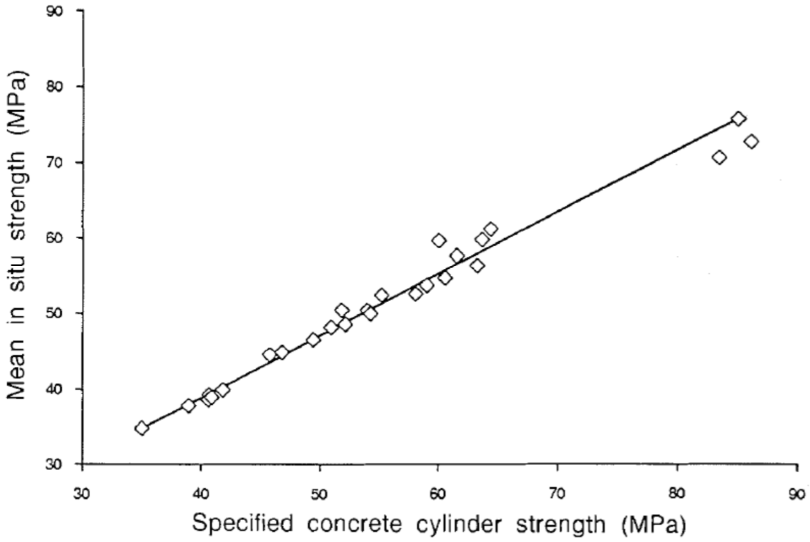

Fig.2.4: Results of regression analysis conducted by Nessim et al (1993) (Taken from Nessim et al., 1993).

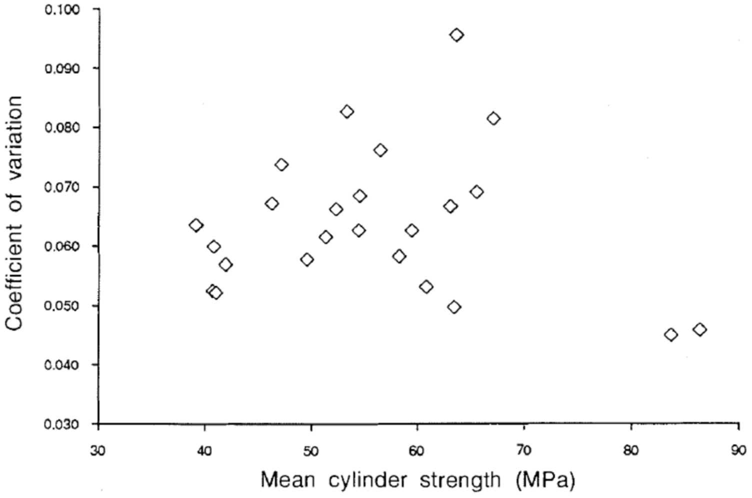

Fig.2.5: Scatter plot of coefficient of variation versus mean cylinder strength. Taken from Nessim et al. (1993).

structures. As a part of the assessment, it was desirable to use newly derived material resistance factors that might reflect a reduced variability for the concrete present within a containment structure. A combination of code equations were recalibrated to reflect the local distribution of concrete. The data collected from Pickering-A and Gentilly-2 containment structures is presented in Table 2.1.

The CAN3-A23.3-M84 Code calculates material resistance factors by scaling the specified compressive strength up to the mean compressive strength, and then scaling back the mean compressive strength to achieve a specified level of probability. This results in Equation 2.39, which is used to calculate the material resistance factors.

$$\phi_c = a_c(1 - b_c \upsilon_c) \tag{2.39}$$

In Equation 2.39, a_c relates the specified strength to the in-situ mean strength, b_c reflects the desired probability of non-exceedence, and υ_c is the material's coefficient of variation. The average standard deviation from Table 2.1 was used along with code acceptance criteria to determine an expression for the 28-day strength given the specified strength. This can be used in the determination of a_c.

Table 2.1: Raw data used by Stephens et al. (1995) in the determination of material resistance factors (Taken from Stephens et al., 1995).

Specified Strength MPa (psi)	28 day Cylinder Strength f_{c28} MPa (psi)	Standard Deviation on Strength σ_{c28} MPa (psi)	Coefficient of Variation on Strength v_{c28} MPa	Predicted Cylinder Strength(3) f_{c28} MPa (psi)	Test - to - Predicted Cylinder Strength Ratio
Gentilly - 2 Complex (1) (1974 - 1982)					
20.7 (3000)	27.6 (4005)	3.45 (500)	0.125	25.6 (3710)	1.08
27.6 (4000)	36.0 (5220)	3.45 (500)	0.096	32.5 (4715)	1.11
34.5 (5000)	40.3 (5845)	3.65 (530)	0.091	39.4 (5715)	1.02
Pickering - A (2)					
20.7 (3000)	28.2 (4090)	3.43 (493)	0.12	25.6 (3710)	1.10

Note:
(1) comprehensive data set compiled by Quebec Hydro.
(2) compiled by C-FER from limited survey of reactor building concrete strength data
(3) strength prediction based on Equation [4.11].

The average coefficient of variation reported in Table 2.1 is calculated to be 0.11 (Stephens et al., 1995). This is slightly more than the coefficient of variations reported by Mirza et al. (1979) which is 0.1 for excellent construction. Stephens et al. (1995) also notes that the coefficient of variation of 0.11 was reported in previously published data.

2.3.4 Bartlett and MacGregor – 1996

Concrete compressive strength typically refers to the 28-day cylinder strength of a concrete sample that is specified by the designer. However, it is common and expected that the actual in-situ strength will be greater than the specified compressive strength. The cylinder strength is routinely tested in the construction of any structure to ensure quality in the material properties. A relationship exists between the specified strength from a designer and the actual compressive strength of concrete within a structure. Bartlett and MacGregor (1996) investigated the relationship between specified strength of concrete and the actual in-structure strength of concrete. The variation between specified and actual compressive strength was disaggregated into two factors: the variation between specified concrete strength and concrete cylinder strength, and the variation between cylinder strength and actual strength within the structure (Bartlett and MacGregor, 1996). The in-structure strength is then calculated as the product of the two factors with the specified compressive strength. The in-structure strength is calculated using Equation 2.40 through Equation 2.42.

$$f_{c,is} = F_1 F_2 (f'_c) \tag{2.40}$$

where:

$$F_1 = (f_{cyl}/f'_c) \tag{2.41}$$

$$F_2 = (f_{c,is}/f_{cyl}) \tag{2.42}$$

The results of statistical regression yielded that F_1 could be modelled as a normal or lognormal distribution. Similarly, F_2 is modelled as a normal or lognormal distribution and is a function of the age in days (a), the cement and fly ash content per cubic metre of concrete (fa^F), the cement content (c), and a Heaviside variable set to 1 if the depth of the member is greater than or equal to 450 mm, and zero otherwise (Z_h). The results of the F_1 and F_2 statistical calibrations are presented in Table 2.2. Equation 2.43 is used to predict the mean value of F_2.

$$\hat{F}_2 = 0.948 + 0.084Z_h + 0.100\ln\left(\left(\frac{a}{28}\right)\left[1 + 0.090\left(\frac{fa^F}{c}\right)\right]\right) \tag{2.43}$$

Table 2.2: Summary of statistical results from Bartlett and MacGregor (1996)

Parameter	Cast-in-Place Concrete		Precast Concrete	
	Mean	COV	Mean	COV
F1	1.25	0.104	1.19	0.05
F2	-	0.14	-	0.14

The regression was repeated assuming that the mean F_2 value had a lognormal distribution which yielded Equation 2.44.

$$ln\{\hat{F}_2\} = ln\left\{0.936 + 0.085Z_h + 0.097\ln\left(\frac{a}{28}\right)\left[1 + 0.88\left(\frac{fa^F}{c}\right)\right]\right\} \tag{2.44}$$

Using the assumption that both F_1 and F_2 follow a lognormal distribution, an expression could be derived for the expected value of the product of F_1 and F_2. The expected value of the product of F_1 and F_2 is described by Equation 2.45.

$$E[F_1F_2] = 1.205 + 0.105Z_h + 0.125\ln\left(\frac{a}{28}\right) \tag{2.45}$$

The product of F_1 and F_2 can be modelled as a lognormal random variable with a coefficient of variation of 0.186 (Bartlett and Macgregor, 1996). Combining Equation 2.40 and Equation 2.45 yields Equation 2.46 which represents an expression for the mean compressive strength within the structure given the specified compressive strength.

$$\bar{f}_{c,is} = \left\{1.205 + 0.105Z_h + 0.125\ln\left(\frac{a}{28}\right)\right\}f_c' \tag{2.46}$$

It is noted that this study considers all construction to be of average quality with the exception of precast concrete.

2.3.5 Nowak and Szerszen – 2003

Nowak and Szerszen (2003) compiled a large database of concrete compressive strength for calibration of the ACI-318 building code. In a similar approach to Bartlett and MacGregor (1996), Nowak and Szerszen (2003) assumed that a bias factor was applied to the specified strength of concrete to determine the actual sample mean for a given compressive strength. It was identified that all categories of concrete (low density, high strength, normal) follow a normal distribution (Nowak and Szerszen, 2003). Deviation from the normal distribution at the lower end of the distribution tails were attributed to outliers in the sample data (Nowak and Szerszen, 2003). Equation 2.47 was developed by Nowak and Szerszen (2003) and is used for calculating the bias factor for all categories of concrete.

$$\lambda = -0.0081(f_c')^3 + 0.1509(f_c')^2 - 0.9338(f_c') + 3.0649 \text{ (ksi)} \qquad (2.47)$$

The mean strength is obtained as the product of the bias factor and the specified strength. It was noted by Nowak and Szerszen that the coefficient of variation for concrete compressive strength was fairly constant across all types of concrete investigated. The average coefficient of variation was 0.101 and the coefficient of variation used in the calibration of the ACI-318 material resistance factors is 0.1.

2.3.6 Bartlett – 2007

For the calibration of the CSA A23.3-04 code, Bartlett (2007) re-examined the F_1 and F_2 factored presented by Bartlett and MagGregor (1996). The results from the 1996 study were compared to the results obtained from Nowak and Szerszen (2003). It was observed that F_1 factor for each study were similar: 1.25 for Bartlett and MacGregor (1996) and 1.24 for Nowak and Szerszen (2003).

Two additional factors were added to Equation 2.40 to account for the variability of in-place strength. The first, $F_{i\text{-}p}$, is used to capture the variability of in-place strength. $F_{i\text{-}p}$ has a mean value of 1.0 and a coefficient of variation of 0.130 (Bartlett, 2007). Additionally, the parameter F_r was added from the Mirza et al. (1979) study to capture loading rate effects. Equation 2.48 was used for the CSA A23.3-04 Code calibration.

$$f_{c,is} = F_1 F_2 F_{i-p} F_R (f'_c) \tag{2.48}$$

2.3.7 Vincent et al. – 2011

An experimental program was conducted by Vincent et al. (2011) to determine the distributions for variability of concrete compressive strength, modulus of elasticity, and tensile strength. The two sources of variation considered were the variability from batching, and the variability from transport to site. The variability from in-situ placement, compaction, temperature history, and curing conditions were outside of the scope of the study defined by Vincent et al. (2011).

Samples were collected in a laboratory, and at various construction sites throughout the city of Adelaide, Australia. Two common strengths were selected for the study: N32 and N40 concrete. The "N" indicates that the mixes are normal concrete, and the numerals indicate the specified strength in MPa. Each set of samples was tested to determine the compressive strength, the modulus of elasticity, and the splitting strength at 7 and 28 days. It was noted by the author that the modulus of elasticity testing is non-destructive and therefore the reported values are the average of three consecutive tests.

The overall amount of data was limited. The number of 7 day samples for each site cured cylinder measurement type ranged from 1 to 6 samples for each parameter with a total of 26 samples. The 28 day samples ranged from 3 to 11 samples for each parameter with a total of 38 samples. The laboratory compressive strength tests for 7 and 28 days consisted of 95 and 116 samples respectively. However the modulus of elasticity for 7 and 28 day tests consisted of a total of 8 samples, and the splitting test a total of 6 samples.

The splitting strength of the samples was converted to the modulus of rupture using relationships established in the literature. This was done because the modulus of rupture was considered important for the prediction of cracking for flexural elements. The results of the experimental program are presented in Table 2.3.

The average coefficient of variation for the 28-day compressive strength tests was 0.12. This is consistent with the results of Mirza et al. (1979), Stephens (1995), and Nowak and Szerszen (2003). Bartlett and MacGregor (1996) suggested a much higher coefficient of variation of 0.186.

Table 2.3: Experimental program results from Vincent et al. (2011).

Parameter	Curing Program	7-day material properties				28-day material properties			
		Mean		COV		Mean		COV	
		N32	N40	N32	N40	N32	N40	N32	N40
Compressive Strength	Laboratory	24.96	32.27	0.09	0.11	37.23	47.01	0.07	0.08
	Site	21.02	26.15	0.07	0.08	28.7	31.92	0.13	0.16
Modulus of Elasticity	Laboratory	29120	35290	0.10	0.07	35709	38350	0.10	0.10
	Site	25750	29390	0.11	0.07	29750	33320	0.13	0.08
Tensile Strength	Laboratory	2.68	3.17	N/A	0.07	3.61	4.27	N/A	0.07
	Site	2.13	2.82	N/A	0.06	3.14	3.48	0.04	0.09

The difference between this study and Bartlett and MacGregor (1996) may be a result of the small sample sizes in Vincent et al. (2011) and Stephens (1995). The variation captured by the Bartlett and MacGregor encompasses more samples, and more factors that influence variability. It is noted that the site cured cylinders exhibit a coefficient of variation of 0.16 which is closer to Bartlett and MacGregor (1996).

Vincent et al. (2011) conducted a linear regression analysis to determine the relationship between the root compressive strength and the modulus of elasticity as well as the root compressive strength and the splitting strength. The following regression model in Equation 2.49 was assumed for both analyses.

$$Y = \theta_1\sqrt{X} + \theta_2 + \delta \tag{2.49}$$

where θ_1 and θ_2 are the regression parameters, and δ is a random variable with a mean of zero and a standard deviation from the regression model residuals. Y represents the parameter of interest, either modulus of elasticity or splitting strength, and X represents the 28-day cylinder strength. The results of each regression analysis are presented in Table 2.4.

2.3.8 Wisniewski et al. - 2012

Wisniewski et al. (2012) summarized their work done on the probabilistic descriptions of concrete material properties aggregated from previous studies in Europe and North America. The authors

Table 2.4: Regression analysis results from Vincent et al (2011).

Y	θ_1	θ_2	Residual Standard Deviation
Modulus of Elasticity	5850.6	0	2846.8
Splitting Strength	0.845	-1.415	0.270

proposed distribution equations for concrete compressive strength based on a total of 534 samples of site cast concrete, and 158 samples of plant cast concrete. These equations were proposed from an exhaustive review of concrete material property statistics, as well as collected experimental data. The model proposed by Bartlett and MacGregor was used, however the parameters F_1 and F_2 were aggregated into a bias factor similar to that of Nowak and Szerszen (2003). The statistical parameters determined by Wisniewski et al. (2012) are presented in Table 2.5

Table 2.5: Statistical parameters reproduced from Wisniewski et al. (2012).

Concrete Type	Nominal f_c' [MPa]	Bias Factor λ_c	Standard Deviation σ_c [MPa]	COV V_c [%]
Site Cast Concrete	25	1.26	2.9	7.7
	30	1.18	3.3	7.5
	40	1.18	3.4	5.8
Plant Cast Concrete	25	1.23	4.0	8.8
	30	1.08	2.3	4.7
	40	1.08	2.4	4.45
	45	1.00-1.02	2.2-2.9	3.9-5.2

The authors noted that these statistical models were in agreement with other researchers, however the coefficients of variation differed. The work by Wisniewski et al. (2012) showed a fairly constant standard deviation which resulted in a changing coefficient of variation. Additionally, the coefficient of variation tended to decrease with increased strength. It is unclear whether the variability observed by other reviewed works is indicative of North American concrete, and that the work by Wisniewski et al. (2012) is applicable to European concrete.

2.3.9 Unanwa and Mahan – 2014

A large numerical study was conducted by Unanwa and Mahan (2014) to assess the statistical properties of concrete compressive strength in California highway bridges. Cylinder data were obtained from the Caltrans Transportation Laboratory. A total of 3269 data points were collected for compressive strengths of 25, 28, and 35 MPa specified concrete strengths from bridges built between 2007 and 2011.

The age of samples at testing, t, ranged from 1 to 100 days. Regression analysis on the samples was conducted to establish a relationship between the cylinder strength and the age of the cylinder. Equation 2.50 through Equation 2.52 represent the results of the regression for 25, 28, and 35 MPa concrete respectively.

$$f_{c,cyl}^{t} = 8.763\ln(t) + 6.731 \tag{2.50}$$

$$f_{c,cyl}^{t} = 12.021\ln(t) - 0.309 \tag{2.51}$$

$$f_{c,cyl}^{t} = 13.0333\ln(t) + 3.248 \tag{2.52}$$

Equation 2.50 through Equation 2.52 were then evaluated at set intervals and normalized based on the specified 28-day strength. Regression of this data resulted in Equation 2.53, which is used to predict the cylinder strength at a time t given the 28-day cylinder strength.

$$f_{c,cyl}^{t} = [0.2752\ln(t) + 0.083] f_{c,cyl}^{28} \tag{2.53}$$

Equation 2.53 was then rearranged to produce Equation 2.54. This can be used as a tool to assess the quality of concrete at early tests by using early test results to predict 28-day cylinder strength.

$$f_{c,cyl}^{28} = \frac{1}{[0.2752\ln(t) + 0.083]} f_{c,cyl}^{t} \tag{2.54}$$

It is noted by Unanwa and Mahan (2014) that there exists significant dispersion in the 28-day cylinder strengths. The authors attributed this dispersion to batch-to-batch variability, and within-batch variability. The statistical parameters of the 28-day strengths are presented in Table 2.6.

Table 2.6: Normalized statistics for 28-day cylinder strengths. Taken from Unanwa and Mahan (2014).

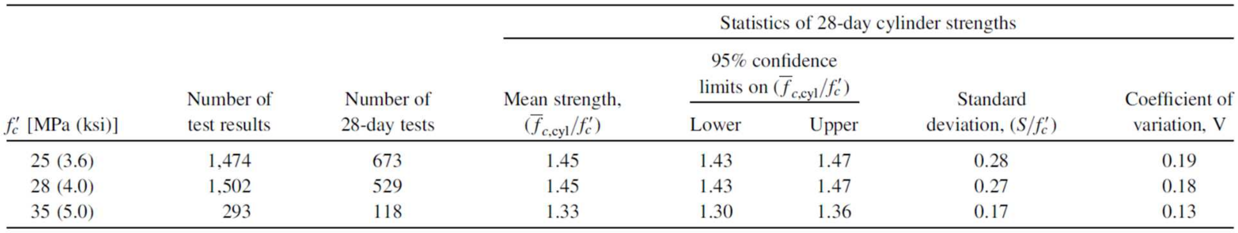

			Statistics of 28-day cylinder strengths				
				95% confidence limits on $(\bar{f}_{c,\mathrm{cyl}}/f'_c)$			
f'_c [MPa (ksi)]	Number of test results	Number of 28-day tests	Mean strength, $(\bar{f}_{c,\mathrm{cyl}}/f'_c)$	Lower	Upper	Standard deviation, (S/f'_c)	Coefficient of variation, V
25 (3.6)	1,474	673	1.45	1.43	1.47	0.28	0.19
28 (4.0)	1,502	529	1.45	1.43	1.47	0.27	0.18
35 (5.0)	293	118	1.33	1.30	1.36	0.17	0.13

In order to determine the distribution of in-place compressive strength for California highway bridges, Unanwa and Mahan (2014) proposed a model for relating the mean in-place compressive strength to the specified compressive strength. This model is shown in Equation 2.55 through Equation 2.58.

$$\bar{f}^{t}_{c,in-place} = f_1 f_2 f_3 f'_c \tag{2.55}$$

where:

$$f_1 = \bar{f}_{c,cyl}/f'_c \tag{2.56}$$

$$f_2 = \bar{f}_{c,hard,28-day}/\bar{f}_{c,cyl} \tag{2.57}$$

$$f_3 = \bar{f}^{t}_{c,hard}/\bar{f}_{c,hard,28-day} \tag{2.58}$$

The parameter f_1 relates the specified 28-day strength to the mean cylinder strength. Unanwa and Mahan (2014) used the data presented in Table 2.6 as the values of f_1 for each of the specified compressive strengths. The parameter f_2 relates the cylinder strength to the in-structure strength at 28 days. Various values were obtained from literature and the average of 0.81 was used. The parameter f_3 is added to convert the 28-day in-structure strength to the strength at any time t. Data from experimental studies in the literature was compiled and a regression analysis yielded Equation 2.59.

$$f_3 = e^{\left[0.3\left(1-\sqrt{28/t}\right)\right]} \tag{2.59}$$

The model proposed by Unanwa and Mahan (2014) was compared against the model proposed by Bartlett and MacGregor (1996). Predictions from both models were found to be in agreement for compressive strengths of 25 MPa and 28 MPa. However the prediction for 35 MPa by Unanwa and Mahan (2014) was lower than that by Bartlett and MacGregor (1996). The authors attribute this to the fact that Bartlett and MacGregor (1996) assumed that the ratio of cylinder strength to specified strength (f_1) is independent of the specified strength. Literature reviewed by Unanwa and Mahan (2014) suggest that this relationship decreases as the specified strength increases. This assumptions is suggested as the major contributor to the discrepancies observed between models (Unanwa and Mahan, 2014).

Unanwa and Mahan (2014) tested their model against actual experimental data collected from a 28 year-old bridge in California. The results of the experimental data concluded that the mean in-place strength of the bridge was 1.57 f_c'. This was close to the predicted relationship which was calculated to be 1.56 f_c'. Unanwa and Mahan (2014) note that this excellent agreement must be validated with additional experimental data from varying ages and structures.

2.4 Steel Material Property Statistics

This section reviews literature that investigates the statistical models of steel material properties as presented in the literature. The parameters reviewed include the steel yield strength, ultimate strength, and modulus of elasticity.

2.4.1 Mirza and MacGregor – 1979

As part of the studies conducted in the late 1970s to determine material resistance factors for limit state design, Mirza and MacGregor (1979) conducted a study of the mechanical properties of reinforcing bars used in reinforced concrete structures. Mirza and MacGregor identified five sources that contribute to the variability of the yield strength of reinforcing bars:

1. variation in yield strength of the material,
2. variation in reinforcing bar cross-sectional area,
3. effect of loading rate,
4. effect of bar size on mechanical properties,
5. and effect of strain at which yielding is defined.

A review of the literature showed that variability within a single bar was minimal, variability within a batch of bars was small, and the variability within a group of bars from different batches may be large. The study conducted by Mirza and MacGregor (1979) was limited to deformed reinforcing bars of Grade 40 and Grade 60 steel.

A number of distributions were fit to the test data for the static yield strength based on nominal cross-sectional area. Basing the variability yield strength on the nominal cross-sectional area is advantageous because the nominal area is used in design and has a strain rate that is closer to the rates observed in actual structural loading (Mirza and MacGregor, 1979). Mirza and MacGregor (1979) noted that a normal distribution was initially selected however it does not accurately capture the behaviour of either tails. A beta distribution was found to be more representative of the data. The beta distribution for Grade 40 and Grade 60 steel are presented in Equation 2.60 and Equation 2.61 respectively. The parameter f_{ys} is the static yield strength in ksi based on the nominal cross-sectional area.

$$PDF = 4.106\left(\frac{f_{ys} - 33}{29}\right)^{2.21}\left(\frac{62 - f_{ys}}{29}\right)^{3.82} \tag{2.60}$$

$$PDF = 7.587\left(\frac{f_{ys} - 54}{48}\right)^{2.21}\left(\frac{102 - f_{ys}}{48}\right)^{6.95} \tag{2.61}$$

A distribution for the ultimate strength of steel was also derived. Similar to the yield strength, the ultimate strength was found to be described by a beta distribution. Equation 2.62 and Equation 2.63 describe the distributions for the ultimate strength of steel based on the nominal cross-sectional area for Grade 40 and Grade 60 steel. The parameter f_{us} is the static ultimate strength in ksi based on the nominal cross-sectional area.

$$PDF = 2.646\left(\frac{f_{us} - 51}{45}\right)^{2.21}\left(\frac{96 - f_{us}}{45}\right)^{3.82} \tag{2.62}$$

$$PDF = 4.922\left(\frac{f_{us} - 84}{74}\right)^{2.21}\left(\frac{158 - f_{us}}{74}\right)^{6.95} \tag{2.63}$$

The modulus of elasticity was determined to be normally distributed with a mean of 201 000 MPa and a coefficient of variation of 0.033.

The selection of beta distributions artificially confines the yield strength and ultimate strength of reinforcing steel to definite lower and upper bounds. This means that the models are not transferable to other grades of reinforcing steel. If other grades of reinforcing steel are selected, it may be reasonable to scale the distributions and range by the ratio of the yield strengths to the actual strengths. However, the accuracy of this procedure is untested and more work is required to assess the viability of the proposed transformation. For now, this author recommends that the reader use these distributions only with 40 ksi and 60 ksi steel.

2.4.2 Nessim et al. – 1993

Nessim et al. (1993) compiled an updated set of data for reinforcing steel bars from a Canadian steel manufacturer. A summary of the data is reproduced in Table 2.7. Steel reinforcement with a nominal yield strength of 400 MPa was tested for bar sizes ranging from 20M to 35M.

Table 2.7: Yield strength data reported by Nessim et al. (1993).

Grade (MPa)	Bar Size	No. of Specimens	Mean yield strength, f_s	Standard Deviation, σ_s	Bias Factor	Coefficient of Variation, V_s
400	20M	98	481	19	1.20	0.040
400	25M	84	470	44	1.18	0.094
400	30M	52	446	22	1.12	0.049
400	35M	40	473	27	1.18	0.057

Nessim et al. (1993) concluded that there is no significant effect due to bar size on the yield strength of a material. It is noted that the yield strength in Table 2.7 is calculated by dividing the yield force by the nominal area. This captures both the variation in actual yield stress and variations in bar cross-sectional area. Additionally, the data are from one manufacturer and thus may contain less variability than reported in the literature. Nessim et al. (1993) concluded that the yield strength could be modelled as a lognormal distribution with mean of 470 MPa and a coefficient of variation of 0.06.

2.4.3 Nowak and Szerszen – 2003

Nowak and Szerszen (2003) compiled an updated set of test data for 60 ksi (420 MPa) steel reinforcement. Data were collected for bar sizes ranging from No. 3 to No. 11. Analysis of the data reviled that no trends existed between the bar diameter and the mean strength. Additionally, Nowak and Szerszen (2003) report that all reinforcement yield strengths can be modelled with a normal distribution that has a bias factor of 1.145 (or a mean of 481 MPa) and a coefficient of variation of 0.05. A summary of the collected data has been reproduced in Table 2.8.

Table 2.8: Yield strength statistical parameters for 420 MPa steel taken from Nowak and Szerszen (2003).

Bar Size	No. of Samples	Mean yield f_y [MPa]	Bias λ	COV V [%]
9.5 mm (No. 3)	72	496.1	1.200	4.0
12.5 mm (No. 4)	79	473.3	1.145	6.5
15.5 mm (No. 5)	116	465.1	1.125	4.0
19 mm (No. 6)	38	476.1	1.150	5.0
22 mm (No. 7)	29	481.6	1.165	5.0
25 mm (No. 8)	36	473.7	1.145	5.0
28 mm (No. 9)	28	475.7	1.150	5.0
31 mm (No. 10)	5	470.2	1.140	4.0
34.5 mm (No. 11)	13	473.7	1.145	3.5

2.4.4 Wisniewski et al. - 2012

Wisniewski et al. collected approximately 500 test results for reinforcing steel from various European manufacturers and distributers in order to assess the modern day variability of steel reinforcement. The reinforcing bar diameters ranged from 10 mm to 25 mm. The results of the study are presented in Table 2.9

Table 2.9: Experimental results of Wisniewski et al. (2012) for steel reinforcement.

Parameter	Nominal Value	Bias λ	COV V [%]
f_{sy}	500 [MPa]	1.21	6.0
f_{su}	550 [MPa]	1.28	5.9
E_s	200000 [MPa]	1.01-1.03	1.0-4.9
ε_s	5%	2.7	24.5
A_s	70 – 726 mm^2	0.92-0.94	4.3-4.4

Wisniewski et al. (2012) noted that the distributions of all parameters in this study were consistent with other statistical models presented in the literature. Based on the data presented in the literature, and the current study, Wisniewski et al. (2012) recommended the following statistical parameters for steel reinforcement. The bias factor is disaggregated for old and new steel to be 1.20 and 1.15 respectively. A strict definition of new and old steel is not provided by the authors. The coefficient of variation for old and new steel should be 10% and 5% respectively. The ultimate strain at failure can be modelled with a lognormal or normal distribution with a mean of 0.1 mm/mm and a coefficient of variation of 15%. The modulus of elasticity for steel can be modelled as a normally distributed random variable with a mean of 202000 MPa and a coefficient of variation of 4%. Lastly the area of steel can be modelled as a normal distribution with a mean of 1.0 and a coefficient of variation of 2%. Wisniewski also identified the correlation matrix between various steel parameters. A strong correlation exists between the yield strength and ultimate strength of steel. Additionally, a negative correlation exists between the area of steel and the yield strength of steel. The correlation matrix is shown in Equation 2.64.

$$\rho = \left[\begin{array}{cccccc} & f_y & f_u & E_s & \varepsilon_s & A_s \\ f_y & 1.00 & 0.850 & 0.00 & 0.00 & -0.407 \\ f_u & 0.850 & 1.00 & 0.00 & 0.00 & 0.00 \\ E_s & 0.00 & 0.00 & 1.00 & 0.00 & 0.00 \\ \varepsilon_s & 0.00 & 0.00 & 0.00 & 1.00 & 0.00 \\ A_s & -0.407 & 0.00 & 0.00 & 0.00 & 1.00 \end{array}\right] \tag{2.64}$$

Wisniewski et al. (2012) also studied the variability of prestressing steel properties. Similar to the reinforcing steel study, based on a review of the literature and a set of experimental results, the following statistical models for prestressing steel were proposed. The ultimate strength can be modelled as a normal or a lognormal distribution with a bias factor of 1.04 and a coefficient of variation of 2.5%. The stochastic properties of prestressing steel is outside of the scope of this study and thus for more information, the reader is referred to Wisniewski et al. (2012).

2.5 Monte Carlo Simulation of Reinforced Concrete

This section outlines the Monte Carlo methods and simulations that are relevant to this thesis. Monte Carlo simulation is a method for generating random simulation results such that the simulation results possess similar statistical properties as an experiment. This is particularly useful when sufficient information is available to describe the input uncertainties in a physical experiment, when a model of the physical phenomena of the experiment is readily available, and when conducting the experiment is limited by available resources (i.e. cost and time). In order to capture the full extremes of an experiment, a large number of experiments are often required.

The Monte Carlo simulations work by generating statistically independent samples that follow the distributions of each of the input parameters. The mathematical relationship describing the variable of interests is then computed for each set of generated samples. This produces a set of outputs that can be statistically analyzed.

Reinforced concrete structural elements are excellent candidates for investigative Monte Carlo simulations. Large scale experimental procedures for reinforced concrete structural elements may not be financially feasible to conduct. Furthermore, reinforced concrete members cannot be reliably mass produced. The aggregate variability of concrete and steel material properties and the immense financial and labour costs associated with testing suggest that experimental studies aimed at evaluating the resistance distributions for reinforced concrete structural elements are infeasible. Thus Monte Carlo simulation is readily used in the reliability analysis of reinforced concrete structures. Several of these Monte Carlo simulations are described in this section.

2.5.1 Ramsay et al. – 1979

Ramsay et al. (1979) studied the short time deflection of reinforced concrete beams under service load conditions using a series of Monte Carlo simulations. A total of 10 T-beams and 10 one-way slabs were analyzed. The simulations did not consider variability in dead and live loading or the long-term effects due to sustained loading.

The theoretical model used in the Monte Carlo simulation determined deflections for the curvature along the length of the beam. The effective moment of inertia presented in Equation 2.65 was used in the study.

$$I_{eff} = I_g \left(\frac{M_{cr}}{M_a}\right)^3 + I_{cr}\left(1 + \left(\frac{M_{cr}}{M_a}\right)^3\right) \leq I_g \tag{2.65}$$

The cracked moment of inertia was assumed to be equal to the moment of inertia of the section when the tension steel began to yield. It was assumed that two regions exist in a fixed-fixed reinforced concrete beam: a region of negative moment, and a region of positive moment. Within these regions, the effective moment of inertia was considered constant.

When the load is applied and the beam begins to crack, moment redistribution is observed. The redistributed moment was computed based on an iterative approach where the elastic moment distribution was assumed, and then the effective moment of inertia was calculated. The moment distribution was then recalculated using the effective moment of inertia in each of the two regions. This was repeated until the moment distribution converged. The curvature was calculated based on the redistributed moment, and subsequently, the deflection was obtained.

The model was verified based on experiments from the literature; however, all of the experiments were simply supported and thus the moment redistribution could not be confirmed with experimental results.

The concrete material properties, the steel material properties, and the variability in member dimension were considered as stochastic inputs to the model. The distributions for these properties were obtained from previous studies. The Monte Carlo simulation was conducted for four load stages and a total of 500 random samples. The results of the Monte Carlo simulation indicated that there is a large increase in coefficient of variation when the applied load is close to the cracking load. As the load increases, the coefficient of variation for the deflection decreases as the section trends towards the cracked moment of inertia. A plot of the coefficient of variation for the deflection is reproduced in Fig. 2.6. This study concludes that the majority of the variability in the stiffness of the beam is due to concrete cracking. It was however noted that in smaller members, the variability in the placement of the bars contributed significantly to the response, and in some cases, the slab reinforcement yielded under service loads.

2.5.2 Mirza and MacGregor – 1982

Mirza and MacGregor (1982) conducted a series of Monte Carlo simulations to determine appropriate material resistance factors for reinforced concrete elements in the CSA A23.3 Code. The study was aimed at incorporating the load combination factors developed by the NBCC at the time. The authors outline the probabilistic approach to safety as a basic reliability random variable shown in Equation 2.66,

$$Y = R - Q \tag{2.66}$$

where R is the distribution of resistance, Q is the distribution of load, and Y is the failure function.

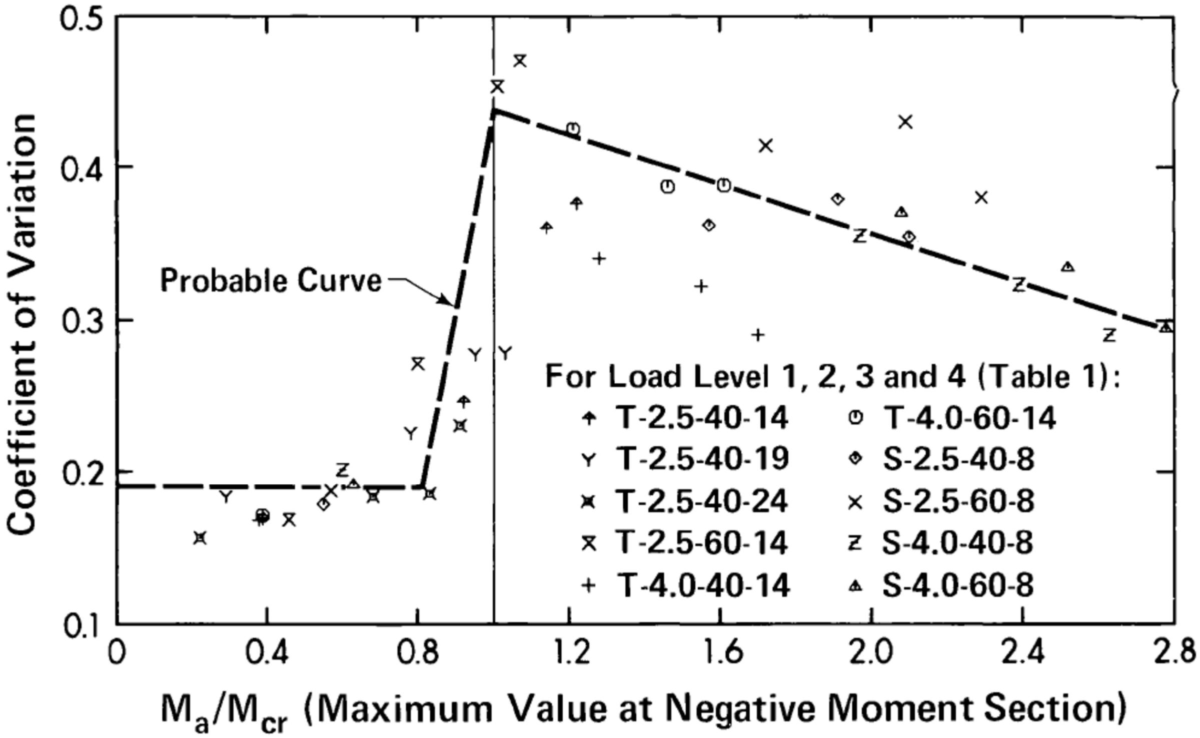

Fig. 2.6: Coefficient of Variation for the deflection of T-beams determined from the Monte Carlo simulations. (Taken from Ramsay et al 1979)

If Y is greater than zero, failure has not occurred. If Y is less than zero, the structure has failed and thus is considered not safe. The mean and the standard deviation are calculated using Equation 2.67 and Equation 2.68 respectively.

$$\bar{Y} = \bar{R} - \bar{Q} \tag{2.67}$$

$$\sigma_Y = \sqrt{\sigma_R^2 + \sigma_Q^2} \tag{2.68}$$

The random variable R was generated by selecting a series of common member sizes and dimensions and conducting a Monte Carlo simulation on each. The structural elements considered included flexural elements, combined flexure and axial elements (both slender and short), and prestressed flexural elements. The random inputs to the Monte Carlo simulation included: concrete strength, modulus of elasticity, and tensile strength; steel yield strength, modulus of elasticity, and bar cross-sectional area; and overall member size variation due to fabrication errors. This produced a distribution of R for each of the common members sizes. The input distributions for concrete and steel material properties were taken from Mirza and MacGregor (1979a) and Mirza and MacGregor (1979) respectively. The statistical properties for the prestressing reinforcement were obtained from a private company. The statistical properties for the dimension of the specimens were obtained from Allen (1970) and Ellingwood (1977).

There were three main assumptions in the Monte Carlo simulations for calculating resistance. The first was that the statistical properties corresponded with average construction and thus were representative of actual structures throughout Canada. Pretensioned prestressed concrete structures are most commonly plant-cast and thus are exempt from this assumption and excellent construction was assumed. Secondly, the effect of strain rates was ignored. Lastly, the statistical properties of reinforced concrete were assumed to be the 28-day cylinder strength. Long-term strength increases and creep effects were not considered in this study.

The resistance for each member was calculated using moment curvature relationships. In the case of a beam-column, the axial load was incrementally increased and the maximum moment from the moment curvature analysis was recorded in order to determine the interaction effects. When analyzing beams, the axial load was simply set to zero. Hognestad's parabola was assumed for the concrete stress-strain response, and the steel was assumed to be linear elastic, perfectly plastic. Tension stiffening effects were not considered and the concrete was assumed to be linear elastic with a brittle failure in tension. The shear resistance for concrete beams and columns was predicted by empirical equations obtained from literature. In the case of a slender column, the moment curvature relationship was used to predict the lateral deflection and second order effects were thus considered.

The Monte Carlo simulation results were normalized based on the nominal resistance. This generated a distribution of the strength ratio between the simulation results and the nominal resistance. The results of the Monte Carlo simulations were then utilized in the computation of the strength reduction factors for the CSA A23.3 Code. The reader is referred to the original paper for a description of how these factors are calculated.

2.5.3 Mirza – 1998

Mirza (1998) studies the distribution present in strength interaction diagrams for composite steel concrete columns. A composite reinforced concrete column consists of a structural steel section encased in a shell of concrete with or without reinforcing steel. This study investigated four short columns and six slender columns all of which were composite steel concrete columns. Each of the columns studied had unique combinations of concrete compressive strength, structural steel ratios, and slenderness ratios. The purpose of this study was to investigate the effect of these parameters on the interaction diagrams, and compare the predicted results with the CSA A23.3-M84 Code.

The slenderness ratios for the short columns were defined as zero, which represented cross-sectional analysis, and 21.9, which was the upper limit above which slenderness had to be considered. For the slender columns, the slenderness ratios were selected as 22.1, 33, and 66. The slenderness ratio of 66 was considered to be the practical limit.

The theoretical model for the concrete columns employed strain compatibility calculations of moment-curvature relationships with varying axial load. For each axial load, the maximum eccentricity was calculated through trial and error assuming a fourth-order deflected shape for the column. The largest curvature at mid-height that maintained equilibrium was used as a point on the interaction diagram. The concrete in compression was modelled using a modified Park and Kent model that considered confinement provided by the stirrups. The concrete tensile response was assumed to be brittle with no considerations for tension stiffening. Both the reinforcing bars and the structural steel were assumed to be linear elastic perfectly plastic.

The statistical properties for the steel and concrete were obtained from previous studies. It is noted that the distribution for the reinforcing steel is different than that of the structural steel. The yield strength for the structural steel follows a modified lognormal distribution with a cut-off. The yield strength for the reinforcing steel follows a beta distribution.

A Monte Carlo simulation was then conducted with 500 samples for each of the 10 columns. Each sample produced an interaction diagram for a column. In addition, the interaction diagram was calculating using the code procedure with all material resistance factors set to 1.0.

The simulation results were plotted as interaction diagrams that show the mean interaction response, the maximum and minimum response, the 1st percentile response, the mean cross-sectional strength (for slender columns), and the CSA prediction. In addition for a given e/h ratio, a histogram of the results is plotted. Fig. 2.7 is an example of the results obtained by Mirza (1998).

Mirza (1998) concluded that the relationship between nominal and theoretical strength is significantly affected by the slenderness ratio. The author recommended that a coefficient of variation of 0.14 to 0.15 can be assumed for compression governed failure. Similarly, a coefficient of variation of 0.06 to 0.08 can be assumed for a balanced or tension failure of a reinforced concrete column. The author further concluded that the CSA Code predictions are acceptable for composite steel concrete columns. Similar strength variability was observed when compared to regularly reinforced concrete columns and thus the resistance factors in the code are applicable to composite steel concrete columns.

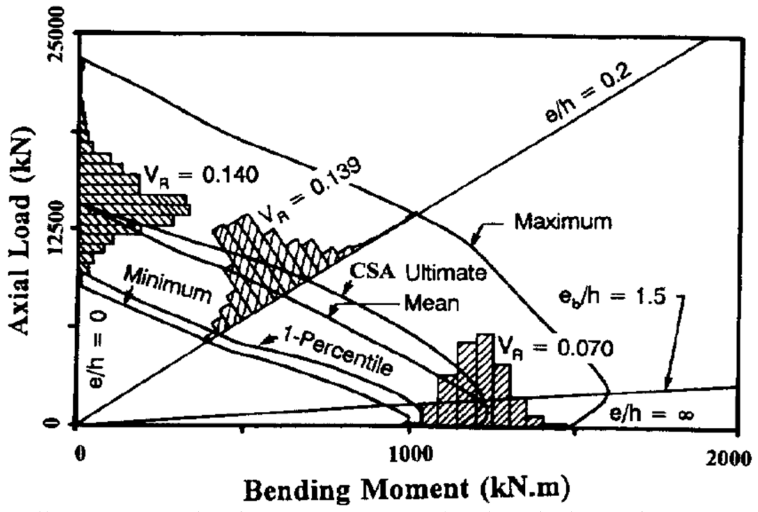

Fig. 2.7: Interaction diagram results from Monte Carlo simulation of a composite steel concrete column. Obtained from Mirza (1998).

2.5.4 Choi et al. – 2004

As an extension of Ramsay et al. (1979), Choi et al (2004) studied the deflection of reinforced concrete slabs and beams using Monte Carlo Simulations. The new study expanded the number of simulation combinations, considering six simply supported one way slabs, three fixed end one way slabs, and three two span continuous T-beams. In addition, the new study used a layered finite element beam approach for analysis of the deflection that considered tension stiffening effects. Lastly, Choi et al. (2004) considered the effects of long-term loading including two loading scenarios and the stochastic prediction of creep and shrinkage. The analytical model was validated using experimental data reported from the literature.

The sources of uncertainty considered by Choi et al (2004) included material properties, dimension properties, and two loading histories. The statistical parameters for the material properties and dimension variation were taken from the literature. The statistical properties for the long-term effects were taken from an ASCE publication. The two loading histories differed in their consideration for construction loading. The first loading history assumed a significant construction load as an instantaneous load. The second loading history did not contain a construction load.

Each parameter was considered independent with the exception of concrete compressive strength, modulus of elasticity, and modulus of rupture. To generate these random variables, the concrete compressive strength was generated randomly. This generated compressive strength was input into empirical equations to predict the modulus of elasticity and the modulus of rupture. These calculated values were assumed to represent the mean for each parameter, and then using the coefficients of variation, the distribution for each parameter could be generated. Using these distributions, a sample for the modulus of elasticity and the modulus of rupture were obtained.

The results of the study were plotted as histograms. It was observed that significant differences existed between various types of the structural elements. For some of the simply supported slabs, the instantaneous deflections were closely grouped about the mean deflection. This indicateed that the slab remained largely uncracked under service loading and thus exhibited small standard deviation. However, the long-term deflection for the same slab showed the reverse trend. A bimodal distribution was observed where the majority of the slab simulations resulted in larger deformations indicating a cracked slab. The deflection histograms of such a slab are illustrated in Fig. 2.8.

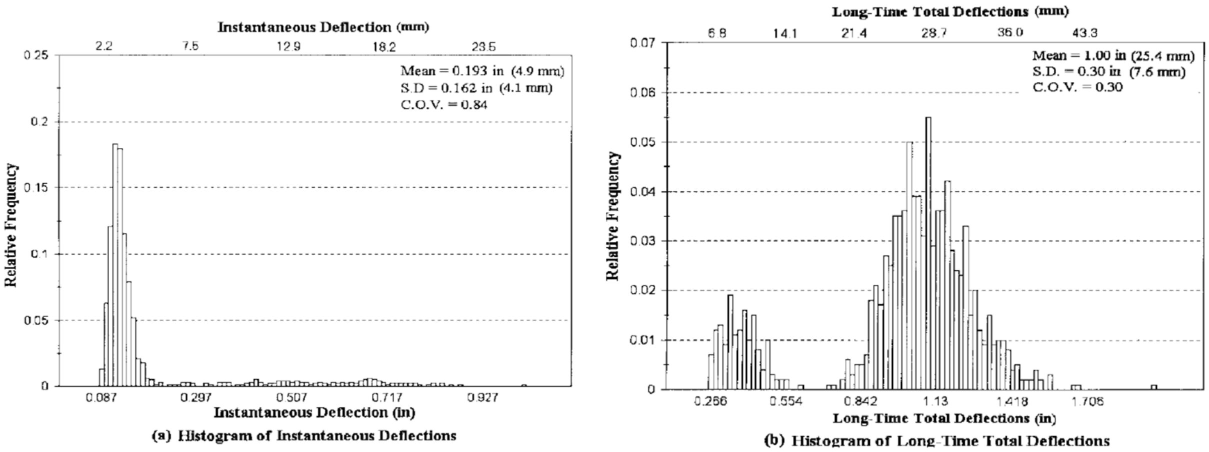

(a) Histogram of Instantaneous Deflections

(b) Histogram of Long-Time Total Deflections

Fig. 2.8: Monte Carlo simulation results for instantaneous and long-term deflection of a simply supported slab. Taken from Choi et al. (2004).

Choi et al. (2004) provided recommendations for the coefficients of variation in the calculation of service load-deflection based on three parameters. The first parameter was the ratio of applied moment to cracking moment, the second parameter was the reinforcement ratio, and the third parameter was the live load to dead load ratio. In general, the coefficient of variation was found to decrease as the applied load exceeded the cracking load. This confirmed the results of Ramsay et al. (1979). The same trend was observed for the increasing reinforcing ratio. This was explained by Choi et al. (2004) as a relationship between expected ultimate load, and increasing reinforcement ratio. As the ultimate limit state design load increased, the likelihood of experiencing a service load that exceeds cracking increased. Thus, structural elements designed with higher reinforcement ratios are more likely to crack under service loads, resulting in a decreased coefficient of variation. A solid relationship was not established for the live load ratio however it was noted the coefficient of variation is lower in the long-term. Choi et al. (2004) notes that the long-term deflection standard deviation is higher, but the mean is also increased resulting in a lower coefficient of variation.

In conclusion, the study confirmed the results observed by Ramsay et al. (1979) and provided a more accurate prediction of the deflections. However Choi et al (2004) recommended that the work be further extended to include uncertainty in the loading history of the structures for a better estimate of long-term deflection distributions.

2.5.5 Vincent et al. – 2011

Vincent et al. (2011) studied the variability of concrete material properties for Australian concrete. An effort was made to differentiate between site cured concrete, and lab cured concrete. The results of the material statistical distributions are presented in Section 2.3.7. The generated distributions were then used to perform a Monte Carlo study on the short-time deflections of two reinforced concrete beams and one prestressed concrete slab.

The theoretical model employed was a deflection equation based on elastic beam theory using an effective modulus of elasticity from the literature. The camber of the prestressed concrete slab was predicted using equations from Collins (1997). The Monte Carlo simulations produced a series of deflection predictions aimed at producing confidence intervals for deflection predictions of a given mix type. The authors established the confidence intervals for a cracked beam, an uncracked beam, and a prestressed slab. The authors noted that the current work could be generalized into a program that could predict confidence intervals for reinforced concrete structures.

2.5.6 Trends in Reinforced Concrete Monte Carlo Simulation Procedures

There are several trends that are common when conducting a Monte Carlo simulation for reinforced concrete structural elements.

Input Parameters

The input parameters most often considered in the literature were the concrete material properties, the steel material properties, and the dimensional properties. The concrete material properties considered include the compressive strength, the modulus of elasticity, and the tensile strength (in the form of direct tension or modulus of rupture). However, in studies concerned with long-term effects, statistical properties were considered for the creep and shrinkage coefficient. The assumed distributions for each of the concrete material properties are presented in Table 2.10.

Table 2.10: Assumed distributions for concrete material properties.

Material Property	Assumed Distribution
Compressive Strength	Normal / Lognormal
Tensile Strength	Normal
Modulus of Elasticity	Normal

The statistical properties considered for reinforcing steel were most commonly the modulus of elasticity, the nominal area of steel, and the yield strength. The assumed distributions for each of the steel material properties are presented in Table 2.11.

Table 2.11: Assumed distributions for steel material properties.

Material Property	Assumed Distribution
Yield Strength	Normal, Beta, or Lognormal
Nominal Steel Area	Truncated Normal
Modulus of Elasticity	Normal

The last common input property was the variation in assumed dimension for a given structural element. This is less important to the current work as a finite element approach will be taken using two-dimensional membrane elements. The type and scale of the structures modelled in VecTor2 may vary widely and thus the in-plane dimensions of the membrane elements encompasses a large range. It is thus difficult to incorporate the in-plane dimensions of the membrane element as a stochastic parameter built into the software. It may be more realistic to allow for user inputs that determine the distribution of thickness of the membrane elements, and that be employed in stochastic simulation. User input models could include stochastic representations of construction tolerances.

Validation of Theoretical Model

In all of the Monte Carlo simulations reviewed, a theoretical model was proposed to describe the parameter of interest. Despite the large range of complexity between studies, all of the studies verified the proposed theoretical model against deterministic results in the literature. It is recommended that for all Monte Carlo Simulations, the theoretical model be validated using results obtained from literature.

Analytical Needs

All of the simulations reviewed were primarily flexural elements. In the case of considering shear as a failure mode, the stochastic parameters were applied to the simplified empirical shear equations. Such an approach likely does not capture the transition in failure mode, and the interaction of shear behaviour and flexural behaviour. Stochastic simulations of shear-critical members, disturbed regions, or any other structural element that deviates from the simplified equations require more advanced analysis tools. Strut and tie models have been shown to represent a lower bound estimate of the strength of such structural elements, and thus it would not be prudent to use such techniques for reliability studies. A requirement then exists to study the reliability of such structures with advanced and accurate finite element models.

2.6 Corrosion in Reinforced Concrete

Corrosion in reinforced concrete structures can have significant implications for performance at the service and ultimate limit states. Structures at risk of corrosion attack often take the form of common infrastructure (eg. reinforced concrete bridges and parking structures). Two types of corrosion are reviewed in this thesis: uniform corrosion and pitting corrosion. The former is easier to predict but can be unrepresentative of real structural conditions. The latter remains a significant challenge as the corrosion tends to be stochastic in nature and exhibit significant spatial variation. This section outlines the basic principles and causes of reinforced concrete corrosion.

Corrosion of steel reinforcement can be approached as an electrochemical process where the iron atoms in the steel reinforcement react with water and oxygen to form a rust by-product. Equation 2.69 through Equation 2.71 are the chemical reactions for the anode, cathode, and overall process respectively.

$$2Fe \rightarrow 2Fe^{2+} + 4e^{-} \tag{2.69}$$

$$O_2 + 2H_2O + 4e^- \rightarrow 4OH^- \tag{2.70}$$

$$2Fe + 2H_2O + O_2 \rightarrow 2Fe(OH)_2 \tag{2.71}$$

Due to the pH of concrete and the formation of the passive layer, corrosion does not occur immediately. The time to corrosion is affected by the moisture content and resistivity of concrete, the temperature of the surrounding atmosphere, the availability of oxygen, and the pH of the pore water (Hunkler, 2005).

The natural alkalinity of concrete typically protects the reinforcement from corrosion. With a pH of 12, a passive layer forms around the reinforcement that prevents corrosion form occurring. There are two processes that destroy this passive layer and thus allow corrosion to occur: carbonation of concrete, and chloride attack (Hunkler, 2005).

Carbonation of concrete is the reduction of pH in the concrete pore water. This occurs when carbon dioxide is naturally dissolved into the pore water and reacts with the alkaline components of the cement paste. Additionally, water is required for this reaction to take place. The pH of the concrete pore water can be reduced from greater than 12 to between 6 and 9. This reduction of pH allows corrosion to occur. Carbonation causes uniform corrosion that leads to early cracking and spalling of reinforced concrete cover. Because the corrosion is uniform, the cross-sectional area is typically minimally affected (Hunkler, 2005).

Chloride attack results in a substantially different from of reinforced concrete corrosion. Corrosion as a result of chloride attack can be extremely localized and may not show any exterior signs of deterioration. The cross-sectional area of the steel reinforcement is significantly affected. The chloride ions destroy the passive layer around the steel reinforcement, reduce the pH of the pore water, increase the moisture content of the concrete, and increase the electrical conductivity of the concrete (Hunkler, 2005).

There are two types of cells in which the galvanic corrosion reactions can occur: a macro-cell and a micro-cell. A macro-cell occurs between different reinforcing bars within a reinforced concrete element. Fig. 2.9 is an illustration of a macro-cell. A micro-cell occurs along the same reinforcing bar. Fig. 2.10 is an illustration of a micro-cell.

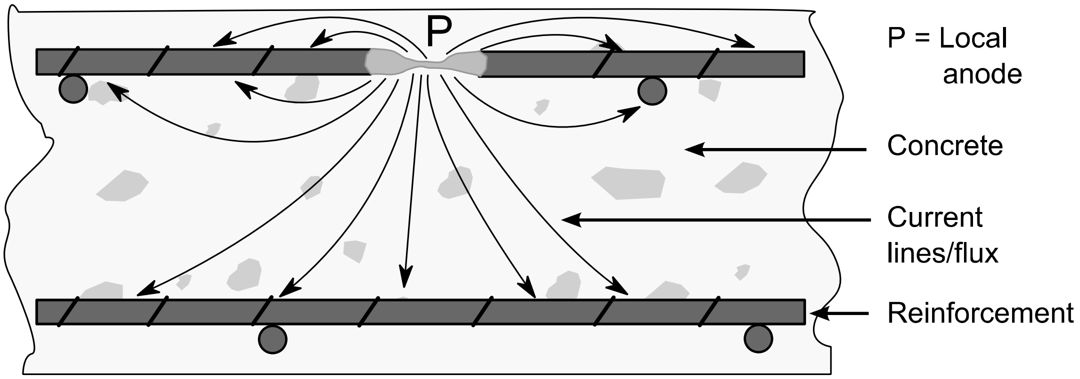

Fig. 2.9: Macro-cell illustrating reinforced concrete corrosion.

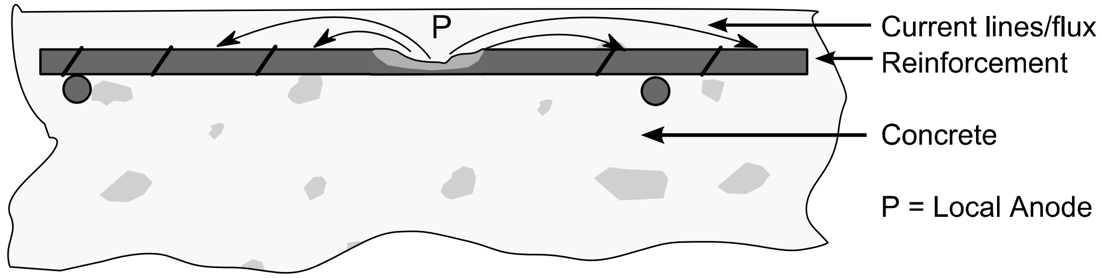

Fig. 2.10: Micro-cell illustrating reinforced concrete corrosion.

2.7 Experimental Behaviour of Corroded Reinforced Concrete

This section reviews experimental studies of reinforced concrete subjected to various forms of corrosion. The studies cover the mechanical behaviour of corroded reinforcing bars, bond strength, and the effects of cover cracking on the structural response of corroded reinforcing bars.

2.7.1 Al-Sulaimani et al. – 1990

Al-Sulaimani et al. (1990) conducted a series of tests to study the influence of corrosion on the bond of reinforcing steel. The experimental program consisted of four test series, with four stages of corrosion within each test series. Series 1 consisted of pullout tests on 10, 14, and 20 mm bars embedded within 150 mm concrete cubes. The embedment length to diameter ratio for each test was 4.0. The average yield strength of the reinforcement was 450 MPa and the average compressive strength of concrete was 30 MPa. Series 2 was identical to Series 1 except that polypropolene fibres were added to the concrete to control cracking during corrosion. Series 3 consisted of 12 reinforced concrete beams with a span of 1000 mm and cross-sectional dimensions of 150 mm x 150 mm. Each beam contained one 12 mm bar as bottom reinforcement, two 10 mm bars as top reinforcement and 6 mm stirrups spaced at 50 mm. The bottom reinforcement was isolated from the rest of the reinforcing cage such that independent corrosion could occur. The Series 3 beams were detailed to have an embedment length of 144 mm which was designed to create a bond failure. The Series 4 tests consisted of 12 beams identical to Series 3 with the exception of the development length which was detailed in accordance with the ACI building code. The development length for the Series 4 beams was 300 mm.

Each test specimen was submerged in liquid and an electric current was passed through the selected reinforcement such that accelerated corrosion would occur. A current density of 2mA/cm^2 was selected based on a pilot program (Al-Sulaimani et al., 1990). The experimental setup was designed such that a steel plate was the cathode, and the reinforcement was an anode. This provided uniform corrosion throughout the reinforcement. The accelerated corrosion setup is shown in Fig. 2.11.

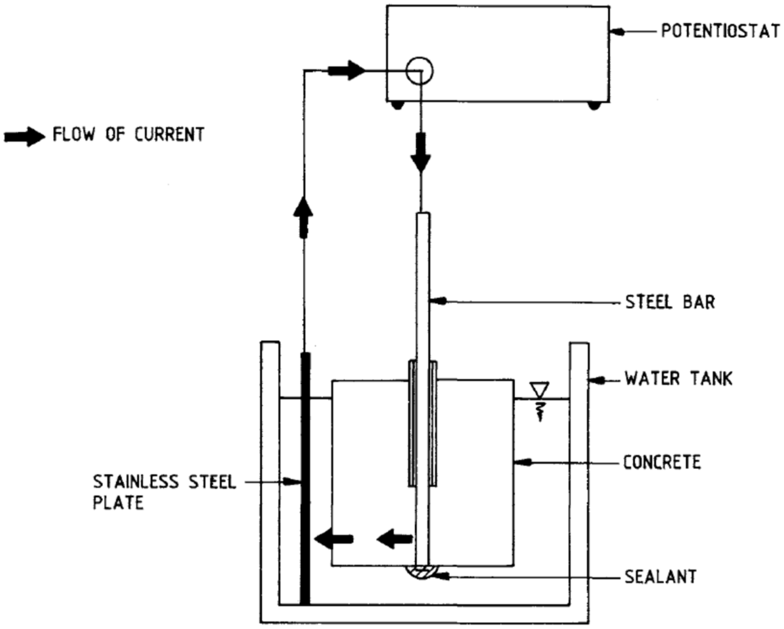

Fig. 2.11: Accelerated corrosion setup. Taken from Al-Sulaimani et al. (1990).

The pullout test specimens from Series 1 and Series 2 were tested on a general testing machine (Al-Sulaimani et al., 1990). The beams from Series 3 and Series 4 were tested as four-point bending test with clear span of 900 mm. Two LVDTs were connected directly to the bottom reinforcement to measure free end slip. Three additional LVDTs measured the deflection of the beam. A schematic of the test apparatus is shown in Fig. 2.12.

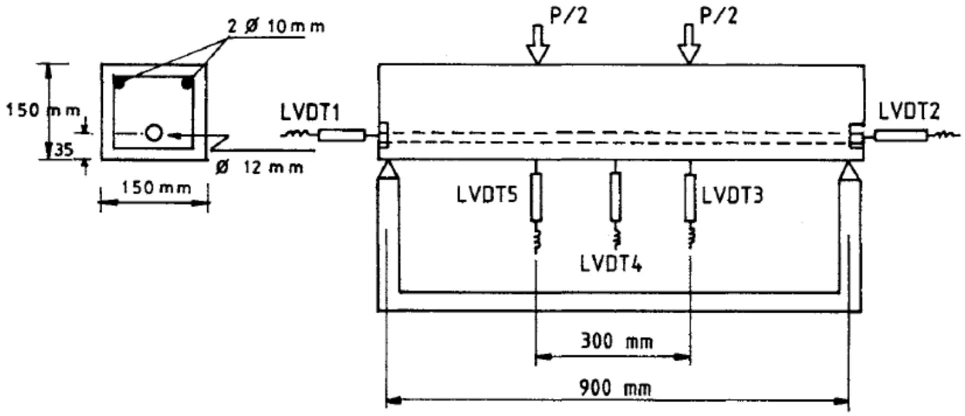

Fig. 2.12: Experimental test setup for the Series 3 and Series 4 beams. Taken from Al-Sulaimani et al. (1990).

The results of the 10 mm Series 1 tests were presented by Al-Sulaimani et al. (1990). The average bond stress was calculated from the external force on the reinforcement and the total bond area. The results of the 10 mm Series 1 tests are shown in Fig. 2.13.

It is clear from Fig. 2.13 that the peak bond stress actually increases with pre-cracking corrosion and decreases significantly with post-cracking corrosion. A plot between peak bond strength and corrosion level is presented in Fig. 2.14.

Fig. 2.14 shows that the bond strength initially increases up to 1 percent and then linearly decreases until the bond strength is negligible. Al-Sulaimani et al. (1990) postulated that the initial increases are a result of the corrosion products increasing the surface roughness and confinement, and the decreases are a results of deterioration in the lugs on the deformed bars, reduction in bar section, and the lubricating effect of the heavy layer of corroded material.

The typical load-deflection curves of the Series 3 and Series 4 tests are plotted in Fig. 2.15. It can be seen from the figure that the Series 3 tests do in fact experience bond failure resulting in a reduced ultimate load. The authors defined a force P_e as the force at which the bond breaks down

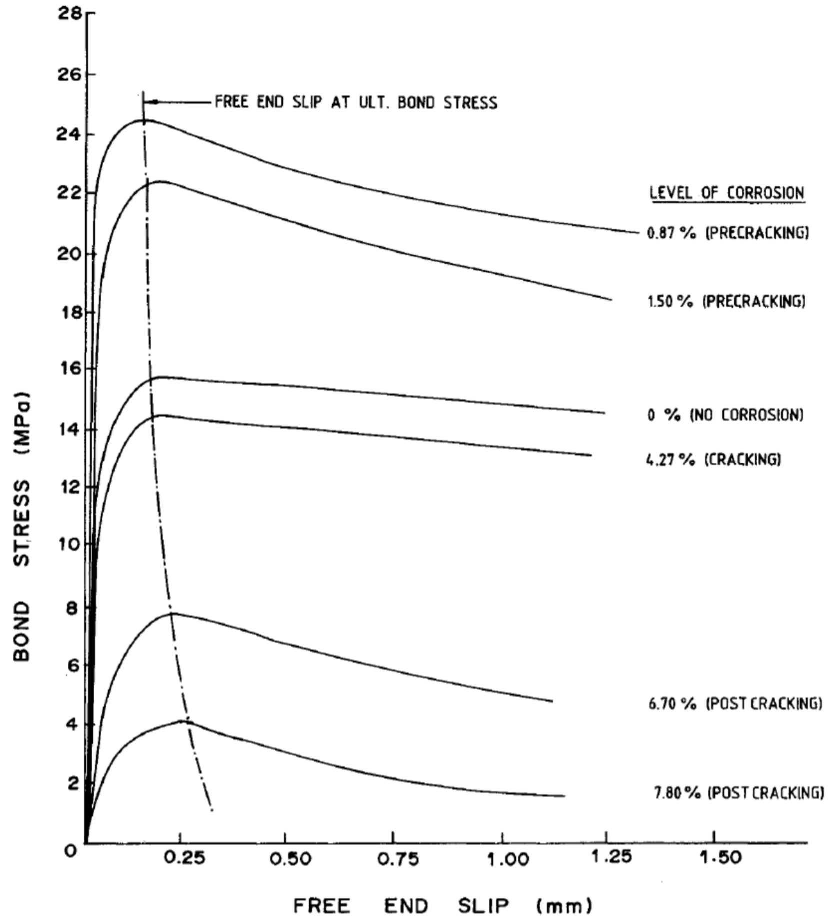

Fig. 2.13: Bond stress vs. free end slip for the 10 mm Series 1 pullout tests. Taken from Al-Sulaimani et al. (1990).

in the Series 3 tests. A plot of the applied force versus the free end slip for the Series 3 and Series 4 tests, shown in Fig. 2.16, illustrates that there is a large jump in free end slip at the associated P_e.

Al-Sulaimani et al. concluded that the ultimate strength of the Series 4 beams was unaffected by bond degredation from reinforcement corrosion. A 12 percent reduction was observed in the ultimate strength of a beam with a 4.5 corrosion percentage; however, the authors attributed this to a reduction in bar area. Finally they concluded the that cover to bar diameter ratio is significant as the corrosion crack initiation occurs at much smaller corrosion percentages with a reduced cover to bar diameter ratio.

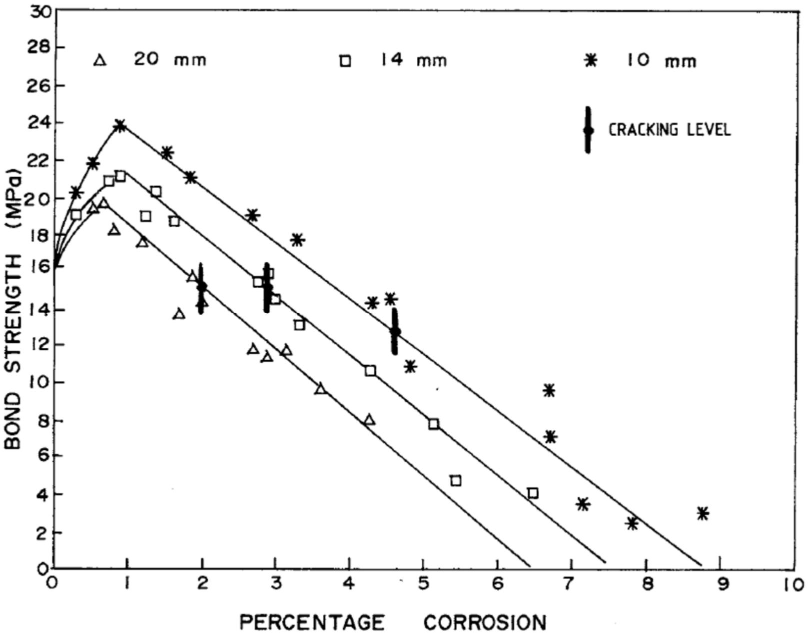

Fig. 2.14: Bond strength versus corrosion percentage for Series 1 pullout specimens. Taken from Al-Sulaimani et al. (1990).

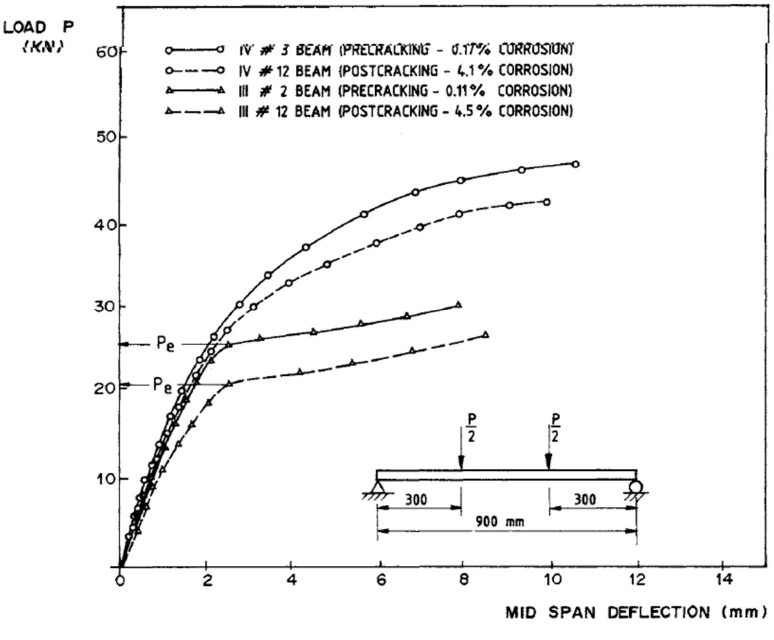

Fig. 2.15: Typical load-deflection curves for Series 3 and Series 4 specimens (Taken from Al-Sulaimani et al. 1990).

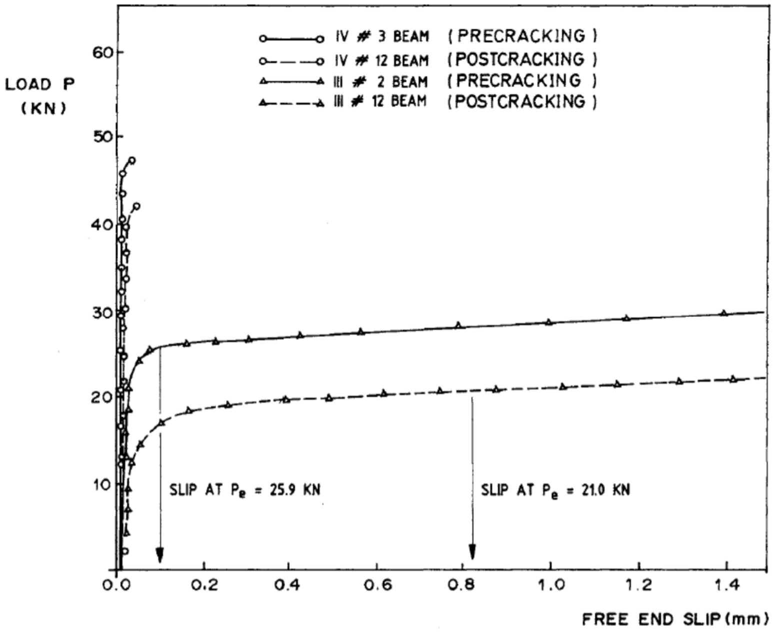

Fig. 2.16: Typical load versus free end slip curves for Series 3 and Series 4 specimens (Taken from Al-Sulaimani et al. 1990).

2.7.2 Almusallam et al. – 1996

Almusallam et al. (1996) studied the relationship between corrosion and bond stress. The authors reviewed several test methods for testing the bond strength of deformed reinforcing bars. The most common test, a concentric pullout test, wa\s considered by the authors as unrealistic due to the induction of compressive forces in the concrete. It was noted that this would increase confinement and therefore increase the bond strength in the test. In order to capture the bond characteristics of flexural elements, a full-scale beam test was advantageous as the concrete and steel are both in tension. However, the cost of the full-scale beams are prohibitive. A cantilever bond test has many advantages over the concentric pullout test and the beam test. The strains in the concrete and steel are similar to those actually experienced in a flexural element. Additionally, the interactions between bond, shear and moment can be modified and captured. The scale of the test is such that the cost is not prohibitive. There are several arrangements of longitudinal and transverse reinforcement that can be tested. Lastly, the ends of the bars can be shielded and de-bonded from the test, thereby avoiding the confinement effects induced by support conditions. Almusallam et al. (1996) selected the cantilever bond test as the most practical and representative bond test to study the bond behaviour of corroded steel reinforcement. A schematic of the test setup is shown in Fig. 2.17. One tension bar was selected with a nominal diameter of 12 mm. The bond length of the specimen was 102 mm. Shear and compression reinforcement were provided to ensure that bond failure would govern the tests. It was noted by the authors that the shear reinforcement was specifically designed such that the shear reinforcement did not confine the tensile reinforcement.

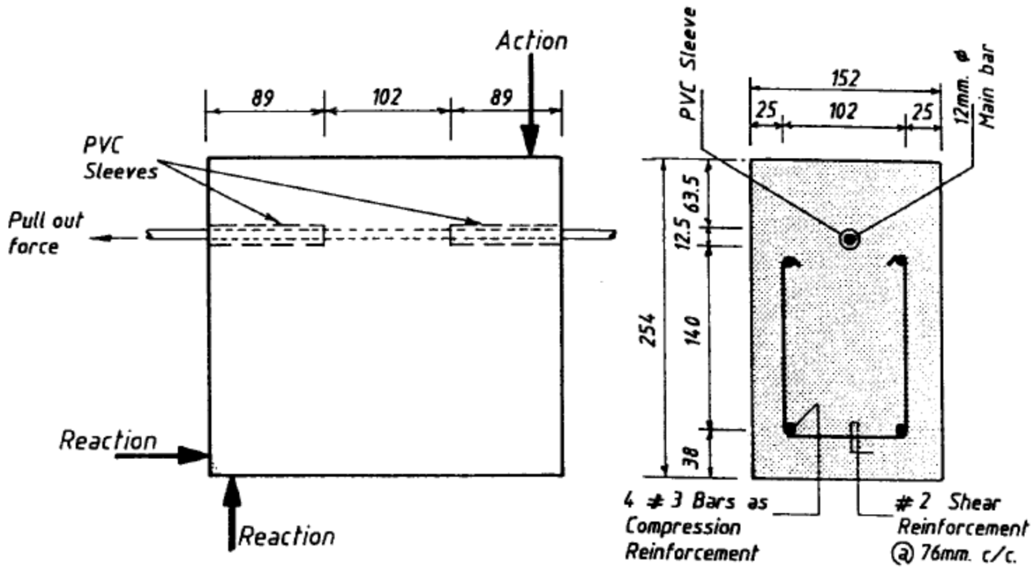

Fig. 2.17: Cantilever pullout test schematic. Taken from Almusallam et al. (1996).

Accelerated corrosion was induced using a procedure similar to that depicted by Fig. 2.11. Corrosion percentage was measured as a ratio of corroded mass to nominal mass. Thus, one percent corrosion represented one percent of nominal mass lost. The results of the tests showed that as the degree of corrosion increased, the bond stress initially increased and then decayed rapidly before reaching a plateau. The experimental ultimate bond strength from the specimens tested by Almusallam et al (1996) are shown in Fig. 2.18.

The results of Almusallam et al. (1996) confirmed results of similar studies that the bond stress increases initially before decreasing dramatically. This is explained by the initial increased surface roughness and confining effects of the corroded material before the concrete has cracked. After cracking begins, there is a complete loss of confinement and a large degradation of the ribs on the deformed bars. At large levels of corrosion, the plateau is explained as the corrosion by-products produce a lubricating effect that results in a constant bond strength.

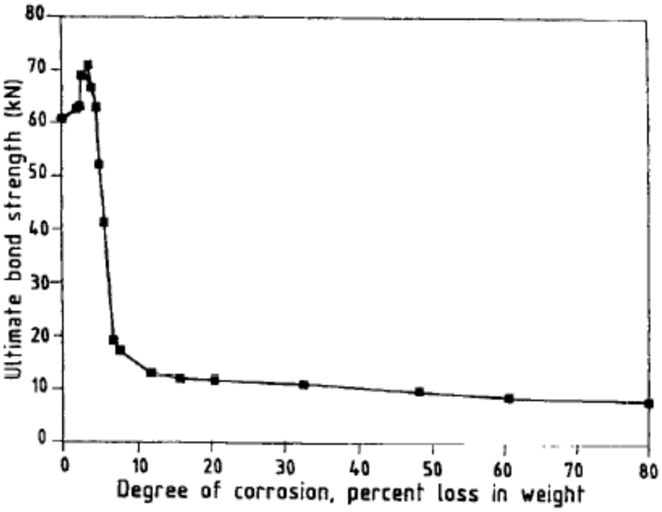

Fig. 2.18: Experimental results of ultimate bond strength versus degree of corrosion. Taken from Almusallam et al. (1996).

The crack width of the concrete heavily influence the bond strength. As the corrosion becomes more severe, the crack widths due to corrosion increase. This causes a loss of confinement resulting in a significantly reduced bond stress. The experimental results of the crack width and degree of corrosion, as well as the relationship between crack width and bond stress are, shown in Fig. 2.19a and Fig. 2.19b respectively.

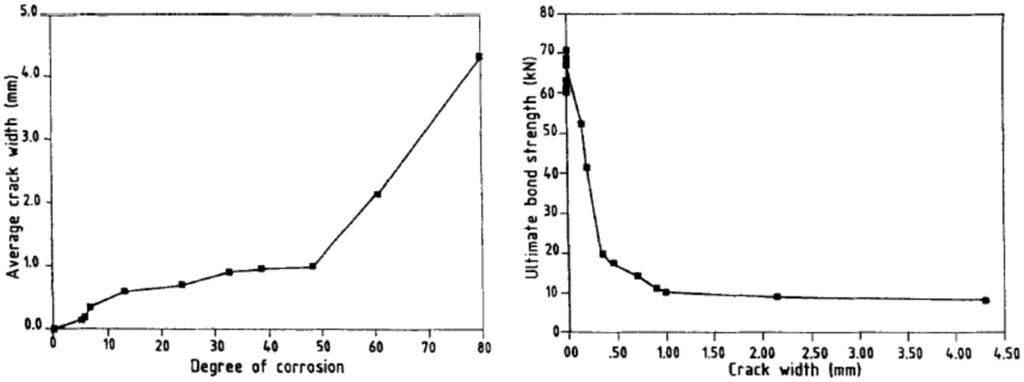

(a) (b)

Fig. 2.19: (a) Degree of corrosion versus average crack width. (b) Crack width versus ultimate bond strength. Taken from Almusallam et al. (1996).

Almusallam et al. (1996) concluded that very little corrosion cracking can result in significant reduction of bond strength. Immediately after corrosion cracking occurs, the failure mode is due to splitting of concrete from hoop stresses and thus is not significantly different than an uncorroded response. However once corrosion is significant, there is a distinct change in failure mode where continuous slip occurs as a result of the lubricating effects of corrosion products.

2.7.3 Rodriguez et al. – 1996

Rodriguez et al. (1996) tested a total of 40 reinforced concrete beams that were subject to various levels of corrosion. The beams differed in reinforcement configuration. Type 11 beams contained a low longitudinal reinforcement ratio with stirrups spaced just below the effective depth. Type 31 beams contained a high reinforcement ratio with stirrups spaced at half of the effective depth. Testing of the beams at various levels of corrosion resulted in a majority of flexural failures. Only the heavily deteriorated bars failed in shear due to pitting corrosion in the transverse reinforcement (Rodriguez et al., 1996). The Type 31 beams failed at compressive strains significantly less than the ultimate strain of $3.5\text{x}10^{-3}$. Rodriguez et al. (1996) concluded that this was due to deterioration effects of the corrosion. In all tests, the authors concluded that bond failure was not a significant factor. The load-deformation responses of the Type 11 beams are presented in Fig. 2.20. The load-deformation plots of the Type 31 beams are presented in Fig. 2.21.

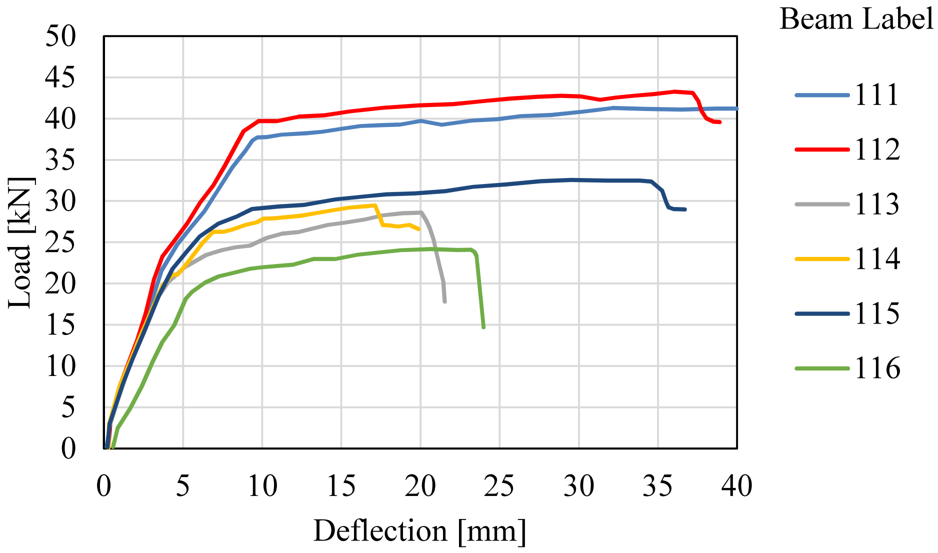

Fig. 2.20: Load-deflection plots for Type 11 beams. Taken from Rodriguez et al. (1996).

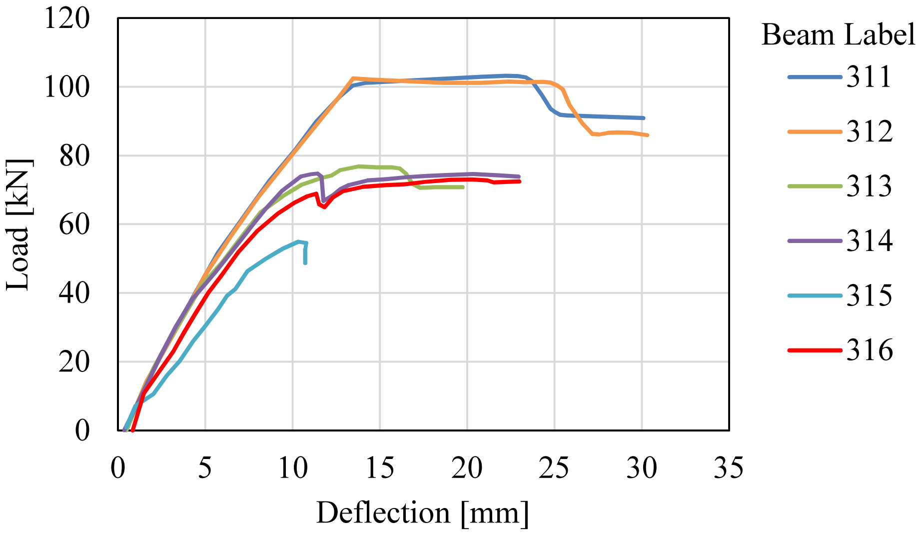

Fig. 2.21: Load-deflection plots for Type 31 beams. Taken from Rodriguez et al. (1996).

2.7.4 Amleh and Mirza – 1999

Amleh and Mirza (1999) studied 14 tension specimens to determine the effect of corrosion on the bond and tension stiffening characteristics. Each specimen consisted of a 20M bar cast in a 100 mm diameter circular concrete section. In total, seven different levels of corrosion were investigated. Amleh and Mirza (1999) identified three ways to evaluate the level of corrosion for steel reinforcement embedded in concrete. The first method considered the width and propogation of longitudinal concrete cracks induced by corrosion of the reinforcement. The second considered a corrosion percentage as the percentage loss of metal by mass. The third considered the minimum cross-sectional area as a percentage loss from the nominal cross-sectional area. The latter was determined by assuming that the yield stress of the reinforcement was constant, and thus the reduced cross-sectional area was determined as the ratio of pre- and post-corroded yield forces multiplied by the nominal cross-sectional area. The minimum cross-sectional area was calculated using Equation 2.72.

$$A_{corr} = \frac{F_{y,corr}}{F_{y,nominal}} A_{nominal} \qquad (2.72)$$

where A_{corr} is the reduced cross-sectional area, $F_{y,\mathrm{corr}}$ is the yield force of the steel determined from experiment, $F_{y,\mathrm{nominal}}$ is the yield force of the uncorroded steel determined from experiment, and $A_{nominal}$ is the nominal cross-sectional area of the reinforcing bar.

Initial analysis of the experimental load-deflection for the corroded (CS4, CS5, CS6), uncorroded (SS1), and bare bar response is shown in Fig. 2.22. The authors note that the uncorroded specimen underwent free shrinkage strains and thus started with a negative strain (Amleh and Mirza, 1999). Fig.2.22 indicates that the tension stiffening effect is almost entirely eliminated for heavily corroded bars. However in order to determine the actual load carrying capacity of the concrete, the stress-strain response must be generated for the steel. This stress-strain response cannot use the nominal area, but instead must use the equivalent cross-sectional area. The stress-strain response calculated by Amleh and Mirza (1999) are shown in Fig. 2.23.

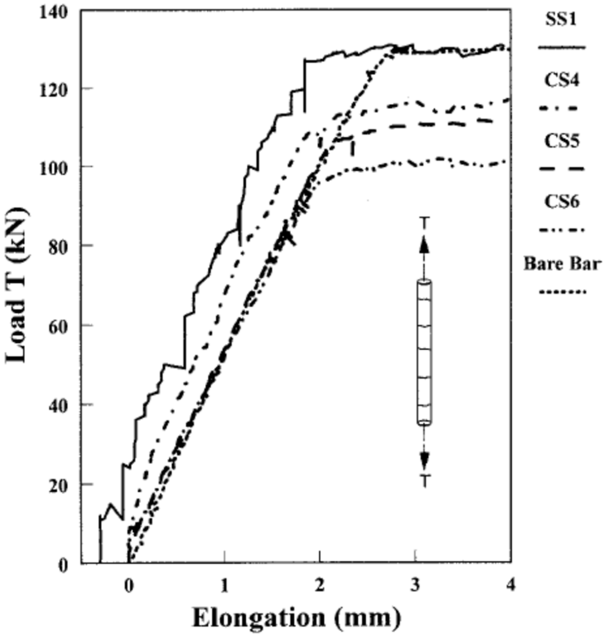

Fig. 2.22: Load-deformation response for tension testing of experimental specimens. Taken from Amleh and Mirza (1999).

Fig. 2.23 reveals that the concrete is carrying some of the load; however, the tension stiffening effect is clearly reduced by corrosion. Amleh and Mirza (1999) also noted that a reduction in the ductility of the reinforcement reduced as the level of corrosion increased. Amleh and Mirza (1999) confirmed the results of similar studies that the bond stress decays rapidly with corrosion and that as the bond breaks down, the tension stiffening effects are reduced.

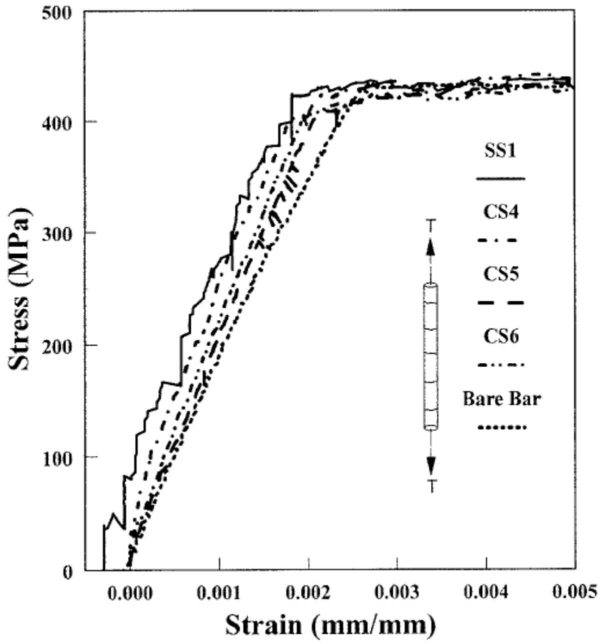

Fig. 2.23: Stress-strain response for tension testing of experimental specimens. Taken from Amleh and Mirza (1999).

2.7.5 Auyeung et al. – 2000

Auyeung et al. (2000) conducted an experimental program aimed at evaluating the effect of corrosion on the bond strength of reinforced concrete elements. After a review of experimental procedures, a modified version of the Danish standard testing method for evaluating the bond strength of a reinforced concrete member was selected. This test involves two reinforcing bars embedded in a concrete block. Load is applied to each reinforcing bar in opposite directions. The specimen is designed such that the concrete does not exhibit tension failure, and that the bars do not yield. One of the reinforcing bars is typically longer than the other to ensure that bond failure occurs in the shorter bar. Auyeung et al. (2000) determined the design development length based on the ACI Building code and then reduced it by 40 percent to ensure bond failure. In all test specimens, a 19 mm diameter bar was used. A schematic of the test specimen is presented in Fig. 2.24.

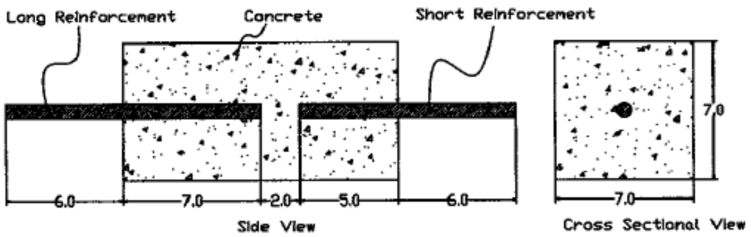

Fig. 2.24: Schematic of the test specimen. Taken from Auyeung et al. (2000).

Uniform corrosion was applied to the short reinforcing bar through the use of two copper plates on either side of the bar. This was done in an attempt to achieve perfectly uniform corrosion along the length of the bar. The exposed ends of the reinforcement were coated in rubber to prevent corrosion. This allowed for good connection to the testing machine. Dial gauges were attached to either end of the reinforcement to determine the bond slip. A diagram of the corrosion setup and the universal testing machine is illustrated in Fig. 2.25.

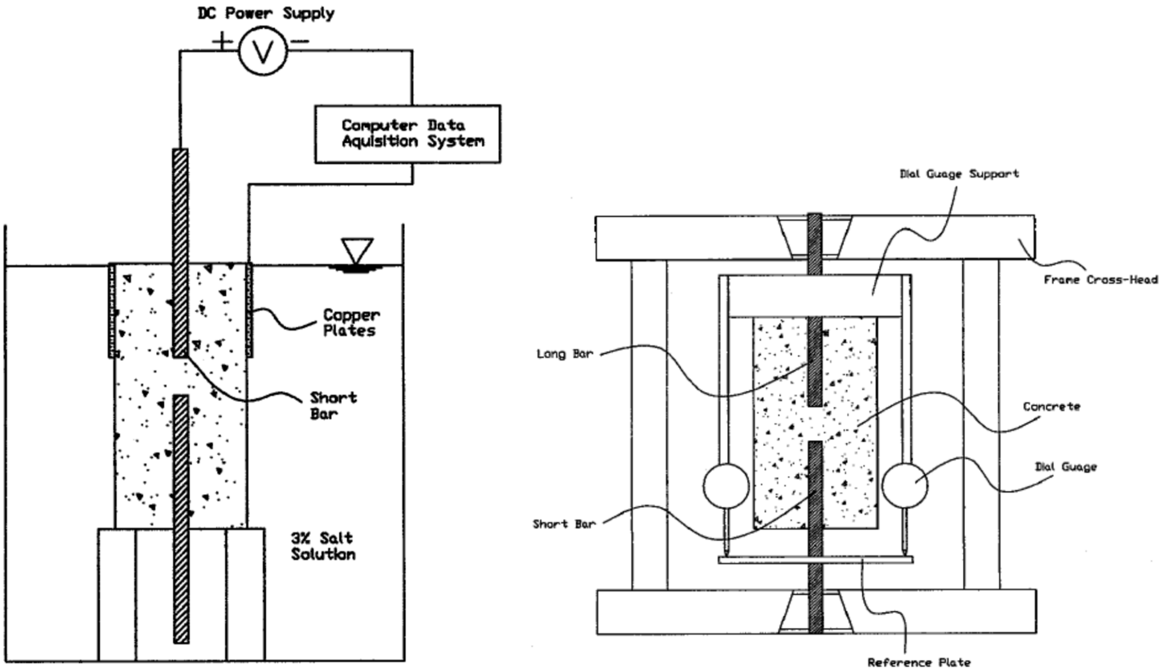

Fig. 2.25: (a) Corrosion experimental setup. (b) Specimen experimental test setup. Taken from Auyeung et al. (2000).

The results of the experimental program showed that when the corrosion reached two percent by mass, cracking was observed in the specimens. Measurement of the mass loss distributed along the length of the bar showed that uniform corrosion was achieved. A plot of the typical mass loss along the bar, and the cumulative mass loss, is shown in Fig. 2.26. Note that if the mass loss is truly uniform, then the cumulative mass loss takes the form of a straight line.

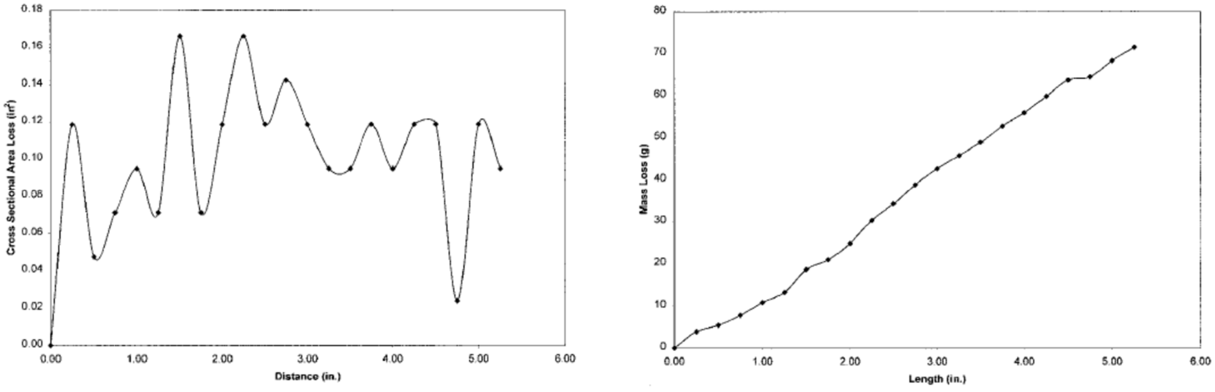

Fig. 2.26: (a) Mass loss along the length of the bar shown by cross-sectional area loss. (b) Cumulative mass loss along the length of the bar. Taken from Auyeung et al. (2000).

Auyeung et al. (2000) described four possible failure modes for the experimental specimens. The first is that pullout failure occurs without splitting of concrete. The second involves a pullout failure along an existing crack. The third failure modes constitutes splitting failure and pullout failure simultaneously. The last failure mode is governed by tension failure of the concrete. The authors observed that specimens with a mass loss of less than two percent failed by the second failure mode, however those with a mass loss of more than two percent failed by the third failure mode. Additionally, the authors noted that specimens with more than two percent of mass loss exhibited a more ductile failure.

The ultimate bond strength of the specimens was determined as the maximum load divided by the bond area. The results confirmed previous results in the literature that a corrosion of less than one percent increased the ultimate bond strength. After a corrosion of one percent, the ultimate bond strength deteriorated rapidly.

When investigating the bond slip at ultimate bond strength, Auyeung et al. (2000) determined that the stiffness of the bond stress – bond slip relationship increased. After a mass loss of two percent, the bond slip stiffness decreased. In all cases, the slip at ultimate bond stress decreased. Regression of the data produced an exponential relationship between the slip at ultimate bond stress and the level of corrosion.

Auyeung et al. (2000) confirmed the experimental behaviour observed by others. In addition, the authors concluded that a corrosion percentage of two percent will cause cracking and spalling of concrete cover. Lastly, they observed that the bond strength is not completely destroyed at high levels of corrosion.

2.7.6 Palsson and Mirza – 2002

The Dickson bridge in Montreal, Quebec was demolished in 1999. During the demolition, 103 samples of steel reinforcement were randomly collected from the No. 5 bridge deck reinforcement. The bridge had exhibited significant signs of deterioration including large areas of spalling. The length of each specimen was approximately 250 mm. The cross-sectional area of uncorroded steel reinforcement ranged from 193 mm^2 to 195 mm^2. The measured areas were found to be smaller than the nominal area of 200 mm^2. The collected specimens were partitioned into four groups:

1. corrosion level of less than 10 percent,
2. corrosion level between 10 and 20 percent,
3. corrosion level between 20 and 30 percent,
4. and corrosion level greater than 30 percent.

The average uncorroded yield and ultimate strengths of the steel were determined from tension testing to be 346 MPa and 590 MPa respectively. The testing apparatus used two gauge lengths. The longer guage length was 75 mm. A shorter gauge length of 25 mm was placed within the longer guage length at the area where failure was believed to occur. This was done because it is suspected that the minimal section would cause localized plastic displacement (Palsson and Mirza, 2002).

The test results showed that the yield and ultimate strength were relatively unaffected by the level of corrosion. However, a significant reduction in ductility was observed for the heavily corroded bars. The average ultimate strain measured by each of the guage lengths is presented in Fig. 2.27.

Fig. 2.27 shows that the ultimate strain is significantly affected by the degree of corrosion. Additionally, the strain in the smaller gauge length is always greater than the strain in the larger guage length. Palsson and Mirza (2002) noted that this supports the hypothesis that localized strain

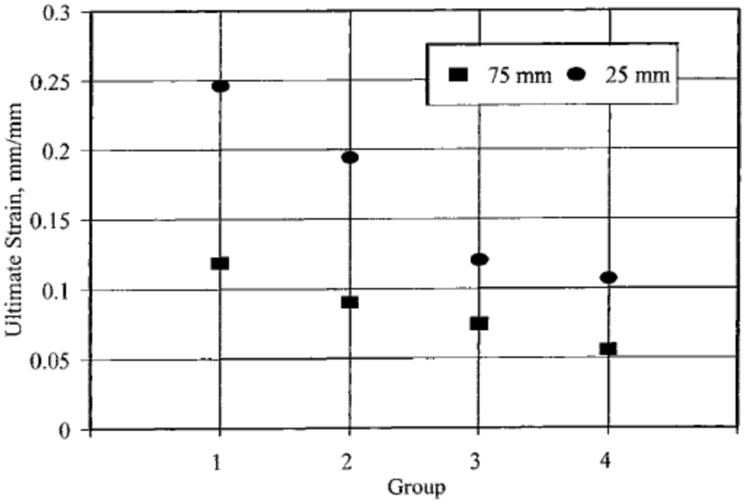

Fig. 2.27: Average ultimate strain for each corrosion group. Taken from Palsson and Mirza (2002).

is governing the failure of the steel reinforcement. A typical stress-strain response, shown in Fig. 2.28, between a Group 1 and a Group 4 specimen further illustrates this point.

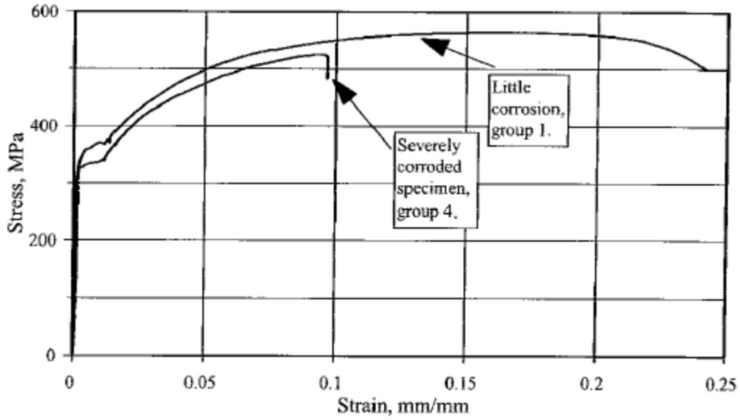

Fig. 2.28: Stress-strain response for corroded reinforcement. Taken from Palsson and Mirza (2002).

Palsson and Mirza (2002) concluded that a very significant loss of ductility is observed in the presence of pitting corrosion. Fig. 2.29 shows the relationship between ultimate strain and percentage of area loss. This can contribute to a dramatic loss of structural toughness as the stress in the corroded reinforcement will increase as cross-sectional area decreases. Thus heavily corroded structures have the potential to completely collapse in a brittle manner (Palsson and Mirza, 2002).

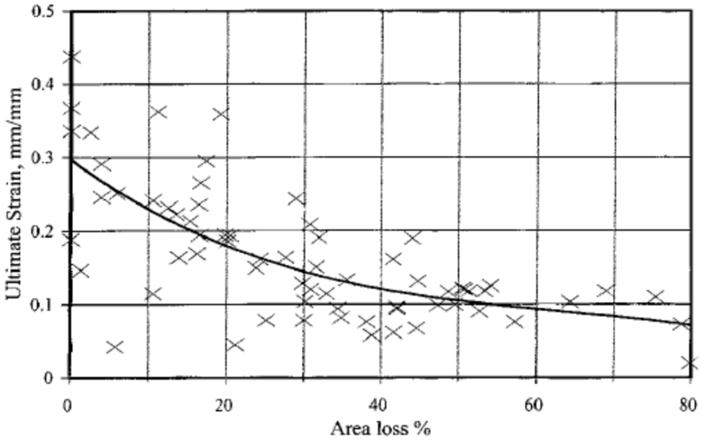

Fig. 2.29: Ultimate strain versus area loss for corroded steel reinforcement. Taken from Palsson and Mirza (2002).

2.7.7 Cairns et al. – 2005

Carins et al. (2005) studied the mechanical properties of reinforcing bars to determine the effects of pitting corrosion on the strength and ductility of steel reinforcement. Two experimental studies were conducted: a simulated corrosion pit, and accelerated corrosion of reinforcement. The simulated corrosion pits were created by using hemispherical drill bits to create various cross-sectional losses. Bar diameters ranged from 12 mm to 24 mm in size and were tested in tension. The typical results of the mechanically deteriorated reinforcing bars are presented in Fig. 2.30.

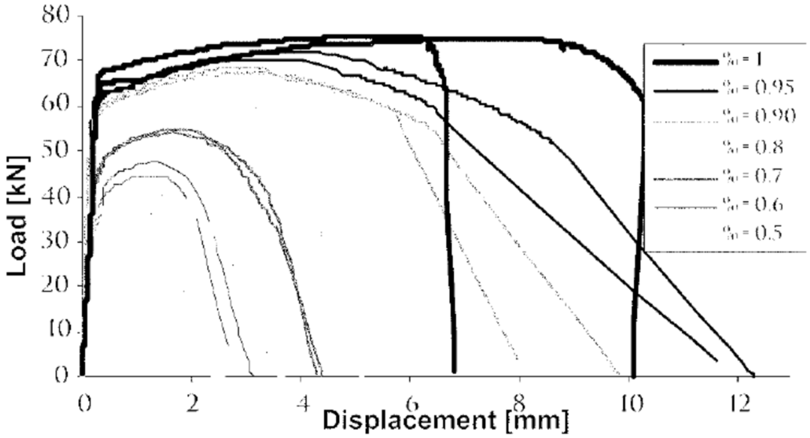

Fig. 2.30: Mechanically deteriorated reinforcing bars. Taken from Cairns et al. (2005).

The ductility of the steel reinforcement was significantly affected by the presence of the reduced cross section. However, the actual corrosion was not being simulated and thus the full effects of corrosion were not captured.

The second experimental program consisted of 25 reinforcing bars, both deformed and smooth, that were subjected to accelerated corrosion. Six of the specimens were cast in concrete for the duration of the accelerated corrosion. Testing of the corroded reinforcement revealed that the yield strength of the material was not affected by the corrosion. A loss of ductility was observed, however the code limits on ultimate strain were still met. The authors hypothesized that the bars were likely to fracture at the section of weakest strength. They noted that this section is most often in areas where the percentage of iron is slightly higher. Corrosion potential for iron is less than that of the other constituent metals and therefore the pits and the weakest section do not coincide. A plot of the yield stress, ultimate stress, and ultimate strain versus corrosion percentage is shown in Fig. 2.31.

2.7.8 Stewart and Al-Harthy – 2008

Stewart and Al-Harthy (2008) conducted an experimental study to determine the statistics of maximum pitting depth for reinforced concrete elements. Two reinforced concrete slabs 500 mm x 1000 mm x 250 mm with 16 mm and 27 mm diameter steel reinforcement were subjected to accelerated corrosion to determine the statistics for the maximum pitting depth.

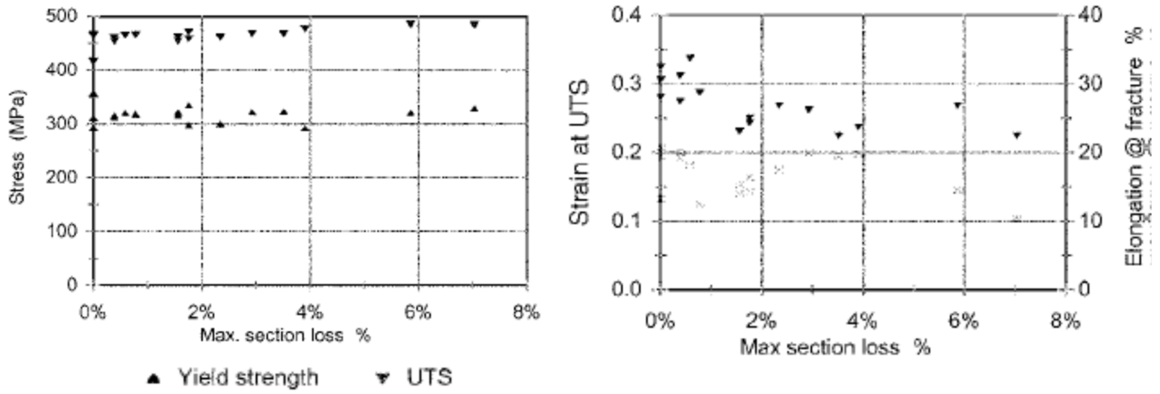

Fig. 2.31: Experimental results versus sectional loss percentage: (a) Ultimate and yield strength, (b) Ultimate strain. Taken from Cairns et al. (2005).

The pitting factor was used to calculate the amount of pitting in the bar. The pitting factor can be calculated using Equation 2.73,

$$R = \frac{p}{P_{AV}} \tag{2.73}$$

where p is the maximum pit depth, and P_{AV} is the penetration based on general corrosion. P_{AV} is calculated using Equation 2.74, where i_{corr} is the current density and t is the time of corrosion.

$$P_{AV} = 0.0116(i_{corr})t \tag{2.74}$$

After the accelerated corrosion had occurred, each bar was divided into lengths of 100 mm and the pitting factor was determined each bar segment. A Gumbel distribution was then selected to represent the maximum pitting depth. The Gumbel distribution takes the form of Equation 2.75.

$$\mu = \mu_0 + \frac{1}{\alpha_0} ln\left(\frac{A}{A_0}\right) \tag{2.75}$$

where A is the surface area used in prediction, A_0 is the surface area of the tests and μ_0 and α_0 are statistical parameters determined from the testing. The results of the tests and the statistical parameters for the Gumbel distribution are shown in Table 2.12.

Table 2.12: Results of experimental study. Taken from Steward and Al-Harthy (2008).

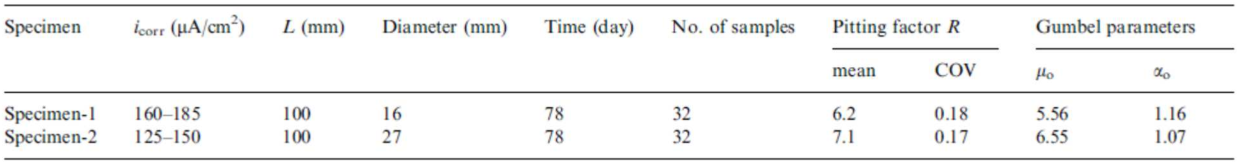

Specimen	i_{corr} (μA/cm^2)	L (mm)	Diameter (mm)	Time (day)	No. of samples	Pitting factor R		Gumbel parameters	
						mean	COV	μ_o	α_o
Specimen-1	160–185	100	16	78	32	6.2	0.18	5.56	1.16
Specimen-2	125–150	100	27	78	32	7.1	0.17	6.55	1.07

2.8 Modelling Corroded Reinforced Concrete

There are several factors that contributed to the deteriorated response of corroded reinforced concrete structures. Coronelli and Gambarova (2004) concluded that a finite element model that captures the behavioural response of corroded reinforced concrete structures should incorporate six aspects: the reduction in steel area of longitudinal and transverse reinforcement; the changes in the ductility of carbon-steel as a results of pitting corrosion; the concrete area reduction resulting from cover cracking and spalling; changes in concrete strength and ductility of concrete in compression due to micro-cracking from expanding reinforcement corrosion products; changes in tension stiffening due to concrete cracking and bond deterioration; and bond dependence on the level of corrosion in the steel reinforcement. This section outlines the proposed models of the factors influencing the structural response of corroded reinforced concrete structures.

2.8.1 Reinforced Concrete Bond Strength Models

The failure of bond in reinforced concrete can occur by two mechanisms. The first involves splitting of the concrete cover creating a total loss of confinement and delamination of the concrete cover. The second mechanism involves the shearing of the concrete keys between the deformed ribs. When considering concrete corrosion, the expansive corrosion by-products often result in cracking of the concrete cover. As a result, the bond failure models are typically concerned with splitting failure governing the bond strength of steel reinforcement. Coronelli (2002) summarized the factors that contribute to the bond strength of reinforced concrete. The primary factor that affects bond strength is the confinement provided by the concrete cover. Other factors that affect the bond strength of corroded reinforced concrete are a reduction in friction coefficients, a reduction in the adhesion between concrete and steel, a reduction in the bearing area of the deformed bars, and a change of rib orientation (Coronelli, 2002). This section presents various reinforced concrete bond models that have been proposed in the literature. A brief discussion of each bond model is included as a summary to this section.

2.8.1.1 Coronelli – 2002

Coronelli (2002) developed an analytical model for the determination of the maximum bond strength of reinforcement. The model is an modified version of an original model proposed by Cairns and Abdullah (1996). The bond strength of a corroded reinforced concrete member is determined by Equation 2.76,

$$\tau_{Max} = k(X) \cdot p^{MAX}(X) + \tau_b^o(X) + \mu(X) \cdot p_{corr}(X) \tag{2.76}$$

where,

X = the level of corrosion in microns,

$p^{MAX}(X)$ = maximum pressure at bond failure,

$p_{corr}(X)$ = pressure due to corrosion,

$k(X)$ $= nc_r \tan(\phi(X) + \delta)/\pi$

$\tau_b^o(X)$ $= nA_{Tr} f_{coh}(X)[\cot\delta + \tan(\phi(X) + \delta)]/(\pi d_b s_r)$

n = number of transverse ribs at a section,

s_r = rib spacing,

A_{Tr} = rib area in the plane at right angles to the bar axis,

c_r = rib shape and area coefficient,

δ = orientation of the ribs,

$\mu(X)$ = friction coefficient $= \tan[\phi(X)] = B - C(X - X_{cr})$

$\phi(X)$ = friction angle between steel and concrete,

$f_{coh}(X)$ = adhesion strength = $D - E(X - X_{cr})$, and

B, C, D, E = regression coefficients.

The model captures the effect of corrosion utilizing the empirical expression for the friction coefficient and the adhesion strength. The effect of reduced rib area is accounted for by a reduction in rib height, which is assumed to be equal to the radial reduction in bar area. The corrosion pressure is calculated by assuming that the cover acts as an elastic beam, with the transverse reinforcement as connecting rod elements. Fig. 2.32 is an illustration of the elastic beam assumed by Coronelli (2002).

The uniform pressure is determined by assuming the displaced shape of the beam, and back calculating the uniform pressure required to achieve a displaced shape. It is assumed that the displacement of each node not connected to a stirrup is equal to the expansion displacement of the

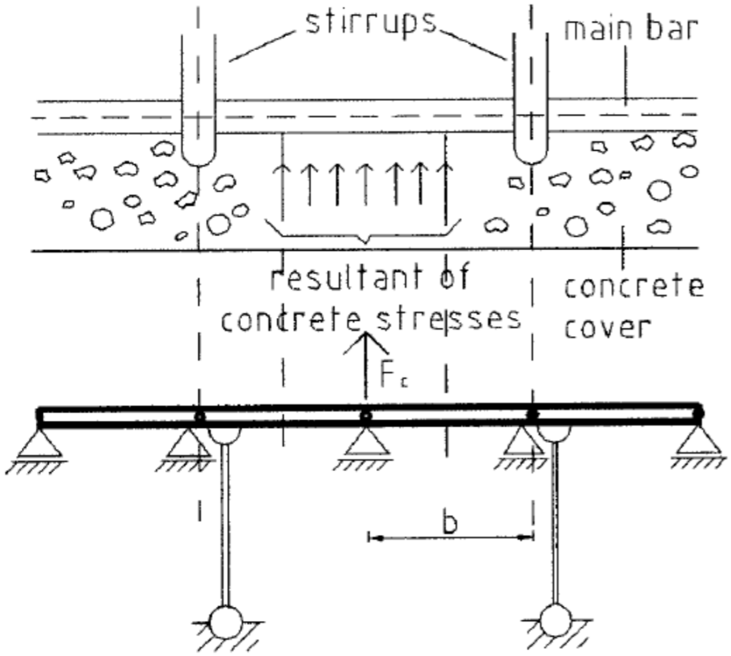

Fig. 2.32: Concrete cover elastic beam model. Taken from Coronelli (2002).

longitudinal bars. Equation 2.77 is derived for the radial displacement of a corroded bar,

$$t = \frac{r_b(n-1)}{r_b + c} X \tag{2.77}$$

where r_b is the radius of the bar, n is the ratio between virgin and corroded area, and c is the concrete cover.

Cornonelli (2002) analyzed the bond strength of several experimental results and achieved reasonable bond strength prediction. It was noted, however, that the analysis results are not fully reflective of field conditions as in most accelerated corrosion tests, only current is applied to the longitudinal reinforcement. This results in differential corrosion between the longitudinal transverse reinforcement. In-situ, the transverse reinforcement is closer to the surface and the currents experienced are the same. Thus the transverse reinforcement may be at the same level of corrosion or greater when compared to the longitudinal reinforcement (Coronelli, 2002). The reduction in the stirrup area is not considered, and additionally a reduced ductility (in the case of pitting corrosion) could result in a sudden loss of confinement and a subsequent loss of bond strength. Additionally, the influence of the ratio between uncorroded and corroded area is not discussed. It has been shown by Wang and Lui (2006) that this can have a significant effect on the predictions of bond strength models.

2.8.1.2 Coronelli and Gambarova – 2004

Coronelli and Gambarova reviewed and suggested a model originally proposed by Rodriguez et al. (1994). The original works of Rodriguez et al. (1994) cannot be obtained at this time and thus the reproduction of Coronelli and Gambarova (2004) is considered sufficient. The model was generated based on regression from experimental data. Equation 2.78 was used to describe the residual bond strength of corroded reinforcement:

$$\tau_{Max} = 0.6\left(0.5 + \frac{C}{d_b}\right) f_{ct}(1 - \beta X^{\mu}) + \frac{kA_{Tr}f_y}{sd_b} \tag{2.78}$$

where: $\tau_{Max}$is the residual bond strength; C is the concrete cover, d_b is the diameter of the longitudinal reinforcing bar; f_{ct} is the splitting strength of the concrete; X is the corrosion penetration depth in mm; A_{Tr} is the cross-sectional area of the transverse reinforcement; f_y is the yield strength of the transverse reinforcement; s is the spacing of the transverse reinforcement; and β, μ, and k are parameters determined from the regression analysis.

The above model was derived from fitting bond test results with different combinations of concrete cover to bar ratio, level of corrosion, and spacing/area of stirrups. Coronelli and Gambarova (2004) noted that the stirrups in the original data used for regression were not corroded. Thus corrosion in the stirrups was introduced by reduction in the area of the transverse reinforcement, A_{Tr} (Coronelli and Gambarova, 2004).

2.8.1.3 Maaddawy et al. – 2005

Maaddawy et al. (2005) presented an empirical model for bond strength of corroded reinforced concrete. The model was developed by Saifullah and Clark (1994), however the original work is not available at this time. The model was based on regression of experimental work by the original authors in which a reduction factor was applied to a bond model originally proposed by Kemp and Wilhelm (1979). The reduction factor was a function of the mass loss of reinforcement, and the current density. Equation 2.79 was used to calculate the maximum bond stress of corroded reinforcement.

$$\tau_{Max} = (A_1 + A_2 m_l)\left(0.55 + 0.24\frac{C}{d_b}\right)\sqrt{f_c'} + 0.191\frac{A_{Tr}f_y}{sd_b} \tag{2.79}$$

where A_1 and A_2 are parameters dependent on the current density, and m_l is the mass loss. The values taken for A_1 and A_2 are presented in Table 2.13.

2.8.1.4 Val et al. – 2006

Val et al. (2006) developed a model for bond strength based on regression analysis of compiled data from the literature. The model aimed to capture the initial increase in strength due to corrosion expansion observed in various experimental studies (Al-Sulaimani et al., 1990; Almusallam et al.,1996). The model was based on a ratio of the maximum bond strength to the uncorroded bond strength. The model proposed by Val et al. (2006) is presented in Equation 2.80:

Table 2.13: Parameters for A1 and A2. Reproduced from Maaddawy et al. (2005).

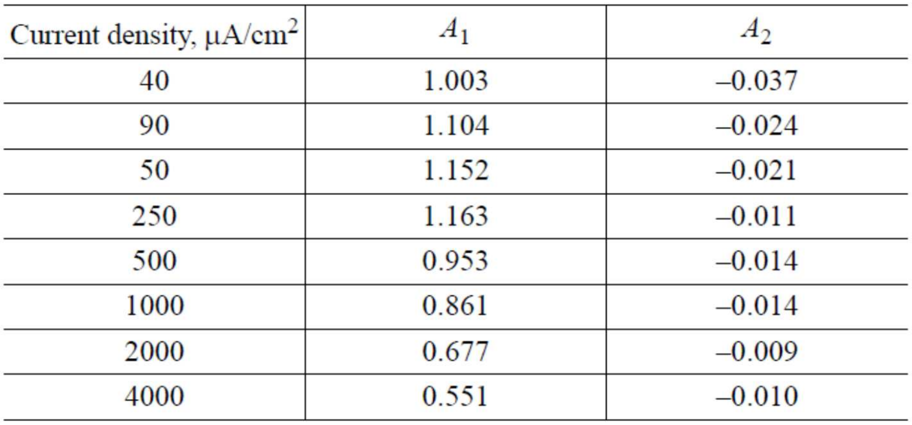

Current density, $\mu A/cm^2$	A_1	A_2
40	1.003	–0.037
90	1.104	–0.024
50	1.152	–0.021
250	1.163	–0.011
500	0.953	–0.014
1000	0.861	–0.014
2000	0.677	–0.009
4000	0.551	–0.010

$$\frac{\tau_{Max}}{\tau_{Max,0}} = \begin{cases} 1 + (k_1 - 1)\dfrac{p}{p_{cr}} & p \le p_{cr} \\ \max[k_1 - k_2(p - p_{cr}); 0.15] & p > p_{cr} \end{cases} \tag{2.80}$$

where: τ_{Max} is the residual bond strength; $\tau_{Max,0}$ is the initial bond strength; k_1 represents the original increase in bond strength; k_2 represents the slope of the bond deterioration curve; p is the depth of corrosion attach, or reduction in bar radius; and X_{cr} is the depth of corrosion attack required to cause concrete cracking. The depth of corrosion required to cause concrete cracking was obtained from the literature by Val et al. (2006) and is calculated using Equation 2.81:

$$X_{cr} = a_1 + a_2\frac{C}{d_b} + a_3 f_{ct} \tag{2.81}$$

where: a_1, a_2, and a_3 are constants obtained from regression; C is the concrete cover; d_b is the longitudinal bar diameter; and f_{ct} is the concrete splitting strength. The parameter k_1 was obtained from regression analysis of experimental results. The parameter is affected by the confinement of the reinforcement, which is affected by the cover to bar diameter ratio, and the reinforcement ratio of the transverse reinforcement. Val et al. (2006) noted that there is insufficient experimental data with a significant amount of transverse reinforcement affecting bond strength. Thus the effect of confinement due to transverse reinforcement was not considered in the k_1 parameter. This was considered conservative because the effect of confinement would increase the bond strength (Val et al., 2006). The parameter k_1 can be calculated using Equation 2.82.

$$k_1 = \begin{cases} 1 & \dfrac{C}{d_b} \leq 1 \\ 1 + 0.085\left(\dfrac{C}{d_b} - 1\right) & \dfrac{C}{d_b} > 1 \end{cases} \tag{2.82}$$

The parameter k_2 represents the rate of decrease of the bond strength. Similar to the parameter k_1, k_2 was considered to be influenced by the confinement; however, unlike k_1, the influence of cover to bar diameter ratio was found to be statistically insignificant and was thus excluded from the regression model of k_2. Equation 2.83 is used to calculate the k_2 parameter, where ρ_{tr} is the transverse reinforcement ratio.

$$k_2 = \begin{cases} 0.005 & \rho_{tr} > 0.25 \\ 0.005 - \dfrac{\rho_{tr} - 0.25}{300} & 0.25 < \rho_{tr} \leq 1 \\ 0.0025 & \rho_{tr} > 1 \end{cases} \tag{2.83}$$

The model proposed by Val et al. (2006) was validated against beam tests conducted by Rodriguez et al. (1996). The finite element model seemed to overpredict the initial stiffness of the specimens as well as overpredict the strength of the specimens. Val et al. (2006) concluded that the stiffness was overpredicted because of the corrosion induced cracking that was not considered in the model and that the strength was overpredicted because pitting corrosion was not considered in the analysis and thus failure of the section due to pitting corrosion was not captured. Fig. 2.33 depicts the analytical results obtained by Val et al. (2006) compared with the experimental results of Rodriguez et al (1996).

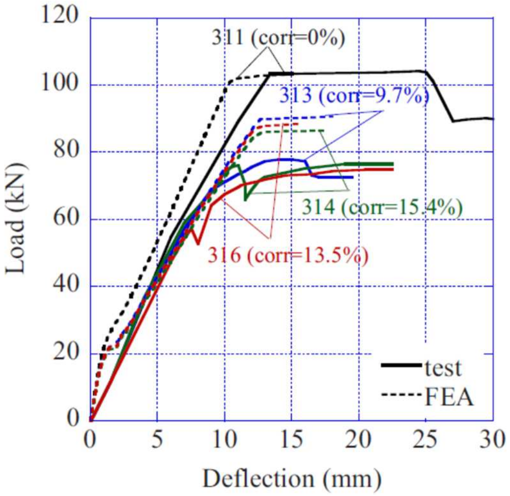

Fig. 2.33: Comparison of analytical results obtained by Val et al. (2006) versus Rodriguez et al (1996). Taken from Val et al. (2006).

2.8.1.5 Wang and Lui – 2006

Wang and Lui (2006) presented a theoretical model for the prediction of bond strength that incorporated the effects of corrosion. The theoretical model determines the pressure due to corrosion effects and the shear stress required to pullout the specimen, and then determines the ultimate shear stress including corrosion effects using Equation 2.84.

$$\tau_u(X) = \tau_{crx} + \tan\alpha \cdot p_{corr} \tag{2.84}$$

where: $\tau_u(X)$ is the ultimate strength of the bond for a corrosion depth X; τ_{crx} is the splitting bond strength; p_{corr} is the radial stress due to corrosion pressure; and α is the angle of the bond failure plane.

The model takes into account corrosion via the direct inclusion of the confining pressure from corrosion expansion. The calculation of this pressure is achieved by idealizing the problem as a circular reinforced concrete section of radius R_c. The cracking point is defined by a radius of R_i below which the radial strain exceeds the cracking strain of the concrete. The bar radius is defined as R_0 and the corrosion penetration depth is defined as X. The radial model is shown in Fig. 2.34.

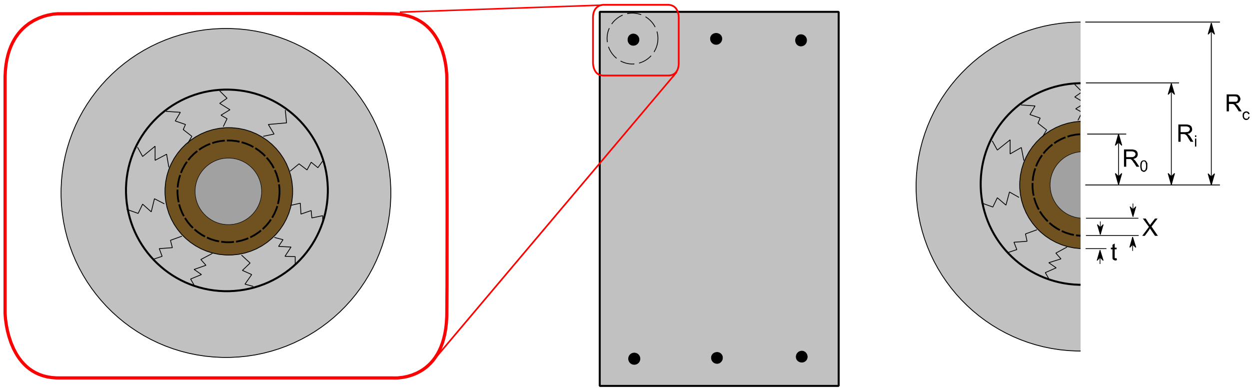

Fig. 2.34: Assumed corrosion expansion model. Reproduced from Wang and Lui (2006).

Using elastic theory, Equation 2.85 was derived and can be solved to calculate the value of R_i for a given corrosion depth X.

$$\frac{(n-1)(2R_0X-X^2)}{R_i+R_0}=\frac{f_t}{E_0}\cdot R_0\cdot\frac{(R_c/R_0)^2+1}{(R_c/R_i)^2+1} \tag{2.85}$$

where: n is the volumetric ratio between corrosion products and virgin steel; f_t is the tensile strength of the concrete; and E_0 is the initial tangent modulus of elasticity. The corrosion pressure is then calculated based on equilibrium conditions using Equation 2.86.

$$p_{corr}\cdot R_0=p_i\cdot R_i+\int_{R_0}^{R_i}\sigma_\theta(r)dr \tag{2.86}$$

where: p_i is the pressure due to the elastic contribution of the uncracked concrete; and $\sigma_\theta(r)$ is the hoop stress within the cracked concrete.

Various solutions to the integral in Equation 2.86 were presented by Wang and Lui (2006). A variable X_{CR} was defined as the critical corrosion penetration depth that causes the entire cover to be cracked, or $R_i = R_c$ (Wang and Lui, 2006). Depending on the level of corrosion, different integration solutions were presented. The critical corrosion penetration depth could then be calculated from Equation 2.85 by assuming that $R_i = R_c$ (Wang and Lui, 2006).

The splitting bond strength was determined by assuming a failure plane at a depth of two times the rib height away from the reinforcement ribs. The failure criterion proposed by Ottosen (1977) was used to solve for the strength of the bond. The maximum bond stress was then calculated based on Equation 2.84.

The model proposed by Wang and Lui (2006) represents an entirely analytical model that does not rely on regression from test results. The model was demonstrated to be in good agreement with experimental results. However dependence is identified by Wang and Lui (2006) on the parameter n, which dictates the ratio of material expansion between virgin material and corroded material. In addition, the model does not account for confinement provided by transverse reinforcement which has been shown by other researchers to significantly contribute to corroded bond strength.

2.8.2 Modelling Effects of Pitting Corrosion

Pitting corrosion has been documented to have an effect on the yield strength, ultimate strength, and ductility of steel reinforcement. Cairns et al. (2005) presented a model to predict the effects of pitting corrosion on reinforced concrete. Equation 2.87 through Equation 2.89 were proposed to model the effects of pitting corrosion on steel reinforcement.

$$f_y = \left(1 - \alpha_y \cdot Q_{corr}\right) f_{y0} \tag{2.87}$$

$$f_u = (1 - \alpha_u \cdot Q_{corr}) f_{u0} \tag{2.88}$$

$$\varepsilon_u = (1 - \alpha_1 \cdot Q_{corr}) \varepsilon_{u0} \tag{2.89}$$

In each case, the mechanical properties deteriorate linearly as a function of two factors: α which controls the rate of deterioration, and Q_{corr}, which is ratio of the average sectional loss and the original cross section.

The values taken for each of the α coefficients in Equation 2.87 through Equation 2.89 vary widely in the literature. Cairns et al. (2005) noted that a review of the literature reveals that a value of α_y and α_u of 0.01 can be used for uniform corrosion and a value greater than 0.01 represents non-uniform corrosion. Other researchers (Stewart and Mullard, 2007; Sewart and Suo, 2009; Stewart, 2012) consistently uses the value of 0.005, originally recommended by Du et al. (2005), for the α_y coefficient to represent the loss of yield strength due to pitting corrosion. The summary of studies compiled by Cairns et al. (2005) show a coefficient of variation of 69 percent for α_y and 65 percent α_u. Additionally, a loss of ductility due to pitting corrosion, α_1 ,was observed to vary greatly between studies from no loss of ductility, ($\alpha_1 = 0$) to a large loss of ductility ($\alpha_1 = 0.039$). Stewart (2009) noted that the corrosion percentage in which a significant loss of ductility is observed is not well-established in the literature. Stewart (2009) defined a transition corrosion percentage of 20 percent, between which ductile and non-ductile behaviour is observed.

Due to the complexity of the corrosion cells, and the variation in material properties, the location of pitting corrosion is not easy to identify on a structure. As a result, two approaches are adapted to model pitting corrosion. In the former approach, the pitting corrosion is assumed to occur in the worst possible area. For example, in a simply supported beam, an engineer may choose to model the pitting corrosion at a location of maximum moment. However, in the case of a reliability analysis, the probability of failure for a structure would greatly be affected by the location of the maximum pitting depth. Thus the location of maximum pitting depth must be a stochastic variable.

Stewart (2009) considers this by defining lengths of equal strength which are determined stochastically. In the case of a beam for example, the beam would be split into segments of a length l_u and a corrosion pitting depth is generated as a sample of a probability distribution for the maximum pitting depth. The associated loss in cross-sectional area and yield strength are then assumed constant over the segment. An illustration of this concept is presented in Fig. 2.35.

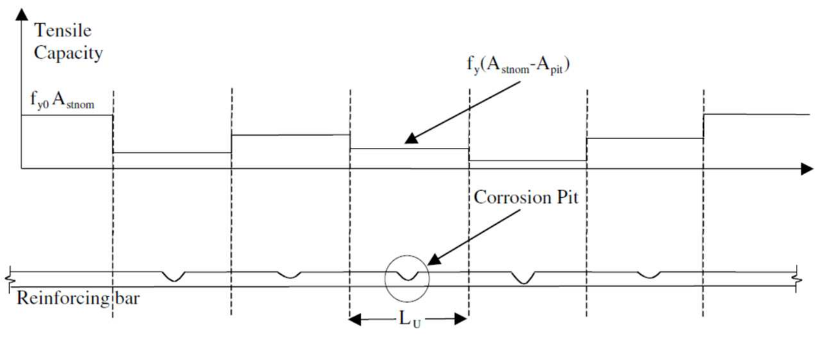

Fig. 2.35: Uniform capacity segments. Taken from Stewart (2009).

One main statistical assumption of the methodology proposed by Stewart (2009) is that each of the uniform capacity length l_u are statistically independent. While this provides the ability to consider the spatial effects of pitting corrosion, the uniform capacity length is at the discretion of the engineer. It would be advantageous to develop a random field approach to the modelling of pitting corrosion along the length of steel reinforcement. Such an approach was adopted by Teixeira et al. (2013) for the modelling pitting corrosion in two-dimensional ship plates. The pitting corrosion was modelled as a two-dimensional lognormal random field. The applicability of such an approach to the corrosion of reinforced concrete requires further investigation.

2.8.3 Corrosion Induced Strain

The expansion of reinforced concrete causes concrete to crack and as a result introduces a strain on the reinforced concrete. Two of the recommended aspects required to capture the response of corroded reinforced concrete can be considered by the resulting tensile strains induced by corrosion cracking. It is important then to determine the induced strains that contribute to compression softening, and reduction in tension stiffening of corroded reinforced concrete.

Coronelli and Gambarova (2004) captured the effects of out-of-plane tensile strains by modelling the cover elements with a reduced compressive strength. The model for the reduced compressive strength was adapted from Vecchio and Collins (1986) and is presented in Equation 2.90.

$$f_c = \frac{f_c'}{1 + K\varepsilon_1/\varepsilon_2} \tag{2.90}$$

where K = 0.1 is recommended. The average tensile strain is computed by assuming that the change in length due to corrosion is equal to the product of the number of bars and the crack width induced by corrosion. The crack width is calculated using an equation originally prosented by Molina et al. (1993). Equation 2.91 was recommended by Coronelli and Gambarova (2004) to calculate the crack widths associated with corrosion.

$$\varepsilon_1 = \frac{n_{Bars}[2\pi(n-1)X]}{b_0} \tag{2.91}$$

In the development of a model for bond stress, Wang and Lui (2006) proposed a method for calculating the hoop strains caused by expansion of corrosion products. Using Equation 2.85 to first calculate the crack front for a given corrosion penetration depth, Wang and Lui (2006) proposed an equation for the hoop strain at any position *r* from the center of a reinforcing bar. Equation 2.92 can be used to estimate the strain at any radius *r*.

$$\varepsilon_\theta(r) = \frac{f_t}{E_0} \cdot \frac{(R_c/r)^2 + 1}{(R_c/R_i)^2 + 1} \tag{2.92}$$

The hoop strains could be converted into crack widths by making assumptions about the radial crack spacing. Alternatively, the equations proposed by Li et al. (2006) could be used to convert the hoop strains predicted by Wang and Lui (2006) into crack widths. The methods proposed by Li et al. (2006) are presented below.

Li et al. (2006) derived Equation 2.93 to calculate the average hoop strain between the cover and the reinforcement.

$$\overline{\varepsilon_\theta} = \frac{1}{R_c - R_0 - t} \int_{R_0+t}^{R_c} \varepsilon_\theta(r)dr = \frac{\left[(R_c)^{\sqrt{\alpha}} - (R_0 + t)^{\sqrt{\alpha}}\right]\left[c_5 + \frac{c_6}{[R_c(R_0+t)]^{\sqrt{\alpha}}}\right]}{\sqrt{\alpha}[R_c - (R_0 + t)]} \tag{2.93}$$

where: α is a stiffness reduction factor to account for the cracked concrete; and c_5 and c_6 are constants obtained from boundary conditions. Simultaneous solution of three equations can be used to calculate c_5, c_6 and α. An expression was also developed to predict the crack width at the surface of the concrete cover. Equation 2.94 can be used to calculate the crack width at the concrete cover surface.

$$w_c = 2\pi R_c\left[\varepsilon_\theta(R_c) - \varepsilon_\theta^{e,m}(R_c)\right] \tag{2.94a}$$

$$w_c = \frac{4\pi(X + t)}{(1 - \nu_c)[(R_0 + t)/R_c]^{\sqrt{\alpha}} + (1 + \nu_c)[(R_0 + t)/R_c]^{-\sqrt{\alpha}}} - \frac{2\pi R_c f_t}{E_{eff}} \tag{2.94b}$$

For consistency in notation, the parameter ds(t) originally proposed by Li et al. (2006) was replaced with (X + t). This is because it is convenient to express the corrosion penetration in reference to the original bar diameter. It is assumed that Equation 2.77, proposed by Coronelli (2002), can be used to determine the parameter t and thus keep consistent notation between proposed models. Similar to Coronelli and Gambarova (2004), the strain due to concrete cracking could be estimated by assuming that the change in width of a concrete specimen is equal to the product of the number of bars and the crack widths.

The effect that transverse reinforcement has on the crack widths and corrosion induced strain is unclear from the discussion of the models presented by Wang and Lui (2006) and Li et al. (2006). Theoretically, it is logical to assume transverse reinforcement would result in a reduction in crack widths, and an associated reduction in compression softening effects. However, transverse and longitudinal reinforcement will corrode simultaneously and, as a result, may cause an increase the crack width. Further investigation into the effect of transverse reinforcement on longitudinal corrosion cracks should be undertaken.

In modelling the effects of tension stiffening and compression softening, two approaches can be taken. The first approach involves reducing the material parameters of the concrete to simulate damage. The second approach involves predicting the strains induced by corrosion products, and applying those strains as pre-strains in a finite element model. The latter approach could be taken when adopting the corrosion modelling of reinforced concrete using MCFT/DSFM. Using models to predict the width of cracks, and the subsequent strain induced in the finite elements, the ability of the implicit formulations implemented in MCFT/DSFM, the ability to capture the effects of corrosion could be investigated.

2.8.4 Research Needs

Of the five requirements for modelling of corrosion of reinforcement, the one most heavily addressed in the literature is the modelling of bond strength of corroded reinforcement. The extensive amount of experimental work regarding the effect of corrosion on the bond strength of steel reinforcement has been used by multiple researchers to develop empirical bond models. However the range of applicability to the empirical models is difficult to discern when applying the models to actual structures that may differ dramatically from experimental conditions. Analytical bond models have been developed for the case of unconfined concrete; however a theoretically rigorous analytical model for the bond strength of corroded reinforced concrete in the presence of confining pressures has not been developed.

There were two types of analytical studies encountered during the literature review. The first involves two-dimensional (cross-sectional) or three-dimensional analysis of the concrete sections to determine the effect of corrosion products (concrete cracking, bond strength, etc.). The second involves the modelling of the strength of deteriorated structural elements. There are few examples of models that model both the deterioration effects and the strength, with Sanchez et al. (2010) being an example. Such models likely require very fine meshing with detailed contact elements between steel reinforcement and concrete elements that can represent the expansion and bond properties required to capture the behaviour of corroded reinforced concrete. A need exists then, for a simplified tool that captures the deterioration effects of corrosion and has the ability to determine the strength of such structural members.

The stochastic parameters involved in pitting corrosion are approached by defining lengths of equal strength, and then modelling them as statistically independent random variables. It may be advantageous to develop a method for generating random fields that model pitting corrosion of steel reinforcement.

CHAPTER 3: EXPERIMENTAL PROGRAM

A large deep reinforced concrete slab strip specimen (PLS4000) was constructed and tested at the University of Toronto by Quach (2016). In a subsidiary experimental program, undertaken by this author, a set of ultrasonic pulse velocity measurements was taken from a grid of points on the Quach specimen to assess the spatial variability of the concrete. The spatial variability was incorporated into the finite element models and the results are discussed. This chapter describes the procedure, results, and analysis of the subsidiary experimental program.

3.1 PLS4000 Specimen Details

The specimen considered herein was a large reinforced concrete slab strip denoted PLS4000. The slab strip was constructed and tested by Quach (2016) as part of an investigation to assess the shear strength of very large unreinforced concrete slabs. For more information on the construction and experimental data for PLS4000, the reader is referred to Quach (2016) and Collins et al. (2015).

The slab strip was segregated into two spans labeled east and west. The west span was 7 metres in length, containing vertical 20M T-headed shear reinforcement spaced at 1500 mm. The east span was 12 metres in length and contained no transverse shear reinforcement. The slab strip contained nine 30M reinforcing bars of Grade 500W steel as longitudinal reinforcement. This equates to a longitudinal reinforcement ratio of 0.656 percent. Three 20M bars were used for crack-control at the top of the slab strip. The specified thickness of the slab strip was 250 mm. Fig. 3.1 shows an elevation of the slab strip. Fig. 3.2 shows the sections of the slab strip for both spans.

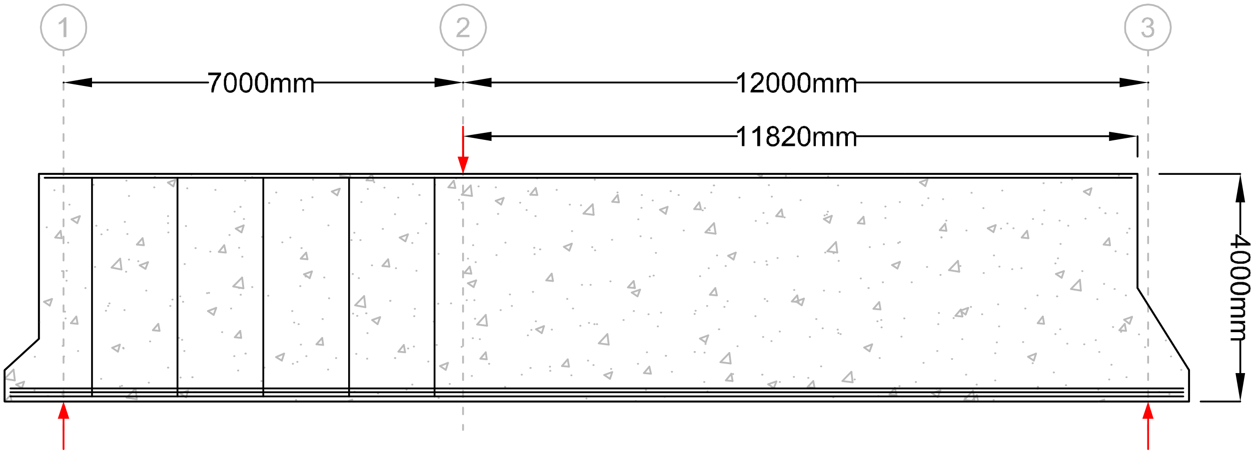

Fig.3.1:Elevation of specimen PLS4000 tested by Quach (2016).

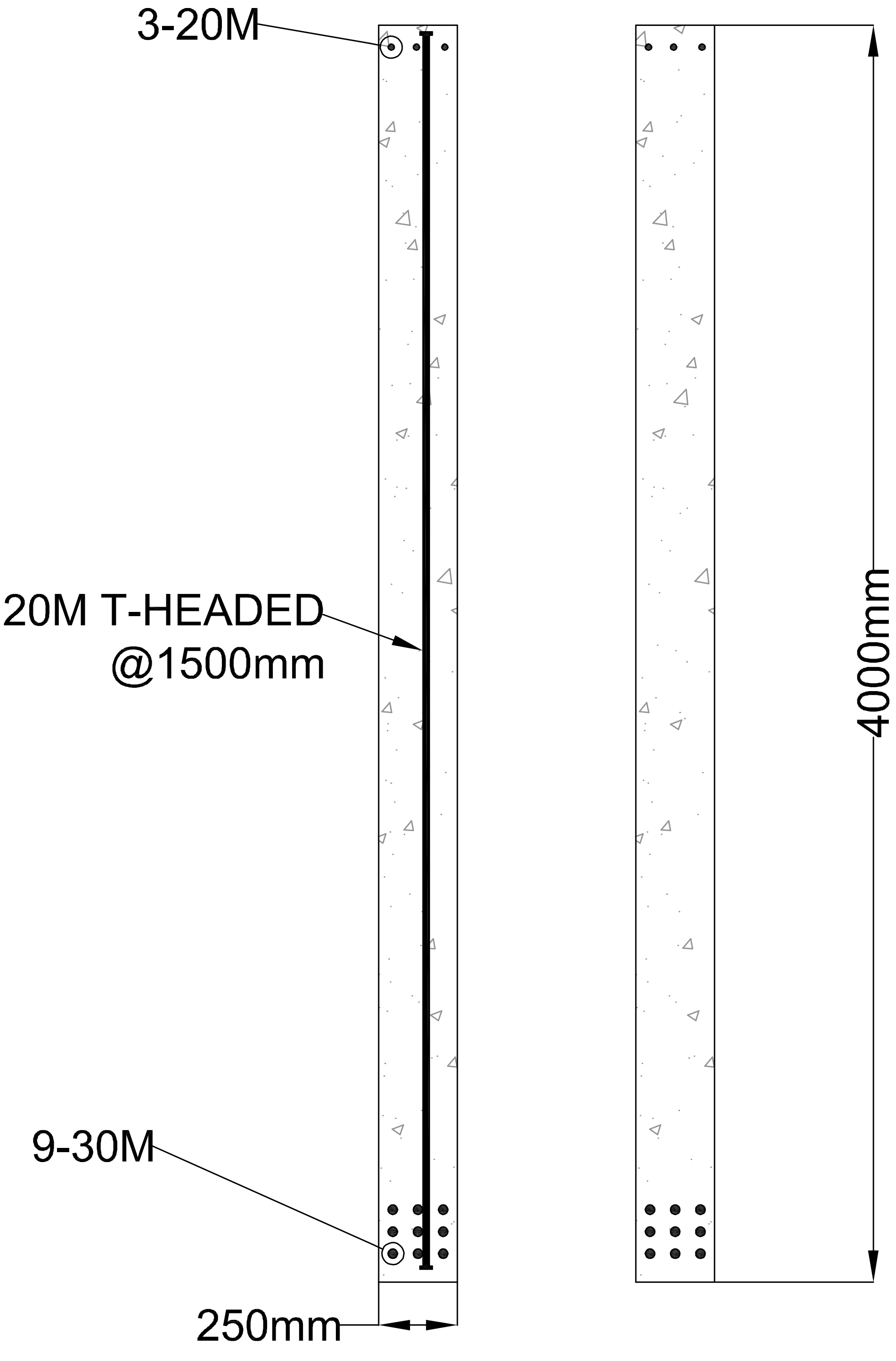

(a) (b)

Fig. 3.2: Section properties of slab strip specimen PLS 4000, tested by Quach (2016).
(a) West span. (b) East span.

3.2 Data Collection Procedure

The objective of the subsidiary study was to determine if statistically significant spatial variability existed between concrete within the same large specimen, and to spatially map the compressive strength using the nondestructive test data. The experimental program involved the collection of ultrasonic pulse velocity (UPV) measurements from the slab strip and from five sets of cylinders. Each set of cylinders contained two cylinders from each batch of concrete (three trucks were used in casting) for a total of six cylinders per set. The cylinders were tested at 7, 14, 22, 28, and 42 days after the cast. For a given set of cylinders, the cylinders were demolded and ground in preparation for compressive strength testing. Ultrasonic pulse velocity measurements were then collected from each cylinder. The experimental setup for the cylinder UPV measurements is shown in Fig. 3.3.

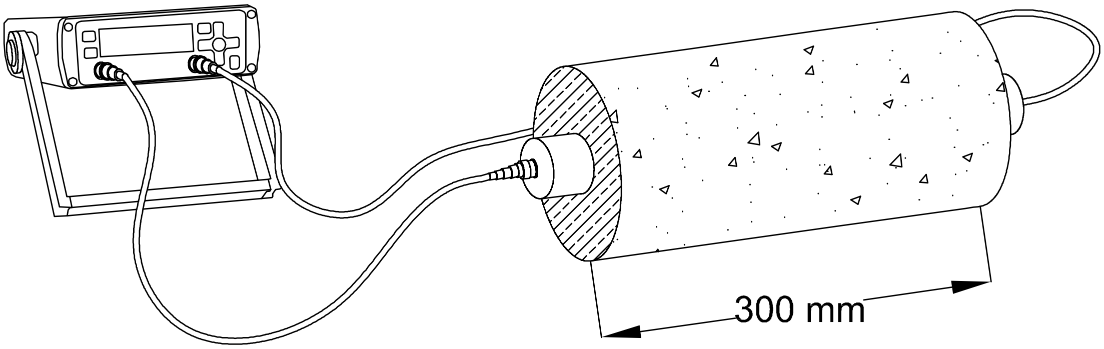

Fig. 3.3: Experimental test setup for compressive strength test cylinders.

For the UPV tests on the main slab strip, a set of grid points was established. Measurements were taken at increments of 500 mm in the vertical direction and between 610 mm and 533 mm in the horizontal direction. The variable spacing of the horizontal coordinates was selected such that the measurements would fall directly between surface seams caused by the formwork. The forms were constructed using prefabricated panels with either a width of 610 mm (24 in) or 457 mm (18 in). At the joints between the panels, vertical and horizontal surface seams were created. Thus in order to avoid the surface seams, the vertical gridlines were centered between adjacent defects. The horizontal gridlines were labeled A through G while the vertical grid lines were labeled 1 through 19. Thus each measurement is spatially referenced by a letter-number pairing (e.g. B3). The grid layout is shown in Fig. 3.4. The grid was measured using a ruler that was suspended from the top of the slab strip. Thus all vertical dimensions are in reference to the top of the slab strip. The ruler was leveled vertically and each grid point was centered between seams. Horizontal and vertical grid points were then checked with a level and a tape measure.

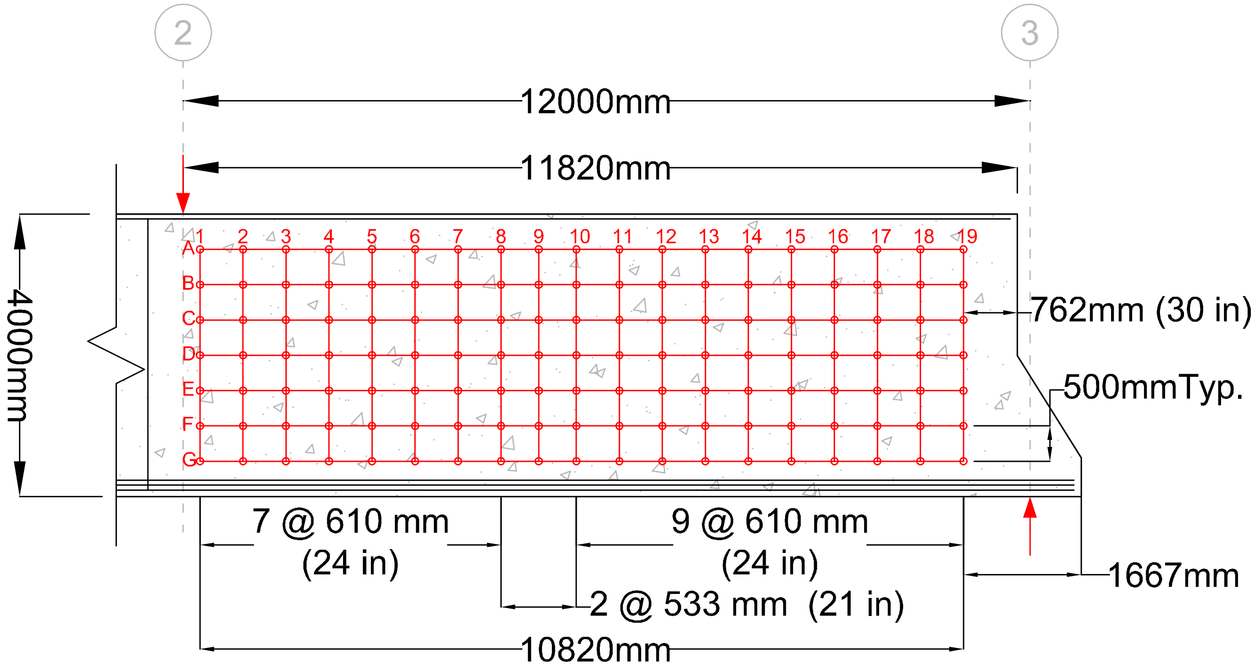

Fig. 3.4: Grid layout of ultrasonic pulse velocity testing.

In addition to the large grid, a smaller grid was established in order to capture a small section of the slab strip at a higher resolution. The smaller grid added two vertical gridlines between each major vertical gridline, and one horizontal gridline between each major horizontal gridline. This created a vertical gridline spacing of approximately 200 mm and a horizontal gridline spacing of approximately 250 mm. The vertical gridlines were designated as M.1 and M.2 where M is the number of the previous major gridlines. For example, the two minor gridlines between major gridlines 4 and 5 are designated 4.1 and 4.2. The horizontal minor gridlines were designated M.5 where M is the letter of the previous gridline. For example, the small gridline between E and F is labeled "E.5". The smaller grid spanned from vertical gridlines 3 to 7 and from horizontal gridlines D.5 to G. The small grid is illustrated in Fig. 3.5.

The UPV instrument only measures the travel time of the ultrasonic pulse. In order to determine the velocity, the thickness of the slab strip must be assessed. The original form work required a series of ties passing through the width of the slab strip in order to hold the forms together. This left a set of holes though the slab strip that were used to measure the width of the slab strip. The location of the holes and surface seams are shown in Fig. 3.6.

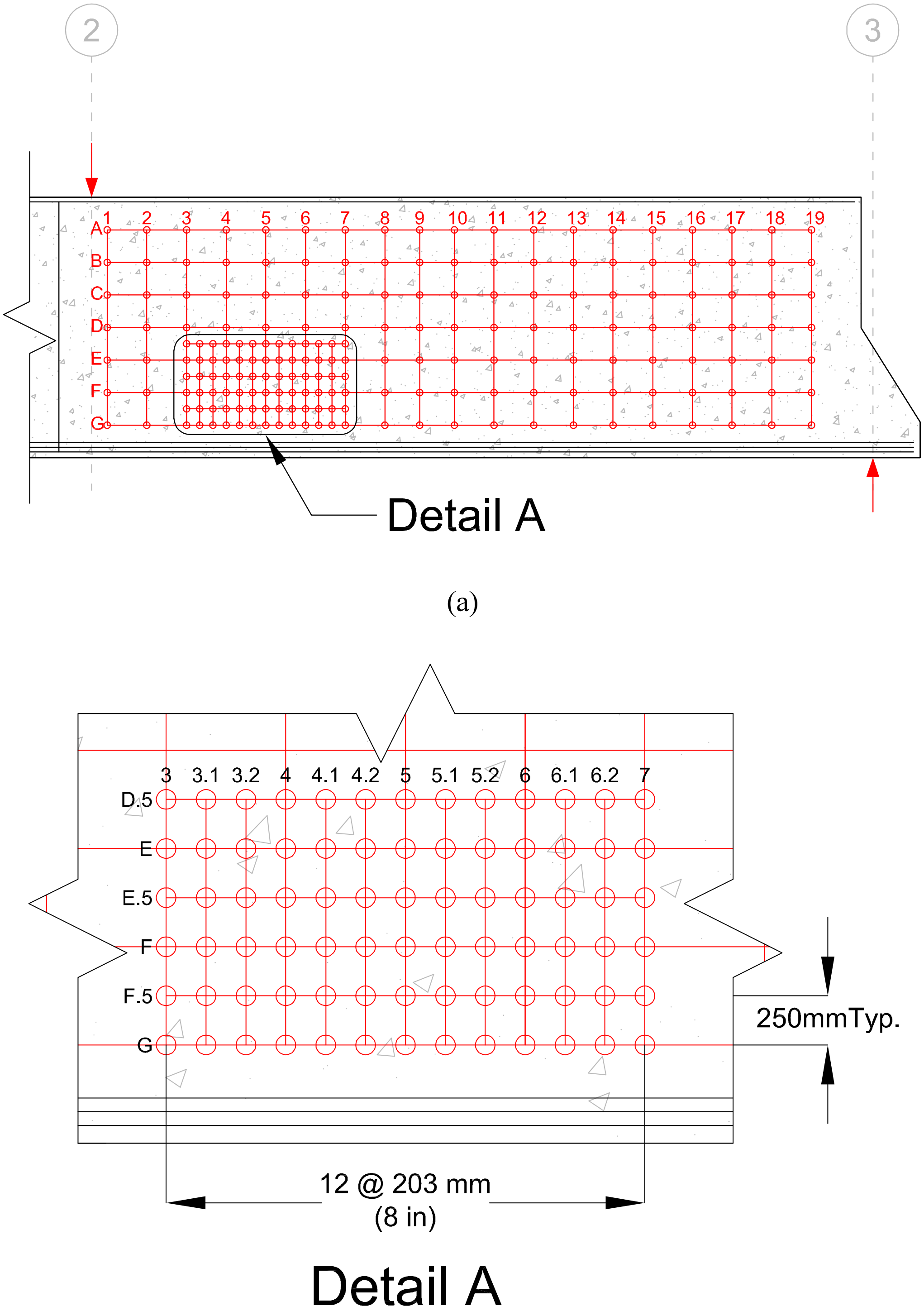

(b)

Fig. 3.5: (a) Global position of small grid. (b) Small grid layout and dimensions.

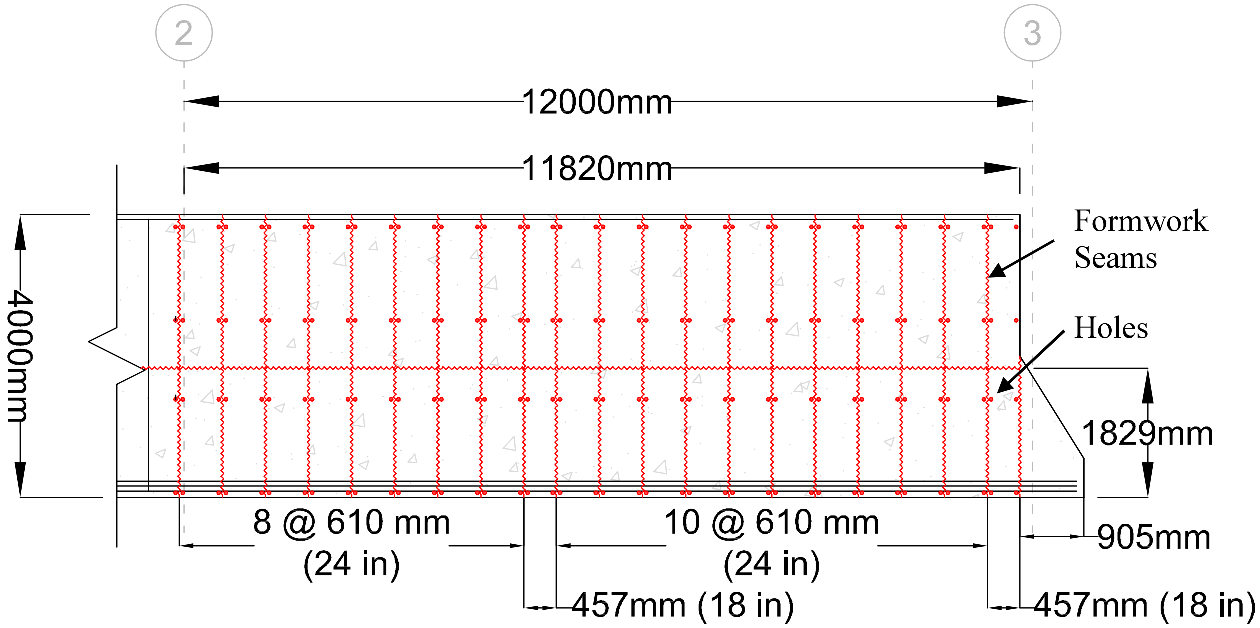

Fig. 3.6: Location of holes and surface seams.

3.3 Experimental Results

This section summarizes the observed experimental data for concrete cylinder tests, the UPV measurements, and the measured widths. Two concrete cylinders from each of the three trucks were tested at 7, 14, 22, 28, 35, and 49 days. The 28-day compressive strength of the concrete cylinders had an average value of 39.4 MPa, which was significantly higher than the specified strength of 25 MPa. Table 3.1 summarizes the compressive strength values for each truck. For each cylinder, UPV measurements were taken. Due to scheduling issues, the UPV measurements were not collected for the 35-day cylinders. In addition, the UPV measurements for the 49-day cylinders were taken at 42 days. The UPV measurements are summarized in Table 3.2. A scatter plot of the measured UPV and compressive strength is shown in Fig. 3.7. It is clear from this plot that a correlation exists between the UPV and the compressive strength of the concrete. These correlations are described in Section 3.4.2.

From the PLS4000 specimen, two grids of UPV measurements were obtained. The main grid was measured at a concrete age of 14 days, and the small grid was measured at a concrete age of 15 days. At each grid point, five UPV measurements were recorded and averaged. To aid in the visualization of the data, a cubic spline interpolation of the main grid is shown in Fig. 3.8. From the figure, it is observed that there was distinct stratification in the vertical direction. The concrete

Table 3.1: Compressive Strength Values for Concrete Cylinders

Test Date		Compressive Strengths [MPa]			
		Truck 1	Truck 2	Truck 3	Average
7 Day	A	27.0	31.8	31.6	30.0
	B	26.8	32.2	30.3	
14 Day	A	32.7	34.9	37.3	35.7
	B	33.9	38.5	37.0	
22 Day	A	37.3	36.9	38.0	37.2
	B	38.0	38.1	35.3	
28 Day	A	38.5	35.6	42.6	39.4
	B	42.0	42.2	35.4	
35 Day	A	37.5	42.1	38.9	41.5
	B	39.1	44.5	46.7	
49 Day	A	42.8	44.7	45.6	43.4
	B	40.6	42.6	44.2	

Table 3.2: Ultrasonic Pulse Velocities for Concrete Cylinders

Test Date		Ultrasonic Pulse Velocity [m/s]				Length [mm]
		Truck 1	Truck 2	Truck 3	Average	T1/T2/T3
7 Day	A	4638	4735	4698	4662	301/298/294
	B	4609	4727	4566		296/299/297
14 Day	A	4842	4844	4754	4814	299/295/299
	B	4793	4851	4801		296/293/299
22 Day	A	4888	4860	4879	4873	304/296/304
	B	4900	4875	4834		303/297/304
28 Day	A	4928	4935	4968	4932	300/303/302
	B	4860	4992	4910		301/301/304
42 Day	A	4944	4981	5033	5002	301/303/301
	B	5018	5012	5022		303/301/305

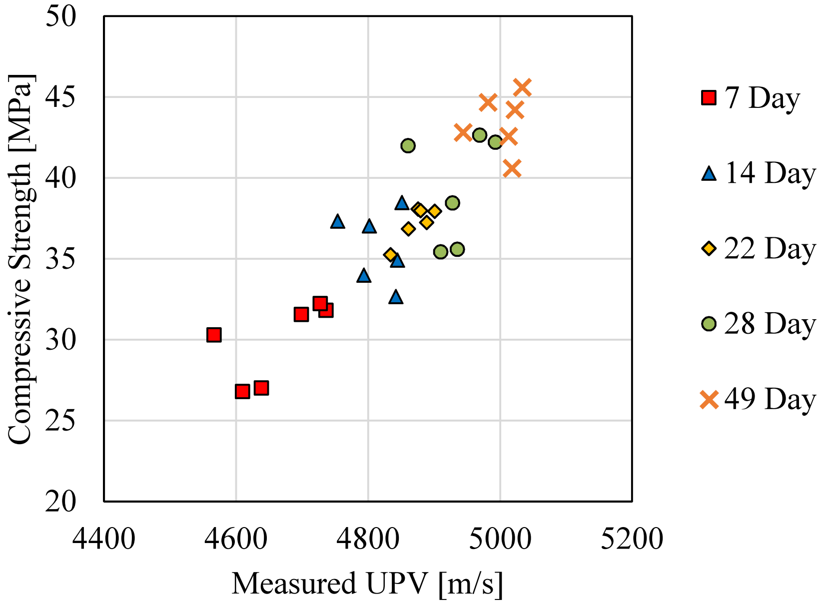

Fig.3.7: Measured ultrasonic pulse velocity versus cylinder compressive strength.

was cast using three trucks each with a lift height of approximately 1 to 1.5 metres. The UPV measurements therefore are consistent with concrete placement. Additionally, the cylinders from the second truck, at 14-day strength, were consistently stronger than those from the other two trucks. This is reflected in the shorter travel time for the ultrasound wave that was observed. The travel time measurements ranged from 50.9 and 54.5 microseconds.

The small grid visualization is shown in Fig. 3.9. The smaller gird also reflects the stratification observed in the main grid; however, it only includes the bottom two lifts.

The stratification boundary in both the main grid and the small grid appears to be at an elevation of approximately 1200 mm.

The thickness of the slab strip was measured at a series of holes that were present in the slab strip (see Fig. 3.6). The slab strip thickness at each grid point was then determined by linear interpolation. The variation of thickness in the slab strip was found to be between 244 and 259 mm for the minimum and maximum measured thickness respectively. A contour of the measured thickness of the slab strip is shown in Fig. 3.10.

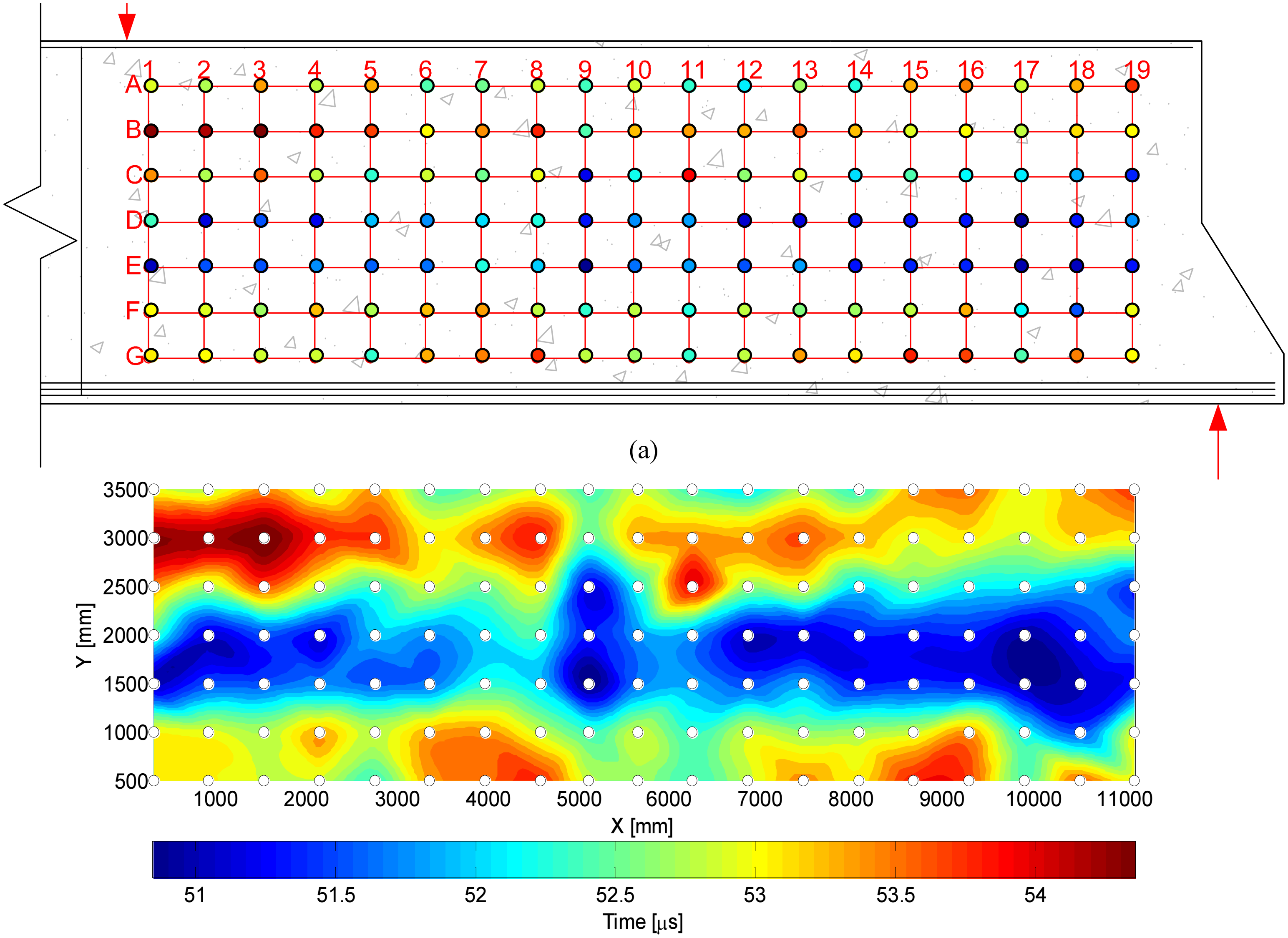

(a)

(b)

Fig. 3.8: UVP time measurements for main grid. (a) Actual data (b)Interpolated data.

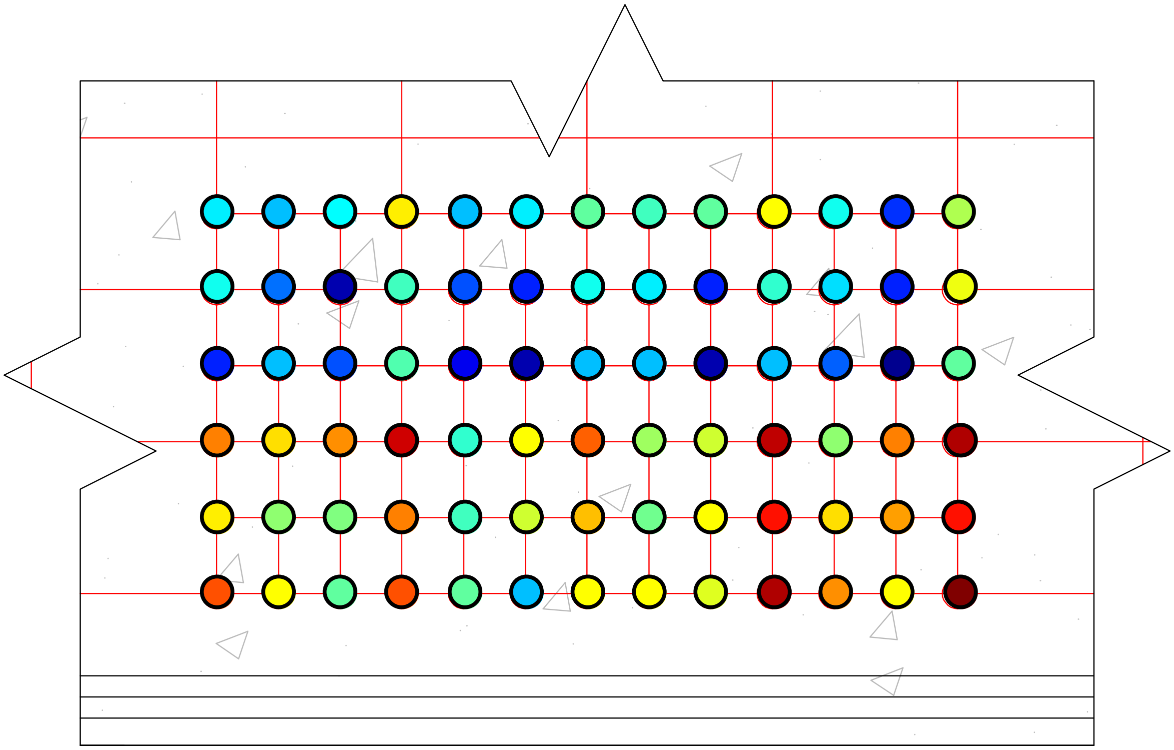

(a)

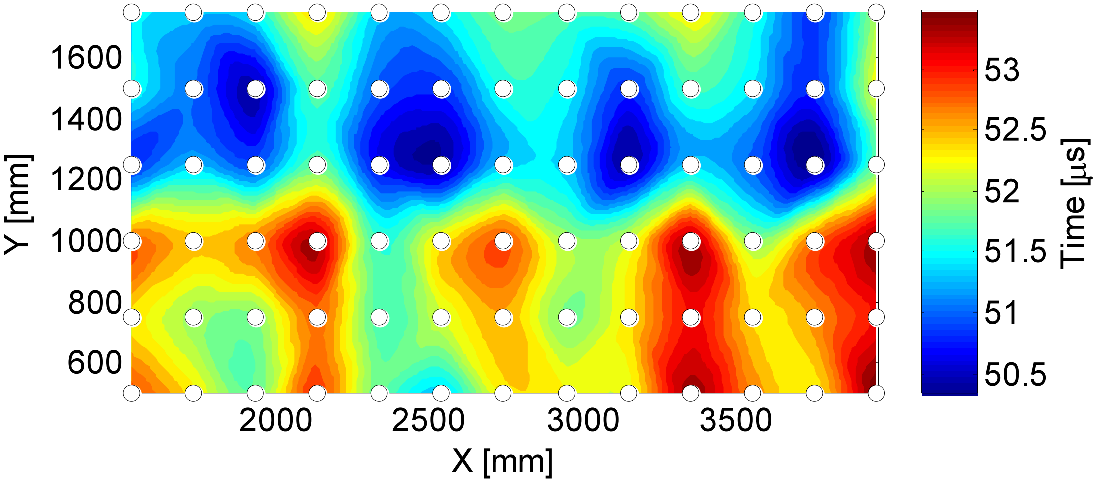

(b)

Fig. 3.9: UVP time measurements for small grid. (a) Collected data (b) Interpolated data.

The ultrasonic pulse velocity was calculated using the measured times and the interpolated thickness. The UPV measurement is calculated using Equation 3.1 where Δx is the measured thickness and Δt is the measured travel time.

$$UPV = \Delta x/\Delta t \tag{3.1}$$

Fig. 3.11shows the interpolated UPV measurements corrected for thickness variations for the large grid. Similarly, Fig. 3.12shows the UPV measurements for the small grid.

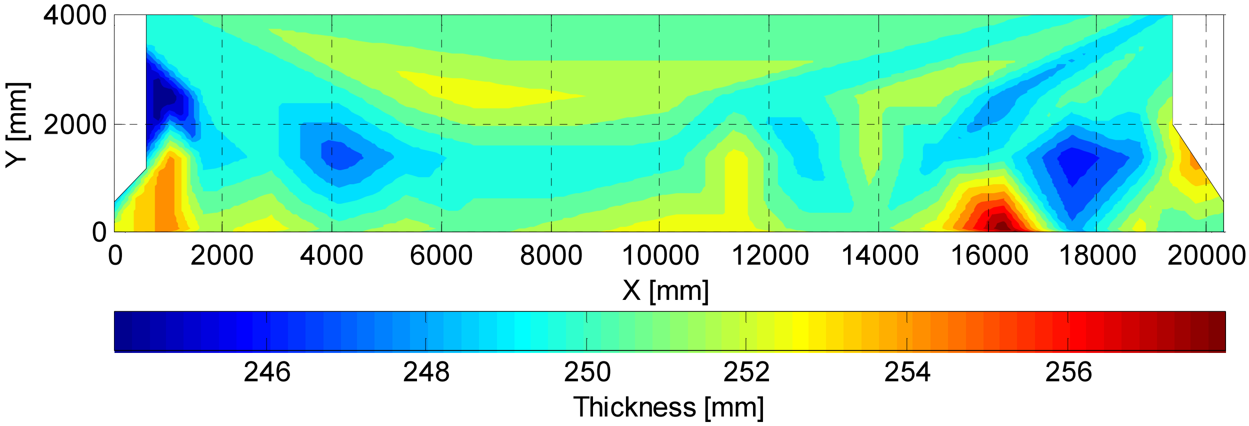

Fig. 3.10: Interpolated plot of measured thickness.

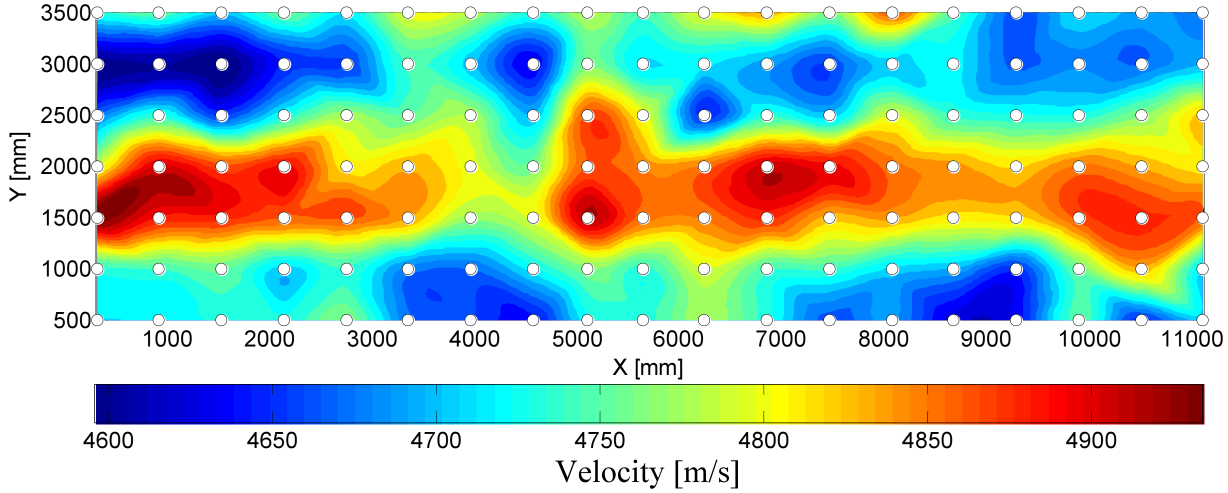

Fig. 3.11: Calculated UPV for large grid with cubic spline interpolation.

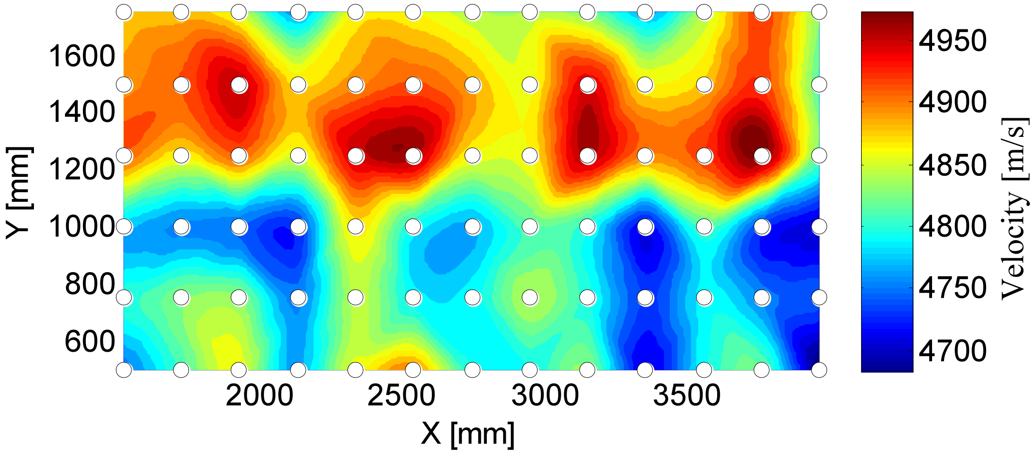

Fig. 3.12: Calculated UPV for small grid with cubic spline interpolation.

3.4 Analysis of Collected Data

In this section, the collected data are analyzed to assess the spatial properties of the concrete. Geospatial statistical methods are employed to determine the spatial characteristics of the slab strip. Kriging maps are developed to interpolate the material properties between the collected data. The thickness of the slab strip, the ultrasonic pulse velocity data, and the concrete compressive strength datasets are addressed.

3.4.1 Slab Strip Thickness

The thickness of the slab strip showed little variation, ranging between 244 mm and 259 mm. The variation of thickness is assumed to be a random variable. The distribution of thickness observed in the slab strip was found to be normally distributed with a mean value of 251.0 mm and a coefficient of variation of 1.0 pecent. The fitted distributions are shown in Fig.3.13. Due to the nature of the thickness variation, changes in thickness occur due to changes in the formwork, and thus one might expect some spatial correlation to exist. However, the experimental semivariogram, plotted in Fig.3.14, reveals that no such spatial correlation exists in the thickness. (For more information on experimental semivariograms, the reader is referred to Section 3.4.3.) This is in part due to the difficulty of measuring the thickness. The thickness was only measured through holes in the slab strip left from the formwork. Thus data could not be collected at small enough lag distances, and the spatial statistical properties of the random field could not be properly assessed. Thus no statistically significant conclusion can be drawn about the spatial statistics of the slab strip thickness.

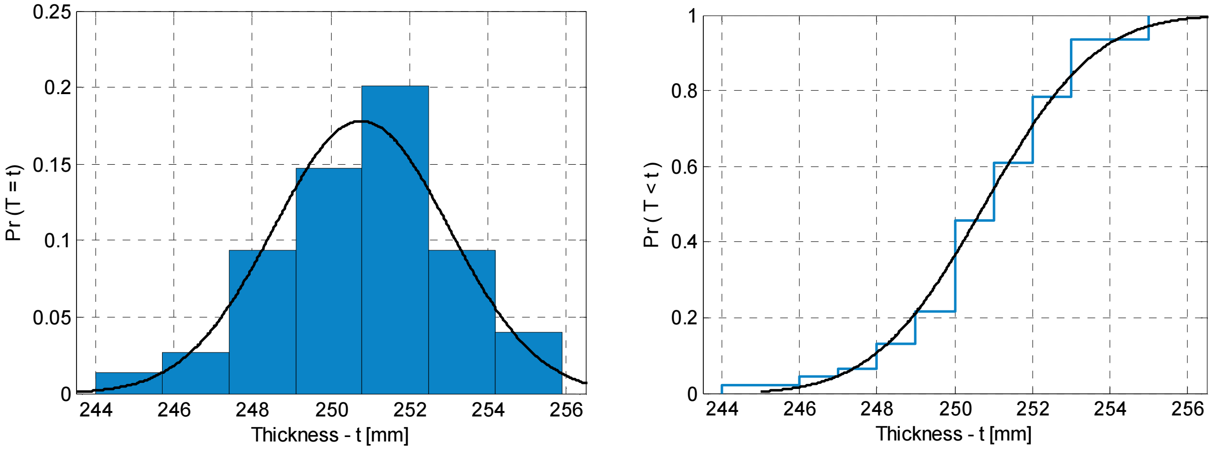

(a) (b)

Fig.3.13: (a) Histogram and fitted PDF of thickness data. (b) Empurical and fitted CDF of thickness data.

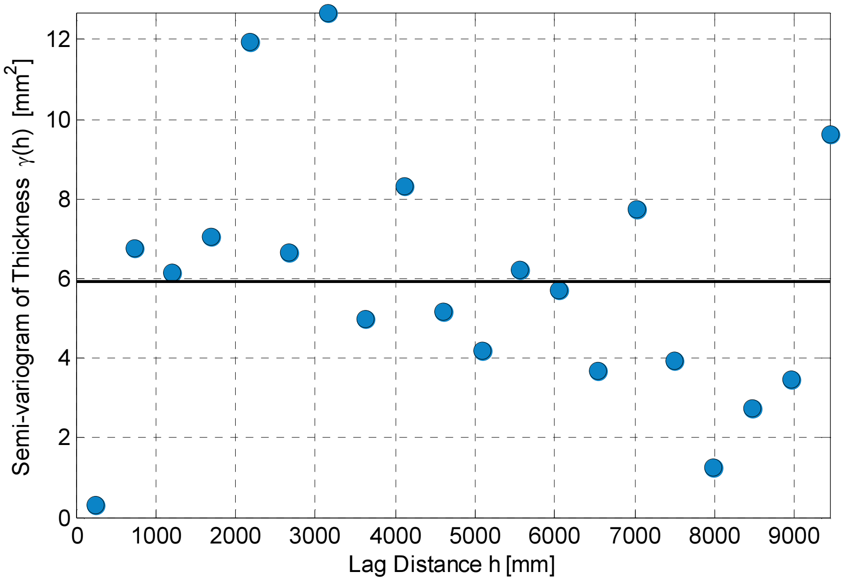

Fig.3.14: Semi-variogram of slab strip thickness.

3.4.2 Concrete Cylinder Data

Concrete cylinders were tested at the ages of 7, 14, 22, 28, 35, and 49 days. For most of the cylinders, the ultrasonic pulse velocity of the concrete was measured. This section discusses the observed trends in the cylinder data. A regression model is developed to relate the ultrasonic pulse velocity to the compressive strength. Additionally, temporal regression models are developed for the compressive strength and ultrasonic pulse velocity.

The regression model adapted from Unwahan and Mahan (2013) was used to evaluate the change in concrete strength versus time. A linear relationship was assumed between the compressive strength, normalized from its 28-day strength, and the natural logarithm of the concrete age in days. Equation 3.2 was developed to describe the compressive strength of concrete.

$$f'_{c,t} = (0.1632 \ln t + 0.4564) f'_{c,28} \tag{3.2}$$

The regression provided an R^2 value of 0.796. This was considered acceptable as the concrete contained both within-batch variation and batch-batch variation. A scatter plot of the collected data and the fitted regression is shown in Fig. 3.15. The regression is also compared against the average of the concrete properties at each test date, shown in Fig. 3.16. This plot reveals good agreement between the test data and the selected regression model.

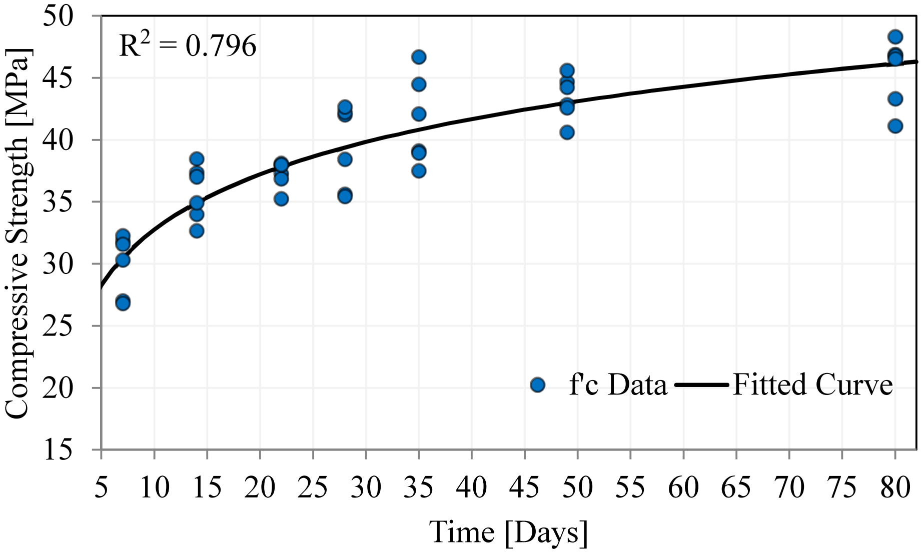

Fig. 3.15: Scatter plot of collected compressive strength data and fitted regression.

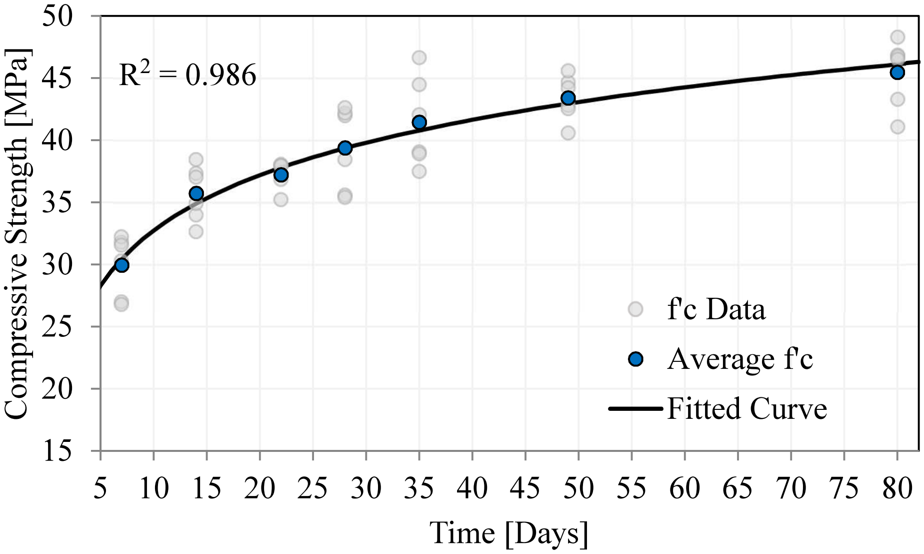

Fig. 3.16: Average daily compressive strength compared against fitted regression.

The same relationship was assumed to relate the evolution of ultrasonic pulse velocity with time. This regression produced a better fit. The R^2 value was calculated to be 0.884. Equation 3.3 relates the ultrasonic pulse velocity with time.

$$UVP_t = (0.038 \ln t + 0.8728) UVP_{28} \tag{3.3}$$

The scatter plot of the UVP versus time is shown in Fig. 3.17. Similar to the compressive strength, when the average of the UPV measurements is compared against the fitted trend, a good agreement is observed.

A third regression model was developed to relate the ultrasonic pulse velocity to the compressive strength of concrete. Panesar and Chidiac (2007) suggested that a linear relationship exists between the fourth root of the concrete strength and the ultrasonic pulse velocity. This relationship was assumed for the regression of the test data. Equation 3.4 is the resulting regression equation.

$$(f_c')^{0.25} = \frac{UPV}{1640} - 0.4968 \tag{3.4}$$

A plot of the test data and the fitted regression is shown in Fig. 3.19. The regression yielded an R^2 value of 0.801. Although this is considered reasonable, it is believed that the regression would be

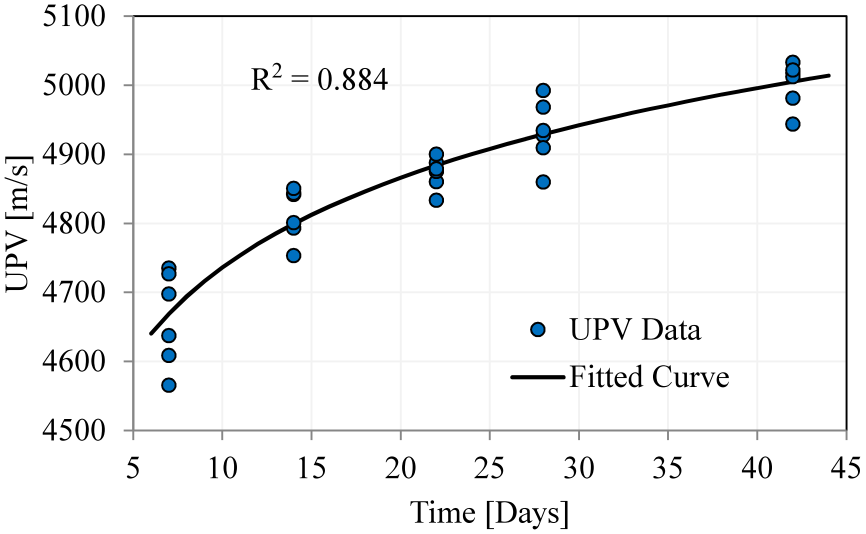

Fig. 3.17: Ultrasonic pulse velocity data versus time and regression model.

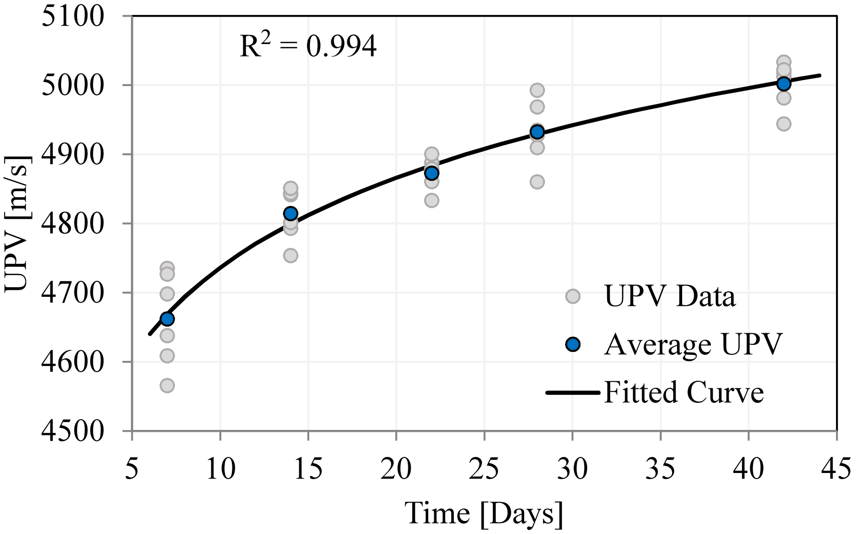

Fig. 3.18: Average ultrasonic pulse velocity compared against regression model.

improved by including 1-Day and 3-Day test data. However only a limited number of cylinders were available for testing. A plot of the fitted regression model with the average UVP and average compressive strengths is shown in Fig. 3.20. This plot reveals that the average values are in good agreement with the predicted model.

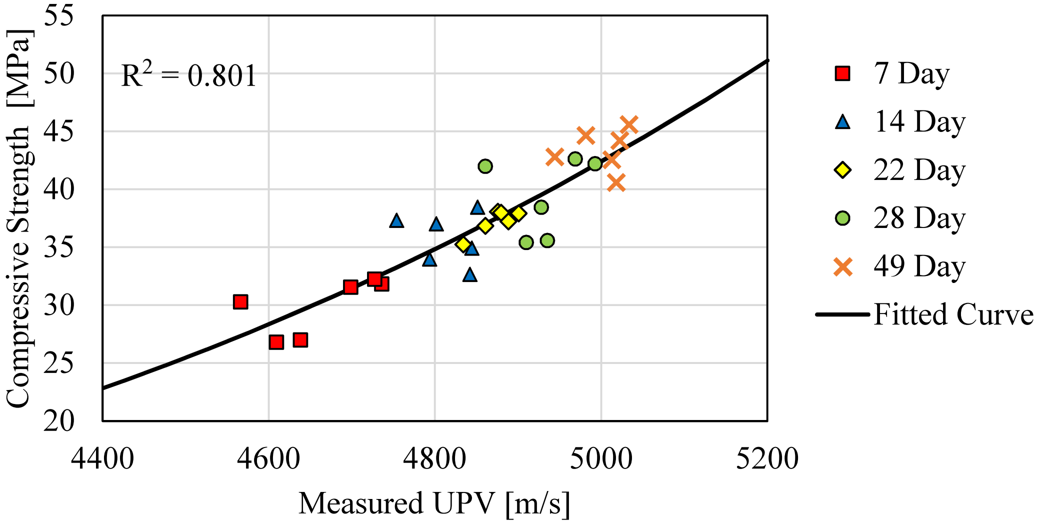

Fig. 3.19: Measured UVP versus compressive strength and fitted regression model.

The residuals from the regression model were analyzed as a random variable. The residuals have a mean of 0.051 MPa and a standard deviation of 2.24 MPa. Least squares regression is based on the assumption of a normally distributed error term. A comparison of the empirical cumulative distribution function for the residuals and a fitted normal distribution confirms this assumption. A KS test on the residuals confirmed the goodness of fit. Thus a normal distribution is considered a good fit for the error parameter in the regression model. A plot of the residuals is shown in Fig. 3.21. A plot of the residuals does not show any positive or negative bias. The empirical and assumed cumulative distribution functions are plotted in Fig. 3.22.

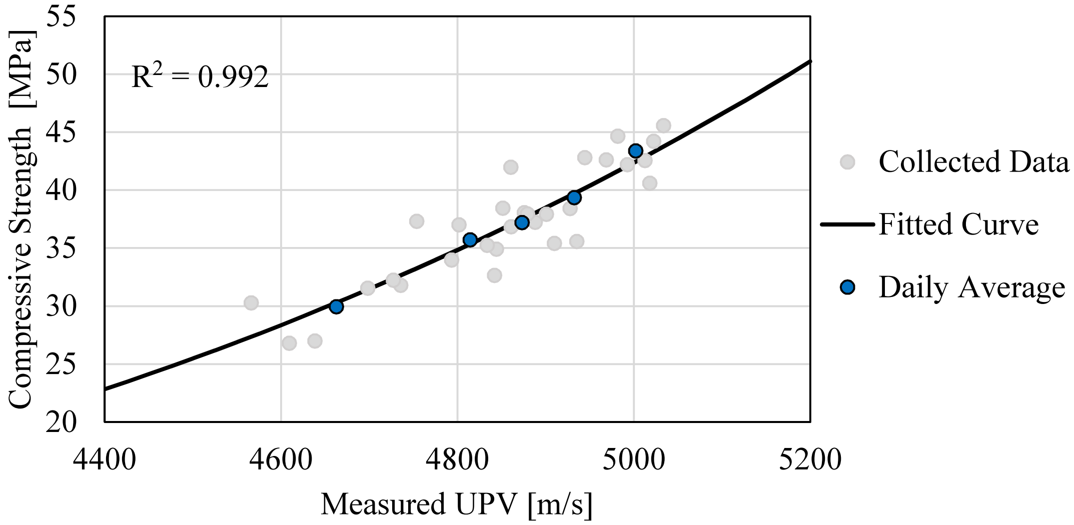

Fig. 3.20: Average UVP versus average compressive strength and regression model.

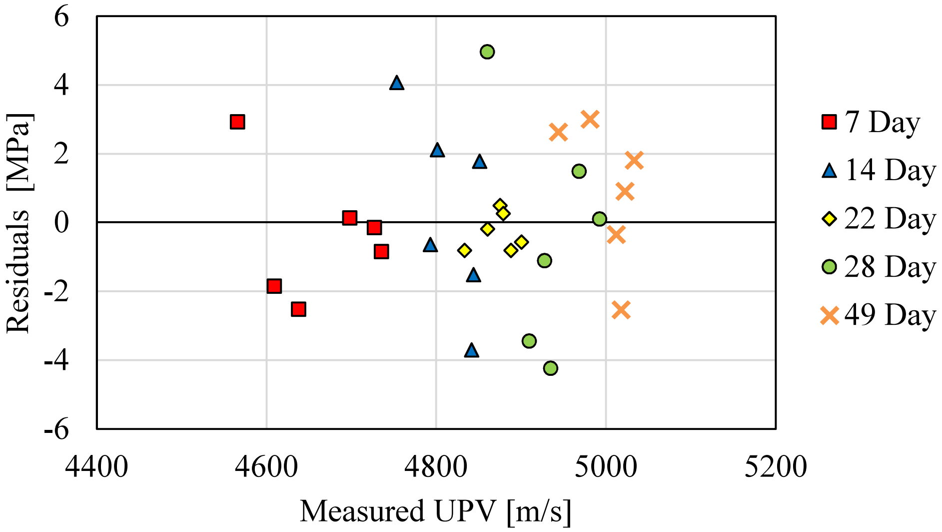

Fig. 3.21: Residuals from regression model.

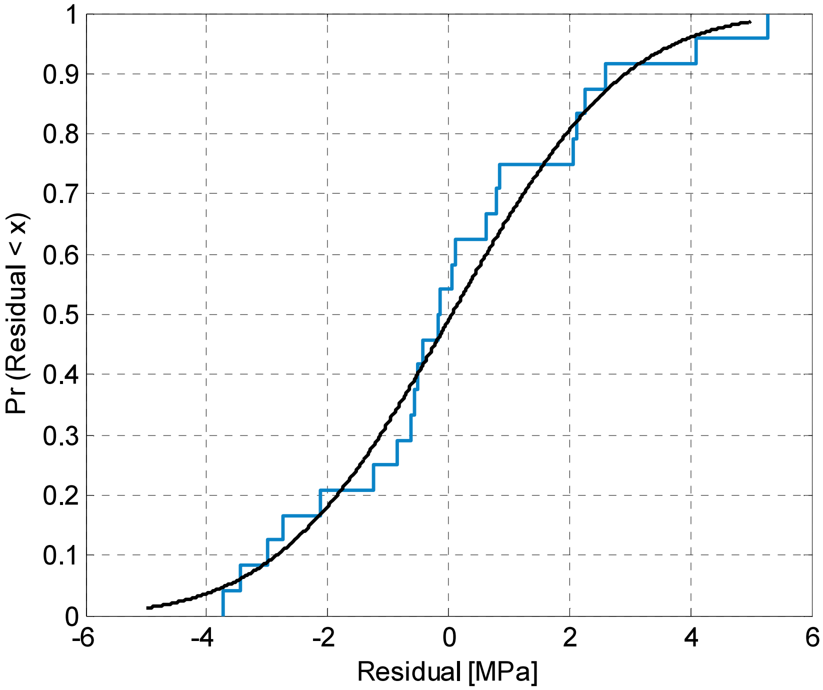

Fig. 3.22: Empirical cumulative distribution function and fitted distribution for residuals.

3.4.3 Spatial Analysis of UPV Measurements

The UPV measurements were all collected from the same concrete specimen. Thus it is logical to assume that the UPV measurements were statistical data from the same population. The UPV was found to be normally distributed with a mean of 4793 m/s and a standard deviation of 82.9 m/s. A KS test and a chi-squared goodness of fit test provided p-values of 0.211 and 0.505 respectively. The histogram and empirical CDF as well as the fitted distribution are shown in Fig. 3.23.

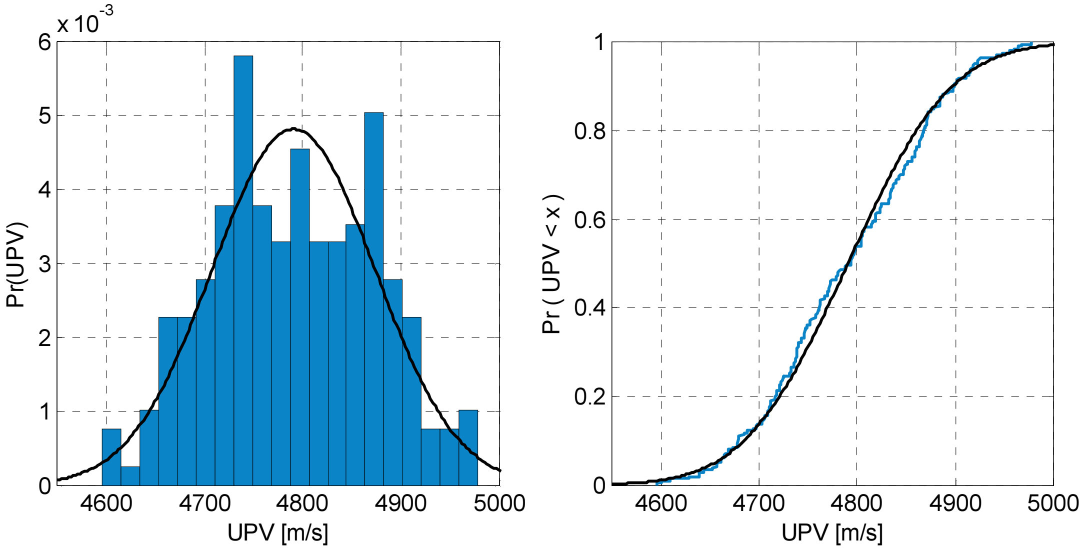

(a) (b)

Fig. 3.23: Experimental UPV data and fitted distributions. (a) Histogram and PDF. (b) Empirical and fitted CDF.

The spatial variability of the UPV measurements is first assessed using ANOVA testing to determine if the variability between points is greater than the variability at a given point due to measurement error. This is done with a replicated two-way ANOVA test where the independent variables are the horizontal and vertical grid positions and the dependent replicated variable is the measured UPV. The null hypothesis assumes that the concrete has uniform material properties everywhere regardless of concrete batch or location. The results of the ANOVA test are shown in Table 3.3.

The ANOVA test reveals that there is statistically significant variability between grid points. Both the X and Y directions have small p-values, suggesting that there is significant variability. In addition, there is no interaction between the X and Y variables. This implies that the variations in the X and Y directions are independent.

Table 3.3: Replicated two-way ANOVA analysis results.

Source of Variation	Sum of Squares	Degrees of Freedom	Mean Square	F Test-ratio	p-value
X-Direction	47.65	18	2.65	3.56	$1.2\text{x}10^{-6}$
Y-Direction	42.52	6	7.04	9.48	$6.6\ \text{x}10^{-10}$
Interaction	14.599	108	0.13	0.18	1.00
Error	395.4	532	0.74		
Total	499.9	664			

The data collected are assumed to be part of a random field. The collected data are thus assumed to be sampled from that random field. In order to interpolate between the sampled points, spatial statistical tools are required. An approach similar to Nguyen et al. (2013) is adopted for this thesis. An empirical semivariogram was constructed from the data set. A semivariogram determines how the data are correlated with distance. In order to predict random fields from collected spatial data, a semivariogram is required (Stein, 1999). An empirical construction of the semivariogram is achieved by employing Equation 3.5.

$$\hat{\gamma}(x) = \frac{1}{2n(x)} \sum_{x_i - x_j = x} \{Z(x_i) - Z(x_j)\}^2 \tag{3.5}$$

where the lag distance, x, is defined as the distance between two points x_i and x_j, $\hat{\gamma}(x)$ is the empirical semivariance for a lag distance x, $n(x)$ is the number of pairs of the lag distance x within the data set, and $Z(x_i)$ and $Z(x_j)$ are the measured values of the random field Z for points x_i and x_j respectively. In the case of this study, the random field Z is defined as the variation of ultrasonic pulse velocity within the concrete slab strip. Note that the assumed random field is two-dimensional. Thus the value $x = x_i - x_j$ is generalized in two dimensions to be the actual distance between two points and is calculated as $x = \sqrt{\Delta X^2 + \Delta Y^2}$. Stein (1999) notes that sets of x are not entirely equal in value. Thus they are usually grouped into bins of similar lag distances. The empirical semivariogram is shown in Fig. 3.24

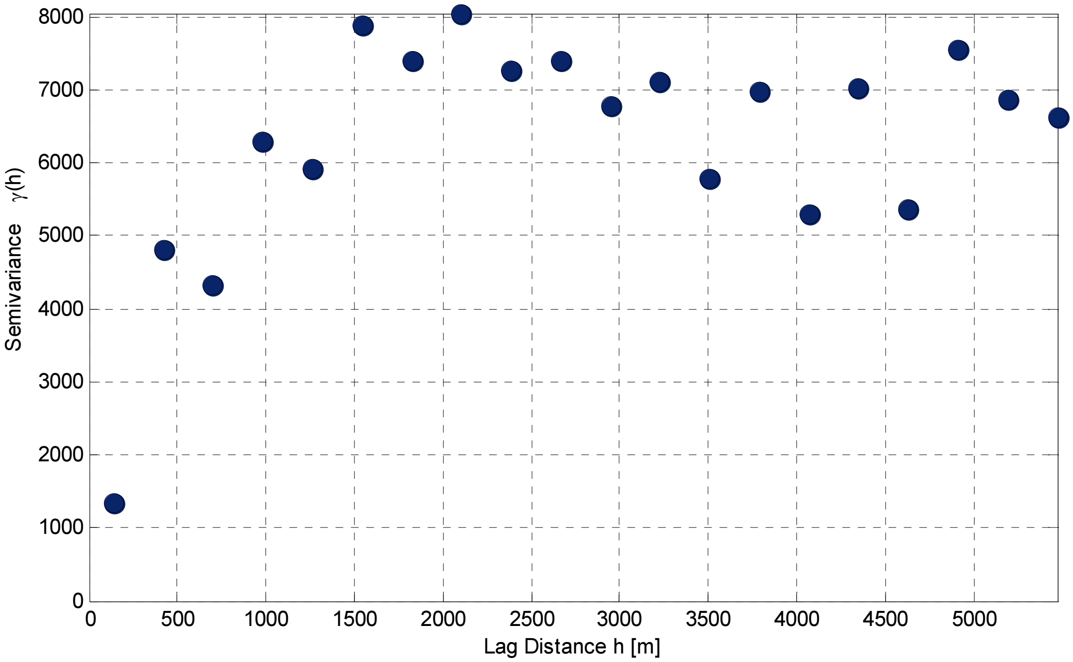

Fig. 3.24: Empirical semivariogram of UPV data.

For the random fields assumed in this thesis, the random field is assumed to have an autocorrelation function. An autocorrelation function is a function that describes the covariance of a random field by the distance between two points within the field (Stein, 1999). This is formally described by Equation 3.6,

$$cov\{Z(x), Z(y)\} = K(x - y) \tag{3.6}$$

where $cov\{Z(x), Z(y)\}$ is the covariance between any two points *x* and *y* in the random field *Z*. *K(x-y)* is the autocorrelation function that can describe the covariance for any two points *x* and *y* based on their difference. Again note that if the random field is higher than one-dimensional, then the quantity *x-y* is the vector length between vectors *x* and *y*. The commonly used isotropic autocorrelation function is the spherical model shown in Equation 3.7,

$$K(r) = \begin{cases} C\left[1 - \frac{3r}{2a} + \frac{r^3}{2a^3}\right] & r \leq a \\ 0 & r > a \end{cases} \tag{3.7}$$

where the variance of the random field is described by $C + C_0$, the parameter C_0 is equal to the nugget effect, r is the lag distance equal to $x-y$, and a is the range of the random field. The nugget effect describes the phenomenon where points at a very close (or the same) distance still exhibit stochastic variability. This is also referred to as the micro-scale variation. The range of a random field is the distance at which two points are no longer correlated. The parameter C is the amount of variance in the random field that is not attributed to spatial variation. The analytical semivariagram can be determined from Equation 3.8.

$$\gamma(r) = var\{Z\} - K(r) \tag{3.8}$$

Substituting the variance of the random field with C + C0 yields Equation 3.9.

$$\gamma(r) = \begin{cases} C_0 + C\left[\dfrac{3r}{2a} - \dfrac{r^3}{2a^3}\right] & r \le a \\ C_0 + C & r > a \end{cases} \tag{3.9}$$

The spherical model was assumed to represent the data. A regression was done to determine the range, sill, and nugget effect. The regression model is plotted with the empirical semivariogram in Fig. 3.25. The semivariogram was found to have no nugget effect; the sill of the semivariogram was calculated to be 6811.3 [m^2/s^2], and the range was calculated to be 1190 mm.

Using the properties of an assumed semivariogram, an ordinary kriging map can be generated from the collected data points. Kriging maps are heavily employed in geospatial interpolation problems and were developed by a mining engineer by the name of D. G. Krige (Stein, 1999). A kriging map is also called the best linear unbiased prediction. Stein (1999) presents a summary on how the kriging maps are calculated. The collected data are assumed to be part of a realization of a random field Z which takes the form shown in Equation 3.10,

$$Z(x) = m(x)^T\beta + \varepsilon(x) \tag{3.10}$$

where $m(x)$ is the mean function, $\varepsilon(x)$ is a random field with a mean of zero with a known covariance structure, and β is a vector of unknown coefficients. Kriging maps can be referred to as universal or ordinary. In the case of an ordinary kriging map, the parameter $m(x)$ is assumed to

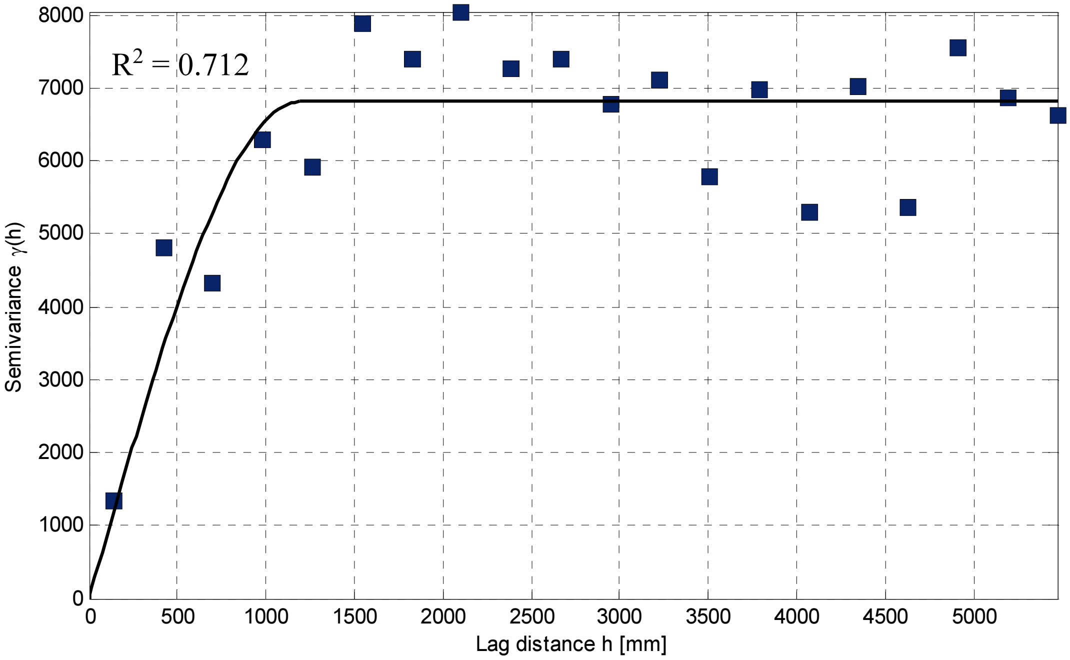

Fig.3.25: Fitted spherical semivariogram for experimental data.

be equal to 1.0 and thus the mean is an unknown constant. In the case of a universal kriging map, the mean function is variable with position. The spatial variation in the point loaded strip is assumed to be an ordinary kriging and thus the mean is constant. Kriging maps are also referred to as the best unbiased linear predictor. The best unbiased linear predictor assumes that the prediction Z(x_0), for a vector of points, x_0, that lie between collected observations, can be represented by the form,

$$Z(x_0) = \lambda_0 + \lambda^T Z \tag{3.11}$$

where $Z = \{Z(x_1), \ldots, Z(x_n)\}$ is a set of observed values of the random field at points x_1 to x_n. This predictor is subject to two constraints:

$$E[\lambda_0 + \lambda^T Z] = E[Z(x_0)] \tag{3.12}$$

and

$$\lambda_0 + \lambda^T M\beta = m(x)^T\beta \tag{3.13}$$

where the measured values of the mean function x_1 to x_n is$M^T = \{m(x_1), \ldots, m(x_n)\}$. Thus it is concluded that,

$$\lambda_0 = 0 \tag{3.14}$$

and

$$m(x_0) = M^T\lambda \tag{3.15}$$

The solution of λ that solves this constrained minimization problem is then considered the best unbiased linear predictor for Z(x_0), calculated as

$$Z(x_0) = \lambda^T Z \tag{3.16}$$

If we select a vector *v* such that,

$$Z(x_0) = (\lambda + v)^T Z \tag{3.17}$$

we can show that,

$$m(x) = M^T(\lambda + v) = M^T\lambda + M^T v \tag{3.18}$$

Because $m(x)=M^T\lambda$, we can see that $M^T v = 0$. In addition, Stein (1999) shows that the best linear prediction for the weighting function is given by,

$$\lambda = K^{-1}k \tag{3.19}$$

where K = cov{Z,Z^T} and k = cov{Z,Z(x_0)} . Thus if a vector μ is selected such that M μ = 0, it follows that,

$$K\lambda - k = M\mu \tag{3.20}$$

In matrix form these two conditions take the form

$$\begin{bmatrix} K & M \\ M^T & O \end{bmatrix}\begin{bmatrix} \lambda \\ \mu \end{bmatrix} = \begin{bmatrix} k \\ m(x_0) \end{bmatrix} \tag{3.21}$$

Where O is a matrix of zeros. This can be rearranged to,

$$\begin{bmatrix} \lambda \\ \mu \end{bmatrix} = \begin{bmatrix} K & M \\ M^T & O \end{bmatrix}^{-1}\begin{bmatrix} k \\ m(x_0) \end{bmatrix} \tag{3.22}$$

Solving for λ yields:

$$\lambda = \{K^{-1} - K^{-1}M(M^TK^{-1}M)^{-1}M^TK^{-1}\}k + K^{-1}M(M^TK^{-1}M)^{-1}m(x_0) \qquad (3.23)$$

Thus using the calculated data, unbiased estimates for values between collected data is estimated. However, the covariance values between the measured values Z and the locations of prediction $Z(x_0)$ need to be known. Thus the autocorrelation function calculated from the fitted semivariogram is used to produce the k matrix. This method was used to produce kriging maps for the ultrasonic pulse velocity at the centre of each of the finite elements in the mesh. The calculated kriging map for the ultrasonic pulse velocity is shown in Fig. 3.26. The conversion of ultrasonic pulse velocity to compressive strength is discussed in Section 3.4.4.

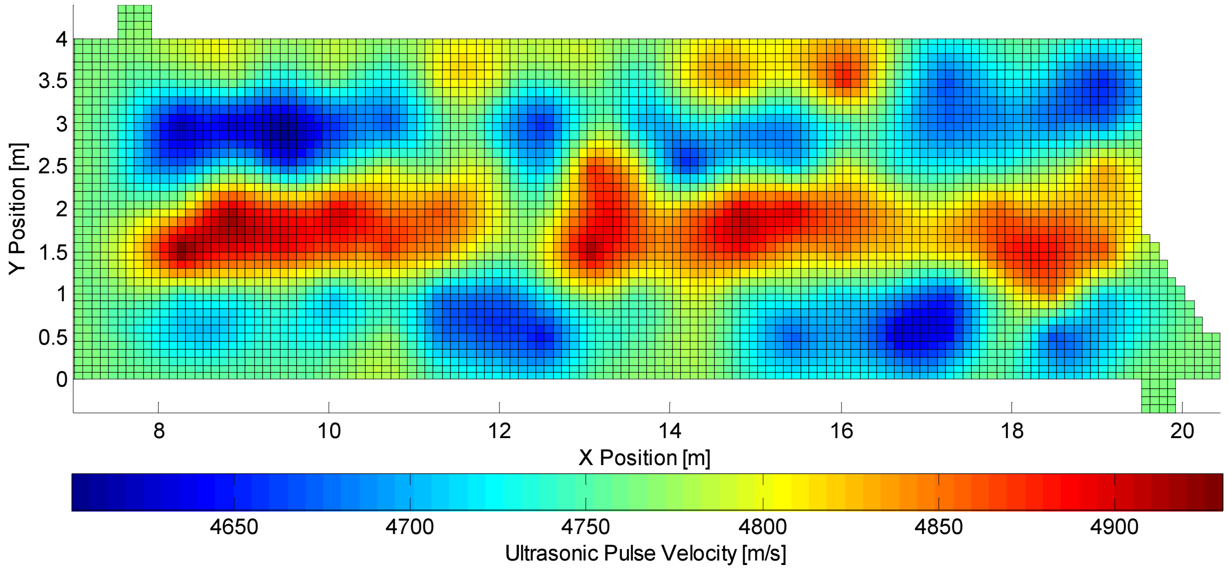

Fig.3.26: Kriging map used for finite element analysis.

3.4.4 UPV Variable Transformation

In order to convert the measured UPV data from the kriging map of the ultrasonic pulse velocity, two transformations were required. The UPV data is transformed from the measured 14-day values to the test day values. Then this UPV is transformed from the 28-day values to the test day (46-day) values, the ratio between the UPV predicted between 14 and 46 days was used as a multiplier to all UPV values uniformly. Then Equation 3.4 was used to calculate the corresponding compressive strength. In order to assess the accuracy of this transformation, Equation 3.3 and

Equation 3.4 were used and compared against Equation 3.2. Fig. 3.27 shows the comparison between measured compressive strength versus time, the prediction from Equation 3.2, and the prediction from Equation 3.3 and Equation 3.4. Equation 3.3 and Equation 3.4 were based on data from 7 to 49 days. Equation 3.2 was based on data up to 80 days. From Fig. 3.27, it can be seen that the error in the collected data for interpolating between 0 and 49 days is reasonably low. However the trend does start to deviate from the Equation 3.2 when extrapolating past 49 days. Testing of PLS4000 ended on day 46, thus the interpolation is considered reasonably accurate. Fig. 3.28 shows the finite element model inputs after the kriging map and variable transformation was applied. The compressive strength for each element is an input variable. The tensile strength and modulus of elasticity were calculated using the equations recommended in the CSA A23.3 code.

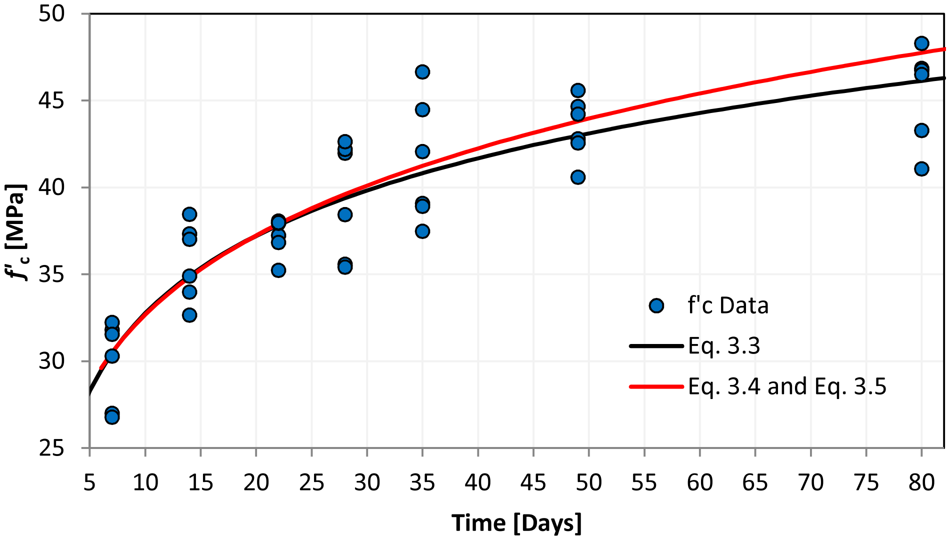

Fig.3.27: Comparison of fitted and calculated compressive strength trend.

3.4.5 Within Member Strength Variation and Spatial Variability

In order to assess the spatial variability, the variability attributed to batch to batch variation must be disaggregated from the variability of the test. It has been shown in the literature that the within-member variation is inflated when the number of batches of concrete cast within a member increases (Bartlett and MacGregor, 1994).

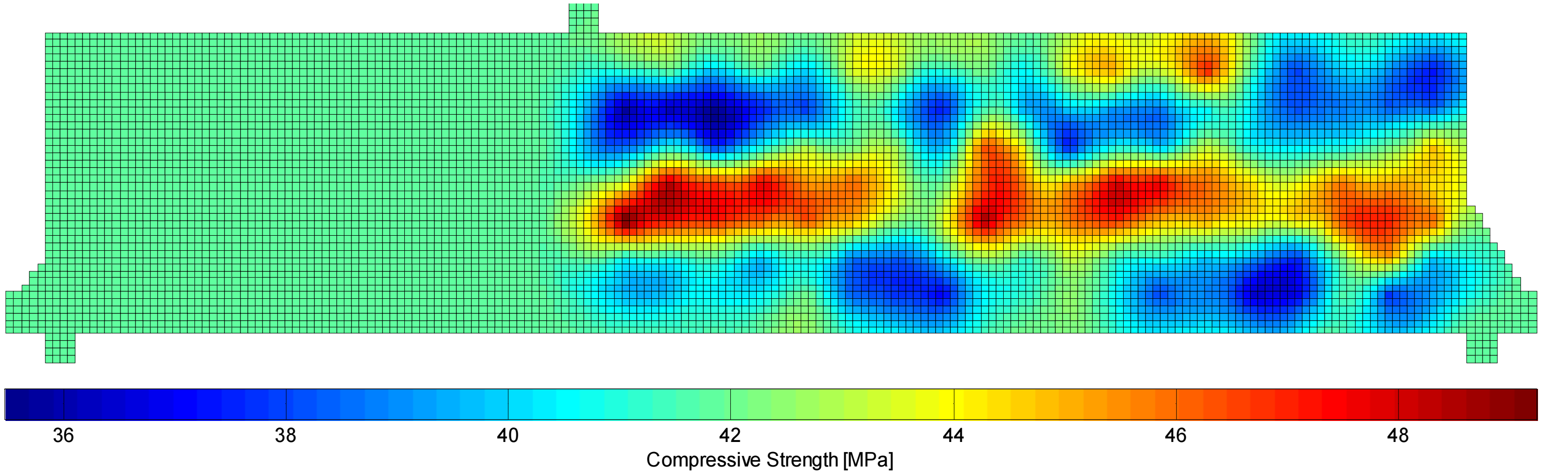

Fig. 3.28: Finite element model inputs with spatial variation of concrete material properties.

The variability due to multiple batches cast in the same member was assessed using the cylinder data. The statistics for each of the cylinders is presented in Table 3.4.

Table 3.4: Statistical parameters for concrete cylinder test data.

Test Date [days]	Mean f_c' [MPa]	Standard Deviation [MPa]	COV [%]
7	29.96	2.45	8.18%
14	35.74	2.23	6.24%
22	37.23	1.08	2.91%
28	39.39	3.35	8.51%
35	41.46	3.59	8.66%
49	43.42	1.79	4.11%
80	45.47	2.71	5.95%
		Mean COV	6.37%

The total coefficient of variation of the UPV test data after regression, V_{EXP}, was calculated to be 0.0784. This coefficient of variation includes the variability due to spatial variation, and due to batch to batch variation. Using the mean coefficient of variation from Table 3.4 as the batch to batch coefficient of variation ($V_{Batch\text{-}to\text{-}Batch}$), the coefficient of variation due to spatial variability (V_S) can be calculated using Equation 3.24.

$$V_S = \sqrt{V_{EXP}^2 - V_{Batch-to-Batch}^2} \tag{3.24a}$$

$$V_S = \sqrt{(0.0784)^2 - (0.0637)^2} \tag{3.24b}$$

$$V_S = 0.0457 \tag{3.24c}$$

Bartlett and MacGregor (1994) analyzed the spatial variation within a set of girders originally tested by Scanlon and Mikhailovsky (1987). They report that the average coefficient of variation for variation due to within-girder spatial variation is 0.043. Thus the coefficient of variation due to spatial variability in this study can be considered reasonable. It should be noted, however, that the influenced of variability due to UPV measurement error is not included and should be addressed in a future study.

3.5 Modelling of Experimental Response

This section describes the observed experimental response of PLS4000 and the finite element models of the structure. The slab strip was modelled both with and without the collected data. A comparison of each model is provided. For more details on the experimental results, the reader is referred to Quach (2016).

3.5.1 Experimental Response

The slab strip was first loaded to fail the unreinforced side. A single point load was applied along grid line two until failure occurred. The testing took place from June 10, 2015 to June 12, 2015. The observed failure mode was a large diagonal crack at a location of approximately five metres from the point of loading on the unreinforced span. A representation of the crack pattern at failure is shown in Fig. 3.29. The experimental response is plotted in Fig. 3.30.

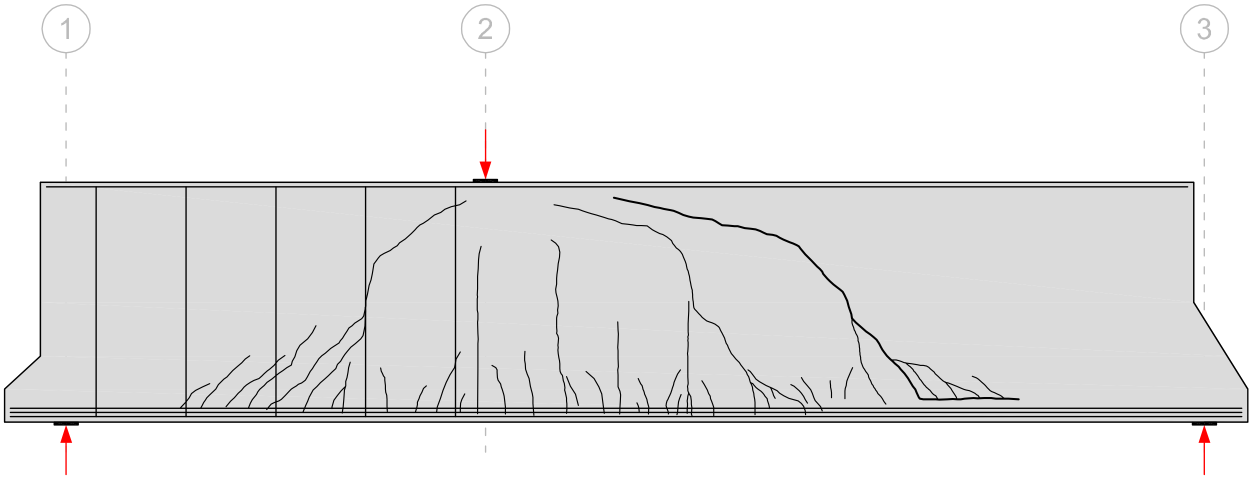

Fig.3.29: Experimental crack pattern at failure.

The slab strip had a self-weight deflection of approximately 1.0 mm and remained uncracked under its self-weight. The structure cracked at an applied load of 200 kN. The response was approximately bilinear until a large shear crack appeared and failed the structure at an ultimate load and deflection of 685 kN and 12 mm respectively.

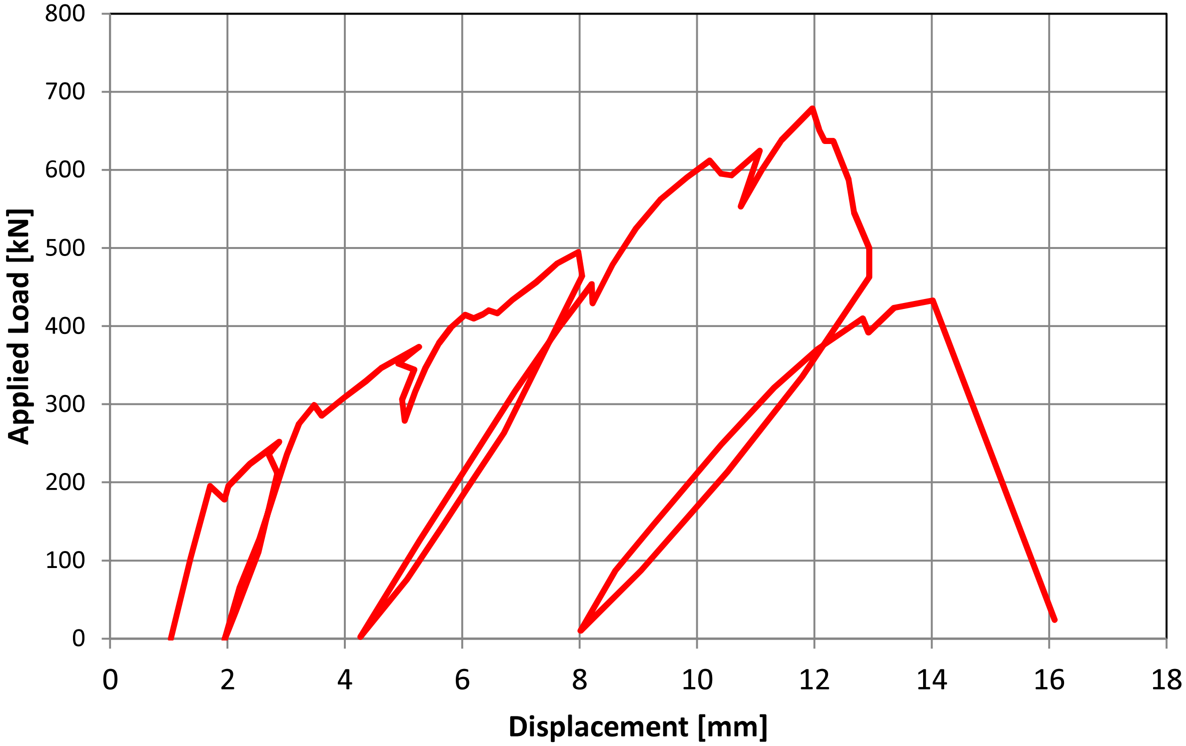

Fig.3.30: Experimental load-deflection plot for PLS4000.

Fig. 3.31 shows an overlay of the experimental crack pattern and the collected UPV data. An overlay of the traced crack pattern and the UPV data reveals some interesting trends. Cracking in reinforced concrete is influenced by the stress field and the local strength variations.

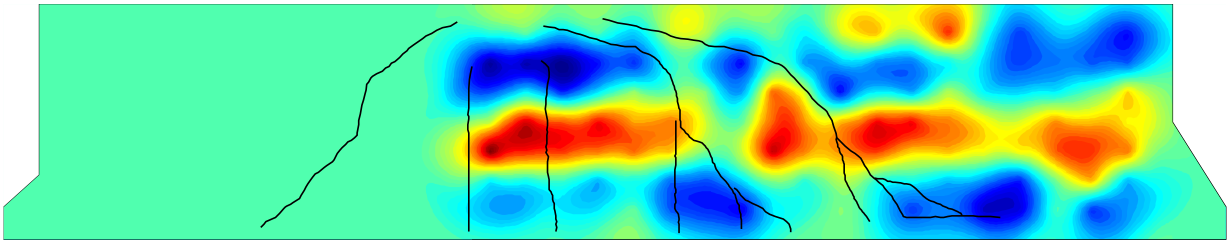

Fig.3.31: Experimental crack pattern and kriging map of collected UPV data.

A study conducted by Koide et al. (1998) showed that probabilistic cracking in unreinforced sections deviated from a deterministic uniform approach. Thus it is possible that in a large unreinforced section, where the failure depends on the transfer of stress along the crack, that the material properties might play a role in the crack pattern. In Fig. 3.31, we see that the two main shear cracks pass between the zones of weakness in the middle layer. This suggests that the variation in tensile strength in the middle layer contributed to the location of cracks and ultimately to the location of the failure crack.

3.5.2 Finite Element Model with Uniform Material Properties

A finite element model was constructed to model the observed experimental properties. The failure of the unreinforced side is particularly sensitive to the assumed crack spacing and tension softening models. A very fine mesh of 8033 elements was used to model the structure. The selected mesh is shown in Fig. 3.32.

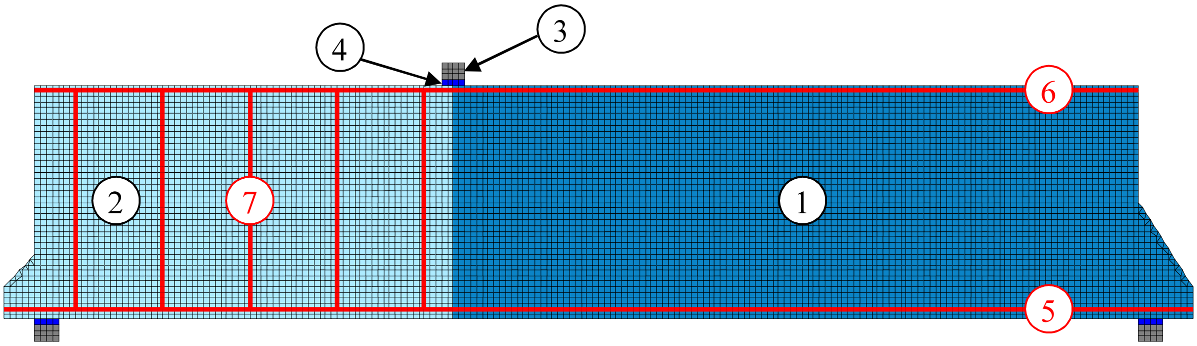

Fig. 3.32: Finite element mesh.

A total of 41 elements were utilized through the depth of the beam. The east and west spans of the beam were modelled using different material types due to the assumed maximum crack spacing. Collins and Mitchel (1997) recommend that for crack spacing in the shear area, the CEB-FIP Code equations be modified for the shear region. These modified equations were used to produce predictions for the crack spacing on either side. Note that for the unreinforced side, the vertical and horizontal crack spacing was assumed to be equal to 4035 mm. The bottom and top flexural reinforcement were grouped into one set of truss bars with total areas acting through the geometric centroid of each bar group. A summary of the model inputs is shown in Table 3.4.

A comparison of the finite element and experimental load-deflection is shown in Fig. 3.33. The finite element model predicted a failure load of 715 kN and a deflection at ultimate of 12.3 mm. The finite element model appears to capture the initial and post-cracking stiffness of the structure;

Table 3.5: Finite Element Model Material Properties

Color /Material	Material #	f'_c/f_y [MPa]	E_c/E_s [MPa]	$\varepsilon'_c/\varepsilon_u$ $\times 10^{-3}$	f'_t/f_u [MPa]	t/A_s [mm/mm^2]	Description
Concrete	1	40	28772	2.13	2.17	250	Concrete West Span
Concrete	2	40	28772	2.13	2.17	250	Concrete East Span
Steel	3	500	200000	5.00	600	250	Bearing Plate Steel
Bearing	4	N/A	28772	N/A	N/A	250	Bearing Material
Steel	5	573	200000	14	685	6300	Bottom Bars
Steel	6	522	200000	17	629	900	Top Bars
Steel	7	522	200000	17	629	300	Vertical T-headed Bars

however, the cracking load predicted by the FE model is about twice that of the experiment. This could contribute to the offset observed in the post-cracking stiffness. This is considered a reasonable prediction of the load-deflection behaviour. Collins et al. (2015) organized a prediction competition where load-deformation predictions were collected before the test. This uniform analysis was submitted as an entry for the prediction competition before the physical testing began. Thus it is a true prediction of the load-deformation behaviour.

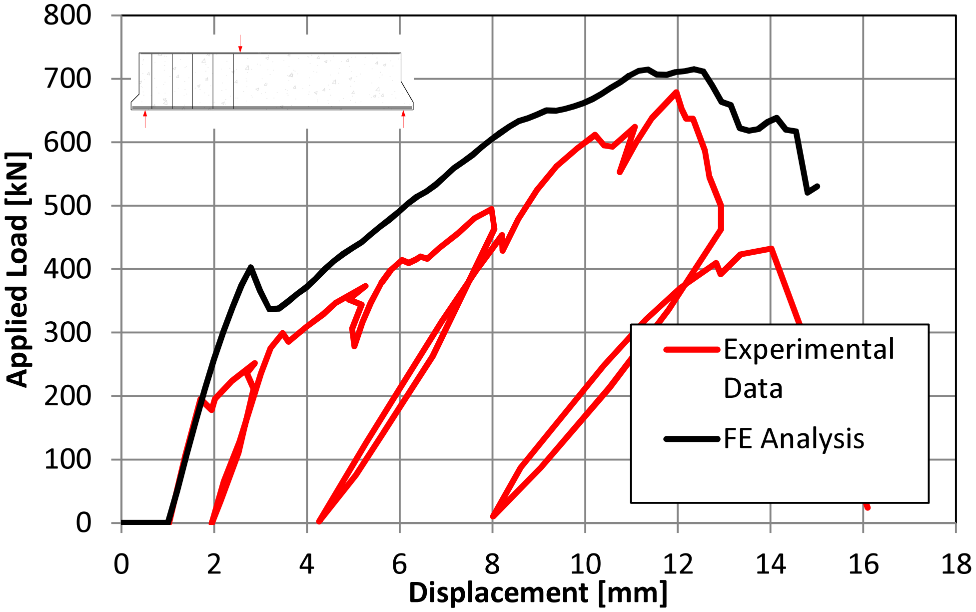

Fig. 3.33: Load-deflection for FE model with uniform properties versus experimental results.

The crack pattern is captured reasonably well by the finite element model. In both cases, a large diagonal crack precipitates the failure; however, in the experiment, two large diagonal cracks were observed. In the finite element model, only one diagonal crack formed and is ultimately responsible for the failure. Fig. 3.34 shows the experimental crack pattern overlaid with the predicted crack pattern.

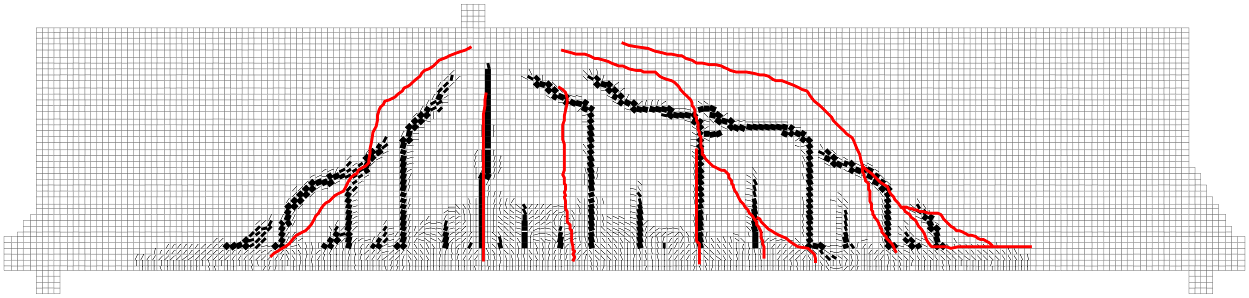

Fig. 3.34: Overlay of FE crack pattern (black) and experimental crack pattern (red) for FEM with uniform material properties.

3.5.3 Finite Element Mode with Spatially Variable Material Properties

The initial finite element model was updated to include the spatially variable properties shown in Fig. 3.28. An additional input file read in scaling factors that changed the compressive strength, tensile strength, and modulus of elasticity of the original model to match that of the measured test data. The FE model predicted a maximum load of 725 kN and a deflection at ultimate of 12.7 mm. Fig. 3.35 compares the FE and experimental crack patterns. Fig 3.36 compares the spatially variable load-deflection to the experimental load-deflection.

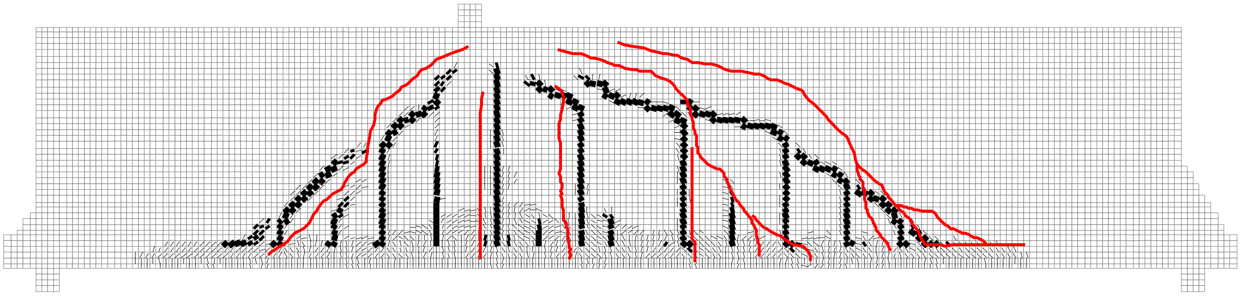

Fig. 3.35: Overlay of FE crack pattern (black) and experimental crack pattern (red) for FEM with spatially variable material properties.

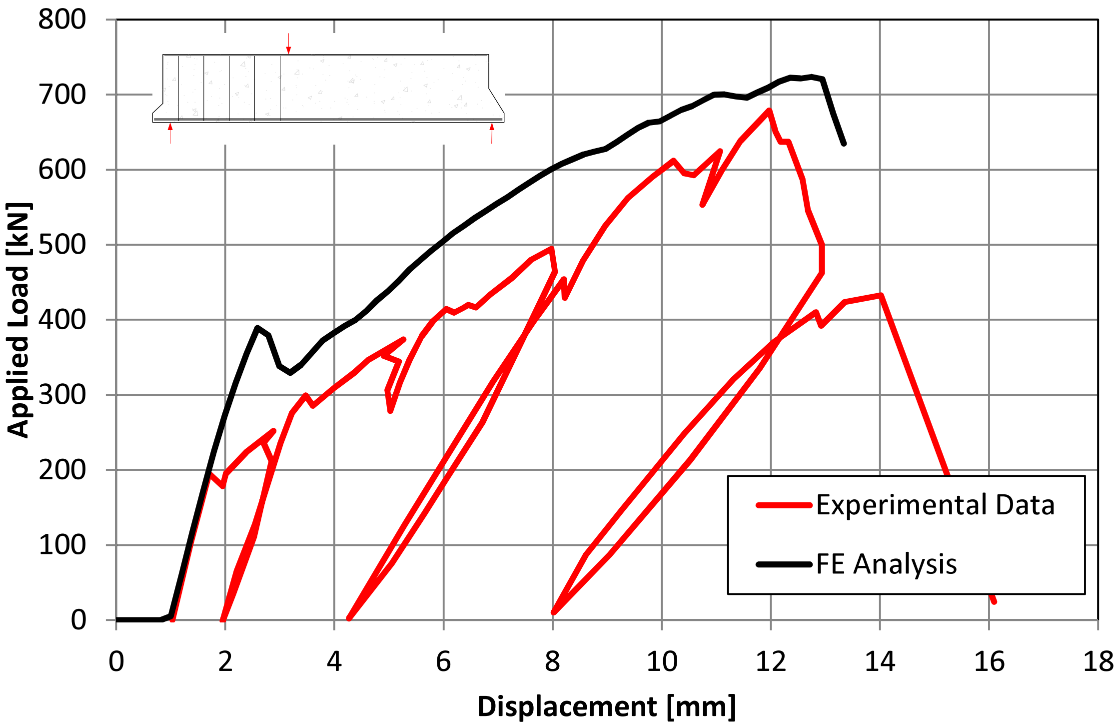

Fig. 3.36: Load-deflection for FE model with spatial variation versus experimental results.

3.5.4 Discussion on the Effect of Spatial Variability on Modelling Large Unreinforced Concrete Structures

In the current formulation of VecTor2, modelling the spatial variations did not have a significant effect on the analysis results. In this study, all model inputs were identical except for the assumption of uniform material properties in the first model. The resulting crack pattern and load-deflection between each analysis were also almost identical deviating only after the peak load. This deviation is considered insignificant as the model tends to become numerically unstable in the post-peak regime. Most likely the minimal difference between modelling techniques can be attributed to the underlying assumptions of the selected software. VecTor2 is most applicable to reinforced concrete structures, where the smeared cracked assumptions govern structural behaviour. Large unreinforced concrete beams are a fracture dominated problem and deviate from the assumptions of the MCFT/DSFM. As a result, the models are sensitive to the calculation of the crack width.

Additionally, the modelling of such a structure with nonlinear finite element analysis is sensitive to the selection of the tension softening model. In the case of the analysis above, a bilinear tension softening model was selected. When the Hodjik model is chosen, the post-cracking stiffness is better captured in the load-deflection, but the ultimate load and deflection are not. This suggests that the selection of the tension softening model is not the underlying issue. The maximum crack width check limits the compressive strength of the elements after the crack width passes a given threshold. This is intended to simulate the loss in aggregate interlock when the crack widths become large. It the current formulation, it does a good job of capturing failure of concrete sections with no transverse reinforcement; however, it results in a model where the peak load is extremely sensitive to the maximum crack spacing.

3.5.5 Concluding Remarks on Spatial Variability in Reinforced Concrete

Cracking in reinforced concrete is inherently stochastic. The cracks will form at a lowest energy state as a combination of applied tensile stress and material weakness. This study measured the spatial variation present within a large unreinforced concrete specimen. The study succeeded in identifying statistical properties of the reinforced concrete. The collected data provide evidence that the failure mode of the unreinforced span is partially affected by the material variability. Both of the large shear cracks occurred between local planes of weakness observed within the middle layer of the concrete. This suggests that shear cracks will propagate through areas of weakness. However, more experimental evidence is required to confirm such assertions. UPV measurements have been identified as an adequate means of measuring material properties within the specimen and should be used on future unreinforced concrete specimens to provide insight into how spatial variation affects a population of structures.

A model with uniform material properties may not currently capture the exact crack pattern, however a reasonable estimate of the load-deflection can be obtained with careful selection of model parameters. In the current formulations of the nonlinear finite element software, VecTor2, the inclusion of spatial variation did not affect the failure mode significantly for the one specimen examined. It is not clear from this study how spatial variation will affect the failure of a structure with symmetric loading. The current test forced the failure to occur on the east side of the specimen, thus the failure location was predetermined. In a symmetrically loaded unreinforced concrete beam, spatial variation may have a significant effect on the location and propagation of the failure crack. In a uniform analysis, a large shear crack will form on both sides of the structure simultaneously. This deviates from experimental results, in which typically a single crack will form on one side of the specimen. Thus this study cannot confirm with certainty that spatial variation in large unreinforced concrete structures is not significant in the modelling process.

3.6 Stochastic Simulation of PLS4000

Stochastic simulation was conducted on PLS4000 in order to assess the senstitivty of the load-deformation response to the material input parameters. A total of 175 simulations were conducted for the specimen. For more information on the stochastic model parameters, mesh, and geometry, the reader is referred to Chapter 5. This section compares the stochastic simulation with the experimental response and discusses the parameters that influence the stochastic simulation results.

Three stochastic input parameters were compared against four load-deformation response metrics. The selected metrics were the ultimate load, the deflection at ultimate loading, the initial uncracked stiffness, and the cracked stiffness. The ultimate load and corresponding displacement were determined by finding a local maximum that results in a change in tangent slope and a drop from the local peak load of greater than 10 percent. The uncracked and cracked stiffness coefficients were determined by linear regression. For the cracked portion of the load-deformation response, the cracked portion was isolated by removing all data with a deflection of less than 4 mm and all data above 75% of the ultimate deflection. An example of the auomated retrival of the four metric is shown in Fig. 3.37.

The three main stochastic parameters included in the simulations were the compressive strength, the tensile strength, and the modulus of elasticity. Each of these parameters was assumed to be an independent random variable for the simulation; however, the mean tensile strength and mean modulus of elasticity were calculated based on the compressive strength. The correlation coefficients for these three paremeters with the four selected metrics were calculated. The corellation coefficients are a usefull tool to determine which input parameters influence the load-deformation predictions. The corellation coefficients are shown in Fig. 3.38.

It can be seen from the results that the ultimate load and corresponding displacement are heavily influenced by the distribution of the tensile strength. The correlation coefficient for tensile strength

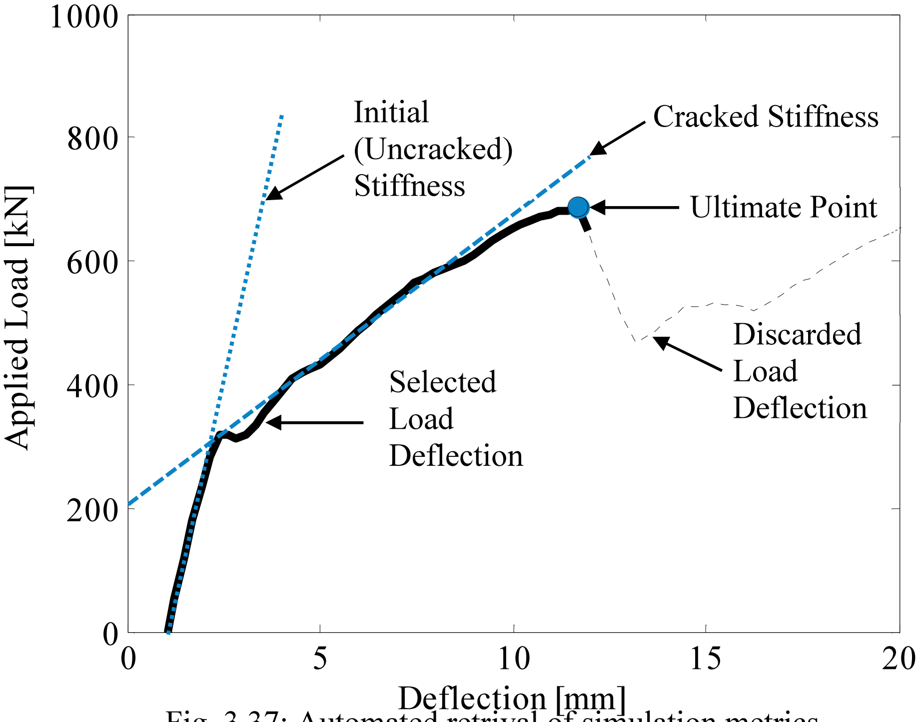

Fig. 3.37: Automated retrival of simulation metrics.

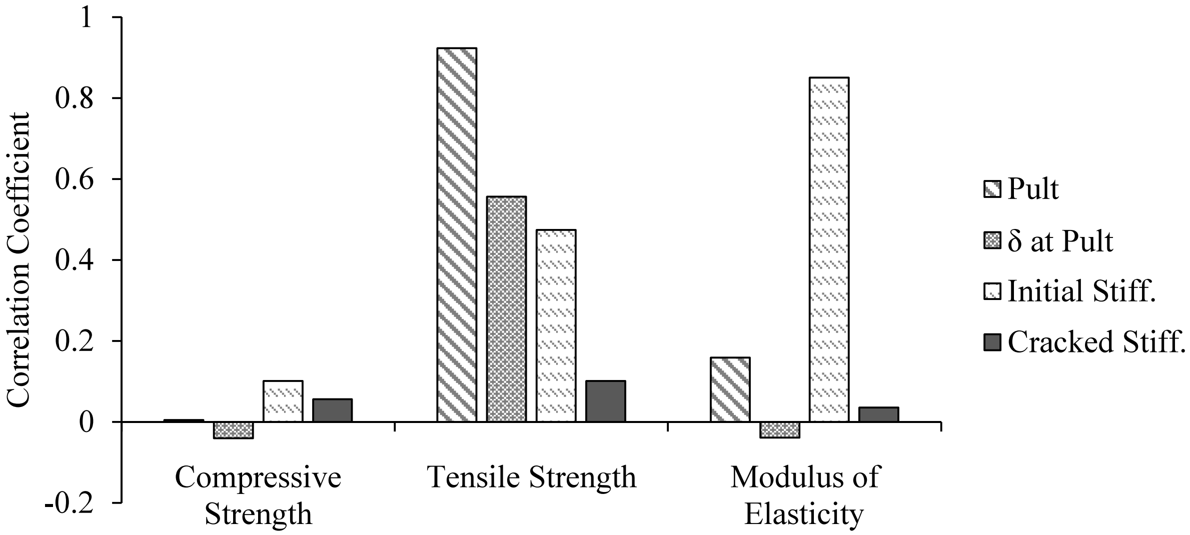

Fig. 3.38: Correlation coefficients for PLS4000 simulation results.

and ultimate load is 0.92. This suggests that the tensile strength is the main contributer to the stochastic variation in member strength. The failure of an unreinforced section in VecTor2 is heavily influenced by the maximum crack spacing and the tension softening response. The maximum crack spacing is constant for this analysis and thus the tension response, which is directly related to the tensile strength, governs the variability. As previously mentioned, the compressive strength is generated independently of the tensile strength. The correlation coefficient between the compressive strength and the tensile strength is -0.052 which confirms the independence of the sampling. In reality, a correlation exists between the tensile strength and the compressive strength, and the corelation coefficients for the compressive strength would not be as low as shown in Fig. 3.38.

The initial stiffness is highly correlated with the modulus of elasticity. This is expected as the finite element model is essentially linear elastic until significant cracking occurs. The tensile strength is also correlated with the initial stiffness, with a correlation coefficient of 0.47. When cracking begins in VecTor2, cracks are smeared initially and thus the structure will retain stiffness until larger, wider cracks are able to form. These larger cracks are what result in the cracked stiffness observed in the load-deformation response. However, the smeared cracks influence the initial stiffness of the load deformation response and thus a corroleation is observed. The post-cracking stiffness appears to be independent of the input parameters. It likely is a function of the location of the wide cracks and the longitudinal reinforcement, which is only partially influenced by the spatially variable input parameters.

A plot of the experimental results with the stochastic simulation is shown in Fig. 3.39. This chart illustrates a few trends in the simulation. The initial stiffness and cracked stiffness of the experimental results are well captured by the stochastic simulations. The experimental specimen had a concrete cylinder strength of 43.4 MPa at the test date. The simulation mean compressive strength is 38.5 MPa. Thus it is reasonable that the mean simulated peak load is 652 kN. This is close to, but below, the experimental peak load of 685 kN. The cracking load is not captured by the stochastic simulations and is generally over-predicted. This is likely a result of the smeared crack assumption in VecTor2. In reality, a large beam with small reinforcement ratios is governed by fracture mechanics. Thus the smearing of cracks near the tensile reinforcement results in a consistent over-prediction of the cracking load. As well, initial tensile stresses due to restrained shrinkage of the concrete were not taken into account in the analyses.

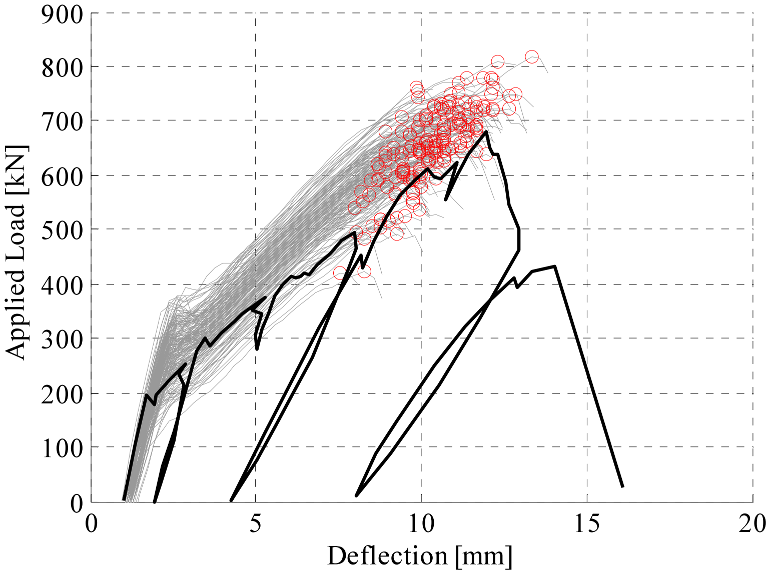

Fig. 3.39: Stochastic simulation results versus experimental load-deflection response.

The peak load and peak deflection were both found to be normally distributed random variables. Confidence intervals at a 99 percent confidence level for peak load and associated deflection were calculated as:

$$509\ kN \leq P_{Ult.} \leq 795\ kN \tag{3.25}$$

$$8.15\ mm \leq \delta_{@P_{Ult.}} \leq 12.43\ mm \tag{3.26}$$

The stochastic simulation reveals the large variability in load-deflection response that may be present in this structure, were it designed and built in the field. When performing stochastic simulations with VecTor2, the full interaction between stochastic inputs and simulation outputs can be analyzed. Multiple failure modes can be identified and disaggregated. Lower bound estimates for deflection or resistance can be established. These estimates are useful for designing capacity protected elements or structural elements with stringent deflection tolerances. Additionally, the results of a stochastic simulation can be used in a reliability analysis, as discussed in Chapter 5.

CHAPTER 4: STOCASTIC SIMULATION – SOFTWARE FORMULATION

This chapter describes the implementation and validation of the software used for stochastic analysis in VecTor2. The stochastic analysis tools added include: random variable generation with default and custom distributions; correlated sampling of random variables; Latin hypercube sampling of independent random variables; and, the generation of random fields. The techniques used for validation of the implementations are discussed.

4.1 Selected Statistical Models for Implementation in VecTor2

The statistical models used in a stochastic simulation of reinforced concrete must be selected by the engineer such that the distributions are representative of in-situ variability. Consideration must be given to the age and location of the structure as both factors can influence the statistical distributions of the material parameters. A plot of each of the considered compressive strength bias factors reveals that the models of Bartlett and MacGregor (1996), Nowak and Szerszen (2003), and Unanwah and Mahan (2013) are in reasonable agreement above 28 MPa (Fig. 4.1). When the statistical variation is considered, all three models are essentially sampling from the same space. The model proposed by Nowak and Szerszen (2003) predicts a larger bias for lower strength concrete. This likely reflects the large database used for their prediction. The recent results presented by Wisniewski et al. (2012) are in good agreement with Nowak and Szerszen (2003). The distributions proposed by Mirza et al. (1979) are significantly lower than other researchers, however these distributions are likely more representative of older concrete structures constructed before 1990. It is however, at the discretion of the user to select an appropriate distribution for the structure being analyzed.

Four statistical models were selected for concrete material properties and two for steel. The models proposed by Mirza et al. (1979) [for concrete] and Mirza and MacGregor (1979) [for steel] have been widely employed in stochastic simulation and in the calibration of building codes (Ramsay et al., 1979; Mirza and MacGregor, 1982; Mirza 1998; Choi et al. 2004). Further work by the Bartlett and MacGregor (1996) provided more detailed models which were subsequently used in building code calibration. Nowak and Szerszen (2003) provided an updated and improved database for the statistical properties of steel and concrete that was used in the calibration of the

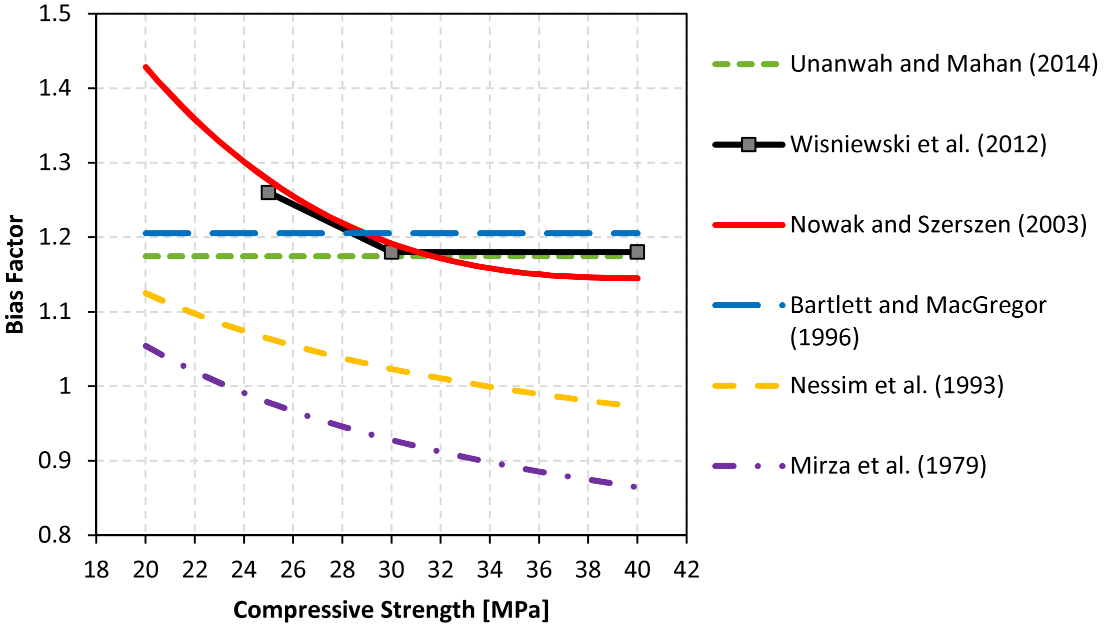

Fig. 4.1: Comparison of mean bias factor for compressive strength of concrete.

ACI-318 Code. Most recently, a study by Unanwa and Mahan (2014) provides results that agree with previous literature and offer updated models for temporal effects on the strength of concrete. A summary of the statistical models implemented in VecTor2 is presented in Table 4.1.

Table 4.1: Selected statistical models implemented in VecTor2

Parameter	Selected Statistical Models
Concrete	
Compressive Strength	Mirza et al., 1979; Bartlett and MacGregor, 1996; Nowak and Szerszen, 2003; Unanwa and Mahan, 2014
Modulus of Elasticity	Mirza et al., 1979
Tensile Strength	Mirza et al., 1979
Steel	
Yield Strength	Mirza and MacGregor, 1979; Nowak and Szerszen, 2003
Ultimate Strength	Mirza and MacGregor, 1979
Modulus of Elasticity	Mirza and MacGregor, 1979

Much work has been conducted into developing statistical models for the strength of reinforced concrete. However due to the nature of a limit state design, focus is placed on the distributions of the yield strength of steel and the compressive strength of concrete. Stochastic simulation of reinforced concrete can evaluate the service limit state in addition to the structural reliability. In the stochastic simulation of service limit states (i.e. deflections), the tensile strength of concrete may have a significant effect on the results of the simulations (Ramsay et al., 1979; Choi et al., 2004). Wisniewski et al. (2012) offered updated statistical models for European steel and concrete properties. Although outside of the current scope, it would be advantageous to develop updated and rigorous statistical models for the modulus of elasticity and tensile strength of concrete, and the ultimate strength and modulus of elasticity of steel for North American materials. Furthermore, in a limit state design, strain hardening effects are neglected. However, in structural reliability analysis, particularly in the investigation of deteriorated structures, strain hardening strength and ductility can be considerable factors that contribute to the reliability of a reinforced concrete structure.

4.2 Random Variable Generator

A stochastic variable generator was created that uses the implicit function RANDOM_NUMBER in the Fortran Library and generates random samples of normal, lognormal, gamma, and beta distributions. These distributions are then used to generate random samples for the concrete and steel material properties. The user selects which distribution to utilize for stochastic analysis. A variety of statistical models from the literature are implemented, as well as the ability to consider user defined statistical properties. The subroutine then builds a matrix that stores the statistical parameters for each selected distribution, and an identifier that indicates which sampling function to call. Once a sample is generated for each distribution, the ratio between the specified value and the sampled value is taken and assigned as a modification factor to each material property.

4.2.1 Uniform Variable Sampling

There are many algorithms designed to generate uniform random variables. A uniform random variable exists within the domain 0 to 1 such that the probability for any value within that range is equal. The most common and widely used algorithm is the congruential method (Graham and Talay, 2013). This method chooses three integers and then computes pseudo-random numbers in a sequence. The samples are generated from Equation 4.1.

$$v_k = av_{k-1} = a^k v_0 (mod\ m),\ \ u_k = \frac{v_k}{m} \tag{4.1}$$

In this case, the selection of the integers in the uniform pseudo-random variable generation is considered outside of the scope of this thesis. The default random number generators in FORTRAN 90 implicit function RANDOM_NUMBER in the Fortran Library will be used. For more information on pseudo-random variable generation, the reader is referred to L'Ecuyer (2012).

4.2.2 Non-Uniform Random Variable Sampling

It is often useful to generate samples of non-uniform random variables. This is most commonly done by inverting the cumulative distribution function (CDF). The CDF represents the area under the probability distribution function (PDF) and is bounded by zero and one. Thus, if the CDF can be inverted such that the independent variable becomes the dependent variable, then the pseudo-random uniform numbers can be directly used to compute a random sample of a non-uniform random variable.

4.2.2.1 Normal and Lognormal Random Variable Sampling

In the case of the normal distribution, the distribution cannot be readily inverted. Thus an expression is required to generate a sample of a normally distributed random variable. This is completed using the Box-Muller Method (Graham and Talay, 2013). Two normally distributed random variables are generated based on two independent uniformly distributed random variables. Equation 4.2a and Equation 4.2b are used to generate samples of normally distributed random variables with a mean of 0 and a standard deviation of 1.

$$X = \sqrt{-2\log(U)}\sin(2\pi V) \tag{4.2a}$$

$$Y = \sqrt{-2\log(U)}\cos(2\pi V) \tag{4.2b}$$

The variables X and Y are statistically independent and can be converted to a distribution with a mean of μ and a standard deviation of σ by using Equation 4.3.

$$Z = \sigma X + \mu \tag{4.3}$$

Note that in Equation 4.3, the independent variable X can be interchanged with Y to generate a statistically independent sample of Z.

In order to generate lognormal distributions, the natural logarithm of the Z variable is taken to generate a sample of W = ln(Z). For more information on lognormal distributions refer to Section 2.1.2.

4.2.2.2 Gamma and Beta Distribution Sampling

The gamma random variable gererator implementation is based on the Marsaglia and Tsang (2000) method. This method works as a selective rejection of a normal random variable and a uniform random variable until the condition in Equation 4.4 is met.

$$\ln(U) < 0.5x^2 + d - dv + d\ln(v) \tag{4.4}$$

where U is a uniformly distributed random sample, and x is a normally distributed random sample with a mean of zero and a standard deviation of one. The variables d and v are given by Equation 4.5a and Equation 4.5b.

$$d = \alpha - \frac{1}{3} \tag{4.5a}$$

$$v = \left(1 + x/\sqrt{9d}\right)^3 \tag{4.5b}$$

The random sample is then calculated using Equation 4.6.

$$V = \frac{dv}{\beta} \tag{4.6}$$

where α and β are the gamma distribution parameters. Marsagila and Tsang (2000) note that performance can be improved if an additional condition is met such that $x > -1/v$. The beta distribution can be sampled by generating two gamma distribution samples and employing Equation 4.7.

$$G = \frac{U}{U+V}(B - A) + A \tag{4.7}$$

where U and V are gamma random samples distributed on U ~Gamma(α,1) and V ~ Gamma(β,1).

4.2.3 Random Variable Generator Validation

The random variable generator was validated using the Kolmogorov-Smirnov (KS) test for goodness of fit and the chi-squared goodness of fit test for each generator. The KS test was selected because of its independence with distribution and sample size. The chi-squared goodness of fit test requires the user to select bin sizes and the selection of bin size can change the null hypothesis. Thus the inclusion of both tests ensures that the generators are working properly.

The results showed that for a general distribution, each of the generators passed the KS test for 10000 random samples. Thus the generators are considered sufficient for use in stochastic simulation. The uniform pseudorandom number generator implemented in FORTRAN has a period of 2^{123} or 1.0634×10^{37}. The maximum number of elements in VecTor2 is 10 000 elements, thus the maximum number of trials for spatially uncorrelated random sampling (each element for a given simulation requires a random sample) before exceeding the period of the generator is approximately 1.0634×10^{33} simulations. The likely number of simulations done with VecTor 2 will not exceed 10000, and thus the simple congruential method is sufficient for pseudorandom number generation.

4.2.4 Verification of Implemented Distributions

Each implemented distribution was verified using a single element to ensure that they were accurately sampling the distributions. The model configurations are shown in Fig. 4.2. Chi-squared goodness of fit test and the KS test were used to test sampled distributions. Stochastic simulations with 1000 samples were used to verify the implementation of the stochastic models.

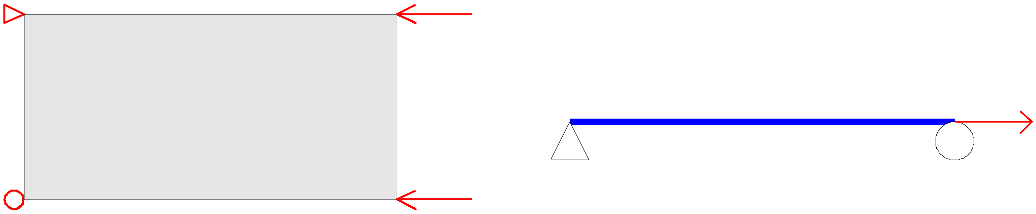

Fig.4.2: Meshes used for testing material property distributions.

4.2.4.1 Concrete Material Properties

Concrete compressive strength, tensile strength, and modulus of elasticity were tested using a single element with the equivalent dimensions of a concrete cylinder. For each distribution test, a set of 1000 simulations were conducted, and the input samples compared. A chi-squared goodness of fit test revealed that all of the sampled distributions matched their theoretical distributions. Additionally, a KS test further confirmed the implementation within VecTor2. A comparison of the load-deflection curves revealed that independence between the compressive strength and the initial tangent modulus was correctly implemented. Fig. 4.3 illustrates this for a subset sample of the verification study. The maximum and minimum sampled compressive strengths are plotted in red, while the maximum and minimum initial tangent modulus are plotted in blue. It is clear that the generated data points, which are assumed independent, are correctly implemented in the software. An example comparison between the sampled and theoretical CFDs is provided in Fig. 4.4. Details on the statistical testing can be found in Appendix C.

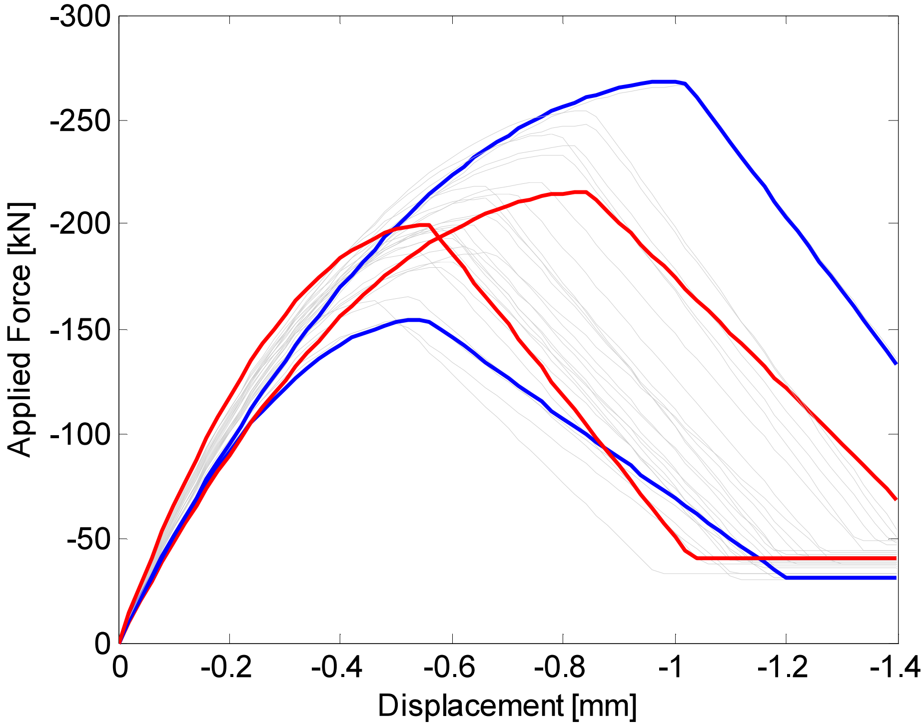

Fig.4.3: Sample of cylinder load-deflection curves showing independence between compressive strength and modulus of elasticity.

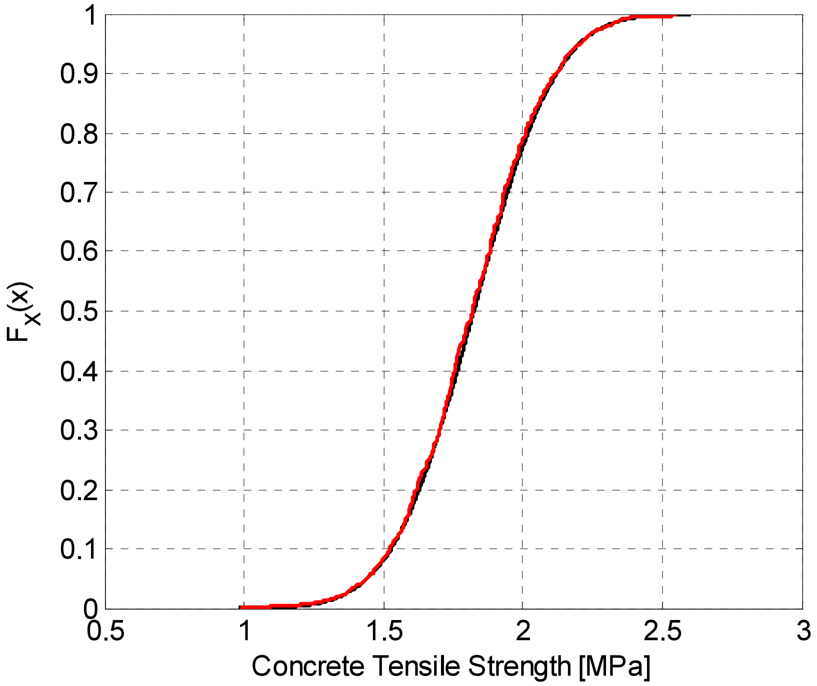

Fig.4.4: Concrete tensile strength distribution verification for Mirza et al. 1979.

4.2.4.2 Steel Material Properties

The steel material properties were tested using a single simply supported truss element. The implemented models tested included Mirza et al. (1979) for yield strength, ultimate strength, and modulus of elasticity; and Nowak and Szerszen (2003) for yield strength. All distributions were tested with a chi-squared goodness of fit test and a KS test. The details on the statistical testing can be found in Appendix A. An example of the generated and theoretical cumulative distributions are presented in Fig. 4.5.

4.3 Latin Hypercube Sampling

Various sampling techniques have been proposed in the literature for use in stochastic simulation. Latin hypercube sampling has been widely employed for stochastic simulation with finite elements (Olsson, 2003). This section introduces and discusses the Latin hypercube sampling technique.

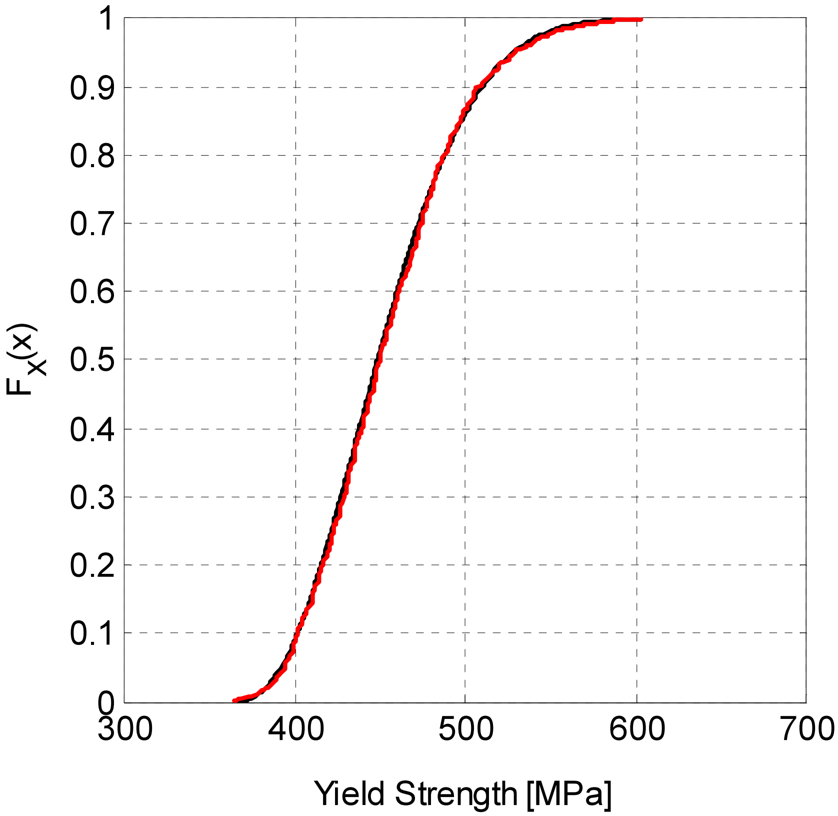

Fig.4.5: Steel yield strength distribution verification for Mirza and MacGregor 1979.

In order to capture the entire range of a statistical distribution, typically a large number of random samples are required when using standard Monte Carlo methods. When there are a large number of stochastic inputs, this often requires an exceedingly large number of samples in order to capture the full range of each input distribution. This can create a simulation scheme that is impractical for analysis and is inherently computationally expensive.

One method to reduce the number of random samples is called stratification. If each of the random variables are stratified such that they are broken up into sections of equal area, a sample can be taken from each of the strata. However, in order to capture the full range of possibilities, a large number of strata are required. Additionally, in a Monte Carlo simulation, there are often multiple random variables. For example, if a Monte Carlo simulation requires five random variables, and each one is partitioned into six strata, the combinations of random samples required to capture a full factorial simulation is 5^6 (or 15 625). This is unrealistic if the Monte Carlo simulation requires considerable computational effort.

A method for reducing the number of required simulations was first proposed by MaKay et al. (1979). This method is able to produce samples that cover the entire distribution range, however reduce the computational effort when compared to full factorial design. In Latin hypercube sampling, a set of random variables (X_i) is defined (where $i = 1$ *to* K). Each distribution is then divided into N strata based on equal probability within a given interval (Fig.4.6(a) and (b)). A random sample is then generated within each interval for each of the random variables. Each interval sample is then randomly paired with other interval samples of another random variable (Fig.4.6c). This has been shown to provide increased accuracy in stochastic simulation for determining the mean and standard deviation of a simulation output. Fig.4.6 illustrates the process of Latin hypercube sampling for a set of two random variables.

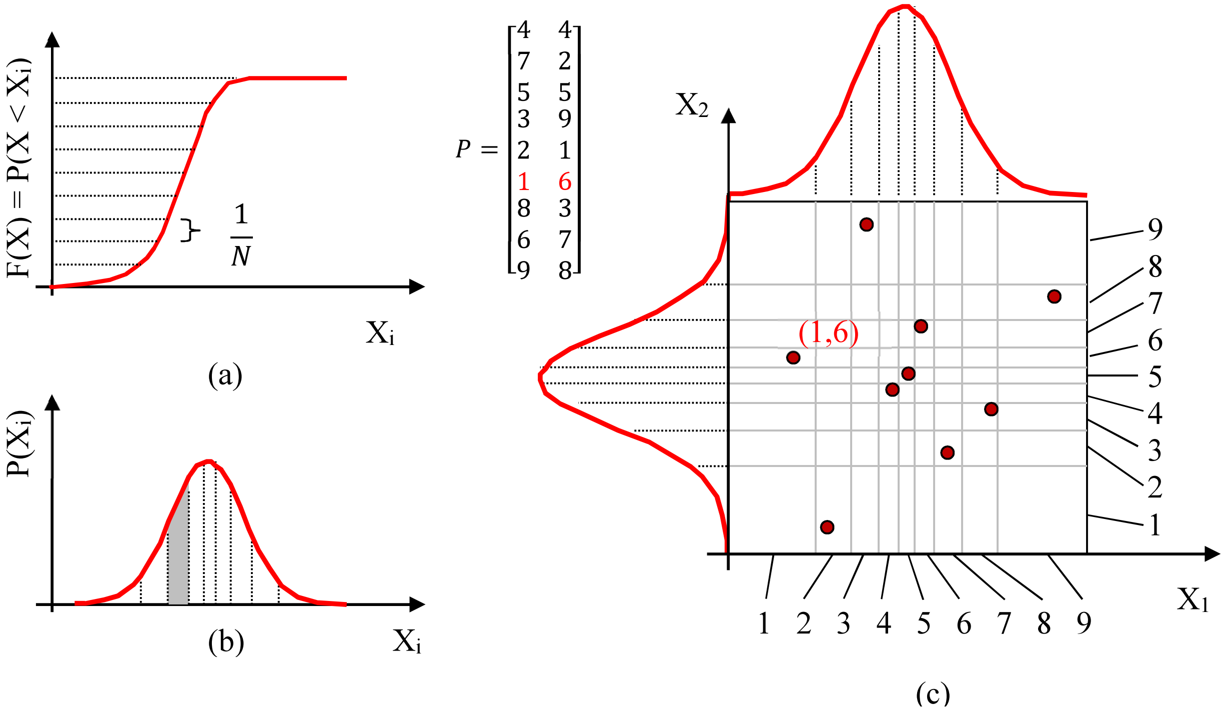

Fig.4.6: Illustration of Latin hypercube sampling.

Olsson et al. (2003) summarized a procedure for generating samples using the Latin hypercube sampling for a set of K random variables. The following procedure is used to generate N realizations of random variables that can be used in a deterministic simulation to generate output distributions.

First an *N x K* permutation matrix, designated *P,* is defined with random permutations in each column from *1 to N*. Next an *N x K* matrix, designated *R,* is defined and populated with uniform random numbers ranging from 0 to 1. The sampling matrix, S, is then calculated using Equation 4.8.

$$S = \frac{1}{N}(P - R) \tag{4.8}$$

The sampling matrix contains random values between 0 and 1 that are evenly distributed among the stratified regions of the cumulative distribution function. Because the columns of the *P* matrix are each independent permutations, each row represents a random pairing of variables. The actual sample values are determined from the inverse of the cumulative distribution function *F(x)*. The sample values are calculated using Equation 4.9.

$$x_{ij} = F_{X_ij}^{-1}(s_{ij}) \tag{4.9}$$

where x_{ij} is the i^{th} sample for the j^{th} random variable in the resulting sample matrix *X*, and $F_{X_ij}^{-1}(s_{ij})$ is the inverse of the cumulative distribution function evaluated at the i^{th} and j^{th} value from the sampling matrix, *S*. Each row of *X* corresponds to one set of random variable inputs that can be used in a deterministic simulation. Completing the deterministic simulation of all rows in the sample matrix will produce output data that can be analyzed as a statistical sample.

4.3.1 Correlation Reduction

Although the realizations of a Latin hypercube sample are randomly paired, it is still possible for undesired correlation to occur between random variable pairings. Fig.4.7 illustrates an example of undesired correlation and the associated correlation reduction.

Olsson et al. (2003) summarized a procedure for correlation reduction that has been shown to work effectively. The spurious correlation is reduced by dividing each element in the P matrix by *N*+1. The resulting values are assumed to be normally distributed with a mean of 0 and a standard deviation of 1. Each value of the P matrix is used to generate a matrix *Y* by employing Equation 4.10.

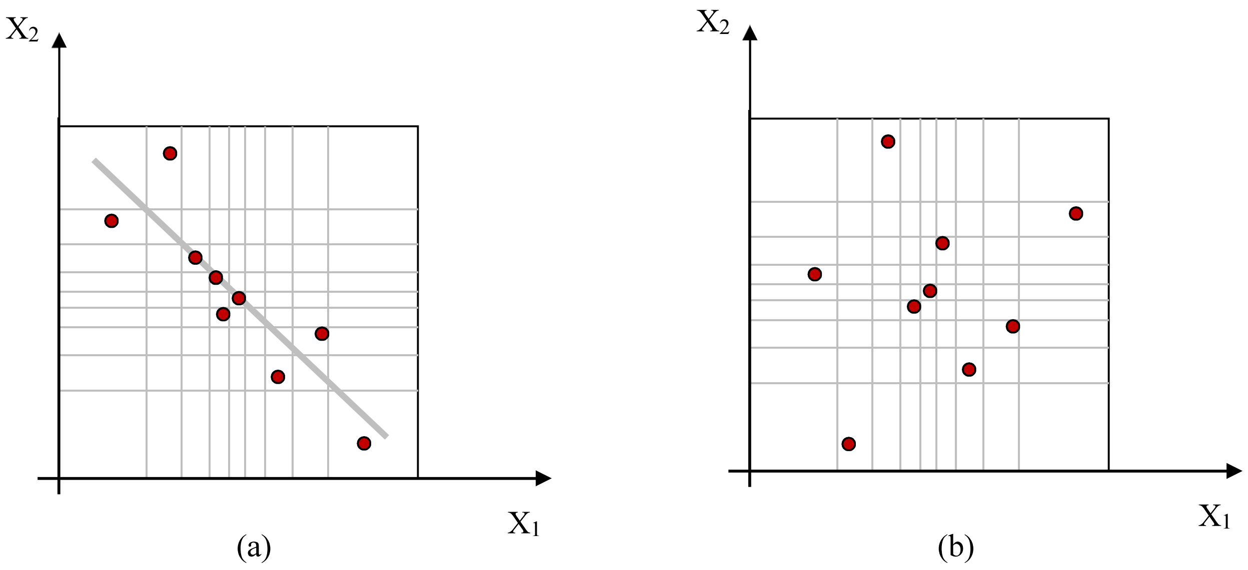

Fig. 4.7: (a) Undesired correlation in random paring of samples. (b) Pairing after correlation reduction.

$$y_{ij} = \Phi^{-1}_{(0,1)}\left(\frac{p_{ij}}{N+1}\right) \tag{4.10}$$

The covariance matrix of Y is then estimated. A Cholesky decomposition is then calculated from the covariance matrix of *Y* to produce Equation 4.11.

$$\bar{L}\bar{L}^T = cov(Y) \tag{4.11}$$

A new matrix Y* is then defined using Equation 4.12, where $\bar{L}$ is a lower triangle matrix computed from Equation 4.11.

$$Y^* = Y(\bar{L}^{-1})^T \tag{4.12}$$

The *P* matrix is then regenerated, and designated *P**, using the *Y** matrix to generate the permutations. The resulting sampling matrix *S* has been shown to have a significantly reduced amount of undesired correlation (Olsson et al., 2003). Olsson et al. (2003) notes that the Cholesky decomposition requires that the number of realizations (*N*) must be greater than the number of random variables (*K*). Additionally, the correlation reduction means that the resulting samples are no longer unbiased estimators.

4.3.2 Implementation in VecTor2

When performing a normal Monte Carlo analysis, the random variables are generated at the start of each analysis. However, when implementing Latin hypercube sampling, the random variables are generated based on stratifications and paired. Each pairing forms the basis of a single analysis. Thus it is required to generate and store the samples for all analyses at the start of the simulation. This section describes the implementation of the Latin hypercube sampling (LHS) technique.

4.3.2.1 Inverse Random Variables

In order to employ LHS, the inverse of random variables are required to be computationally evaluated. The Newton-Raphson nonlinear solution scheme was used to compute the inverse of the CDF. The implemented scheme follows Equation 4.13:

$$x^{i} = x^{i-1} - \frac{G(x)}{G^{-1}(x)} = x^{i-1} - \frac{CDF\left(x^{i-1}\right) - F(x)}{PDF\left(x^{i-1}\right)} \tag{4.13}$$

where *F(x)* is the value of the CDF for which *x* is to be determined. Thus functions for the PDF and CDF of *x* were required. These functions were implemented for normal, lognormal, and beta distributions. The error function was used to evaluate the inverse of any CDF by transforming X into a standard random variable Z and employing Equation 4.14.

$$CDF(x) = \frac{1}{2}\left(1 + \operatorname{erf}\left(\frac{Z}{\sqrt{2}}\right)\right) \tag{4.14}$$

The variable Z is calculated using Equation 4.15.

$$Z = \frac{X - \mu}{\sigma} \tag{4.15}$$

When evaluating the CDF of a lognormal distribution, the lognormal variable is converted into its normal mean and standard deviation and Equation 4.16 is employed.

$$Z = \frac{\log(X) - \mu}{\sigma} \tag{4.16a}$$

where:

$$\sigma = \sqrt{\ln\left(1 + \frac{VAR[X]}{(E[X])^2}\right)} \tag{4.16b}$$

$$\mu = \ln(E[X]) - \frac{1}{2}\sigma^2 \tag{4.16c}$$

For the beta distribution, the CDF was calculated using the incomplete beta function. The incomplete beta function is calculated using Equation 4.17.

$$B(x; \alpha, \beta) = \int_0^x t^{\alpha-1}(1-t)^{\beta-1}dt \tag{4.17}$$

The incomplete beta function requires that *x* be normalized between zero and one. This is computed using the bounds of the beta function: *a* and *b*. Thus *x* is computed using Equation 4.18

$$x = \frac{(X-a)}{(b-a)} \tag{4.18}$$

The inverse of the CDF function is then computed using Equation 4.19.

$$Z = \frac{B(x; \alpha, \beta)}{B(1; \alpha, \beta)} \tag{4.19}$$

The computed value is then transformed back into the original distribution by applying the inverse of Equation 4.18 which yields Equation 4.20.

$$X = (b-a)Z + a \tag{4.20}$$

4.3.2.2 Fisher-Yates Shuffle

With the development of a function that can compute the inverse of random variables, a sampling matrix is then constructed using the process described in Section 4.2. The generation of a random permutation matrix is done using the Fisher-Yates shuffle. The pseudocode for the Fisher-Yates shuffle is presented below:

```
Generate ordered P matrix of size n x 1
FOR i = n-1 TO 1 STEP -1
  Generate U ~N[0,1]
  K = Floor(i*U)+1
  Swap row K with row I
END FOR
Generate U~N[0,1]
K = Floor((n-1)*U)+1
Swap row K with row n
```

This code is used to generate the P and S matrices required to enable LHS. Each entry of the S matrix is then converted into a sample using the distribution parameters of each column and the inverse CDF function. This X matrix is then stored and used for all of the analyses for the simulation.

4.3.3 Verification of Implementation

In order to test the implementation of the method, 5000 simulations were conducted to assess the maximum error. Each simulation sampled 25 to 1000 samples using straight Monte Carlo sampling (MCS) and Latin hypercube sampling (LHS). An example of a realization is provided in Fig. 4.8.

The simulation comparing MCS and LHS illustrates the effectiveness of using Latin hypercube sampling for stochastic simulations with a small number of analyses. The prediction of the mean and the standard deviation show significant improvement, even for the maximum error. As shown on Fig. 4.9 and Fig. 4.10, a simulation size of 200 results in a maximum error on the sampled mean and the sampled standard deviation of 1% and 5%, respectively. This is a significant improvement

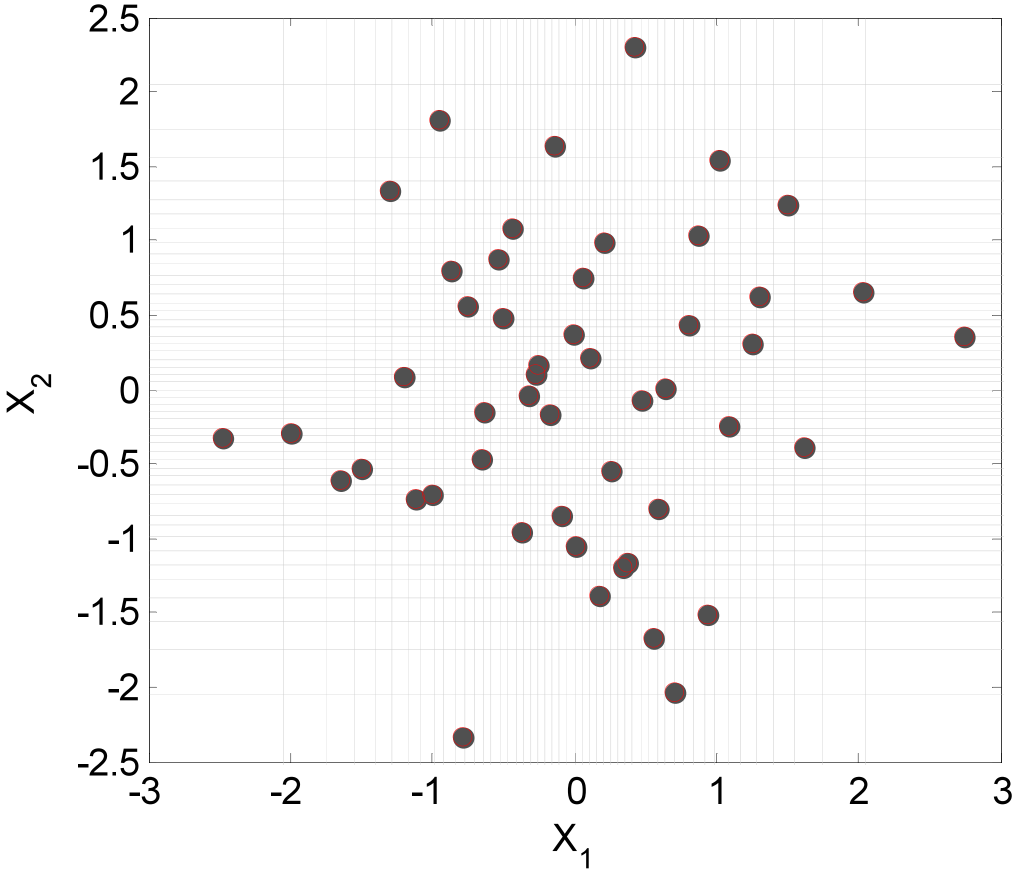

Fig. 4.8: Realization of 50 Latin Hypercube samples.

when compared to the Monte Carlo simulation samples which exhibit a maximum error for the mean and standard deviation of 25% and 20% respectively. The simulation both verifies the implementation and exhibits its usefulness in small sample stochastic simulations.

4.4 Correlated Sampling

Multiple empirical functions have been developed to express the relationships between the compressive strength of concrete and its tensile strength or elastic modulus. These relationships are based on regression analysis of experimental data. If concrete compressive strength exhibits variability for a given specified strength, it is thus reasonable to assume that a correlation exists between the tensile strength and modulus of elasticity for a given compressive strength. Correlated sampling can thus be a useful tool for the sampling of reinforced concrete material properties.

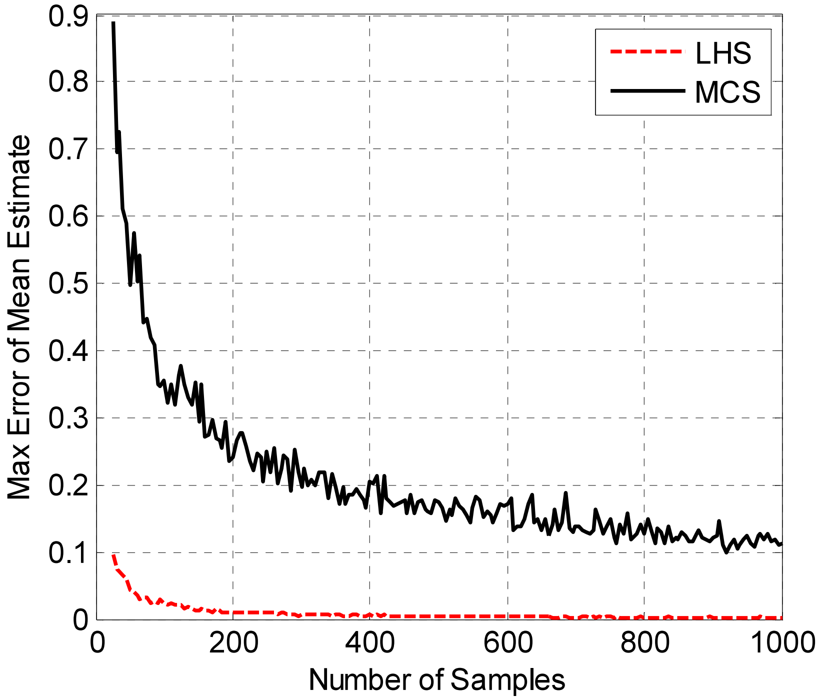

Fig. 4.9: Maximum error for estimate of mean.

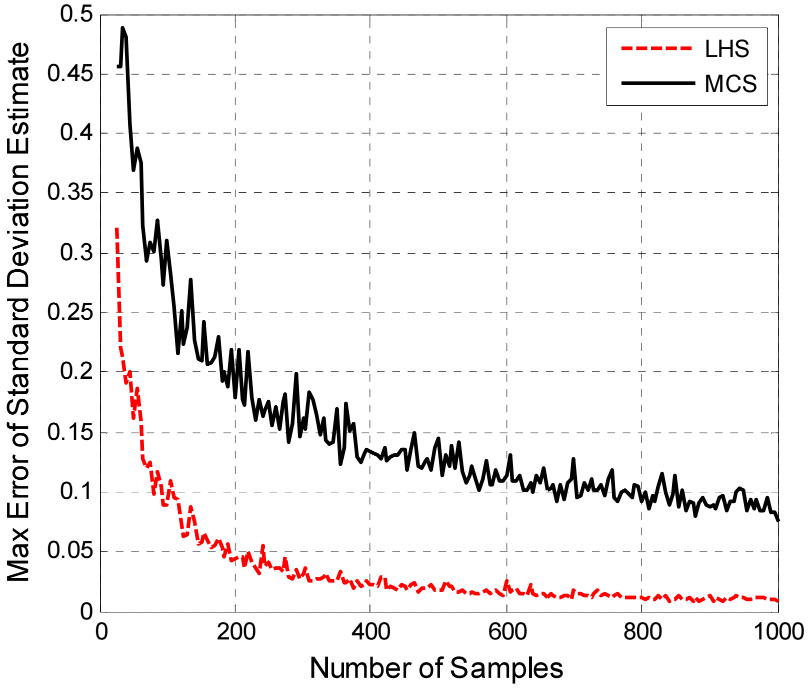

Fig. 4.10: Maximum error for estimate of standard deviation.

In order to achieve correlated sampling for a non-Gaussian distribution, or for a set of data where correlation exists but each random variable follows a unique distribution, a multivariate distributional transform is used. In this case, a vector Z is generated on a multivariate Gaussian distribution with a mean of $\{\mu_i = 0\}$ and a standard deviation (or dispersion matrix) of $[\Sigma] = [\rho]$. Ripley (1987) presents a method for generating samples from a P-dimensional multivariate distribution. A set of uniform independent random variables are transformed to a set of dependent random variables through the use of Equation 4.21.

$$\{Z\} = \{\mu\} + [S]\{V\} \tag{4.21a}$$

where:

$$[\Sigma] = [S][S]^T \tag{4.21b}$$

$$\{V_i\} \sim N[0,1] \tag{4.21c}$$

The transformation matrix [S] is derived from the original dispersion matrix. A Cholesky decomposition of the dispersion matrix is used to calculate the transformation matrix. For each value of Z, the inverse of the sample is used to generate a set of data points bounded by [0,1] that have the desired correlation. This is done using Equation 4.22.

$$\{U\} = \begin{bmatrix} \Phi(Z_1) \\ \vdots \\ \Phi(Z_P) \end{bmatrix} \tag{4.22}$$

The sample is then transformed into the desired distribution through use of the inverse method. Equation 4.23 illustrates the calculation of a sample.

$$\{X\} = \begin{bmatrix} \mathrm{G}_1(U_1) \\ \vdots \\ \mathrm{G}_\mathrm{P}(U_P) \end{bmatrix} \tag{4.23a}$$

where:

$$G_i(U) = \Phi_i^{-1}(U) = \mathrm{F}_i^{-1}(U) \tag{4.23b}$$

This method is used to generate correlated samples within VecTor2. It should be noted that the selection of the dispersion matrix, or in this case the correlation matrix, requires statistical data that are not available. Thus no default correlation coefficients are recommended for reinforced concrete material properties.

4.4.1 Implementation in VecTor2

Correlated sampling in VecTor2 is sampled during individual simulations. This is the same approach taken for the basic Monte Carlo sampling method. The generation of correlated samples is illustrated by the following pseudocode.

```
Step 1:  Compute S matrix from $\Sigma$ matrix.
Step 2:  Calculate the Z matrix where $V_i \sim N[0,1]$
Step 3:  Calculate the U matrix
Step 4:  For each required distribution, evaluate the inverse cumulative distribution function $G_i(U)$ to obtain the X matrix.
```

The selection of correlation coefficients is at the discretion of the user. The user is able to input the correlation coefficients between concrete compressive strength, tensile strength, and modulus of elasticity. Note however, that the method of sampling requires that the matrix be positive definite. This requirement means that the user cannot specify contradictory correlations between random variables. For example, if a strong positive correlation exists between a random variable X_1 and X_2, and a strong correlation exists between random variable X_2 and X_3, then the current method does not allow for a strong negative correlation to exist between X_2 and X_3. These negative correlations can be achieved by processes such as simulated annealing (Vorechovsky and Novak, 2009); however, this is considered beyond the scope of the current work.

4.4.2 Verification of Implementation

The implementation of correlated sampling was verified by comparing the theoretical and the generated covariance matrix. The covariance matrix was evaluated comparing the norm of the difference between the sampled and actual covariance matrix. This is calculated mathematically using Equation 4.24, where S is the sampled covariance matrix and C is the desired covariance matrix.

$$\varepsilon = \frac{\|S - C\|}{\|C\|} \tag{4.24}$$

The error statistic should be as minimal as possible. A simulation was conducted to assess the error in the sampling of the correlation matrix. In this simulation, random samples with samples sizes 25 to 1000 at increments of 5 were taken. This process was repeated 1000 times to develop statistics on the sampling error. Due to the computational limitations of VecTor2, conducting a large number of samples may not be feasible. Thus it is important to understand the mean sampling error expected at various levels of correlation.

4.4.3 Correlated Latin Hypercube Samples

The method described above can be extended to induce correlation into Latin hypercube samples. This is achieved by substituting the vector {V} with a set of Latin hypercube samples that are normally distributed with a mean of zero and a variance of one. The implementation of this technique allows the user to take advantage of the accuracy of LHS for small sample size simulations without forcing the input parameters to be independent random variables. The following pseudocode illustrates how to generate correlated Latin hypercube samples.

```
Step 1: Compute S matrix from Σ matrix.

Step 2: Generate V* as an N x R Latin Hypercube sample matrix where Rj~N[0,1]

Step 3: Each row of the LHS matrix is used to generate Z such that:

        ${Z} = {\mu} + [S]{V^*_{i,j=1toR}}^T$

Step 4:   Calculate the U matrix

Step 5:   For each required distribution, evaluate the inverse cumulative distribution
          function $G_i(U)$ to obtain the X matrix.
```

When compared against correlated Monte Carlo samples, the correlated Latin hypercube (CLH) samples provide a marginal improvement on the estimate of the correlation matrix, and a large improvement on the estimate of the mean and standard deviation. The generation of CLH samples was evaluated by simulation. One thousand simulations were conducted to evaluate the ability to estimate the covariance matrix, the mean of each random variable, and the variance of each random variable. Each simulation consisted of the generation of a set of samples with sample sizes ranging from 25 to 1000 at an interval of 5. The covariance matrix was evaluated by using the sum of squared difference of the upper triangular portion of the matrix using Equation 4.24.

The difference between the CLH samples and MC samples is shown in Fig. 4.11. The CLH samples appear to provide a marginal improvement over basic Monte Carlo sampling, however the real advantage of the method is illustrated by comparing the estimation of the mean and variance. The comparison of each method is illustrated in Fig. 4.12, Fig. 4:13, and Fig. 4.14.

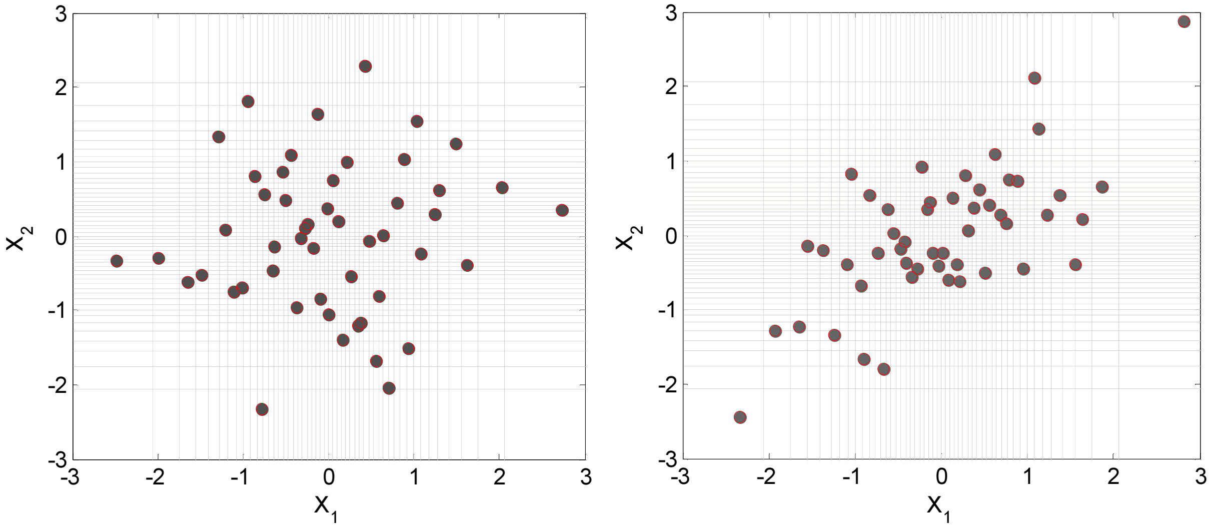

(a) (b)

$$S_{LHS} = \begin{bmatrix} 1 & 0.08 \\ 0.08 & 1 \end{bmatrix} \qquad S_{CLHS} = \begin{bmatrix} 1 & 0.67 \\ 0.67 & 1 \end{bmatrix} \tag{4.25}$$

$$C_{LHS} = \begin{bmatrix} 1 & 0.00 \\ 0.00 & 1 \end{bmatrix} \qquad C_{CLHS} = \begin{bmatrix} 1 & 0.70 \\ 0.70 & 1 \end{bmatrix} \tag{4.26}$$

Fig. 4.11: (a) Uncorrelated Latin hypercube realization (b) Correlated Latin hypercube realization.

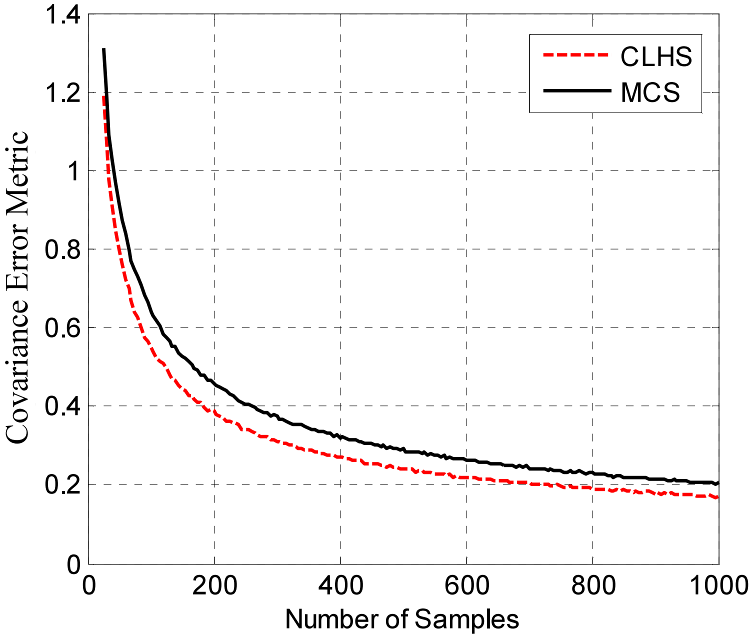

Fig. 4.12: Estimation of Covariance Matrix; CLH sampling versus MC sampling.

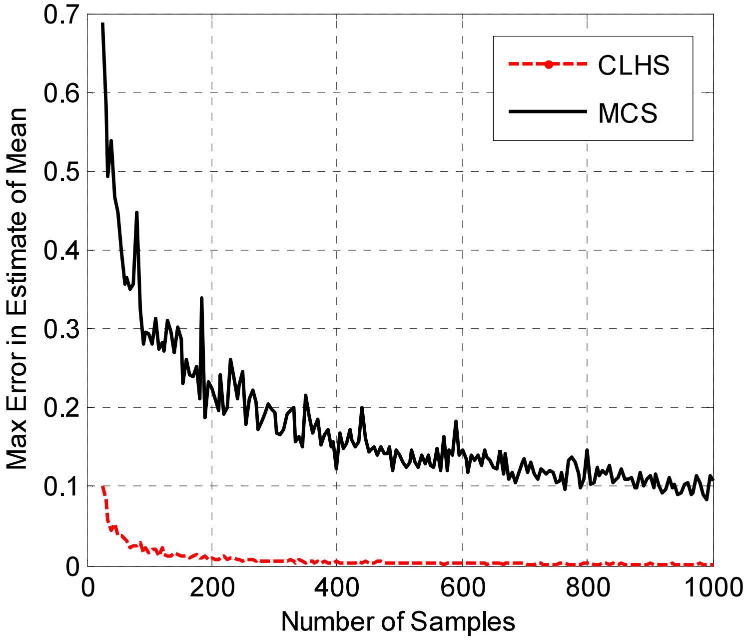

Fig. 4.13: Max Error estimate of the mean value for correlated Latin hypercube sampling versus correlated Monte Carlo sampling.

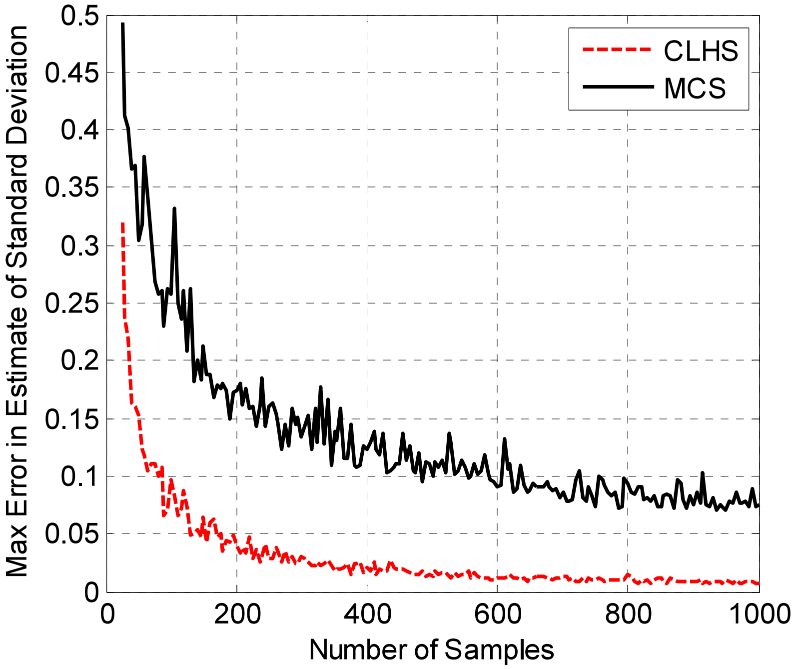

Fig. 4.14: Max Error estimate of the standard deviation for correlated Latin hypercube sampling versus correlated Monte Carlo sampling.

4.5 Random Field Generation

Random variations of material properties do not only occur from structure to structure, but also within a structure. In the case of a finite element simulation, each element can be assumed to take on a random value of a material property. However, the elements cannot be assigned a truly random value. Independent random sampling of individual finite elements would produce unrealistic conditions as maximum and minimum values could be assigned to adjacent elements. It is logical to assume that a correlation exists between adjacent elements, creating gradient-like transitions. Thus a method is required to generate stochastic samples of spatially distributed randomness that captures the spatial correlation between adjacent finite elements. This can be done using random fields.

Random fields are spatially correlated stochastic samples which follow a specified distribution. A common type of random field is called a Gaussian random field. It takes its name from the spatial correlation function, which takes on a Gaussian shape. Random fields can be N-dimensional, however, for the purpose of this thesis, only one-dimensional and two-dimensional random fields are discussed. A one-dimensional random field might be used to describe spatial variations in the corroded area of steel reinforcement. A two-dimensional random field could describe spatial variation in concrete compressive strength within a large structural element. A comparison between independently generated element values and spatially correlated random values is shown in Fig. 4.15.

4.5.1 Covariance Functions

Random fields are defined by their covariance function. This function describes the spatial change in covariance. For application to finite elements, it is convenient to descretize the covariance functions into a covariance matrix. Choi et al (2006) summarized three popular covariance functions that can be used in the generation of random fields. The first function is the exponential covariance function. The covariance is modelled as an exponential decay and is calculated using Equation 4.27,

$$C_{ij} = C_o \, exp\left[-\left|\frac{\Delta x_{ij}}{L}\right|\right] \tag{4.27}$$

where, C_{ij} is the calculated covariance between the i^{th} and j^{th} element, C_o is the desired variance of the random field, L is the correlation length of the random field (after a length of L, elements are statistically independent), and Δx_{ij} is the linear distance between the i^{th} and j^{th} element. Similarly to the exponential form, a Gaussian covariance model can be described by Equation 4.28.

$$C_{ij} = C_o \, exp\left[-\left(\frac{\Delta x_{ij}}{L}\right)^2\right] \tag{4.28}$$

The Gaussian covariance model has a slope of zero when Δx_{ij} is equal to zero. This produces a smoother gradient between adjacent elements (Choi et al., 2006).

Lastly, for spatial processes that are characterized by discontinuities in the random field, a nugget-effect model can be used (Choi et al., 2006). The nugget-effect model is described by Equation 4.29.

$$C_{ij} = \begin{cases} C_o if \ |\Delta x_{ij}| = 0 \\ 0 \ if \ |\Delta x_{ij}| > 0 \end{cases} \tag{4.29}$$

Each of the presented covariance functions are plotted in Fig. 4.16.

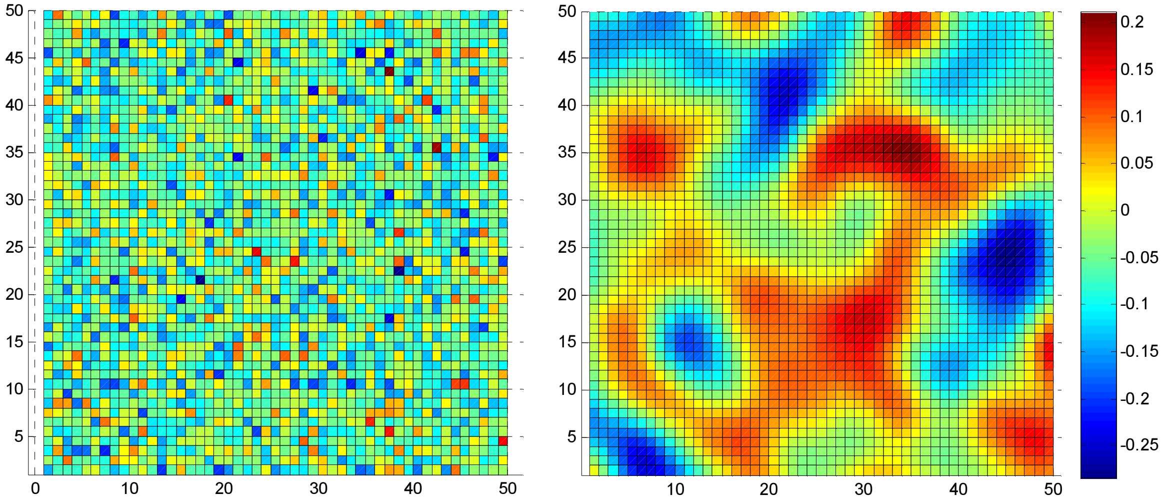

(a) (b)

Fig. 4.15: Illustration of (a) spatially independent random samples and (b) spatially correlated random samples.

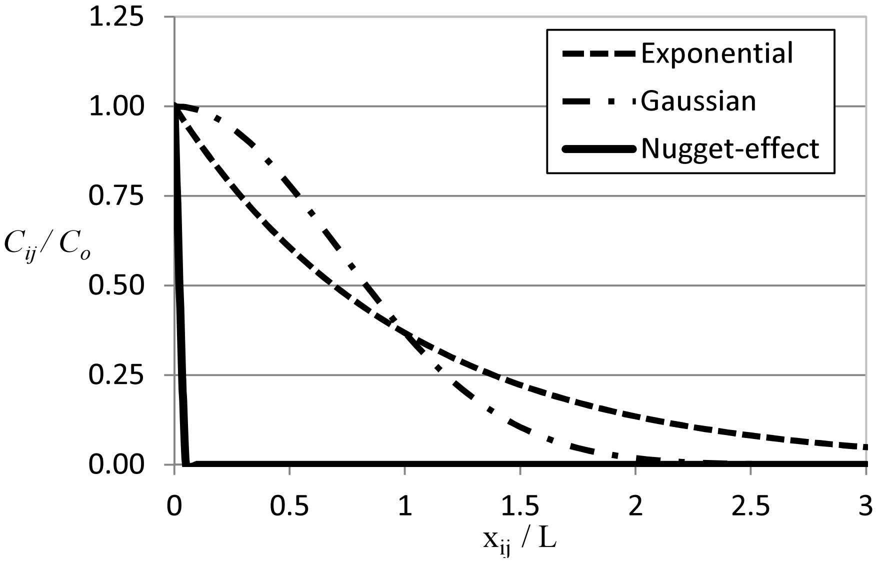

Fig. 4.16: Covariance models for random field generation.

4.5.2 The Karhunen - Loeve Transform

The Karhunen - Loeve transform (KL transform), also called the orthogonal transform, is a method for generating random fields (Choi et al, 2006). The KL transform can be used for both the continuous and discrete problems, however because finite elements produce a discrete set of elements (with constant properties within elements) only the discrete formation of the KL transform is discussed.

The KL transform transitions the random variables in correlated space to a set of random variables in uncorrelated space. Thus, the transformation takes the form of an eigenvalue problem where each of the transformed random variables are independent and thus can be generated independently.

In correlated space, each random variable is assigned a designation of X_i where i ranges from 1 *to* N_v. N_v represents the total number of random variables (and in a finite element simulation would be equal to the number of elements). A set of random variables in uncorrelated space are designated Y_i where i ranges again from *1 to* N_v.

Each element in the discretization is used to derive a correlation matrix using the equations presented in Section 4.4.1. This correlation matrix is then decomposed using Equation 4.30,

$$C_{XX} = \Phi\Lambda\Phi^{\mathrm{T}} \tag{4.30}$$

where C_{XX} is the discretized covariance matrix, Φ is the eigenvector matrix, and Λ is the diagonal Eigen value matrix with eigenvalues λ_1 to λ_{Nv} (Vorechovsky and Novak, 2005).

A set of independent random variables can now be generated. Each random variable corresponds to one of the eigenvalues and has a mean of zero and a standard deviation of $\sqrt{\lambda_{Nv}}$.

Once the independent random variable samples are generated, they can be converted back into correlated space using Equation 4.31 (Vorechovsky and Novak, 2005).

$$X = \Phi Y \tag{4.31}$$

In the case of a two-dimensional random field, the X values are mapped to their corresponding element numbers.

It is noted by Vorechovsky and Novak (2005) that not all of the eigenvalues and corresponding eigenvectors need to be calculated. A plot of the percentage of sum of eigenvalues against the number of random variables reveals that a large number of the eigenvalues do not contribute to correlated space. Thus only partial computation of the eigenvalues and eigenvectors is required. This concept is illustrated in Fig. 4.16. Note that as the correlation length (represented as d in Fig 4.17) gets longer, the required number of eigenvalues decreases.

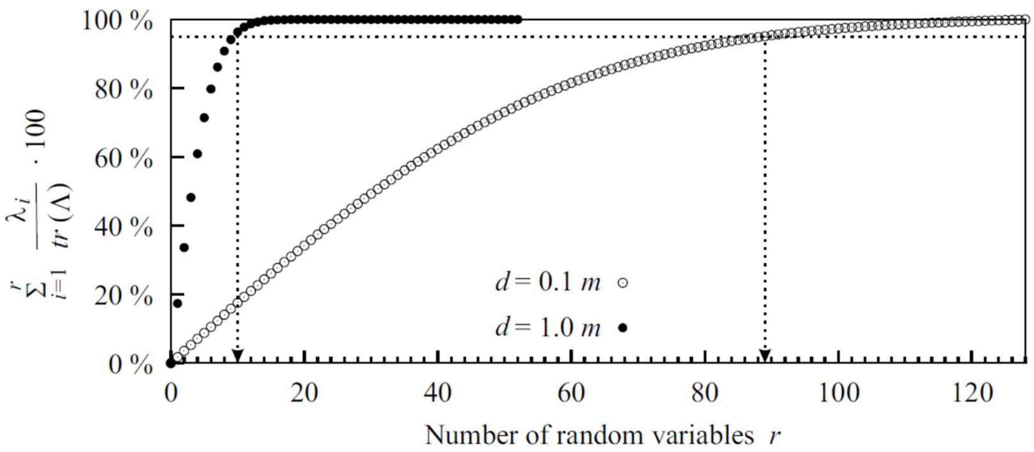

Fig. 4.17: Reduction in random variables in uncorrelated space. Taken from Vorechovsky and Novak (2005).

Due to the large number of independent random variables used in the generation of random fields, Latin hypercube sampling has been shown to be advantageous when employing random fields in stochastic simulations (Vorechovsky and Novak, 2005).

The number of independent random variables that contribute to the random field generation can be arbitrarily selected by the user. However, the generation of random fields can also be treated as an optimization problem where the quality of a random field is assessed, and the optimal number of eigenvalues that contribute to correlated space is determined. This optimization serves primarily to improve computational efficiency and is thus excluded from the scope of this thesis.

4.5.3 Implementation in VecTor2

The implementation of random field generation into VecTor2 is done through the use of the Intel Eigen Solver DSYEVX. The Intel Eigen Solver is based on the FEAST algorithm originally developed by Polizzi (2009). The user selects the number of eigenvalues that they wish to compute. The following pseudocode illustrates how random fields are generated in VecTor2.

```
Step 1: Compute covariance matrix for finite element mesh.
Step 2: Calculate eigenvalues and eigenvectors.
Step 3: Generate samples in uncorrelated space each with a mean of zero and a standard
        deviation of $\sqrt{\lambda_i}$.
Step 4: Convert the samples back into correlated space.
Step 5:  Scale the distribution to match selected statistical models.
Step 6: Calculate tensile strength and modulus of elasticity based on compressive strength
        random field.
```

Note that the current implementation in VecTor2 requires that the user select a normal distribution for the concrete compressive strength. If a non-Gaussian random field is desired, a future implementation could include a method similar to the generation of non-Gaussian correlated samples. The Gaussian random field could be transformed to a non-Gaussian random field through use of the inverse method. Additionally, the current method assumes a correlation coefficient of 1.0 between concrete compressive strength, concrete tensile strength, and modulus of elasticity. It may be advantageous in the future to implement independent realizations of concrete material properties. However, assuming complete independence deviates from known statistical correlations between the compressive strength of concrete and the tensile strength or modulus of elasticity. It would be thus advantageous to expand the generation techniques to include generation of cross-correlated random fields.

4.5.4 Verification of Implementation

The implementation was verified by creating a 2000 mm by 2000 mm square mesh with 1600 elements. A random field realization was then generated for a total of 1000 samples. The mesh used for validation is shown in Fig. 4.18 along with a realization of the generated random field.

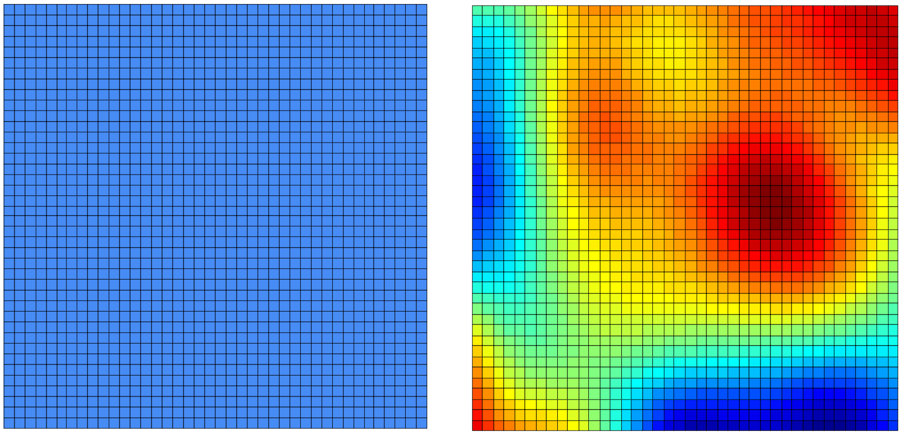

(a) (b)

Fig. 4.18: (a) Random field test mesh and (b) Generated random field realization.

A histogram of the collected scaling factors confirms that both at each point, and overall, the selected distribution is being captured. The histograms are shown in Fig. 4.19.

The mean and standard deviation for each element exhibits small spatial variability in the simulated values. However, the amount of variation is minimal and thus considered acceptable. Fig. 4.20 shows the spatial variability of the coefficient of variation, which captures the spatial variability of the mean and standard deviation.

The implementation of the covariance function was tested by calculation of empirical semivariograms for the generated data. The average of the empirical covariance matches the theoretical covariance as shown in Fig. 4.21.

4.5.5 Latin Hypercube Sampling and Random Field Generation

The inclusion of LHS in the random field generation has shown to produce a better representation for random fields when employed in small number stochastic simulations (Vorechovsky and Novak, 2005). The procedure for generation of random field was augmented such that the samples

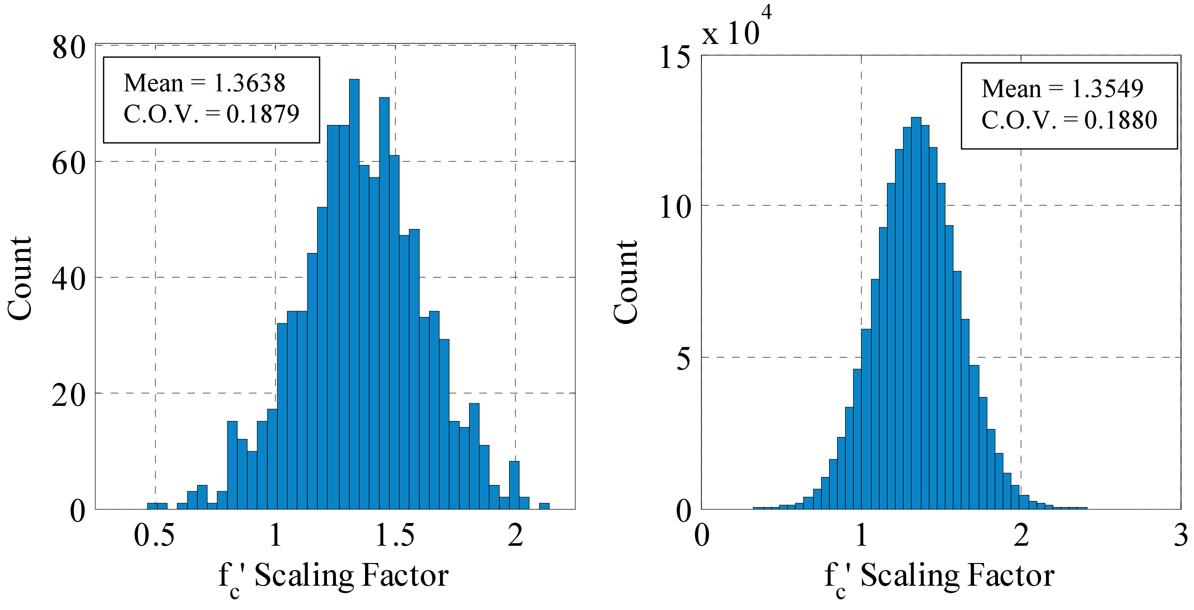

(a) (b)

Fig. 4.19: (a) Histogram for a single element (b) Histogram for all elements.

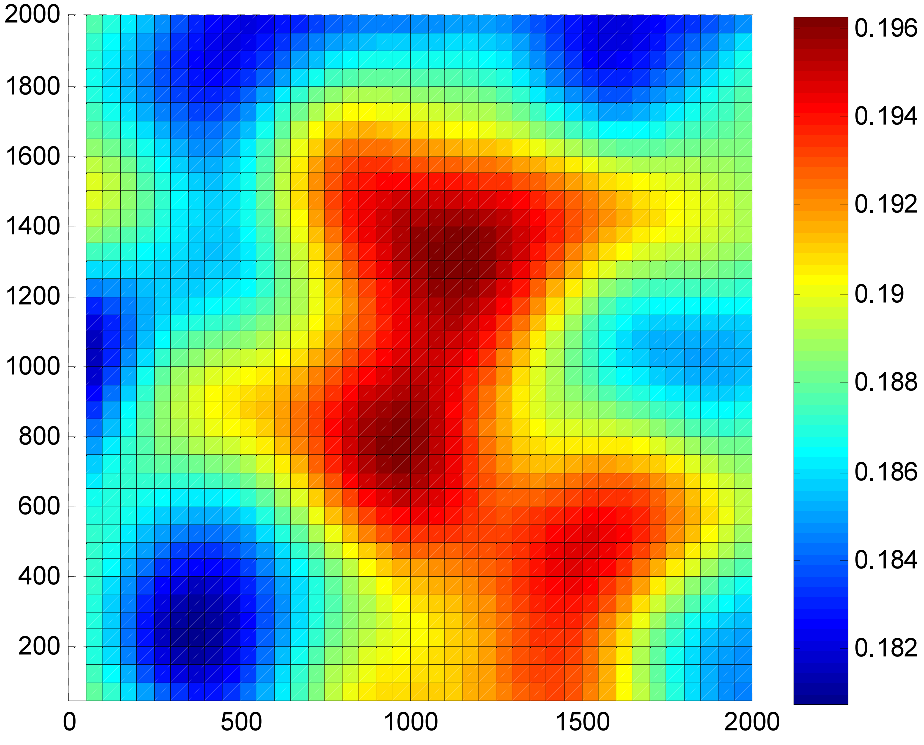

Fig. 4.20: Spatial variation of simulated coefficient of variation.

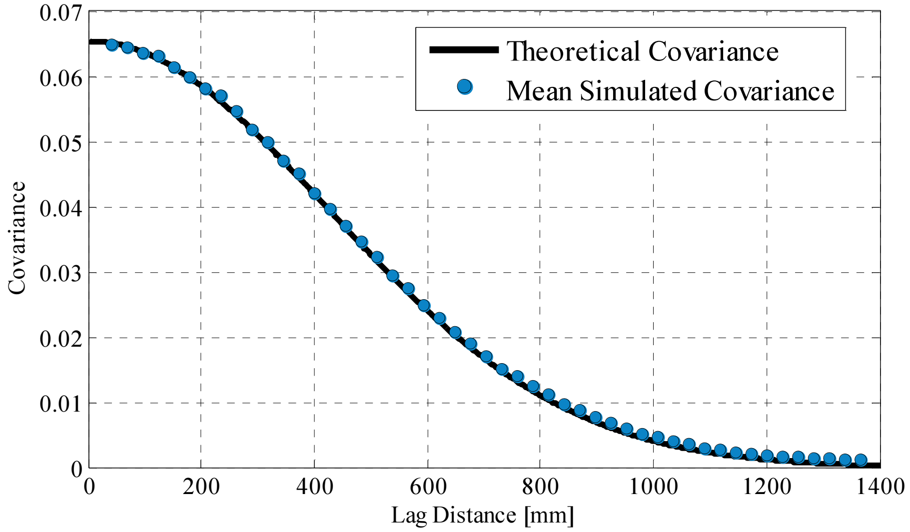

Fig. 4.21: Theoretical and mean simulated covariance function for generated random field samples.

in uncorrelated space are generated with the LHS technique. The following pseudocode illustrates the implementation in VecTor2.

```
Step 1: Compute covariance matrix for finite element mesh.
Step 2: Calculate eigenvalues and eigenvectors.
Step 3: Generate Latin hypercube samples in uncorrelated space each with a mean of zero
        and a standard deviation of $\sqrt{\lambda_i}$.
Step 4: Convert the samples back into correlated space.
Step 5: Scale the distribution to match selected statistical models.
Step 6: Calculate tensile strength and modulus of elasticity based on compressive strength
        random field.
```

The implementation was tested using the techniques illustrated in Section 4.4.4. For detailed test results the reader is referred to Appendix C.

4.5.6 Alternate Sampling Technique for Random Fields

In the previous formulation, the random field statistics are assumed to be the same as the material variability statistics. However, it has been observed in the literature (Bartlett and MacGregor, 1995) that the variability attributed to spatial variation is much lower than the global variability. The same conclusion was drawn from the experimental study in Chapter 3. Thus a sampling technique that will sample from the global distribution and capture the local variability is required.

An alternate sampling technique is thus proposed wherein the local mean of the random field is sampled from the global distribution, and then the random field is generated that reflects the local variability. The following pseudocode is used in the alternate sampling implementation.

```
Step 1: Generate local mean for random field simulation, $\mu_{local}$.
Step 2: Generate realization of a random field, $R_{N[0,1]}$.
Step 3: Scale the random field as $R_{Actual} = \mu_{local} + \mu_{global} V_{sp} \times R_{N[0,1]}$.
```

R_{Actual} is the realization of the random field applied to each simulation trial, μ_{local} is the sampled random variable from the global concrete distribution, μ_{global} is the mean of the global concrete distribution, and V_{sp} is the coefficient of variation due to spatial variability.

Initially, the local mean was used with the coefficient of variation for spatial variability to determine the local standard deviation. However, this was found to be unrepresentative of the global distribution. Consider a local sample that is much smaller than the mean, an extreme value on the lower tail. If this local value is used for the variability, it artificially increases the density of samples in that region. Thus when analyzing the data as a global set of random variables, the lower tail contains samples of variables that far exceed the probability distribution function. When the global mean was used to sample spatial variability, much better simulation of the global distribution was observed.

This phenomenon is attributed to the ratio between the number of stochastic trials and the number of elements. In a large structure with spatial variation, the number of elements may be in excess of 3000. Similarly, due to computation limitations the number of stochastic trials may be between

50 and 500. Thus for extreme values, the number of samples at that extreme is artificially inflated due to the fact that the number of elements (and thus number of unique sampling points) is larger than the samples. This is the main vulnerability of sampling with this method.

An empirical test of the following implementation was conducted on a mesh with 1600 rectangular elements. The random field length was set at 200 mm with the mesh being a 1000 x 1000 square. A coefficient of variation of 0.05 was selected for the random field. The concrete strength was modelled using the distributions generated by Nowak and Szersen (2004a). Five sets with 50, 100, 200, 500, and, 1000 simulations respectively were generated in order to assess the accuracy of the sampling method. Two statistics were then pulled out of the sampled data. The first was the distribution of mean values for each random field simulation. This was calculated by taking the mean of each random field visualization as a set of data. The second set of data encompassed the entirety of the sampled data treating each element like a realization of a random variable. The random field had a mean of 0 and standard deviation calculated using Equation 4.32.

$$\sigma_{RF} = V_{SV}\mu_{Global} = V_{SV}\lambda f_c' = 0.05 \times 1.2 \times 30\ MPa = 1.8\ MPa \tag{4.32}$$

where σ_{RF} is the random field standard deviation, V_{SV} is the coefficient of variation due to spatial variability, λ is the bias factor for concrete, and f_c' is the compressive strength of concrete. Note that the coefficient of variation for the resulting global distribution can be approximated using Equation 4.33.

$$V_{Total} = \sqrt{V_{f_c'}^2 + V_{SV}^2} \tag{4.33a}$$

$$V_{Total} = \sqrt{(0.10)^2 + (0.05)^2} = 0.112 \tag{4.33b}$$

The results of the simulation are summarized in Table 4.2. Note that all of the global random field samples fail to pass the chi-squared goodness of fit test, however the mean of each random field successfully passes the distribution fitting test.

It is suspected that this is due to poor sampling at the tails of the distribution. Two quantile-quantile plot (q-q plot) of the mean random field data and the global random field data are presented in Fig. 4.22.

Table 4.2: Results of simulated random field data.

Sample size	Sampled Mean		Sampled COV		p-value	
	Mean RF	Global RF	Mean RF	Global RF	Mean RF	Global RF
50	1.1594	1.1594	0.1010	0.1113	0.0992	Failed
100	1.1857	1.1857	0.1073	0.1168	0.0863	Failed
200	1.1975	1.1975	0.1122	0.1214	0.2527	Failed
500	1.1870	1.1870	0.1076	0.1176	0.6104	Failed
1000	1.1892	1.1892	0.1009	0.1166	0.1166	Failed

Fig. 4.22 reveals that the global random field samples a normal distribution reasonably well with the exception of the tails of the distribution. The mean random field data also deviate at the tails; however, the deviation is limited to a few points. It is likely that the small deviation of the mean random field data is extrapolated into a larger deviation at the global level. This is a result of the fact that for a deviated mean sample, there are 1600 samples within the random field. Thus this sampling method does not sample the distribution tails correctly and, as a result, fails the distribution fitting tests at the global level. Despite failing the goodness of fit tests, this method produces correct estimates of the mean and coefficient of variation of a sampled distribution. This, coupled with the fact that the first order reliability method is primarily employed in this thesis, means that the sampled tails are of diminishing importance to a curve fitting approach to reliability.

4.6 Disturbed Stress Field Model Error

Any analytical model is an approximate representation of reality. As such the analytical model will not be a perfect representation of the physical system. When conducting a stochastic analysis, uncertainties are categorized into three major categories: uncertainty due to material properties, uncertainty due to geometry, and uncertainty due to modelling. The uncertainty due to material properties and geometry can be directly measured from a population of experimental data. The uncertainty model must be determined through comparison between experiments and model predictions. If the actual resistance is designated as R, and the model prediction designated as Rn, the relationship between the actual and predicted resistance is modelled by Nowak and Szerszen (2003) using Equation 4.31.

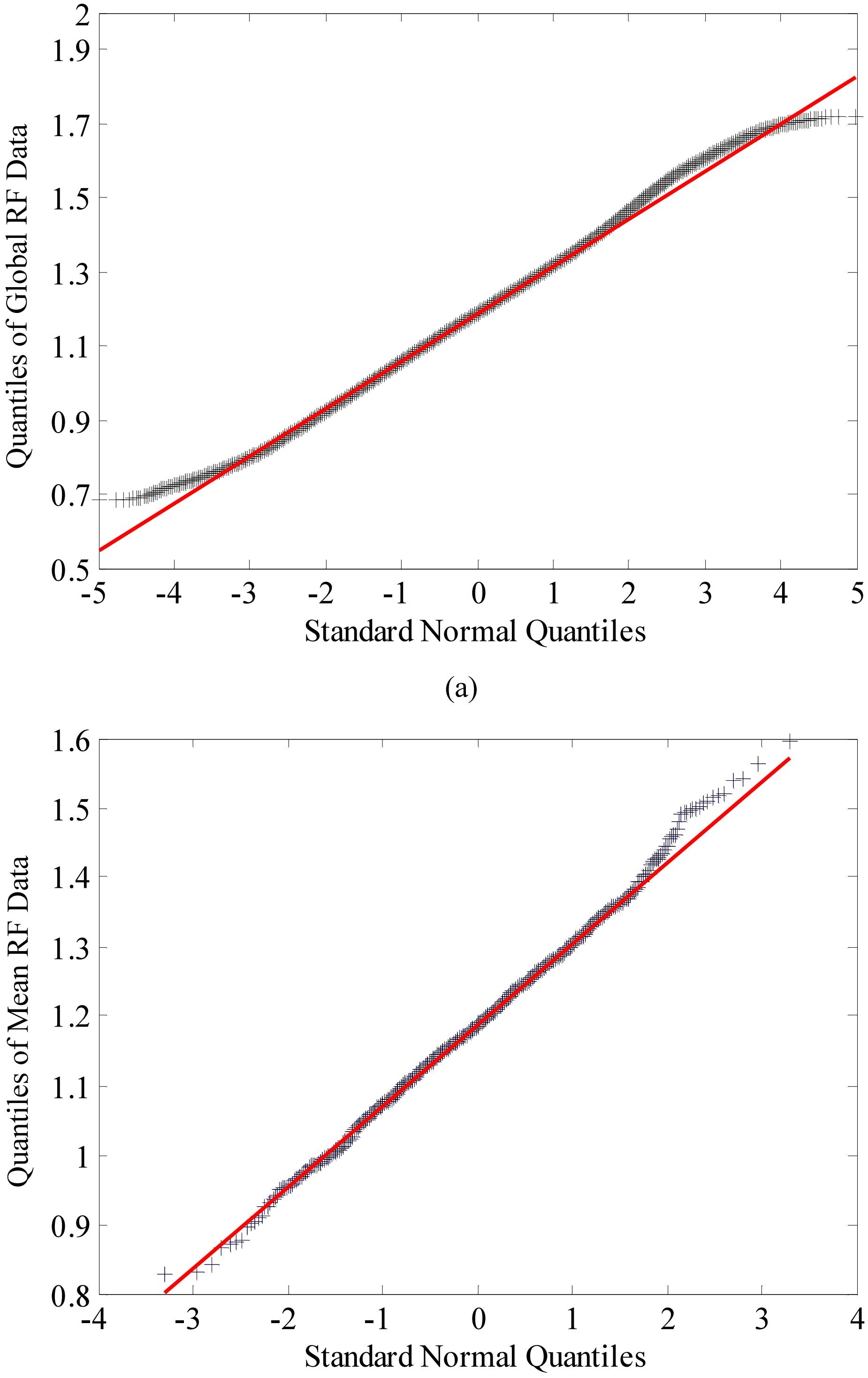

(a)

(b)

Fig. 4.22: Quantile-quantile plots for (a) Global RF data and (b) Mean RF data.

$$R = \lambda_P \lambda_F \lambda_M R_n \tag{4.34}$$

The material uncertainty is captured by λ_M, the fabrication or geometric uncertainty by λ_F, and the professional or model uncertainty by λ_P. For use in stochastic simulations, the statistical properties of the professional factor need to be determined. The MCFT and DSFM element formations are largely derived on the experimental behaviour observed in panel tests. It is thus appropriate to use panel tests to determine the statistical properties of the professional factor. This was done by comparing the properties of R/Rn for a sample of panel tests. Table 4.3 shows the panel tests and their MCFT and DSFM predictions, along with the R/Rn factors for each test.

Table 4.3: Comparison of Experiment vs. Model Predictions for MCFT and DSFM. Reproduced from Vecchio et al. (2001).

Panel	f_c' [MPa]	ρ_x [%]	ρ_y [%]	Loading $\sigma_x : \sigma_y : \nu$	ν_{u-exp}	$\frac{\nu_{u-exp}}{\nu_{u-MCFT}}$	$\frac{\nu_{u-exp}}{\nu_{u-DSFM}}$
PV10	14.5	1.79	1	0:0:1	3.97	1.056	1.045
PV11	15.6	1.79	1.31	0:0:1	3.56	0.989	0.967
PV12	16	1.79	0.45	0:0:1	3.13	0.984	1.044
PV16	21.7	0.74	0.74	0:0:1	2.14	1.070	1.070
PV18	19.5	1.79	0.32	0:0:1	2.04	0.879	0.922
PV19	19	1.79	0.71	0:0:1	3.95	0.959	0.978
PV20	19.6	1.79	0.89	0:0:1	4.26	0.960	0.960
PV21	19.5	1.79	1.3	0:0:1	5.03	0.998	0.953
PV22	19.6	1.79	1.53	0:0:1	6.07	0.978	0.903
PV23	20.5	1.79	1.79	-0.39:-0.39:1	8.87	1.232	1.109
PV25	19.3	1.79	1.79	-0.69:-0.69:1	9.12	1.225	1.129
PV27	20.5	1.79	1.79	0:0:1	6.35	0.978	0.859
PV28	19	1.79	1.79	0.32:0.32:1	5.8	1.015	0.889
PA1	49.9	1.65	0.82	0:0:1	6.4	1.027	1.021
PA2	43	1.65	0.82	0:0:1	6.22	1.007	1.002
PHS1	72.2	3.23	0	0:0:1	2.95	0.966	1.025
PHS2	66.1	3.23	0.41	0:0:1	6.66	1.031	1.096
PHS3	58.4	3.23	0.82	0:0:1	8.19	0.902	0.907
PHS4	68.5	3.23	0.82	0.25:0.25:1	6.91	0.986	1.025
PHS5	52.1	3.23	0.41	0.25:0.25:1	4.81	1.099	1.170
PHS6	49.7	3.23	0.41	-0.25:-0.25:1	9.89	1.124	1.124
PHS7	53.6	3.23	0.82	-0.25:-0.25:1	10.3	0.905	0.868
PHS8	55.9	3.23	1.24	0:0:1	10.8	1.009	0.977

Table 4.3 (Continued): Comparison of Experiment vs. Model Predictions for MCFT and DSFM. Reproduced from Vecchio et al. (2001).

Panel	f'_c [MPa]	ρ_x [%]	ρ_y [%]	Loading $\sigma_x{:}\,\sigma_y{:}\,\nu$	ν_{u-exp}	$\frac{\nu_{u-exp}}{\nu_{u-MCFT}}$	$\frac{\nu_{u-exp}}{\nu_{u-DSFM}}$
PHS9	56	3.23	0.41	-0.25:-0.25:1	9.37	0.991	1.002
PHS10	51.4	3.23	1.24	0.25:0.25:1	8.58	1.002	0.993
PB6	17.6	1.09	0	1:0:1	1.15	0.850	0.921
PB8	20.4	1.09	0	2.98:0:-1	0.8	0.808	0.829
PB10	24	1.09	0	5.94:0:-1	0.56	0.833	0.838
PB14	41.1	2.02	0	3.01:0:-1	1.54	0.960	1.079
PB16	41.7	2.02	0	1.96:0:-1	1.42	0.835	0.850
PB17	41.6	2.02	0	5.93:0:-1	1.22	0.978	1.049
PB18	25.3	2.2	0	0:0:-1	1.72	0.819	0.819
PB19	20	2.2	0	1.01:0:-1	1.28	0.766	0.876
PB20	21.7	2.2	0	2.01:0:-1	1.42	0.922	1.049
PB21	21.8	2.2	0	3.08:0:-1	1.42	1.000	1.144
PB22	17.6	2.2	0	6.09:0:-1	1.03	0.926	1.029
PB29	41.6	2.02	0	2.02:0:-1	1.49	0.842	0.949
PB30	40.4	2.02	0	2.96:0:-1	1.48	0.919	1.041
PB31	43.4	2.02	0	5.78:0:-1	1.15	0.916	0.983
PB32	57.7	2.2	0	3.01:0:-1	1.49	0.898	0.978

The global material and fabrication factors can be ignored for laboratory tests because the material properties and geometry are well known and documented. However local variation in material and fabrication must be considered. The approach taken by Mirza and MacGregor (1982) is adopted for determining the model error. The error between measured and modelled experimental data is split into three categories: model error, test error, and specimen error. The model error is what is used for the professional factor. Test error represents the difference between actual and measured applied loads and displacements, and the specimen error arises from in-batch variation of material properties and measured dimensions. The coefficients of variation for test error and specimen error recommended by Mirza and MacGregor (1982) are assumed when determining the model error for MCFT and DSFM. The bias factor and coefficient of variation from direct comparison of MCFT model results was determined to be 0.966 and 0.105 respectively. Similarly, for the DSFM, the model factor has a bias factor of 0.987 and a coefficient of variation of 0.093. Thus the coefficient of variation for the model factor is determined using Equation 4.32

$$V_{model} = \sqrt{{V_{t/c}}^2 - {V_{test}}^2 - {V_{spec}}^2} \tag{4.35a}$$

$$V_{MCFT} = \sqrt{0.105^2 - 0.03^2 - 0.045^2} = 0.090 \tag{4.32b}$$

$$V_{DSFM} = \sqrt{0.093^2 - 0.03^2 - 0.045^2} = 0.076 \tag{4.32c}$$

Thus the professional factor for MCFT can be modelled with a mean of 0.966 and a coefficient of variation of 0.090. The DSFM professional factor can be modelled with a mean of 0.987 and a coefficient of variation of 0.076. The DSFM methodology is employed in VecTor2, thus all realiability simulations using VecTor2 can be modelled with the professional factors calculated for DSFM. The DFSM professional factor was found to be normally distributed. A chi-squared goodness of fit test and a KS test produced p-values of 0.262 and 0.979. The empirical CDF of the DSFM ratios is plotted in Fig. 4.23.

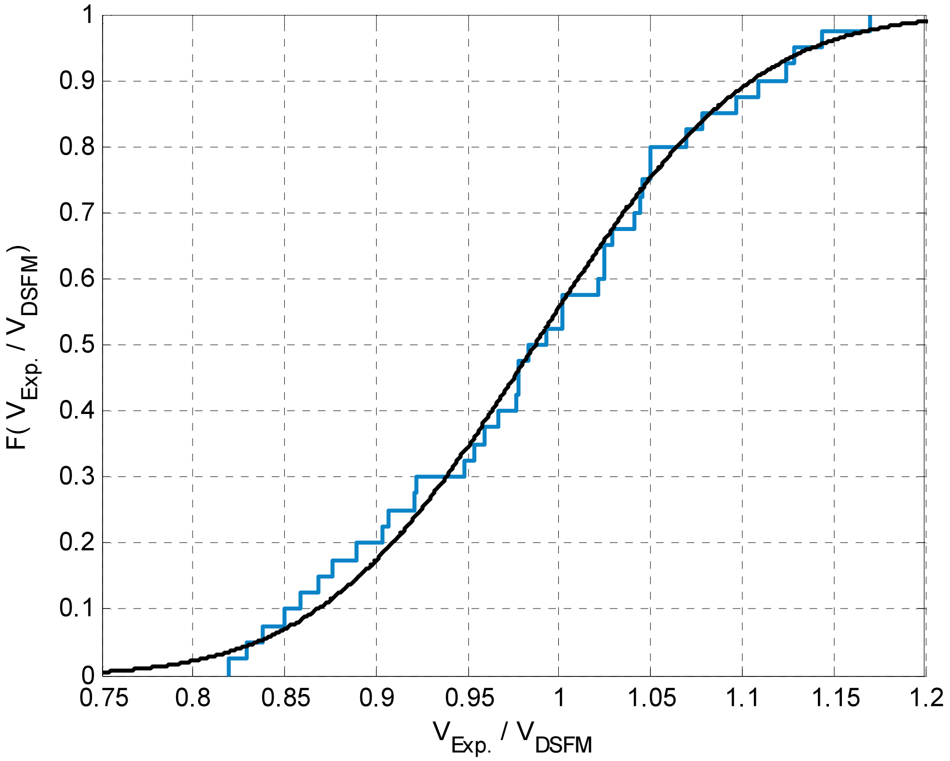

Fig. 4.23: Normal distribution fit for model bias factor for DFSM results.

In the current implementation of stochastic simulation in VecTor2, the stochastic simulations produce Rn values that include the variation due to material properties. The variation due to geometry is currently not a feature in the VecTor2 implementation. Thus the analysis results from VecTor2 can be analyzed statistically to determine the distribution parameters of a random variable Rn which includes material property variation. The actual resistance random variable is then calculated based on Equation 4.33.

$$R = \lambda_P R_{VT2} \tag{4.36}$$

where λ_P represents a random variable for the model error in VecTor2. The resistance and model random variables are assumed to be statistically independent, and thus the probability density function for R is calculated using Equation 4.34.

$$P[R] = P[\lambda_P]P[R_{VT2}] \tag{4.37}$$

The professional factor and the VecTor2 resistance model are assumed to be statistically independent. Thus the mean and the coefficient of variation of the final resistance model can be calculated using Equation 4.35, which is used by Nowak and Szerszen (2003).

$$\mu_R = \mu_P \cdot \mu_{R_{VT2}} \tag{4.38a}$$

$$V_R = \sqrt{{V_P}^2 + {V_{R_{VT2}}}^2} \tag{4.35b}$$

The final resistance model *R* can be used in a reliability study based on simulation results generated by VecTor2. The generalization of R to include the DSFM professional factor will ensure that simulation results are more representative of reality. The implemented stochastic sampling routines now allow for a variety of stochastic simulations techniques that are useful in determining the reliability of reinforced concrete structural elements. This software is particularly useful for the American code, where each member has a capacity reduction factor, and these factors are determined through stochastic simulation (Nowak and Szerszen, 2003b). The ability to capture nonlinear shear behaviour of reinforced concrete from a reliability framework may help future code calibrations, and provide a tool for engineers who need to ensure a level of reliability for an atypical structural element. It is noted that the professional factor for each type of structure modelled with VecTor2 will differ. The reader is referred to Section 5.3 for more information on the professional factors.

4.7 Post-processing of Stochastic Simulation Results

Stochastic simulations can produce large volumes of data. For example, an analysis with 300 simulations, each with 75 load stages, generates a total of approximately 22800 output files. Typically, these output files are read by post-processors Janus (Chak, 2014) or Augustus (Bentz, 2000). When the number of simulations becomes large, manually post-processing the data, even with the help of the post-processors is a tedious task. As a result, several post-processing techniques are employed and discussed in this section.

There are several analysis result parameters that are useful for the post-processing of stochastic simulation, the most basic of which are the sampled material modification factors. These data are written into files for each trial named “TRIAL_X.C2E” where the X represents the trial number. They contain all of the stochastic modification factors for concrete and steel.

Two post-processors were developed in MATLAB for use with the stochastic simulations in this thesis. The first is a visualization post-processor GUI that can view the model input parameters, and visualize the stochastic modification factors to material properties. This is particularly useful when spatially variable material properties are used in a stochastic analysis. The user can load the analysis job results, and a visualization of the mesh with the stochastic modification factors can be loaded. Fig. 4.24. shows the layout of the post-processor and an example of a loaded mesh with spatially variable properties.

In addition to displaying the stochastic properties, material properties, and material types, the post-processor is also capable of plotting the crack pattern for a given trial and selected load stage. Fig.4.25 shows an example of a crack pattern with the spatial variation. In the second part of the figure, the mesh is removed from the main specimen for a clearer visualization of the crack pattern.

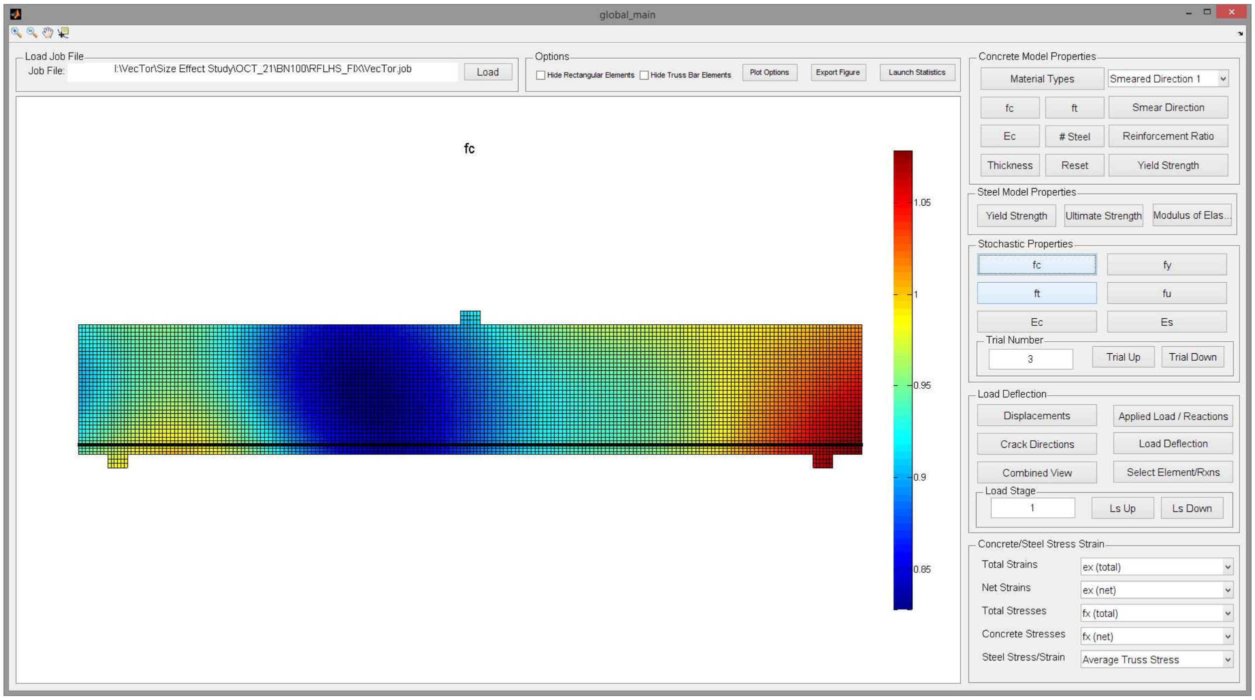

Job File: I:\VecTor\Size Effect Study\OCT_21\BN100\RFLHS_FIX\VecTor.job

Smeared Direction 1

Trial Number: 3

Load Stage: 1

Total Strains: ex (total)

Net Strains: ex (net)

Total Stresses: fx (total)

Concrete Stresses: fx (net)

Steel Stress/Strain: Average Truss Stress

Fig. 4.24: Stochastic post-processor.

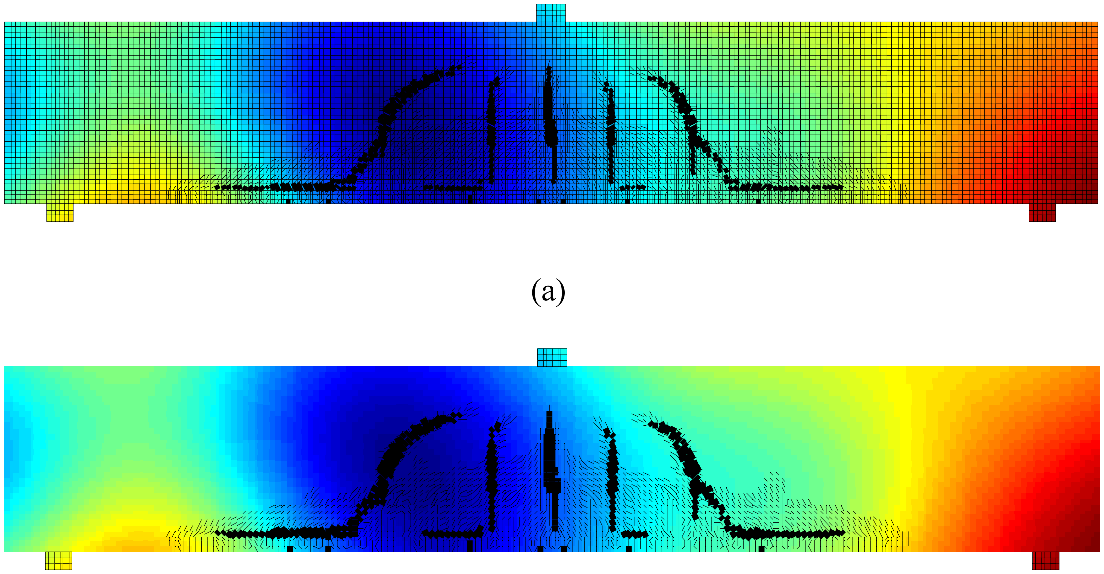

(a)

(b)

Fig. 4.25: High quality visualization of stochastic material properties and analytical crack patterns: (a) With mesh (b) With mesh removed.

The second post-processor is not intended for visualization, but rather for data retrieval. Similar to the first-post processor, the second retrieves and analyzes each simulation load-deflection curve and determines the point of failure. This program is highly specialized for monotonic load-deflection curves that exhibit shear failure or flexural rupture. There are two main challenges to overcome when determining the failure point. The first is that a shear failure in the current formulation may not be accompanied by a complete loss of load bearing capacity. The nature of the finite element models for a deflection controlled analysis often allows them to continue the load-deflection response after the main shear failure has occurred. Fig. 4.26 is an example of such a phenomenon. The automated post-processor thus has to distinguish between the actual failure and the absolute maximum. This is accomplished by enforcing three criteria: the ultimate load is greater than cracking load; after the ultimate load, there is a change from positive slope to negative slope; and the load drops more than 10 percent of the local maximum.

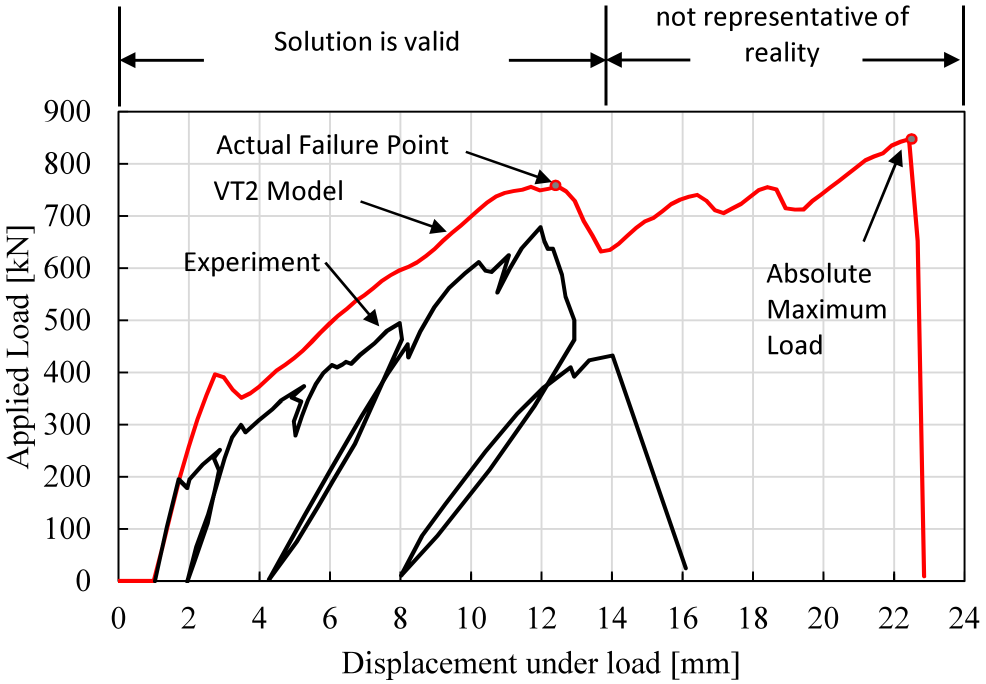

Fig. 4.26: Numerical error after failure in VecTor2 model.

Using these three criteria, the point where the data is discarded is established. The maximum is then taken as the maximum point in the remaining data. This method produces a reasonable estimation of the ultimate load for unreinforced concrete shear failure. Although it has not been thoroughly tested, this method should work for a generalized load-deflection curve that may be a shear or flexure failure, with or without ductility. In the case of a ductile failure that doesn't contain bar rupture, no data is discarded and thus the absolute maximum is used. One main limitation of this method is that it assumes that the structure has failed at some point in the analysis. If failure has not occurred, then this method will not identify it. As a result, manual inspection of the data is recommended to identify suspicious load-deflection curves requiring greater scrutiny.

CHAPTER 5: RELIABILITY OF SHEAR CRITICAL REINFORCED CONCRETE BEAMS WITH NO TRANSVERSE REINFORCEMENT

The following chapter presents a case study that highlights the potential applications of the implemented software pertaining to stochastic simulation. Stochastic simulation can be applied to a wide variety of structural problems including the development and validation of simplified design equations, the assessment of probabilistic deflection calculations, and the assessment of the reliability of structural elements. A series of deep beams with no transverse reinforcement are simulated and their reliability is discussed.

The size effect is a well-documented phenomenon that has been incorporated, along with various formulations of the Modified Compression Field Theory, into several design codes around the world (CSA A23.3, AASHTO, Eurocode 2). The size effect in most cases is an additional parameter that is applied to the shear strength that results in diminishing returns on the concrete contribution to shear stress when the depth of the beam increases. It is unclear how the size effect affects the computed reliability of the reinforced concrete beam elements. Additionally, the professional factor that VecTor2 exhibits for reinforced concrete structures with no transverse reinforcement has not been identified. The purpose of this study is to assess the reliability indices for North American building codes and also determine if the reliability of shear-critical beams with no shear reinforcement is independent of the size effect when modelled with VecTor2. The determined reliability indices are calculated for the CSA A23.3-14 code and the ACI 318-14 code and compared with target reliability indices. Four reinforced concrete beams were selected from literature for stochastic simulation. Each of the beams contain no transverse reinforcement and each of the beams possess similar longitudinal reinforcement ratios. A plot of the normalized shear stress versus actual deflection for each beam is plotted in Fig. 5.1.

The first two beams, BN50 and BN100, tested by Podgorniak-Stanik (1998) (and reported by Collins et al. 2008), had depths of 500 mm and 1000 mm respectively. The next beam, YB2000, tested by Yoshida (2000) (and reported by Collins et al. 2008), had a depth of 2000 mm. The last beam, PLS4000, was a slab strip tested by Quach (2016) (and reported by Collins et al. 2015) and had a depth of 4000 mm. Beams BN50, BN100, and YB2000 had a thickness of 300 mm. The slab strip PLS 4000 had a thickness of 250 mm. The properties of each beam are summarized in Table 5.1

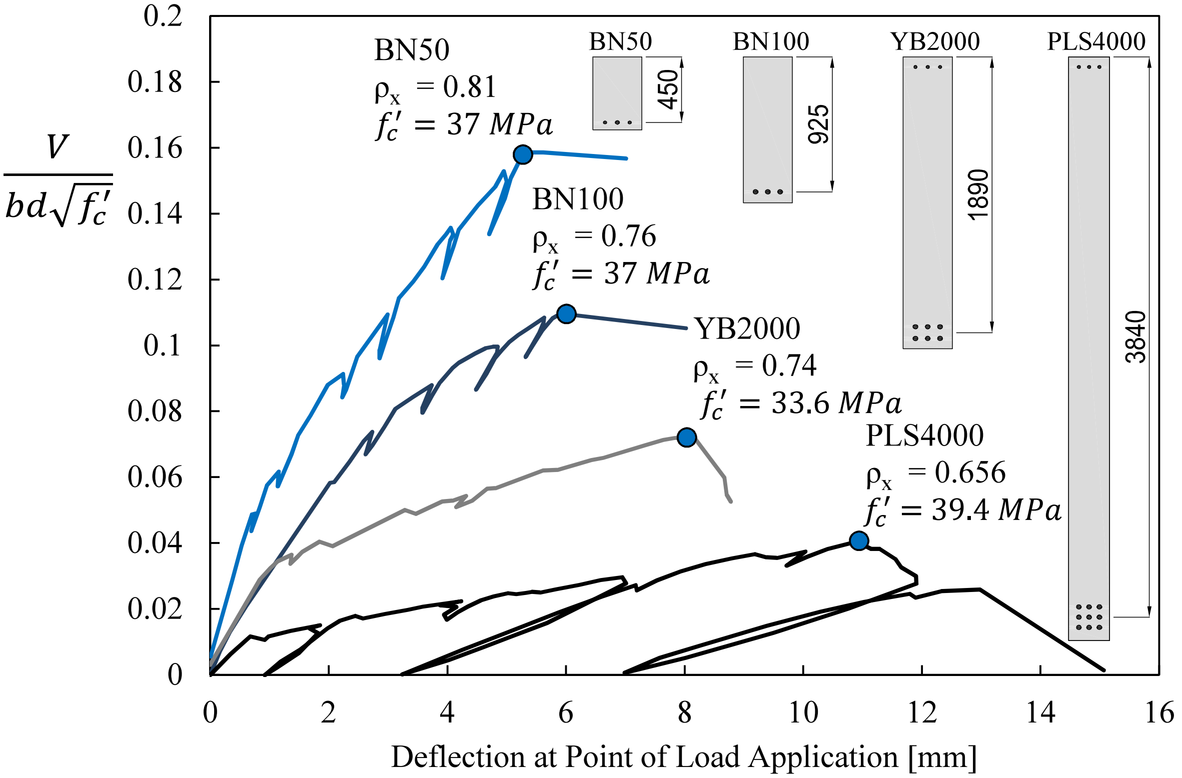

Fig. 5.1: Normalized shear stress for selected beams: BN50, BN100, YB2000, and PLS400.

Table 5.1: Properties of selected specimens.

Specimen	b [mm]	d [mm]	a/d	f_c' [MPa]	A_g [mm]	f_y [Mpa]	$\rho_{Long.}$ [%]
BN 50	300	450	3.00	37	10	483	0.81
BN 100	300	925	2.92	37	10	550	0.76
YB 2000	300	1890	2.86	33.6	10	447	0.74
PLS 4000	250	3840	3.13	39.4	14	573	0.656

All of the selected beams had similar compressive strengths, reinforcement ratios, span-to-depth ratios, and widths. The only main variability between specimens was the depth and the yield strength of the longitudinal reinforcement. However, all of the specimens were shear-critical and did not yield the longitudinal reinforcement. Thus it can be concluded that the only significant difference between the selected specimens was the depth.

Each of the beams was tested to failure and failed via a diagonal shear crack. A scaled comparison of the crack patterns is shown in Fig. 5.2.

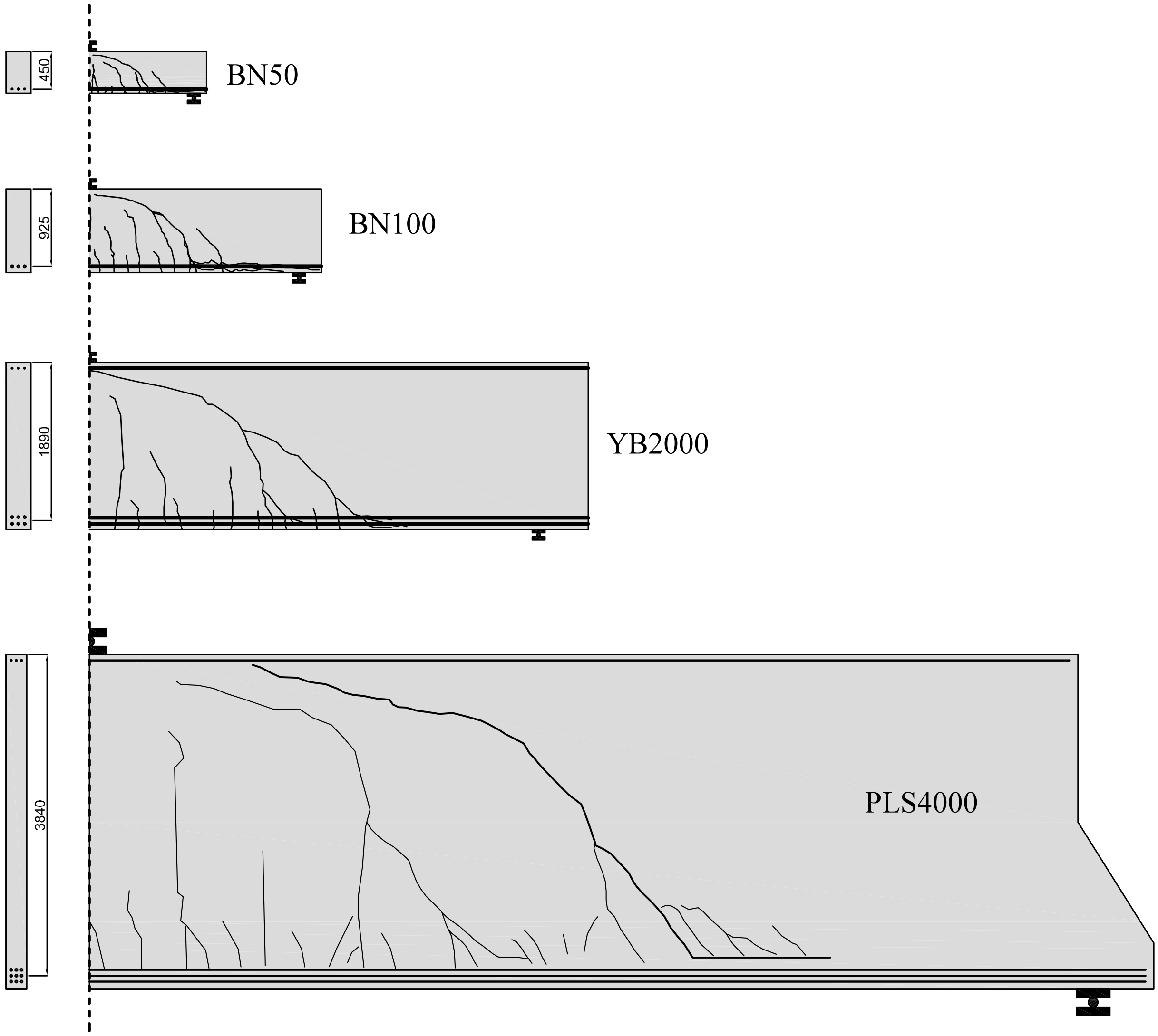

Fig. 5.2: Comparison of crack patterns for selected specimens.

The following sections describe the experimental response, the deterministic finite element modelling, the results of the stochastic simulation, and the reliability analysis.

5.1 Deterministic Finite Element Models

This section compares the experimental behaviour of each of the selected beams with the associated finite element models. The load-deflection response for each of the experiments, the crack pattern, and failure mode are discussed. The important parameters in the finite element model are presented and discussed.

For all models, the predicted load-deflection response is sensitive to the assumed maximum crack spacing. As a result, a consistent estimation of the maximum crack spacing based on the CIB-FIB code was used. In the case of beams with no transverse reinforcement, the maximum crack spacing predicted by Equation 5.1 was assumed to govern both directions (Collins and Mitchell, 1997).

$$s_{mx} = 2\left(c_x + \frac{s_x}{10}\right) + 0.25k_1\frac{d_{bx}}{\rho_x} \tag{5.1}$$

c_x is the distance between the top of the reinforcement and the mid-height of the shear area, s_x is the horizontal spacing of the longitudinal reinforcement, d_{bx} is the diameter of the longitudinal reinforcing bars, and ρ_x is the longitudinal reinforcement ratio. The parameter k_1 is taken as 0.4 for deformed reinforcing bars.

5.1.1 BN50

Specimen BN50 represents the smallest specimen in the series and is generally not considered to have a large depth. BN50 had a depth of 500 mm, and a span of 1450 mm. A finite element mesh with a total of 20 elements through the thickness and an average element size of approximately 25 mm by 25 mm was used. A plot of the finite element mesh is shown in Fig. 5.3. The steel bearing plates for the applied load was modelled by one layer of steel plate material and one layer of bearing material. The longitudinal reinforcing steel was modelled using truss elements. A maximum crack spacing of 693 mm was determined using Equation 5.1. The material properties of the finite element model for BN50 are summarized in Table 5.2.

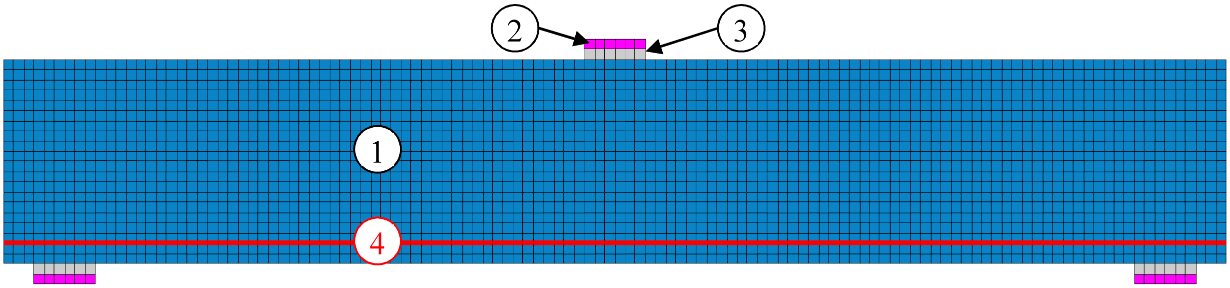

Fig. 5.3: Finite element mesh for BN50.

Table 5.2: Material properties for BN50 finite element model.

Color /Material	Mat. #	f'_c or f_y [MPa]	E_c or E_s [MPa]	ε'_c or ε_{sh} $x10^{-3}$	f'_t or f_u [MPa]	t or A_s [mm/mm^2]	Description
Concrete	1	37	27095	2.08	2.01	300	Concrete
Steel	2	500	200000	5.00	600	300	Bearing Plate Steel
Bearing	3	N/A	28772	N/A	N/A	300	Bearing Material
Steel	4	483	200000	14.00	667	1100	Bottom Bars

The BN50 specimen was tested at the University of Toronto by Podgorniak-Stanik (1998) as part of a series of tests to determine the influence of skin reinforcement on the shear strength of reinforced concrete members. Specimen BN50 exhibited a bilinear response and a brittle failure at an ultimate load of 261 kN and a deflection of 5.6 mm. The failure was the result of a large shear crack opening up in the specimen. The crack pattern at failure is depicted in Fig. 5.4.

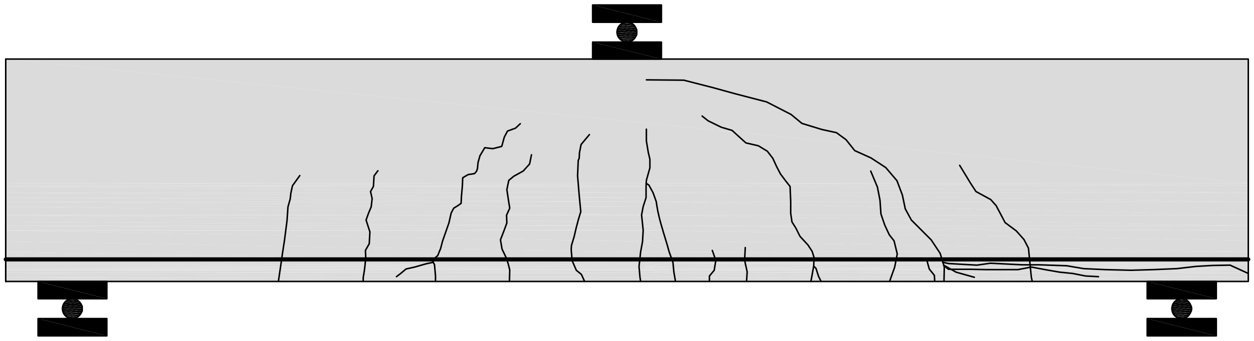

Fig 5.4: Experimental crack pattern of specimen BN50 at failure.

The finite element model was able to capture the experimental response of the specimen reasonably accurately. The predicted ultimate load and displacement were 266 kN and 4.8 mm respectively. A plot of the experimental load-deflection response and the finite element prediction is shown in Fig. 5.5. The finite element model tends to overestimate the pre-cracked stiffness of the response but produces a reasonable estimate for the post-cracked stiffness of the experimental response. The model was calibrated to reduce the tension stiffening effect from the bars by artificially decreasing the effective bar diameter. This was done because current implementation of the tension stiffening effect. For discrete bars, the tension stiffening effect is modelled as a uniform tension stiffening response that influences concrete 7.5 bar diameters away from the bar. In the case of BN50, the there are two 20M bars and one 25M bar. So assuming that the 20M bars govern the tension stiffening, 7.5 bar diameters away is a distance of 150 mm. With the truss bars sitting at 50 mm up from the bottom, the total height from the bottom of tension stiffening concrete is 200 mm. This means that 40 percent of the beam is tension stiffened. For the type of shear failure observed, tension softening tends to govern the failure and the experimental response. Thus artificially reducing the bar diameter results in a better prediction of the load-deformation response. The influence of this calibration should be investigated further. However, the current calibration for the reduction in bar diameter is considered acceptable.

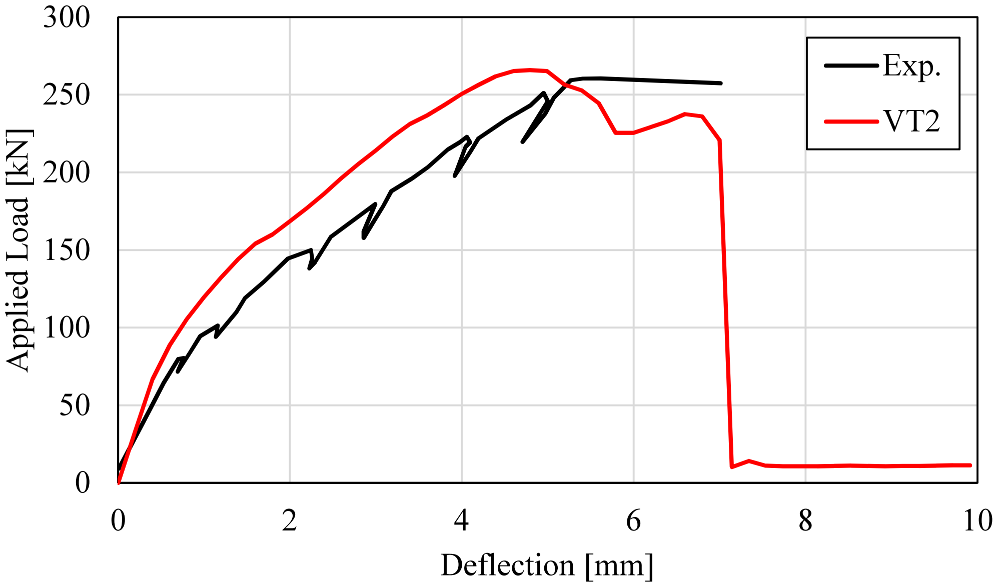

Fig. 5.5: BN50 experimental (black) vs. finite element (red) load-deflection response.

5.1.2 BN 100

Specimen BN100 represents the second of the beams with no transverse or skin reinforcement in the series tested by Podgorniak-Stanik (1998). A finite element mesh of 7194 elements was constructed. A plot of the finite element mesh is shown in Fig. 5.6. A total of 21 elements were used through the depth of the beam with an average element size of approximately 50 mm by 50 mm. The bearing plates were modelled with a combination of steel and bearing material. The reinforcing steel was modelled with discrete truss bars. A maximum crack spacing of 1226 mm was determined using Equation 5.1. Table 5.3 outlines the details of the finite element model.

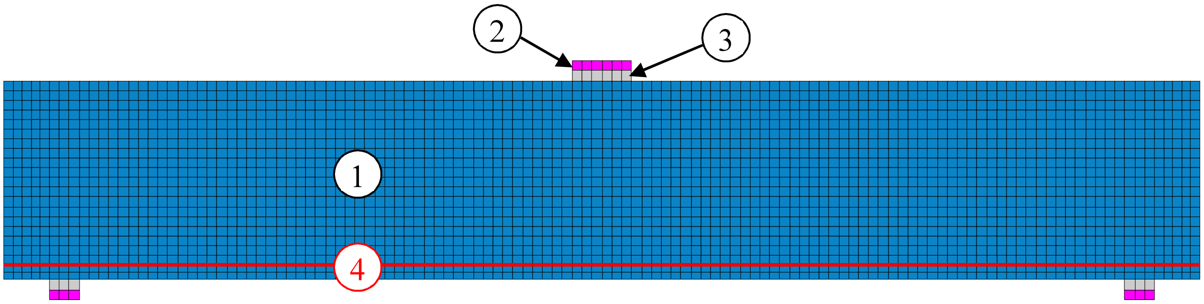

Fig. 5.6: Finite element mesh for BN100.

Table 5.3: Material properties for BN100 finite element model.

Color /Material	Mat. #	f'_c or f_y [MPa]	E_c or E_s [MPa]	ε'_c or ε_{sh} $x10^{-3}$	f'_t or f_u [MPa]	t or A_s [mm/mm^2]	Description
Concrete	1	37	27095	2.08	2.01	300	Concrete
Steel	2	500	200000	5.00	600	300	Bearing Plate Steel
Bearing	3	N/A	28772	N/A	N/A	300	Bearing Material
Steel	4	550	200000	15.00	825	2100	Bottom Bars

A large shear crack formed on the east span of the beam. The onset of failure occurred at a peak load of 370 kN and a peak deflection of 5.87 mm. The crack plot for BN100 is depicted in Fig. 5.7.

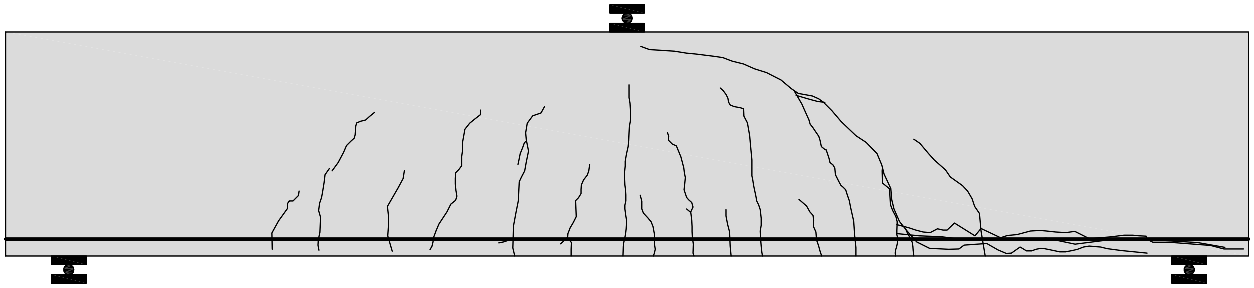

Fig. 5.7: BN100 crack pattern.

The finite element model predicted a peak load of 406 kN and a peak deflection of 5.98 mm. This was in reasonably good agreement with the experimental results. A comparison of the experimental and predicted load-deflection response is shown in Fig. 5.8. Note that the initial stiffness predicted by the finite element model is much stiffer than the experimental results. It is possible that the beam was pre-cracked due to accidental loading before testing or due to restrained shrinkage. However, because the peak response is modelled reasonably well, and the initial stiffness of the other three specimens was in good agreement with the experimental results, this discrepancy is not considered important to this study.

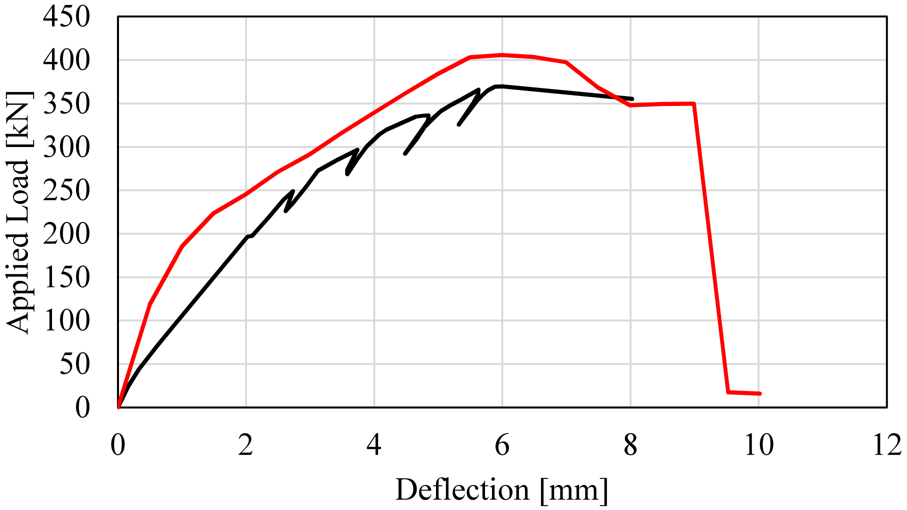

Fig. 5.8: BN100 experimental (black) vs finite element (red) load-deflection curves.

5.1.3 YB2000

Specimen YB2000 was tested by Yoshida (2000) as part of a series of deep beam tests with varying amount of transverse reinforcement. The specimen is reported in the literature as YB2000/0 however because the other specimens are not being considered in this study, the designation has been shortened to YB2000 for the purpose of this thesis. Note that the east span of the specimen is in fact YB2000/0 and the west span is YB2000/9. The specimen was modelled as tested, and thus the finite element model incorporates both YB2000/0 and YB2000/9. However, the results in this study refer strictly to the YB2000/0 results. The finite element mesh is shown in Fig. 5.9. A maximum crack spacing, determined using Equation 5.1, was calculated to be 2181 mm. The material properties for the model are shown in Table 5.4

The beam failed via a diagonal shear crack on the east span. This mode of failure was forced by the experimental setup as the west span contained strengthening reinforcement. The failure occurred at an applied load of 461 kN and a deflection of 8.0 mm. The crack pattern is shown in Fig. 5.10.

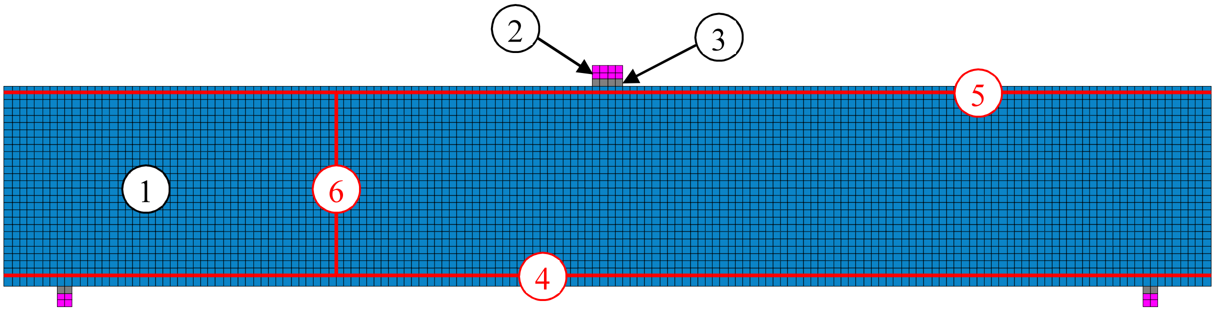

Fig. 5.9: Finite element mesh for YB2000

Table 5.4: Material properties for YB2000 finite element model.

Color /Material	Mat. #	f'_c or f_y [MPa]	E_c or E_s [MPa]	ε'_c or ε_{sh} $\times 10^{-3}$	f'_t or f_u [MPa]	t or A_s [mm/mm^2]	Description
Concrete	1	31.8	25622	2.04	1.86	300	Concrete
Steel	2	500	200000	5.00	600	300	Bearing Plate Steel
Bearing	3	N/A	28772	N/A	N/A	300	Bearing Material
Steel	4	447	200000	14.80	610	4200	Bottom Bars
Steel	5	433	200000	14.10	638	900	Top Bars
Steel	6	470	200000	14.50	470	645	T-head shear reinf.

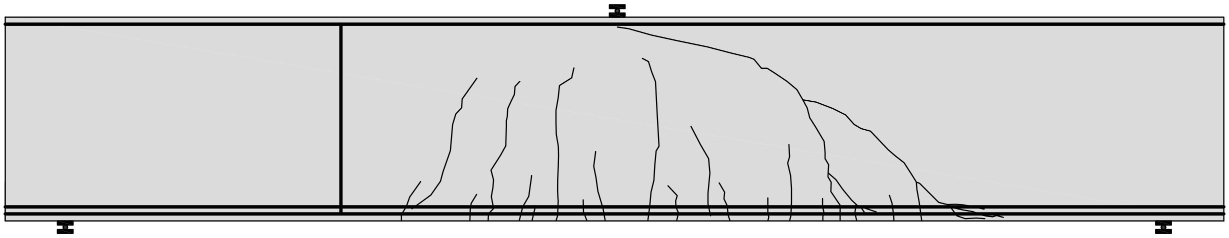

Fig. 5.10: YB2000 experimental crack pattern.

The finite element model was able to produce a reasonable prediction for the initial stiffness, and cracking load of the YB2000 specimen. However, the post-crack stiffness, ultimate load, and deflection at ultimate were overestimated. The finite element model predicted a failure load of 562 kN with a deflection of 8.79 mm. A comparison of the finite element and experimental load-deflection curves are presented in Fig. 5.11. Although the finite element prediction overestimates the experimental response by approximately 22%, it was considered reasonable enough to continue with stochastic simulation.

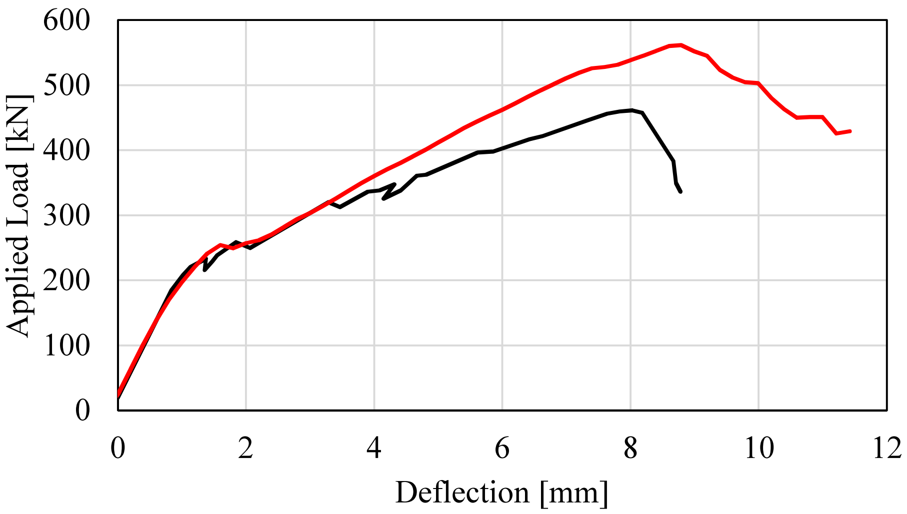

Fig. 5.11: YB2000 experimental (black) vs finite element (red) load-deflection curves.

5.1.4 PLS4000

The specimen PLS4000 was recently tested at the University of Toronto by Quach (2016). This large deep beam specimen was meant to represent a slice of a deep slab foundation. Such structural elements are being used in the designs of hydro dam structures or as mat foundations for high-rise structures. The specimen and the finite element model are extensively described in Chapter 3. The mesh used for simulation is shown in Fig.5.12. A maximum crack spacing of 4035 mm was selected based on Equation 5.1. A summary table of the material properties is shown in Table 5.5.

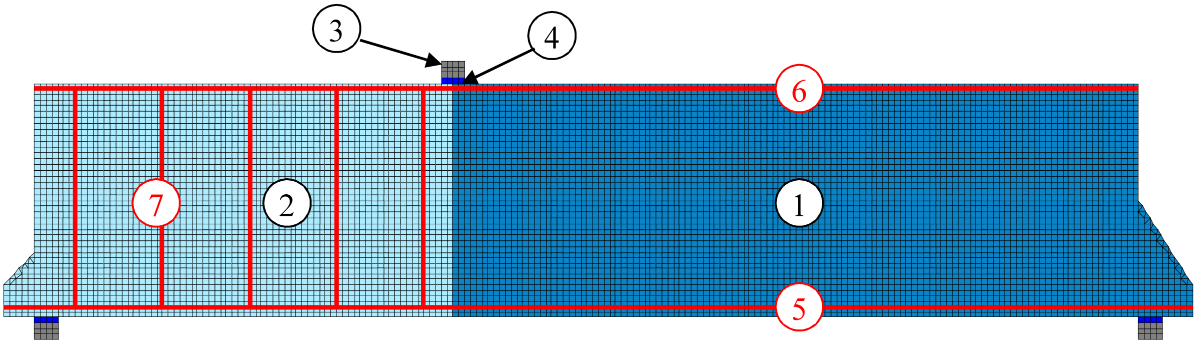

Fig. 5.12: PLS4000 finite element mesh.

Similar to specimen YB2000, this test was designed to have two shear failure tests in one specimen. The west span contained 20M T-headed shear reinforcement spaced at 1500 mm. The east span contained no transverse reinforcement and is thus the subject of this study.

Table 5.5: Material properties for PLS4000 finite element model.

Color /Material	Mat. #	f'_c or f_y [MPa]	E_c or E_s [MPa]	ε'_c or ε_{sh} $x10^{-3}$	f'_t or f_u [MPa]	t or A_s [mm/mm^2]	Description
Concrete	1	40	27898	2.09	2.09	250	Concrete (east span)
Concrete	2	40	27898	2.09	2.09	250	Concrete (west span)
Steel	3	500	200000	5.00	600	250	Bearing Plate Steel
Bearing	4	N/A	28772	N/A	N/A	250	Bearing Material
Steel	5	573	200000	14.00	675	6300	Bottom Bars
Steel	6	522	200000	17.00	585	900	Top Bars
Steel	7	522	200000	17.00	585	300	T-head shear reinf.

The experimental crack pattern for the failure of the east span is shown in Fig. 5.13. The specimen failed after two large shear cracks developed. The peak load was 685 kN with a peak deflection of 12 mm. The eastern-most shear crack was the failure crack.

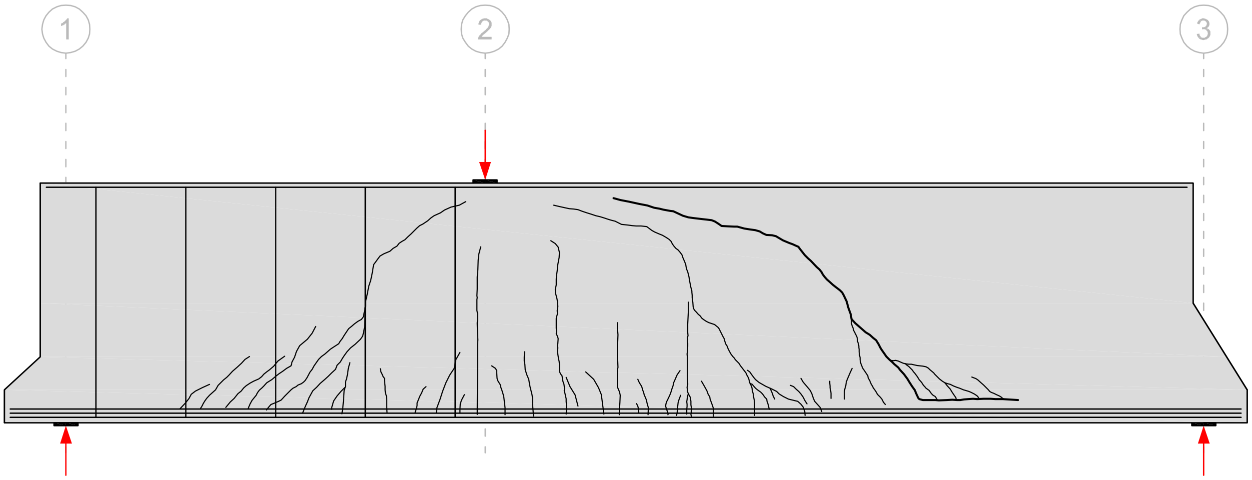

Fig. 5.13: PLS4000 experimental crack pattern.

The finite element analysis load-deflection was submitted as a blind prediction in the prediction competition. It predicted a peak load of 761 kN and a deflection at peak load of 12.2 mm. A comparison of the experimental and finite element load-deflection curves is shown in Fig. 5.14.

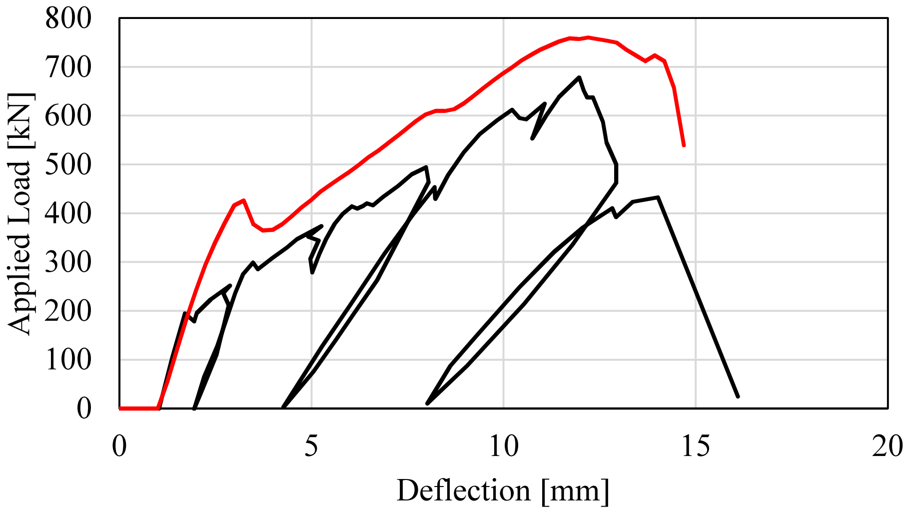

Fig. 5.14: PLS4000 experimental (black) vs finite element (red) load-deflection curves.

All four deterministic finite element models were reasonably successful in predicting the experiments, given the high degree of scatter obtained from various other modelling procedures and software for such elements. Failure modes, peak load, and deflection at peak load were all predicted with reasonable accuracy. Continuing challenges include the prediction of cracked stiffness, the cracking load, and the simulated crack pattern. A summary of the deterministic finite element models is presented in Table 5.6.

Table 5.6: Summary of deterministic finite element modelling.

Specimen	P_{Exp}	P_{VT2}	P_{Exp} / P_{VT2}
BN50	261	265.8	0.980
BN100	370	405.6	0.912
YB2000	461	561.6	0.821
PLS4000	685	760.5	0.900
		Average	0.903
		COV	0.072

5.2 North American Building Code Calculations

The stochastic simulation results are compared to the Canadian (CSA A23.3-14) and the American (ACI-318-14) building codes. This sections outlines the computation of the shear strength of reinforced concrete for the Canadian and American building codes.

The CSA A23.3-14 code calculation required the applied moment and applied shear force to be known. Collins et al. (2015) note that the ratio between moment and the product of the shear times the shear depth can be taken as 2.10 for the Toronto size effect series. The CSA code calculation requires iteration based on the assumed applied shear and moment. If the maximum shear is unknown, a guess is supplied and the moment acting on the section is calculated using the specified ratio. The procedure for determining the shear strength of a member using the CSA A23.3 general method is summarized in Fig. 5.15.

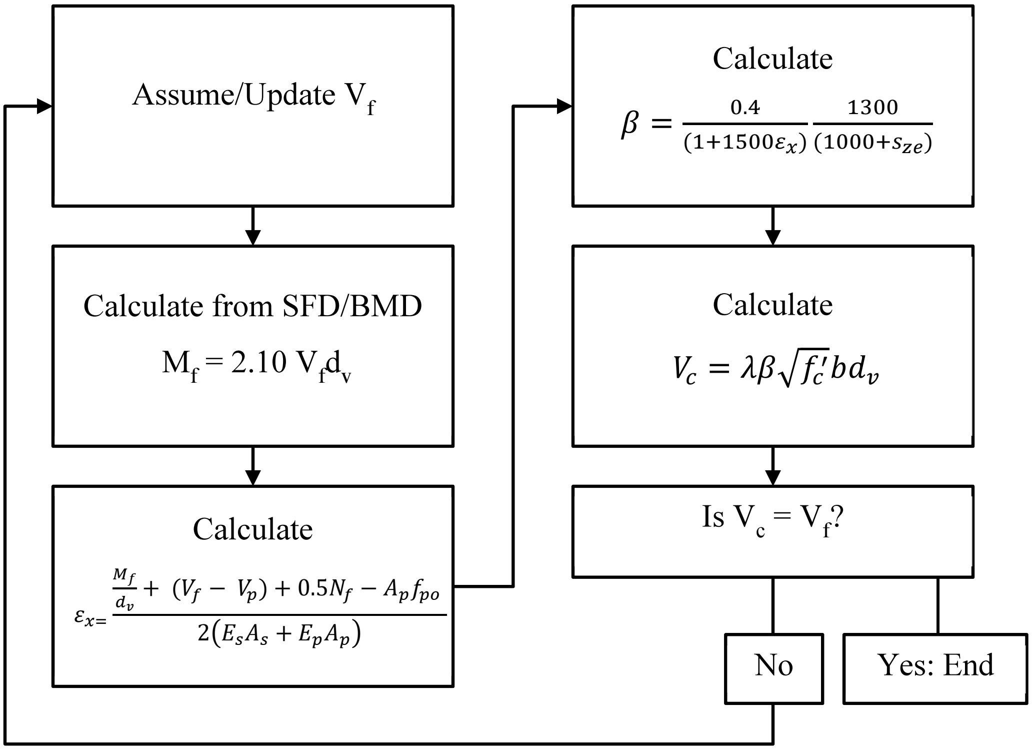

Fig. 5.15: CSA A23.3 General Method for the shear strength of reinforced concrete.

In addition to the Canadian code calculation, the strength of the section for each test specimen was assessed using ACI 318-14. Unlike the Canadian code, the ACI take a simplified approach assuming a constant shear stress. The shear stress is calculated using Equation 5.2 or Equation 5.3.

$$V_c = 2\sqrt{f_c'}b_w d \quad [lbf] \tag{5.2a}$$

$$V_c = 0.167\sqrt{f_c'}b_w d \quad [kN] \tag{5.2b}$$

$$V_c = \left(2\sqrt{f_c'} + 2500\rho_x \frac{Vd}{M}\right) b_w d \quad [lbf] \tag{5.3a}$$

$$V_c = \left(0.167 + 8.174\,\rho_x \frac{Vd}{M\sqrt{f_c'}}\right)\sqrt{f_c'}b_w d \quad [kN] \tag{5.3b}$$

Equation 5.2 (ACI Eq. 11-3) is the basic equation for the concrete contribution to the shear strength of a reinforced concrete section. Equation 5.3 (ACI Eq. 11-5) is a slightly more complicated equation that accounts for the influence of combined moment and shear on the shear strength of a flexural element. A plot of the respective code predictions is shown in Fig. 5.16. In the case of this plot, the shear is generalized into a metre width section. Each of the experimental results for the selected specimens is plotted on the figure. These results were determined as the summation between the applied shear, and the shear due to the self-weight of the specimen. The calculated experimental shear force is shown in Table 5.7.

Table 5.7: Summary of experimental shear calculations.

Specimen	d [mm]	P_{EXP} [kN]	V_{EXP} [kN]	V_{DEAD} [kN]	V/m [kN/m]
BN50	450	260.5	130.3	3.4	445.5
BN100	925	369.8	184.9	13.5	661.2
YB2000	1890	461.2	230.6	24.4	850.0
PLS4000	3840	678.8	250.1	101.1	1404.6

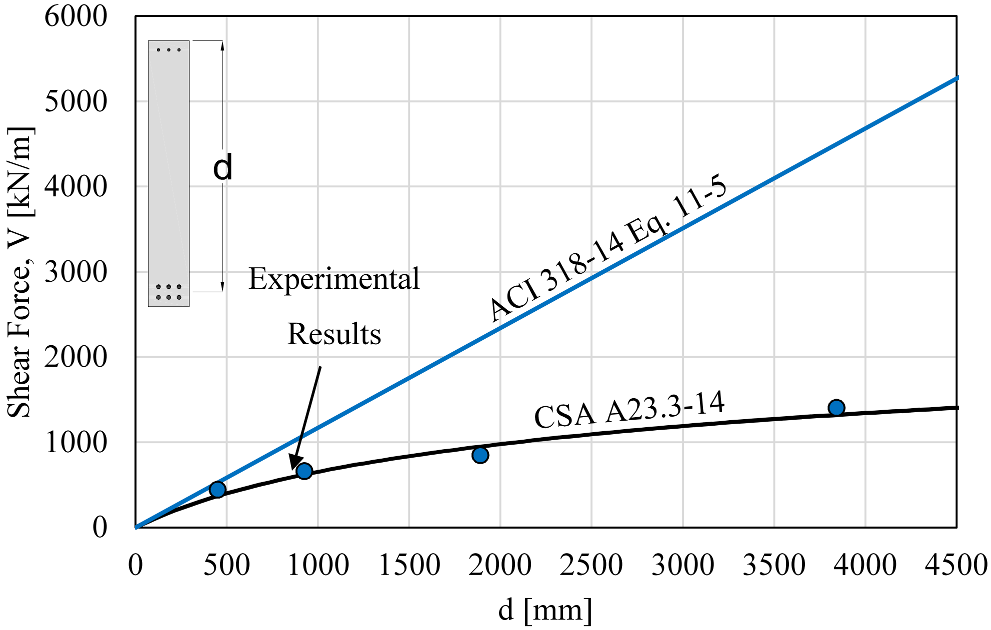

Fig. 5.16: Code Calculations comparing the selected specimens, the ACI-318-14 code and the CSA A23.3-14 code.

5.3 VecTor2 Professional Factor for Shear Critical Beams with No Transverse Reinforcement

Since the creation of the original limit state design method in the late 1970s and early 1980s there has always been an understanding that despite the best efforts of structural engineers, the simulation of structural behaviour will always be an approximation to reality. Thus it is important to quantify and understand how analysis tools used for reliability analysis are representative of reality. In a stochastic simulation, the ideal model provides an exact replication of real behaviour if the input information is perfectly correct. However, most analysis tools are never perfect and all rely on simplifying assumptions that create uncertainty in the model results. The definition of a professional factor in this study is an additional random variable that captures the uncertainty derived from modelling, even with perfect information. This model is incorporated into the material resistance model as a product between the VecTor2 specific professional factor, the fabrication factor, and the VecTor2 predicted resistance model. This is reflected in Equation 5.4.

$$R = R_n \times M \times P \times F \tag{5.4a}$$

$$R = R_{VT2} \times P \times F \qquad (5.4b)$$

VecTor2 is a generalized finite element program and, as such, it will model different structures with varying degrees of accuracy. For example, consider the statistics published by Vecchio et al. (2001). The bias factor for beams, shear walls, and panels were reported as 1.000, 1.011, and 1.022 respectively. Similarly, the coefficient of variation for those elements were reported as 5.3%, 20.3%, and 9.6% respectively. Thus although all three examples show a bias factor of approximately 1.0, the coefficient of variation due to model uncertainty varies significantly depending on which structural element is selected for modelling. These reported numbers are calculated as P_{VT2} / P_{Exp}. However, for the purpose of this study, the inverse ratio is required.

In the current study, shear-critical beams with no transverse reinforcement are being modelled. In order to assess the professional factor for VecTor2 shear-critical beams, a large number of beams must be modelled. The database published by Reineck et al. (2013) contains a total of 744 shear critical beams that were tested under a one-point or two-point bending test; all with span to depth ratios greater than 2.41. The total of 744 was reduced to a subset of 680 by removing all the T-beams. Although it is easy to model T-beams in VecTor2, it was decided that using rectangular beams was sufficient. Additionally, this eliminates any possible out of plane (3D) influence on planar (2D) results. The set of beams was additionally refined by removing all beams without sufficient or reliable information. This means that if any reported test did not include the parameters required to model it, it was removed from the list of selected beams. Note that 64 of the selected beams do not contain information on their aggregate size, but contained otherwise sufficient information. This resulted in a set of 371 beams that fell into two groups, each with a subgroup. The beams were classified as Type A if the beams were a one-point bending test, and Type B if the beams were a two-point bending test. A second designation was given to beams with or without compression reinforcement; the designations of 1 and 2 were added to the initial designation. For example, a Type A1 beam is a one-point bending test with no compression steel. Similarly, a Type B2 beam is a two-point bending test with compression steel. A schematic of the two beam types is shown in Fig. 5.17.

In Fig. 5.17, there are eight parameters that are used for the generation of the structure files. The most common parameters are *h*, *d*, *d'*, *L*, and *c* which denote the height, distance to bottom reinforcement, distance to top reinforcement, length of beam, and length of constant moment zone respectively. Additionally, there are three parameters which reference the bearing plate information: *ba*, *aa*, and *af*, which denote the distance between the edge of the beam and centerline of the reaction bearing plate, width of reaction bearing plate, and width of loading plate (half the width of loading plate for Type A and full width of loading plate for Type B) respectively.

This final group of 371 beams was selected to be modelled with VecTor2. The selected beams, compared with the original subset, are shown in Fig. 5.18. From the figure it can be seen that the selected specimens are fairly representative of the complete data set.

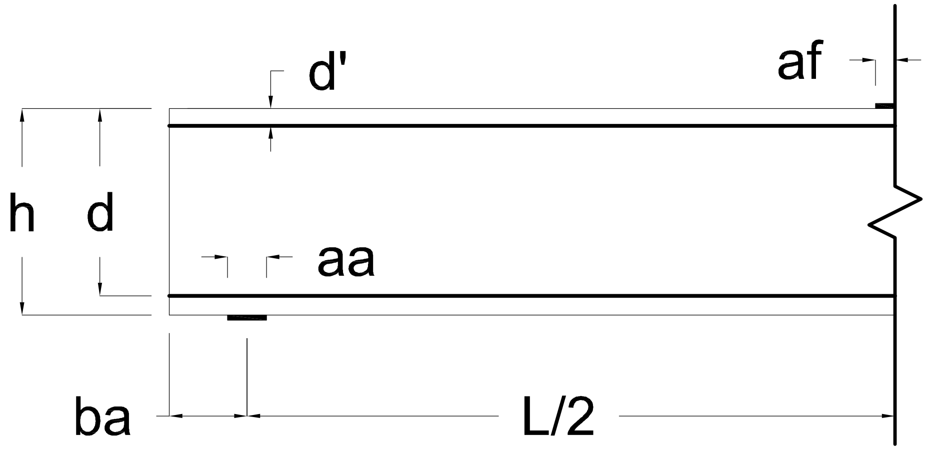

(a)

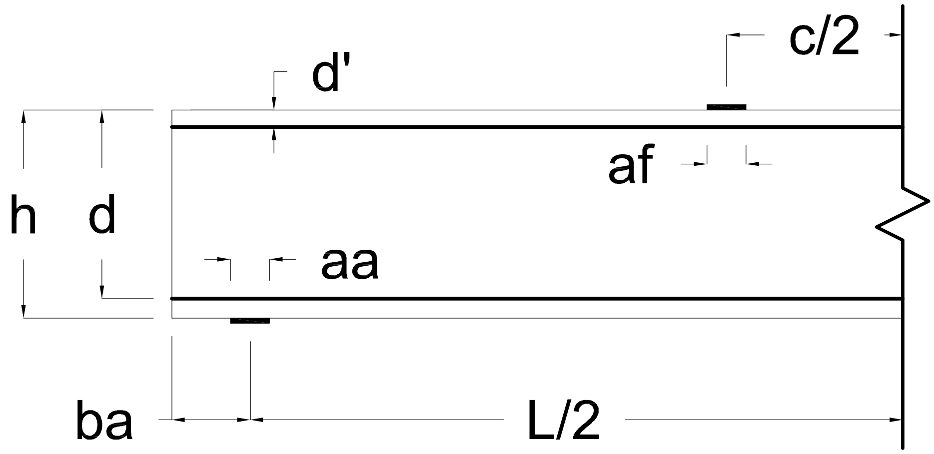

(b)

Fig. 5.17: Basic schematics for mesh generation. (a) Type A beam, (b) Type B beam.

For the analysis of the selected data, a few simplifying assumptions were made; the first was that the bottom steel reinforcement could be modelled as a single layer of reinforcement with a centerline equal to the centroid of the reinforcement. Each beam was assumed to be perfectly symmetric and thus only half of the beam was modelled around the plane of symmetry. The maximum crack spacing for each beam was assumed to be equal in both directions, and governed by Equation 5.1, which was reported by Collins and Mitchell (1997).

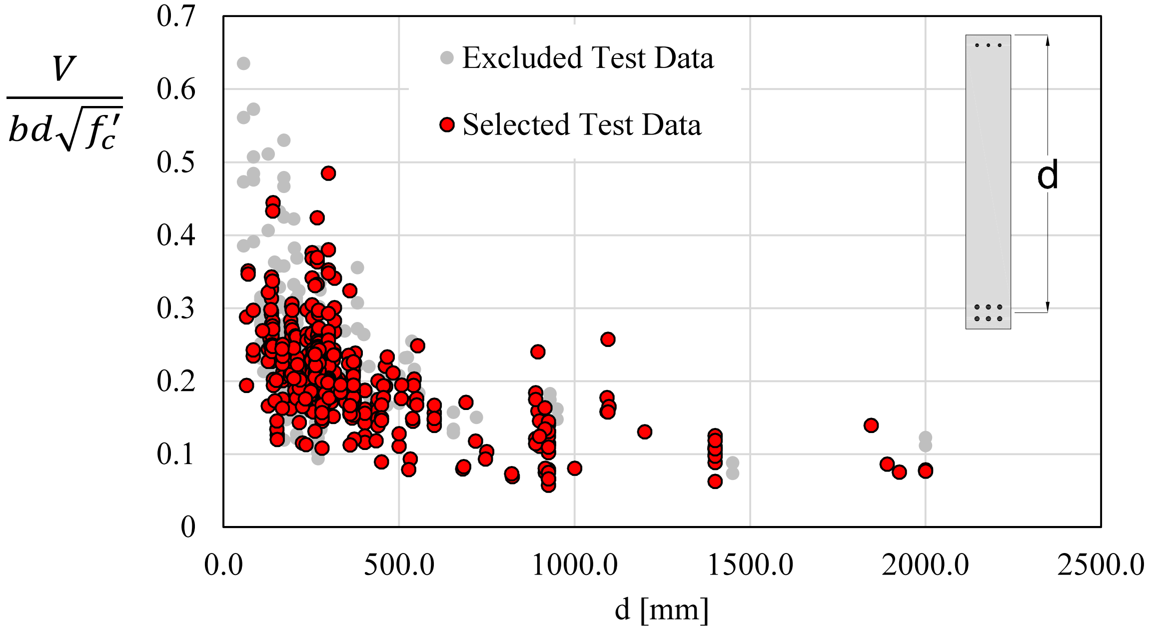

Fig. 5.18: Selected test results versus rejected test results.

Lastly it was assumed that the reinforcement is perfectly bonded to the concrete; no slip between the concrete and the steel is assumed. This last assumption is considered to be reasonable because only shear tests with deformed reinforcing bars were selected, thus reducing the likelihood that a test is critical to the bond of the reinforcement.

VecTor2 requires material properties, node list, incidence list, support conditions, and loading conditions in order to properly model the structural response of the beams. Thus for each beam, a unique structure file and two load case files were required to properly define the finite element model for the beam. A pre-processor, Formworks+, has been extensively developed at the University of Toronto to create user-friendly generation of structure and load case files. However, manual input into Formworks+ would constitute a significant cost in resources and time. To avoid such an issue, an automated pre-processor was developed that read the input information for each beam and generated the structure file and the load case files required for analysis.

Beam YB2000 is included in the database and is modelled as part of the reliability study. Thus the automated structure and load case file generator can be compared against a mesh created manually. The generated mesh is shown in Fig. 5.19.

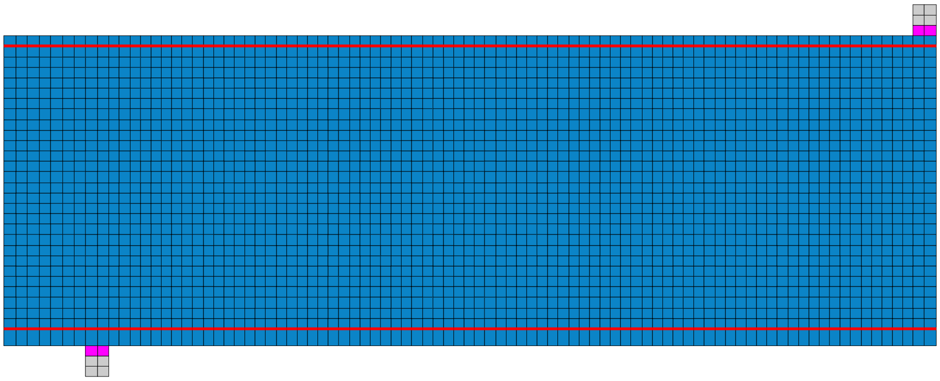

Fig. 5.19: Automatically generated finite element mesh.

The automatically generated mesh contained vertical rollers along the right edge and a horizontal roller at the left support. A unit displacement was applied in the vertical direction along the right edge. Additionally, gravity loading was applied to each concrete element. A comparison of the predicted responses is shown in Fig. 5.20.

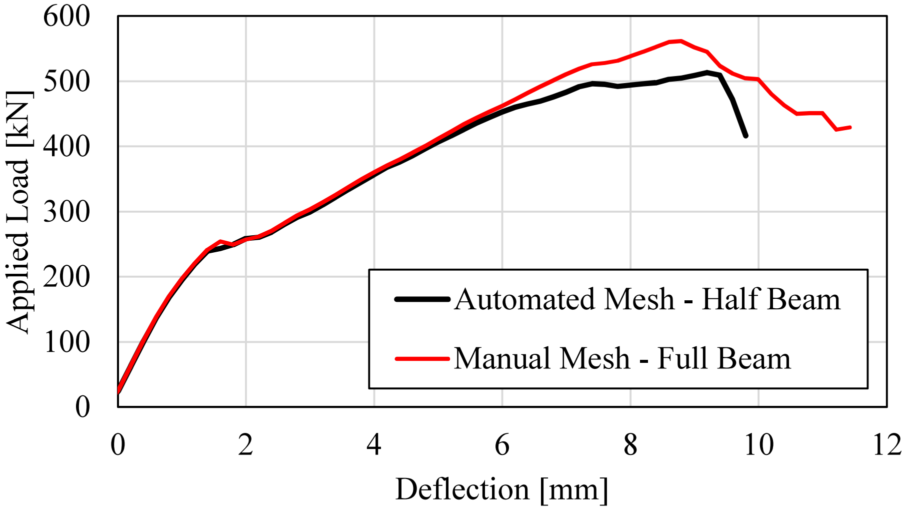

Fig. 5.20: Comparison of automated mesh with manual mesh for YB2000.

Both meshes contained similar mesh sizes (the automated mesh had 29 elements through the thickness and the manual mesh had 27 elements through the thickness) and identical bearing plate and material properties. However, the manual finite element model contained the actual reinforcement configuration for the YB2000 specimen. Thus the manual model is not perfectly symmetric. The load-deflection response for the automated mesh and the manually made mesh are identical until approximately 80% of the peak load. VecTor2 relies on a maximum crack width equation that reduces the stiffness of elements parallel to the crack direction once the crack width becomes too large. This simulates the loss of aggregate interlock that permits the transfer of shear stress across a crack. The difference in the load-deflection responses around the point of failure could be attributed to the mesh asymmetry; which forces the failure for the manual mesh to one side and thus the crack width check to one side. The models redistributed their stress to adjacent elements in different ways, resulting in a deviation in the load-deflection response. Thus the failure was not exactly the same between the half-model and the full model.

Even with the automated model generation, a method to run the VecTor2 executable for each of the analysis was required. A script was developed that runs each of the executables thereby additionally increasing the automation. Finally, a post-processor was developed to obtain the results.

The automated process was not without errors; of the selected 371 beams, 53 of the automatically generated meshes produced errors when running. Thus these 53 models were excluded from the reported results. This was considered acceptable as the sample size of 318 is considered sufficient to estimate the professional factor. The normalized shear stress for the experimental results and the simulation results are calculated for each specimen. Equation 5.5 is used to calculate the normalized shear stress.

$$\tau_{Normalized} = \frac{V}{bd\sqrt{f_c'}} \tag{5.5}$$

A plot showing the normalized shear stress for the experimental data versus the simulated data is shown in Fig. 5.21. It can be seen from the plot that there is significant scatter in the prediction of the shear strength using VecTor2. The data do appear to capture the behaviour of all of the beams reasonably well. Additionally, the majority of the tests fall on under the equal ratio and thus are conservative predictions of the shears strength.

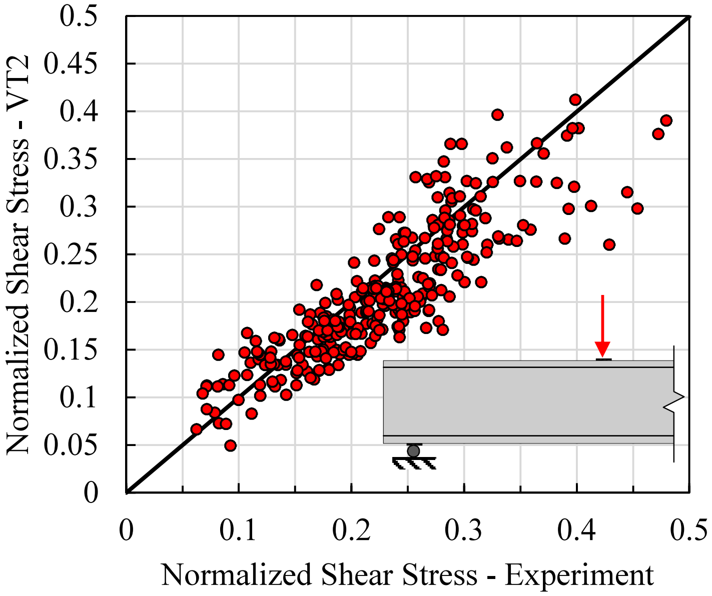

Fig. 5.21: Comparison of experimental and theoretical normalized shears stresses.

The professional factor is modelled as a random variable that is equal to the ratio between the experimental and predicted peak load. It is calculated using Equation 5.6.

$$P = \frac{V_{Exp}}{V_{VT2}} \tag{5.6}$$

This ratio was calculated for each simulation and analyzed as a set of data. The calculated professional ratios were found to be normally distributed with a mean of 1.106 and a coefficient of variation of 0.183. The mean value of the professional factor is also reported as the professional bias factor. A histogram showing the normal distribution fit is shown in Fig. 5.22. A chi-squared goodness of fit test and a KS test were performed. Both tests confirmed the goodness of fit and provided p-values of 0.172 and 0.372 respectively. Thus the professional factor can be modelled as a normal distribution.

The uncertainty due to the testing and the difference between assumed specimen properties and actual specimen properties is incorporated into the computation of the professional factor using the same method as Bartlett and MacGregor (1996). The values for V_{test} and V_{spec} are taken as 0.030 and 0.045 respectively (Bartlett and MacGregor, 1996). The coefficient of variation for the professional factor is calculated using Equation 5.7.

$$V_p = \sqrt{{V_{t/c}}^2 - {V_{test}}^2 - {V_{spec}}^2} \tag{5.7a}$$

$$V_p = \sqrt{(0.183)^2 - (0.03)^2 - (0.045)^2} = 0.174 \tag{5.7b}$$

Thus the coefficient of variation for the professional factor can be taken as 0.174.

As previously stated, a total of 53 results were excluded from the original set of data. The removal of these analysis results was based on four main criteria: the model contained a numerical error and did not complete the analysis (Model Error), the beam was modelled without any longitudinal reinforcement (Mesh Error), the specimen did not fail the beam under the applied displacement (Not Failed), or the automated retrieval of the model results provided suspiciously high or low peak load-deflection results (Suspicious). Fig. 5.23 shows a comparison of the original 371 test results and highlights the results identified as erroneous.

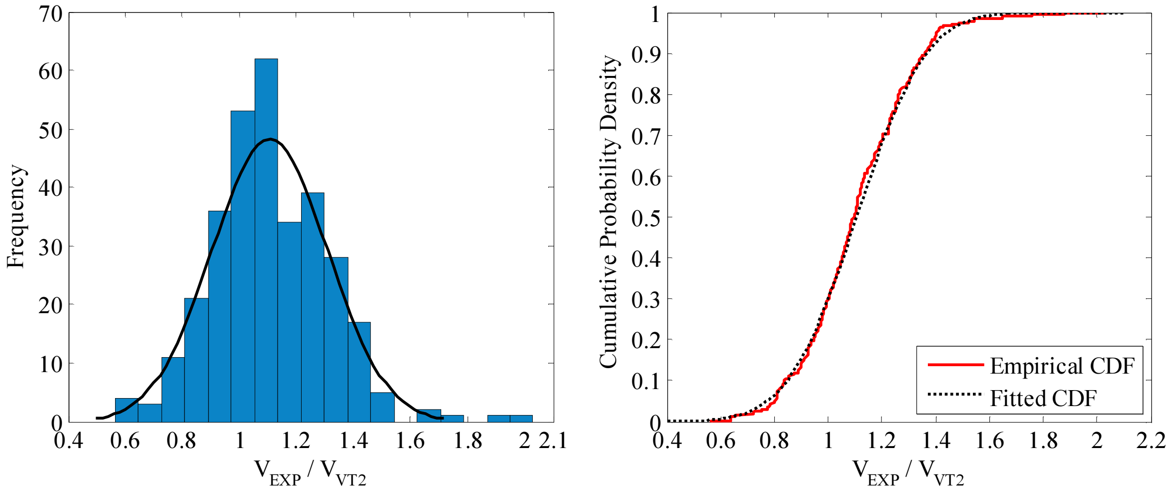

Fig. 5.22: Histogram and fitted distribution for the VecTor2 professional factor.

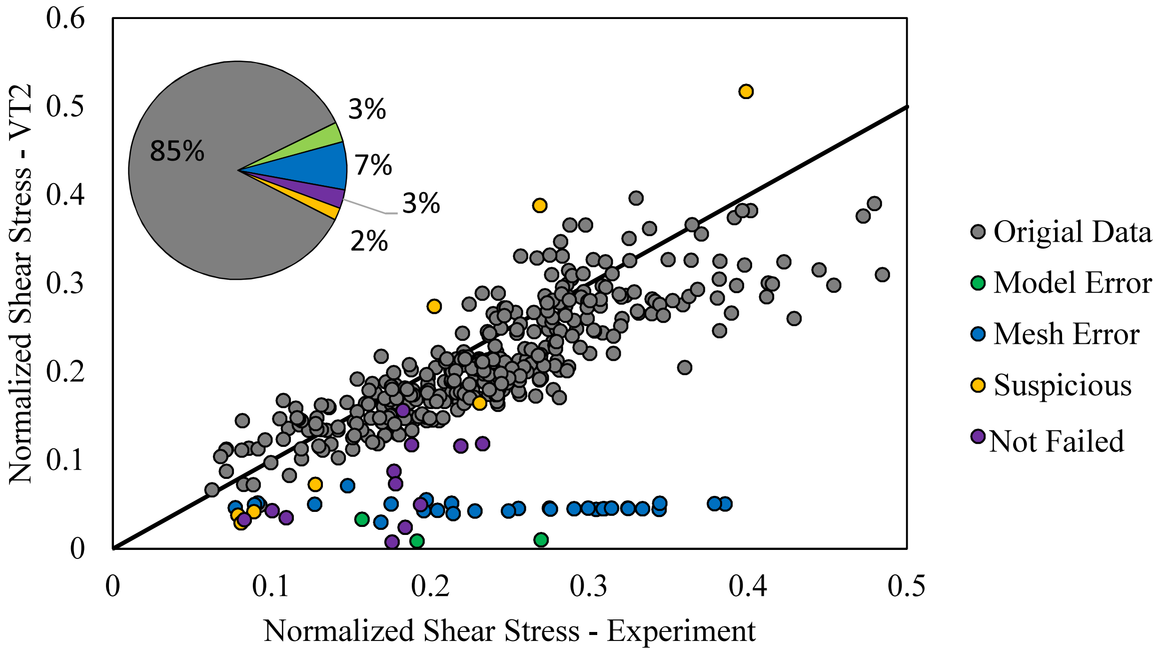

Fig. 5.23: Illustration of removed data points disaggregated by removal rationale.

The results identified as suspicious were based on visual inspection of the load-deflection curve without comparing the test to predicted ratio. It is interesting then, that most of the selected test results fall on the periphery of the test-to-predicted ratio cloud. Only eight of the tests were considered to be suspicious. The suspicious results were mostly due to errors in the automated retrieval of the peak load. The specimens fell into three categories: the automated result overpredicted the strength due to a common phenomenon where the structure continues to hold load after the main shear crack is formed; the automated result interprets the cracking point as the failure point; or the analysis fails prematurely in an unrealistic manner. For the first two causes, the actual failure point is clear based on the load-deflection and crack patterns and can be selected manually. For the third cause, these three tests were selected for removal because the testing apparatus was inverted such that the gravity force was applied upward (from the frame of reference of the model). Fig. 5.24 shows the suspicious data points after manual selection of maximum point and the data points selected for removal.

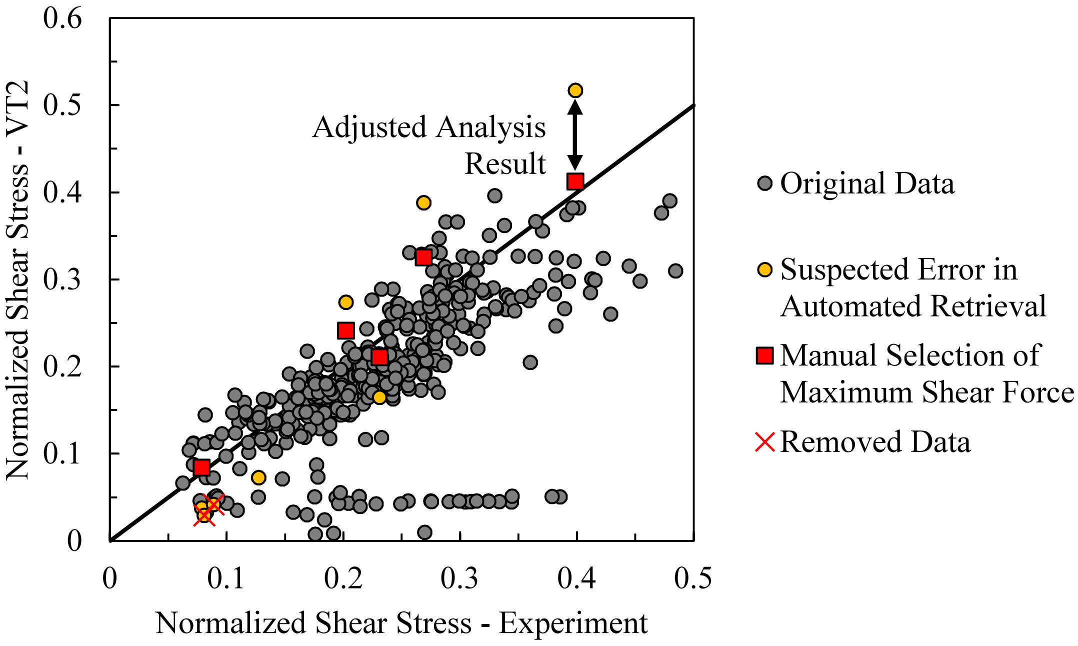

Fig. 5.24: Adjustment or removal of suspicious data.

The analysis of the selected test data was repeated with the CSA A23.3 code and the ACI-318 code. These analyses were done not for the purpose of developing professional factors for the CSA A23.3 code or the ACI-318 code, but rather to compare the results from each code to VecTor2. The CSA code and VecTor2 are both implementations based on the Modified Compression Field Theory. The CSA code simplifies the original Modified Compression Field Theory and is calibrated for analysis of flexural elements (Bentz, 2000). VecTor2 uses the Disturbed Stress Field Model (Vecchio et al., 2000) and expands on the Modified Compression Field Theory by including shear slip along the cracks. The results for the CSA code are shown in Fig. 5.25.

It can be seen that for most of the test results, the CSA code is conservative. It becomes partially unconservative for specimens that develop lower shear stress. However, given the overall scatter, it is reasonable to assume that the mean value of the CSA equations are good predictors of the shear strength, and that the variability observed in the figure is acceptable given the simplicity of the model. It is worth noting that VecTor2 also experiences significant scatter in these regions, although does not appear to have an unconservative bias.

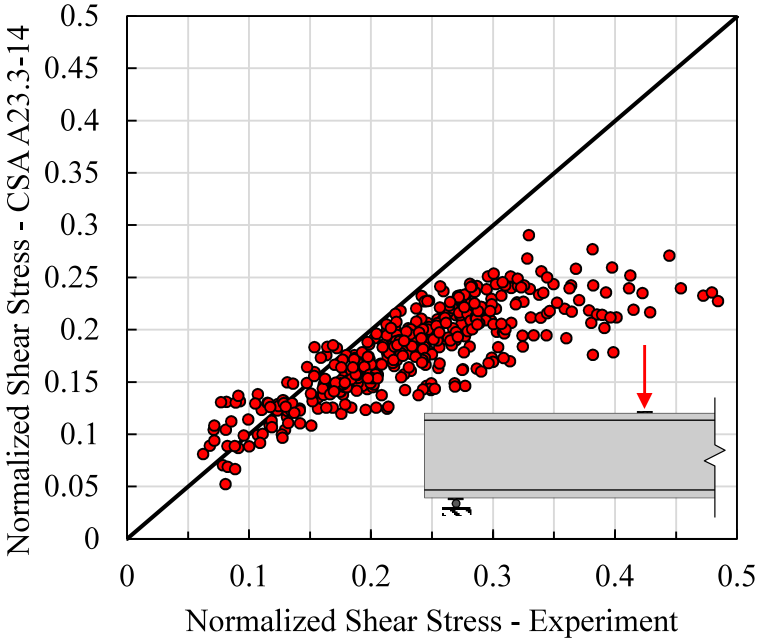

Fig. 5.25: CSA A23.3-14 predictions for shear strength vs. normalized shear strength.

It is also evident in Fig 5.25 that the CSA code conservatively predicts tests which can develop high shear stress. During the early experimental exploration of the shear strength of concrete, researchers often designed beams with large tensile reinforcement in order to induce a shear failure. However, it was not understood at the time that the presence of large amounts of longitudinal reinforcement reduce the overall tensile strains in the shear zone and thus artificially strengthen the shear strength of such beams. When the results are disaggregated, the effect of the reinforcing ratio on the CSA predictions becomes clear. Fig. 5.26 shows the disaggregated results for the CSA predictions. The data has been split into two categories: longitudinal reinforcing ratio greater than or less than two and a half percent. Two and a half percent was selected as a large, yet realistic reinforcing ratio. It is clear from the figure that most of the tests poorly captured by the CSA code have a reinforcement ratio above 2.5 percent.

Finally, the ACI 318-14 code is compared to the test results. The ACI code essentially assumes a constant shear stress is developed, and then allows for some variation due to the reinforcement ratio, applied moment, and shear. However, this generally only benefits the shear strength. As previously mentioned, there is no size effect parameter for the shear strength of concrete. This is

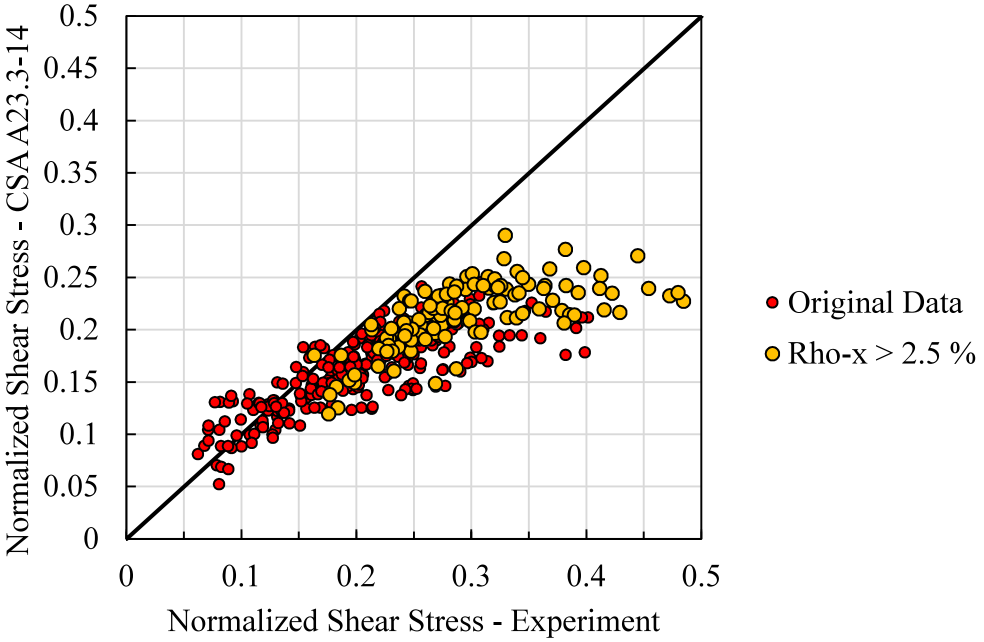

Fig. 5.26: Disaggregated CSA predictions with $\rho_x \geq 2.5\%$

clearly evident in Fig. 5.27, which plots the ACI predictions against the experimental results. This figure shows that, for the majority of test results, the ACI predictions are conservative. However, after a point in which the ACI predictions equal the experimental predictions, the ACI code quickly becomes unconservative. This is discussed further in Section 5.6, which assesses the reliability of the ACI code in consideration with the size effect.

A comparison of all three code predictions and the depth of the specimen is presented in Fig. 5.28 and Fig. 5.29. Fig. 5.28 shows the scatter plot of the predictions for all three analysis methods. The ratio of calculated to experiment (note: this is the inverse of the professional factor) is shown in the figure. The figure shows that while the ACI code exhibits the most scatter, the predictions from the CSA code and VecTor2 are not without scatter. Fig. 5.29 takes the average value of the calculated to prediction compared against the depth to depth to tensile reinforcement. The depth to tensile reinforcement is averaged in bins of 250 mm, and the number of specimens in each bin is indicated in the figure. This figure illustrates the scatter in VecTor2 and CSA code predictions. The CSA code seems to generally predict the strength of the specimens conservatively. The unconserviative nature of the ACI code can be seen as the blue lines (with the exception of three beams with 1000 < d < 1250) continue to increase. Further discussion on the reliability of the code predictions is presented in Section 5.6.

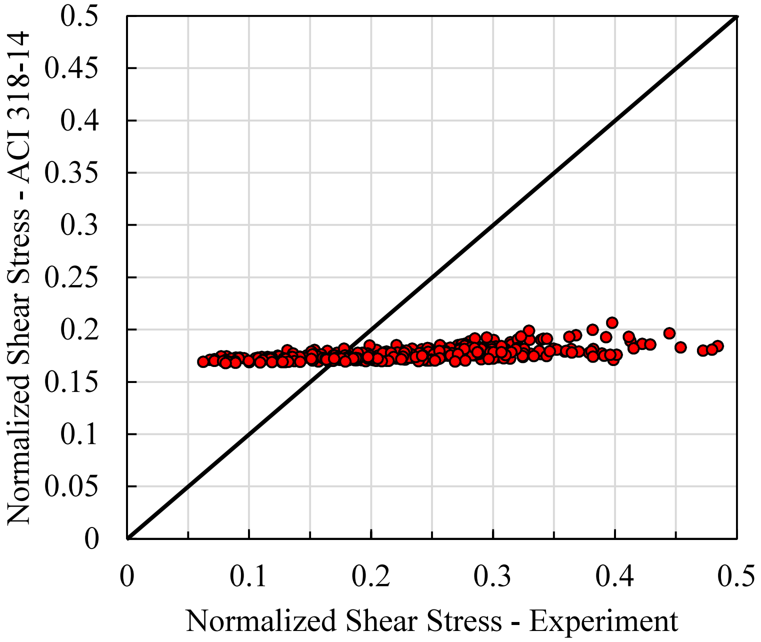

Fig. 5.27: ACI 318-14 predictions for shear strength vs. normalized shear strength.

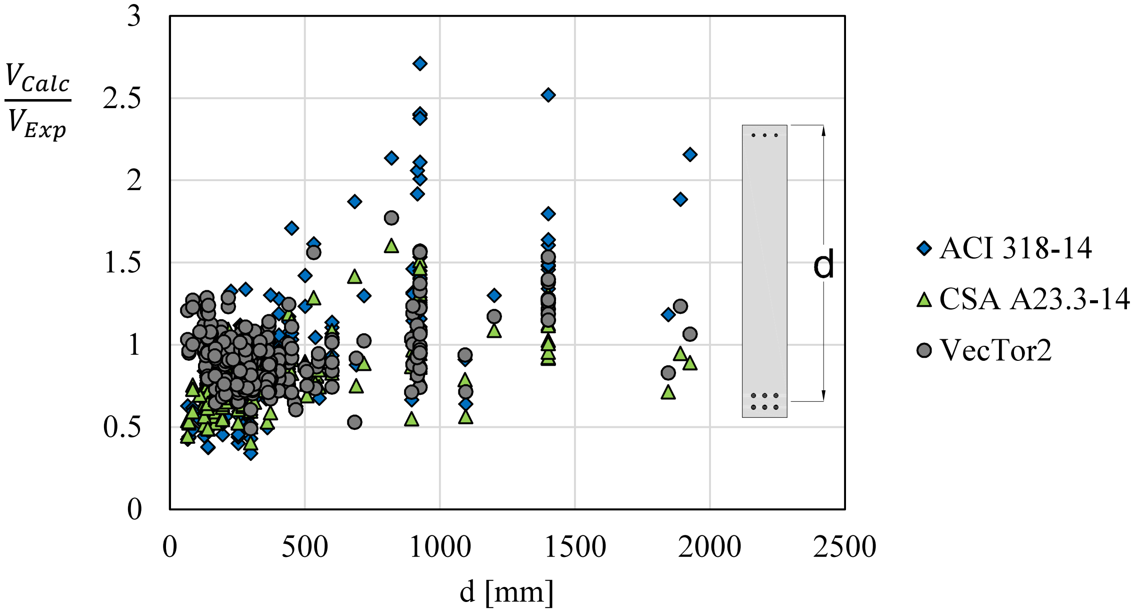

Fig. 5.28: Scatter plot of calculated to experimental ratios versus depth to tensile reinforcement.

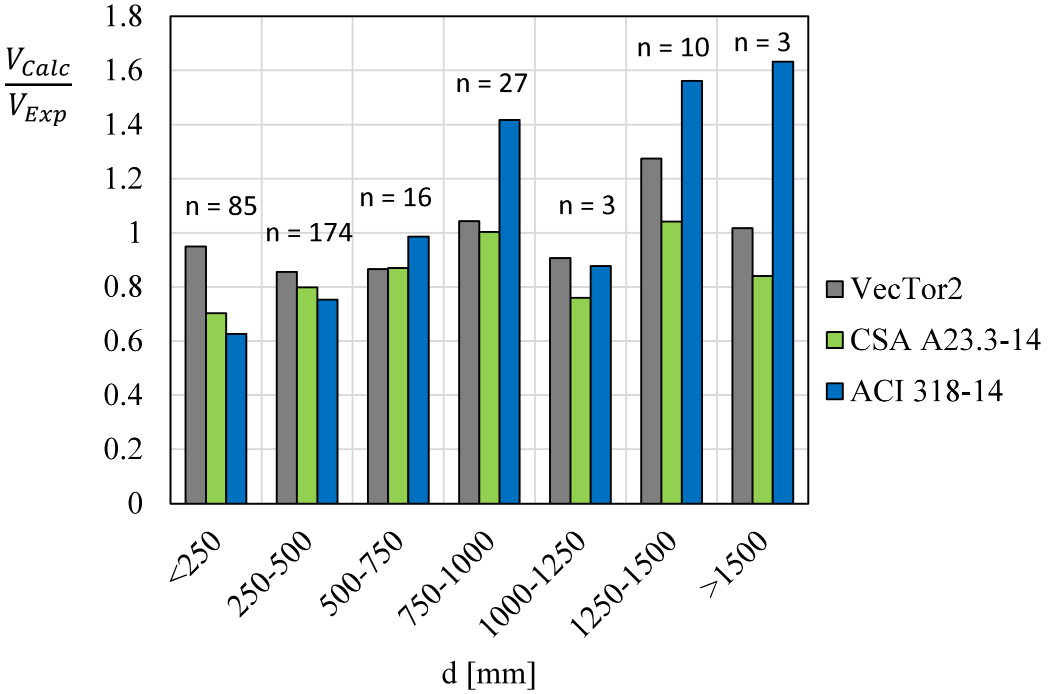

Fig. 5.29: Disaggregated averages of calculated to experimental ratios versus depth to tensile reinforcement.

5.4 Stochastic Simulation Results

Stochastic simulation was conducted for each of the selected specimens from the Toronto size effect series. The number of simulations for each specimen varied based on computation time. Each simulation consisted of a random field using Latin hypercube sampling for the specified concrete strength, assumed to be 30 MPa. The steel properties were assumed to be deterministic. This was done because of the limited influence of the steel on the behaviour of the unreinforced concrete. The strain in the steel is influenced only by the steel modulus of elasticity, which exhibits only small variability. The number of simulations and stochastic analysis parameters are outlined in Table 5.8.

Mirza et al. (1979) provide functions to estimate the mean value of the tensile strength and modulus of elasticity from the compressive strength; however, updated approximations have been substituted in place of the original functions. As a result, the standard deviation is calculated using the coefficient of variation provided by Mirza et al. (1979) but not the mean value.

Table 5.8: Stochastic simulation input properties for reinforced concrete.

Variable	Model	Mean Value [MPa]	Standard Deviation [MPa]	Coefficient of Variation [%]
Compressive Strength $f_c' = 30\ MPa$	Bartlett and MacGregor (1996)	38.57	7.14	18.6
Tensile Strength $f_t' = 1.81\ MPa$	Modified Mirza et al. (1979)	1.81	0.23	12.7
Modulus of Elasticity $E_c = 25084\ MPa$	Modified Mirza et al. (1979)	25084	2006.7	8.0

The distributions from Table 5.8 represent the global distributions. However, as discussed in Section 4.5.6, the local spatial variation is much lower. For the purpose of this study, the spatial variation due to the random fields was based on the measured properties of PLS4000 outlined in Chapter 3. A correlation length of 1200 mm and the random field coefficient of variation of 5.0% were selected. The simulation results produce a series of load-deflection curves. The peak load for each curve needs to be identified. A script was employed to read the stochastic simulation results, and identify the peak load. A typical plot of the stochastic simulation results is plotted in Fig. 5.30.

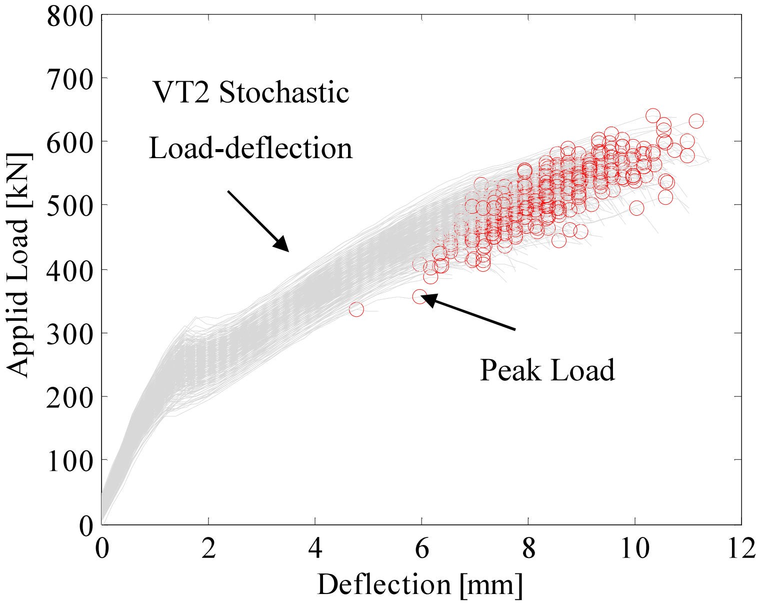

Fig. 5.30: Example of stochastic simulation results. Simulated load-deflection for YB2000.

The peak load from each stochastic simulation can be analyzed as a set of random data. A statistical distribution is fitted to the results of each simulation. Fig. 5.31 shows an example of the distribution of the peak load for specimen YB2000.

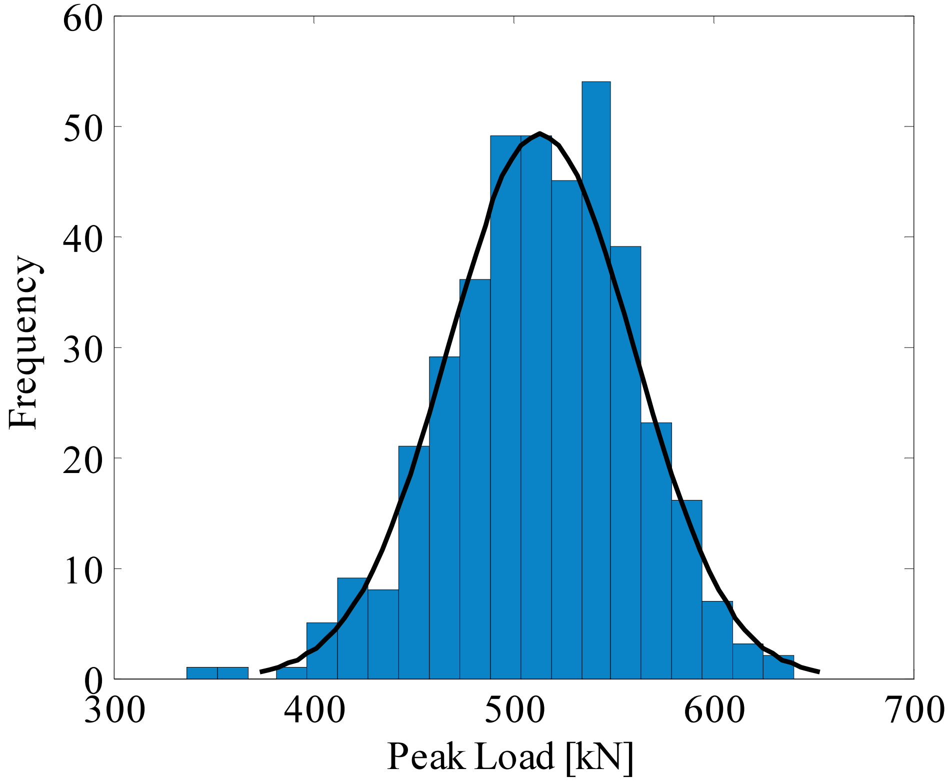

Fig. 5.31: Statistical Distribution of Peak Load for specimen YB2000.

The results of each simulation were determined to be normally distributed. A chi-squared goodness of fit test and a KS test were used to assess the fits. The p-values for each statistical test are shown in Table 5.9. The average bias factor and coefficient of variation are also presented in the table. These average values are used in the reliability analysis.

Each of the stochastic simulations showed a mean value very close to the nominal resistance calculated by the CSA A23.3 general method. A plot of the general method compared with the stochastic simulation results is presented in Fig. 5.32. The simulation results were transformed from applied peak load to shear force per metre.

Table 5.9: Stochastic Simulation Results.

Specimen	No. of Simulations	Statistical Distribution	$\mu_{Peak\ Load}$ [kN]	$\lambda = \frac{\mu_{Peak\ Load}}{R_{CSA}}$	Simulated COV	p-value χ^2 / KS
BN 50	200	Normal	235.0	1.200	0.116	0.563 / 0.342
BN 100	300	Normal	324.4	1.040	0.092	0.932 / 0.475
YB 2000	398	Normal	513.9	1.101	0.091	0.464 / 0.536
PLS4000	175	Normal	652.3	1.226	0.112	0.365 / 0.134
			Average	1.142	0.103	

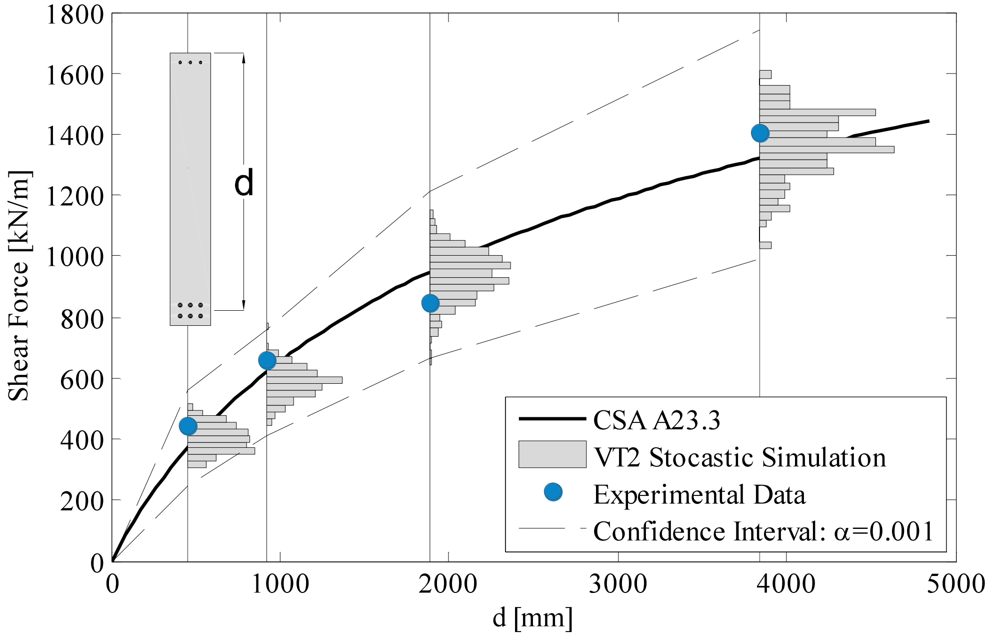

Fig. 5.32: Comparison of stochastic simulation results, experimental results, and CSA-A23.3-14.

5.5 Load Statistics

For a typical reliability analysis, the load statistics are based on the load combinations and the loads acting on the global structure. In the case of this study, there is no global structure, and no specific live load can be defined for each of the specimens. Thus, in order to assess the reliability of each specimen, an approach similar to Szerszen and Nowak (2003) is adopted. Equation 5.8 is defined as the loading ratio, ψ.

$$\psi = \frac{D}{D + L} \tag{5.8}$$

If the loading ratio ranges from 0 to 1, the live load can be determined based on the dead load and the loading ratio or vice versa. Thus either the dead load or the live load need to be selected for the reliability analysis.

The live load can be divided into two categories: the sustained live load, and the transient live load (Nowak and Collins, 2000). The sustained live load is also referred to as the load at any arbitrary point in time, while the structure is under normal occupancy. The transient live load represents conditions when the load is at a maximum. Transient live loads occur randomly and are difficult to predict (Nowak and Collins, 2000). Szerszen and Nowak (2003) compiled loading statistics from the literature which are presented in Table 5.10.

Table 5.10: Statistical parameters for loading. Taken from Szerszen and Nowak (2003).

	Arbitrary-point-in-time load		Maximum 50-year load	
Load Component	Bias	COV	Bias	COV
Dead Load (cast-in place)	1.05	0.10	1.05	0.10
Dead Load (plant-cast)	1.03	0.08	1.03	0.08
Live Load	0.24	0.65	1.00	0.18
Snow	0.20	0.87	0.82	0.26
Wind	0	0	0.78	0.37
Earthquake	0	0	0.66	0.56

5.6 Size Effect, Reliability, and North American Building Codes

This section discusses the methodology and results of the reliability analysis for the selected Toronto Size Effect series specimens. Two sets of reliability analyses are conducted. The first set looks at the reliability of each individual specimen. The second looks at the reliability of the specimens as a whole, in comparison with North American building codes.

The specimens being analyzed are not part of a real structure, and thus they have no real definition of live load and dead load. It is for this reason that the loading ratio is specified. However, if the dead load is simply the self-weight of the specimens, then the ratio between nominal strength and self-weight decreases as the depth of the beam increases. Thus, when calculating the reliability of a given structural element with unknown dead and live loads, a different approach is required. Two methods are considered; both rely on codified predictions for the nominal resistance of the member. For this analysis, the CSA code is used for the nominal resistance.

Method 1

For the first method, the dead load is considered an unknown value, the nominal resistance is considered to be known, and the loading ratio is specified. The limit state function can be described using Equation 5.9.

$$\gamma_D D + \gamma_L L \leq \phi R_n \tag{5.9}$$

In the case of this study, CSA load factors and material resistance factors will be assumed. Thus the load factors for dead and live load are taken as 1.25 and 1.5 respectively. With respect to the resistance factor, the beams are shear-critical without any transverse reinforcement. Thus the resistance factor for the structural element can be taken as the material resistance factor for concrete ($\phi_c = 0.65$). The load and resistance factors are substituted into Equation 5.9 to produce the limit state function considered in this reliability analysis.

$$1.25D + 1.5L \leq 0.65R_n \tag{5.10}$$

where D and L are the specified dead and live loads respectively, and R_n is the nominal resistance. Assuming that the structural specimen was designed according to the CSA code, the nominal resistance, R_n, can be calculated. This only leaves the specified dead load as an unknown. Substituting the load resistance factor from Equation 5.8 into Equation 5.10 and solving for the specified dead load yield Equation 5.11.

$$D = \frac{0.65R_n}{1.25 + 1.5\frac{1-\psi}{\psi}} \tag{5.11}$$

The mean values of the dead and live loads can be found by applying Equation 5.12.

$$\mu_D = \lambda_D D \tag{5.12a}$$

$$\mu_L = \lambda_L L \tag{5.12b}$$

The standard deviation is then calculated as the product of the computed mean value and the coefficient of variation. The statistical parameters for the loading that satisfy the code limit state equation have now been determined. Szerszen and Nowak (2003) note that a realistic loading ratio for beams ranges from 0.3 and 0.7; however, a loading ratio between 0 and 1 is used for this analysis.

This first method is useful for comparing the reliability between the selected specimens because the nominal resistance and statistical parameters for each are known. Thus the unknown loading parameters on the tested specimens can be determined to calculate code acceptable loading.

Method 2

For the second method, a dead load is assumed. The required nominal resistance is then computed by solving Equation 5.10 for the nominal resistance. This is illustrated in Equation 5.13.

$$R_n = \frac{\phi}{\gamma_D D + \gamma_L L} \tag{5.13a}$$

$$R_n = \frac{0.65}{\left(1.25 + 1.5\frac{1-\psi}{\psi}\right) D} \tag{5.14b}$$

The nominal resistance can then be used to determine the statistical parameters of the member resistance curve. Thus a model that relates the nominal resistance and the mean resistance is required. A bias factor is generally used to relate the mean resistance with the nominal resistance. The statistical resistance model used for this analysis is shown in Equation 5.14.

$$R = R_n \times M \times P \times F \tag{5.14}$$

where M is the material property parameter, $R_n \times M$ is taken as the results of the stochastic simulation, F is the fabrication factor, and P is the professional factor. The statistical properties of R can be calculated as:

$$\mu_R = \lambda_R R_n \tag{5.15}$$

$$\sigma_R = V_R \mu_R \tag{5.16}$$

where μ_R and σ_R are the mean and standard deviation of the resistance, λ_R is the bias factor for the resistance, and V_R is the coefficient of variation. The bias factor and the coefficient of variation can be determined using Equation 5.17 and Equation 5.18 respectively.

$$\lambda_R = \lambda_M \times \lambda_P \times \lambda_F \tag{5.17}$$

$$V_R = \sqrt{(V_M)^2 + (V_P)^2 + (V_F)^2} \tag{5.18}$$

Where $\lambda_M = 1.016$ is the bias factor for M calculated in Section 5.4, $\lambda_P = 1.13$ is the bias factor for P calculated in Section 5.3, $\lambda_F = 1.004$ is the bias factor for F calculated in Section 3.4.1, $V_M = 0.103$ is the coefficient of variation for M calculated in Section 5.4, $V_P = 0.170$ is the coefficient of variation for P calculated in Section 5.3, and $V_F = 0.01$ is the coefficient of variation for F calculated in Section 3.4.1.

It is worth noting that the fabrication factor in this study only considers the width of the specimen. A study by Mirza and MacGreggor (1979b) reports that the beam width bias fabrication factor for a total of 315 specimens is calculated as 1.005 with a coefficient of variation of 0.8 percent. Nowak and Szerzen (2003) based their fabrication width factor on a study done by Ellingwood (1980) and reported a bias factor of 1.01 with a coefficient of variation of 4.0 percent. The present study measured a bias factor of 1.004 with a coefficient of variation of 1.0 percent. All studies recommend a normal distribution for the fabrication factor. The collected data in Section 3.4.1 are in reasonable agreement with previous studies in the literature and thus used for the current reliability analysis.

For cases where there are multiple load combinations, Method 2 can be employed where the maximum nominal resistance, R_n, is computed from each load combination. The resulting statistical parameters then use Turkstra's Rule for load combinations (Nowak and Collins, 2000). Turkstra's rule used the combination of statistical parameters at their maximum value (over a period of time) and the statistical parameters at any point in time. The total load is defined in Equation 5.19.

$$Q = X_1 + X_2 + \cdots + X_n \tag{5.19}$$

Turkstra's rule required that for n load combinations, n possible combinations of the load statistics must be considered. The maximum value of the load variable is computed using Equation 5.20.

$$Q_{max} = \max \begin{cases} \max(X_1) + X_2^{apt} + \cdots + X_n^{apt} \\ X_1^{apt} + \max(X_2) + \cdots + X_n^{apt} \\ \vdots \\ X_1^{apt} + X_2^{apt} + \cdots \max(X_n) \end{cases} \tag{5.20}$$

Thus the mean and standard deviation for Q_{max} can be calculated using Equation 5.21 and Equation 5.22 respectively.

$$\mu_{Q_{max}} = \max \begin{cases} \mu_{max\,X_1} + \mu_{X_2}^{apt} + \cdots + \mu_{X_n}^{apt} \\ \mu_{X_1}^{apt} + \mu_{max\,X_2} + \cdots + \mu_{X_n}^{apt} \\ \vdots \\ \mu_{X_1}^{apt} + \mu_{X_2}^{apt} + \cdots \mu_{max\,X_n} \end{cases} \tag{5.21}$$

$$\sigma_{Q_{max}}^2 = \sigma_{\max(X_k)}^2 + \sum_{other\ components} \left(\sigma_{X_i}^{apt}\right)^2 \tag{5.22}$$

Note that the computation of the standard deviation requires that the governing load combination be identified. The standard deviation then uses the maximum value statistics for the governing load combination with the sum of the arbitrary point in time values for the remaining loads. So in the case of computing the nominal resistance using Equation 5.14a, the resulting statistical parameters follow Turkstra's rule using the maximum 50-year load for the principal load and the arbitrary point in time load for the companion loads. Note that the dead load is considered a companion load unless it is the only load in a given load combination.

With the statistical parameters for the loading and the resistance, the reliability index can be calculated for either method using Equation 5.23.

$$\beta = \frac{\mu_R - \mu_Q}{\sqrt{{\sigma_R}^2 + {\sigma_Q}^2}} \tag{5.23}$$

The second method takes the opposite approach to the first method. It requires a bias factor for the nominal resistance which can take any value depending on the assumed dead load. It is noted that both methods produce identical results for reliability, regardless of the assumed dead load, if the statistical parameters for the resistance are identical. The second method has the advantage of being able to consider multiple load combinations. Fig. 5.33 shows the results of both methods for PLS4000. Note that the bias factor for Method 2 was calculated as the ratio of the code calculated nominal resistance to the simulated mean resistance.

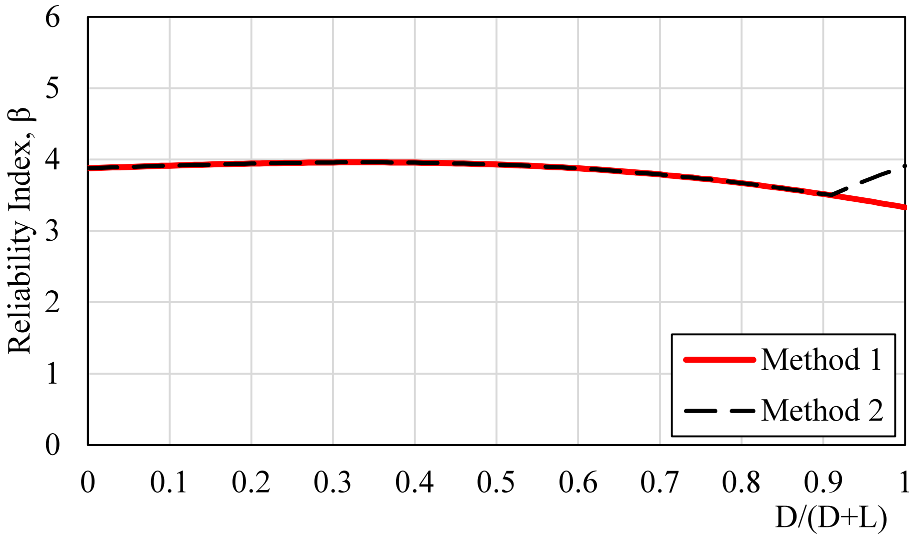

Fig.5.33: Comparison of Method 1 and Method 2 calculation for PLS4000 (without fabrication and professional factors).

The only difference between the methods occurs at the right hand side of the figure where Method 2 governs. This deviation occurs when Method 2 switches its governing load combination from 1.25D + 1.5L to 1.4D. This occurs because the live load is less than 10 percent of the dead load. However, Method 1 is more convenient to calculate for the selected specimens and thus used in the reliability analysis.

The reliability for each specimen is calculated using the first method and the CSA code predictions for the nominal resistance. The results of the reliability analysis are shown in Fig. 5.34. The CSA reliability for all specimens is almost identical. This is in part due to the similar material factor bias coefficients and coefficients of variation, but also due to the professional factor. The variability of the professional factor dominates the variability of the resistance model, and thus all bias factors and coefficients of variation for each specimen trend toward the same value. The average reliability index for the CSA code calculations, for each specimen, is 2.96. This is below the target reliability index of $\beta_T = 3.5$ suggested by Nowak and Szerszen (2003).

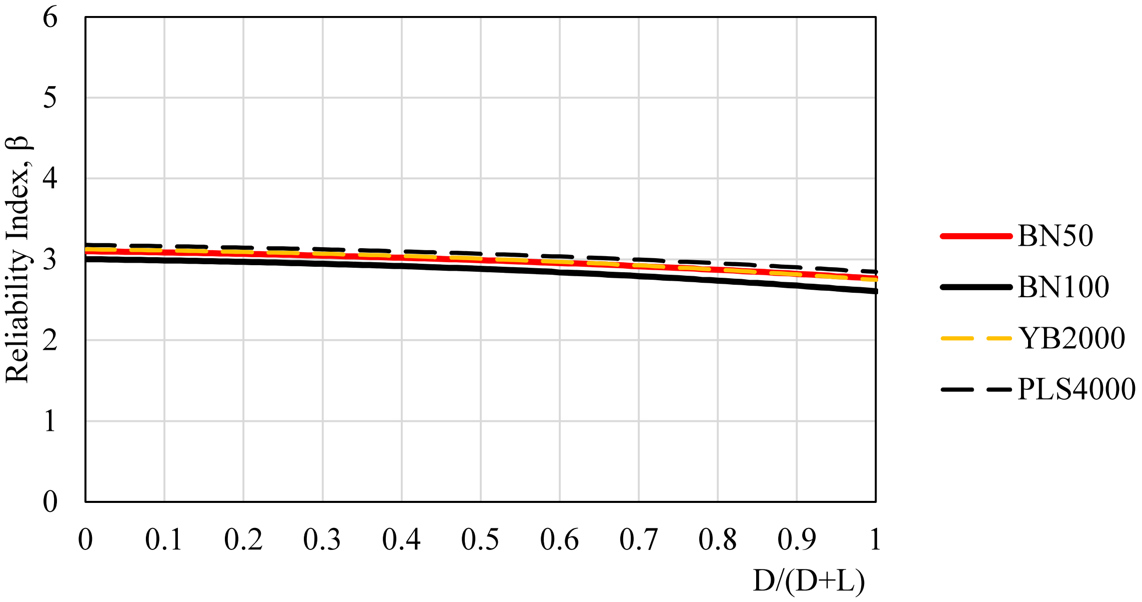

Fig. 5.34: Reliability index for CSA-A23.3.

The same procedure is repeated in Fig. 5.35 to produce the reliability using the ACI-318 code. However, the ACI load and member resistance factors were used. In addition to the current results, the reliability using the resistance models produced by Rakoczy and Nowak (2013) and Nowak and Szerszen (2003) are shown. It can be seen that the reliability for shear-critical members for specimen BN50 is closest to that of the recommended resistance model parameters suggested by Rakoczy and Nowak (2013). This is consistent with the agreement of the nominal resistance between the ACI-318 code and the CSA-A23.3 code for shallow elements. However, as the depth of the element increases, the uncoservative nature of the ACI-318 code becomes clear. The average reliability indices for BN100, YB2000, and PLS4000 are 2.79, 2.13, and -0.05

respectively. This equates to a probability of failure of 0.3%, 1.6% and 51.8% respectively. Thus the consideration of the size effect in the reliability of shear-critical members should not be ignored by the ACI-318 code. It is worth noting that for all ACI reliability calculations, the nominal resistance is calculated in accordance with ACI 318 Clause 11.4.6.1 which states:

> *...A minimum area of shear reinforcement, $\boldsymbol{A_{v,min}}$, shall be provided in all reinforced concrete flexural members (prestressed and nonprestressed) where $\boldsymbol{V_u}$ exceeds $\mathbf{0.5\phi V_c}$...*

The nominal resistance meeting code requirements is thus taken as half of the concrete contribution. Thus the reliability in this study encompass structures that currently meet all code requirements for beams, but do not meet the code level reliability.

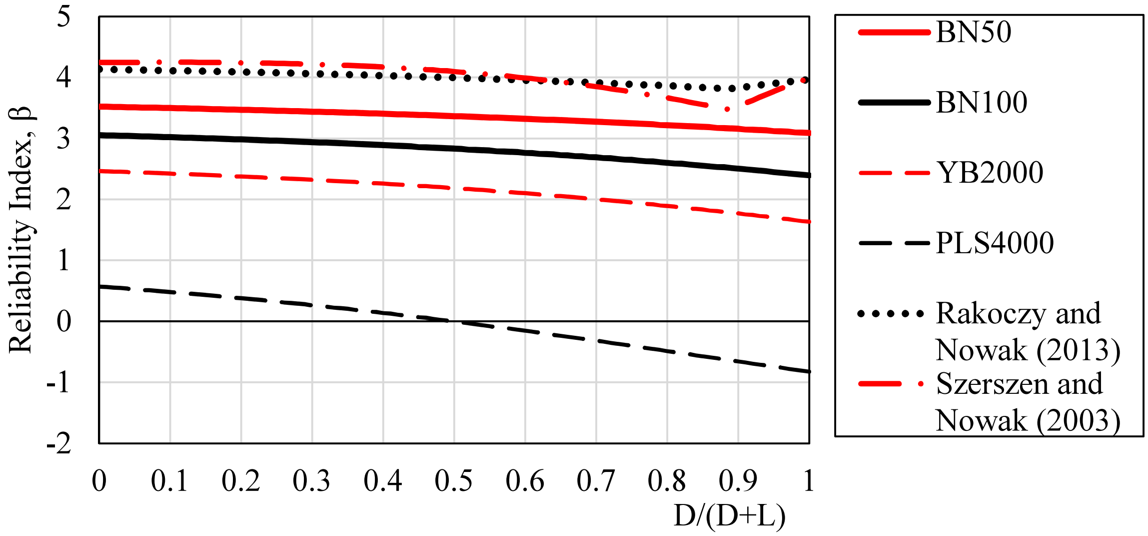

Fig. 5.35: Reliability index for ACI-318-14.

5.7 Influence of Spatial Variation on the Reliability Calculations

In all of the reliability calculations presented in Section 5.6, spatial variation was considered via random field generation. However, the deterministic simulations of Chapter 3 suggested that the local variability had little to no effect on the prediction of ultimate load, and crack pattern. This section discusses the merits of including random fields for reliability analysis of large deep beams without transverse reinforcement.

One of the important distinctions when discussing how spatial variation of material properties influences predicted structural behaviour is symmetry of the crack patterns. However, in almost all experimental data with a plane of symmetry, failure and large shear cracks occur on only one of the two sides (In an analysis model with a plane of symmetry, both sides develop a perfectly symmetric crack pattern). Cracks are formed as a combination of local material weakness and applied stress at a given location. A location of locally high strength still may form a crack if the stress is high enough. To illustrate this point, consider a two-point bending test of an unreinforced concrete beam, similar to a modulus of rupture test. In the first case, uniform material properties are assumed, and in the second case, spatially variable material properties are assumed. The stochastic properties of the concrete are shown in Table 5.8 and are the same as the main stochastic simulations. Fig. 5.36 shows how the crack pattern for the uniform material properties is always predicted as symmetric and identical for each simulation. In contrast, the simulations with spatial variation exhibit crack patterns that stem from a zone of weakness. Additionally, the localized zones of strength have reduced crack widths, or have remained uncracked all together. This example highlights the influence that spatial variation can have on the crack pattern; however, there are important distinctions to make.

In Fig. 5.37, the concrete element is governed by tension softening response. In the presence of reinforcement, the tension stiffening phenomenon results in a crack pattern that is less sensitive to the material properties. In Fig. 5.37, the first two trials result in two cracks forming, in similar locations to the analysis with uniform material properties. In the third trial, only one crack forms. A local maximum and minimum of material properties in trial three occur where the two cracks would form in the uniform analysis. The addition of the transverse reinforcement, and the associated tension stiffening, has reduced the effect of spatial variation.

The analysis was repeated a third time, this time including transverse shear reinforcement with a reinforcement ratio of 0.05%. With the inclusion of the reinforcement in both directions, the entire response is subject to tension stiffening. As shown in Fig. 5.38, the effect of spatial variation is further reduced with trial one and trial three very similar to the uniform analysis. Trial two exhibits two vertical cracks; however, one is influenced by a local zone of weakness.

The above simulations illustrate two findings that are pertinent to the reliability of shear-critical beams with no transverse reinforcement. The first is that crack patterns in unreinforced concrete elements (where tension softening governs) are affected more by spatial variability than tension stiffening. Thus for larger specimens, in which the concrete governed by tension softening response makes up a larger percentage of the total area, spatial variability should have a greater influence on the crack pattern than for smaller members. Additionally, the generated random fields are based on a correlation length that is assumed independent of the size of the specimen. Thus a larger beam will have more localized areas of strength and weakness than a smaller beam, which may resemble more uniform material properties. Secondly, the above simulations illustrate that the inclusion of orthogonal reinforcement supports the basis for the assumptions in the Modified Compression Field Theory and the Disturbed Stress Field Model. The reinforcement strongly influences the behaviour of the concrete; the crack spacing becomes uniform, and the influence of the concrete variability does not govern.

5.8 Concluding Remarks

Reliability analysis of reinforced concrete beams with no transverse reinforcement was successfully completed using VecTor2 stochastic simulation to generate the resistance models. Stochastic simulations for each selected specimen was performed with the number of simulations for each specimen ranging between 175 to 398. The strength of each beam was found to be normally distributed and exhibited a similar coefficient of variation. The average bias factor for the four beams based on a CSA-A23.3 nominal strength prediction is 1.142. The average coefficient of variation is 10.3 percent. These factors represent the material variability of the members.

In addition, the professional factor for VecTor2 models of reinforced concrete beans with no shear reinforcement was established via the successful deterministic modelling of 318 beams. VecTor2 underpredicts the strength of reinforced concrete beams in general although a large amount of scatter is observed. A bias factor of 1.106 with a coefficient of variation of 17.4% are the recommended professional factor statistics. This professional factor was incorporated into the results of the stochastic simulations to form the basis of the reliability analysis.

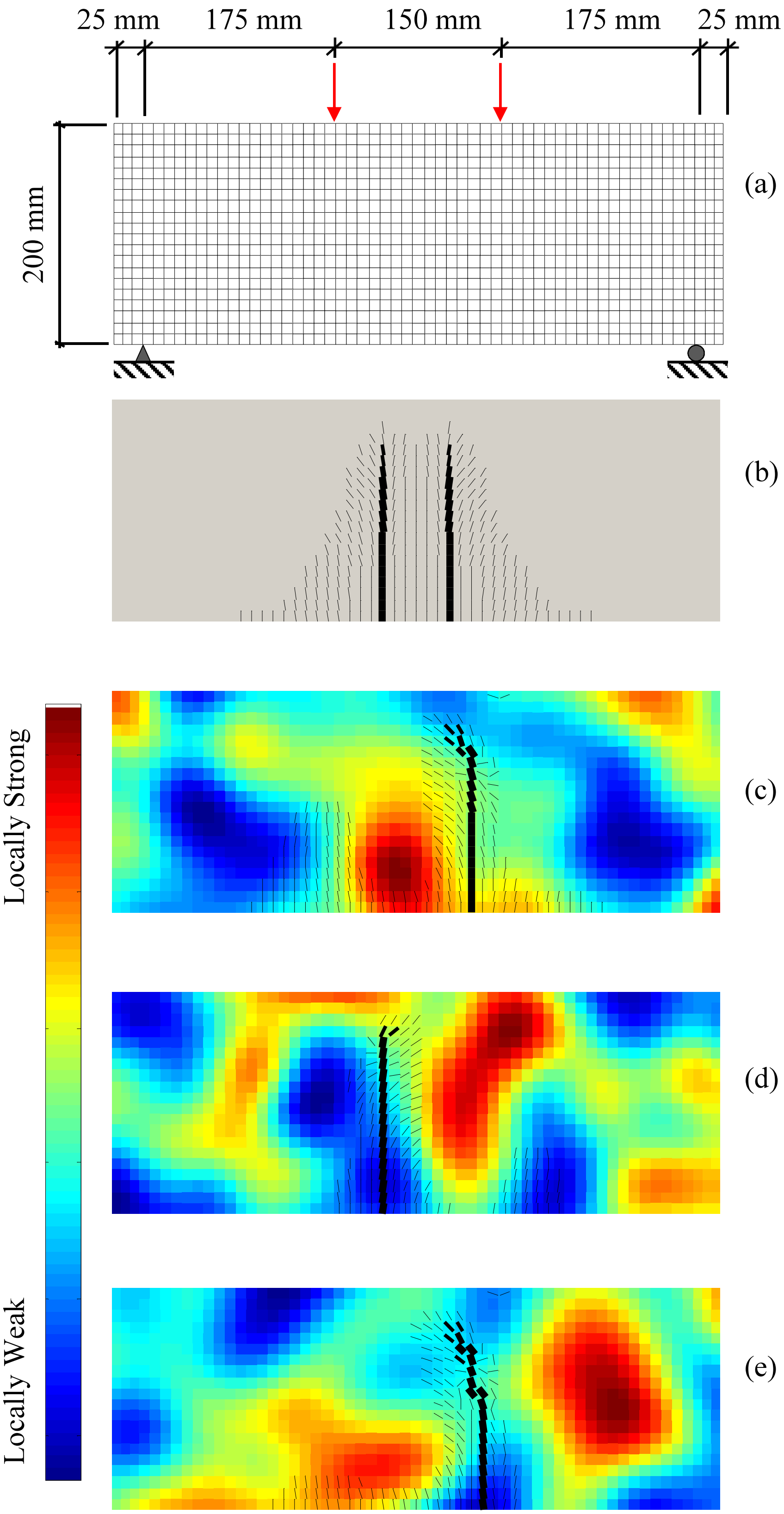

(a) Finite element mesh
t = 200 mm

(b) Uniform material properties

(c) Stochastic simulation with
random fields – Trial 1

(d) Stochastic simulation with
random fields – Trial 2

(e) Stochastic simulation with
random fields – Trial 3

Fig. 5.36: Comparison of crack pattern for uniform and spatial variation simulations.

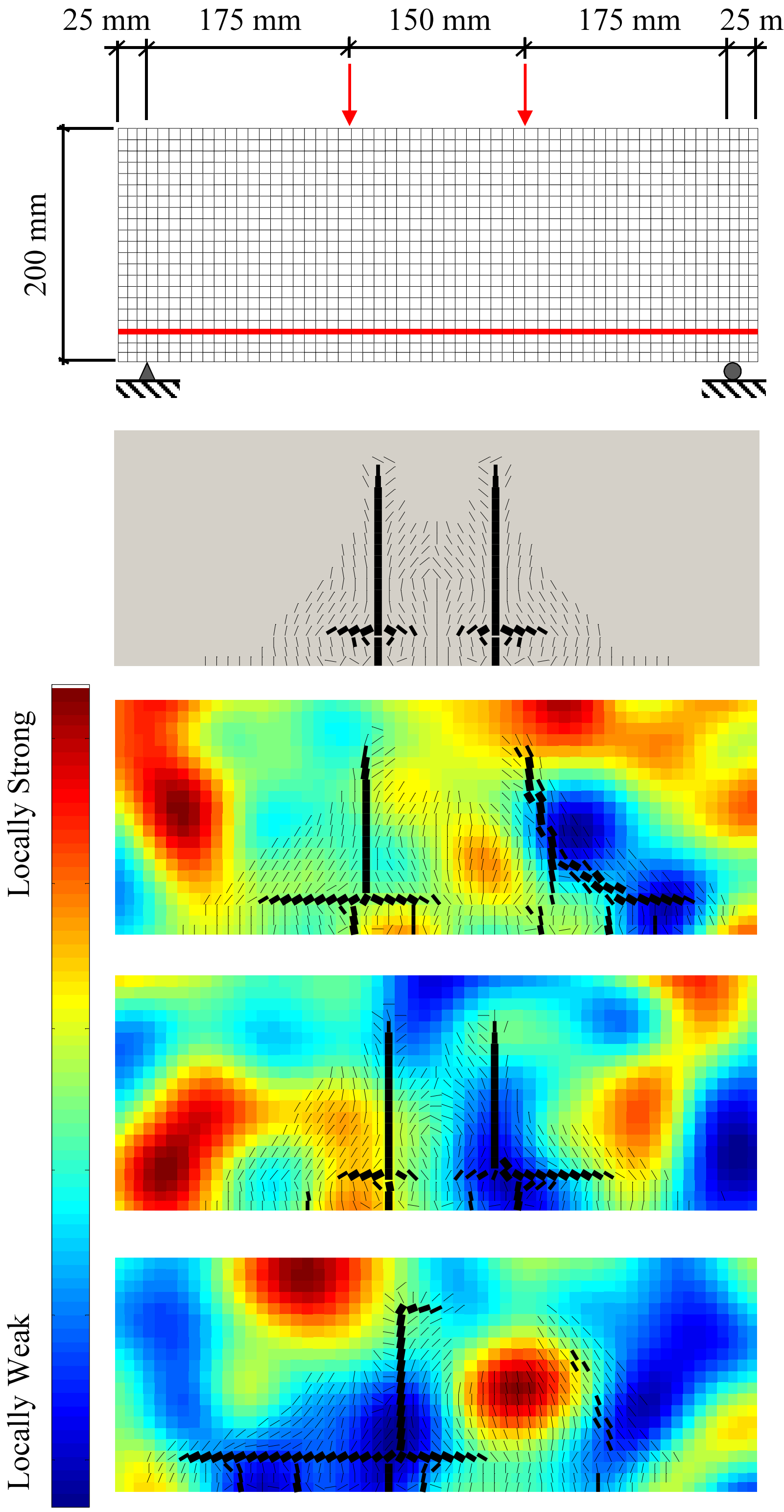

(a) Finite element mesh – with longitudinal steel, $\rho_x = 0.14\%$; t = 200 mm

(b) Uniform material properties

(c) Stochastic simulation with random fields – Trial 1

(d) Stochastic simulation with random fields – Trial 2

(e) Stochastic simulation with random fields – Trial 3

Fig. 5.37: Comparison of crack pattern for uniform and spatial variation simulations with longitudinal reinforcing bars.

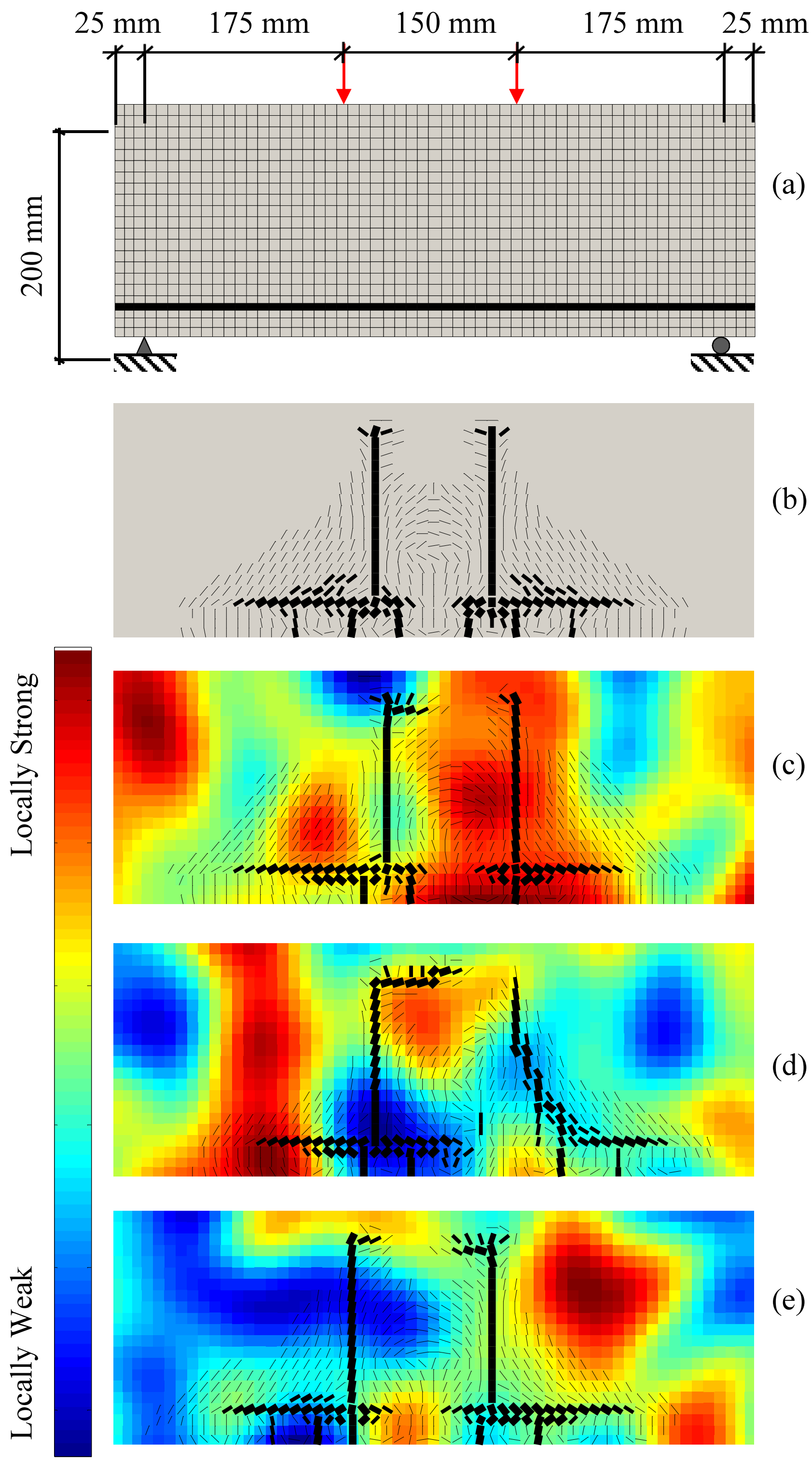

(a) Finite element mesh – with longitudinal steel, $\rho_x = 0.14\%$, and transverse reinforcement $\rho_y = 0.05\%$ t = 200 mm

(b) Uniform material properties

(c) Stochastic simulation with random fields – Trial 1

(d) Stochastic simulation with random fields – Trial 2

(e) Stochastic simulation with random fields – Trial 3

Fig. 5.38: Comparison of crack pattern for uniform and spatial variation simulations with longitudinal reinforcing bars and transverse smeared steel.

Reliability analysis was conducted for the CSA A23.3-14 code and the ACI 318-14 code calculations for nominal member resistance. The respective code load factors and member resistance factors were applied. For the CSA-A23.3 code, the member resistance (ϕ) factor was assumed equal to the material resistance factor (ϕ_c). This was considered acceptable because the concrete shear strength equation exclusively contributes to the predictions. A target reliability index of 3.5, taken from the literature, was assumed to satisfy code level reliability requirements. The reliability index determined for the CSA-A23.3 code is 2.96. This is significantly below the target reliability. This suggests that a material resistance factor of 0.65 is not low enough to reach the target reliability for this class of members.

The reliability index could not be determined for the ACI code in general. This stems from the exclusion of the size effect resulting in a different bias factor for each specimen. A plot of the average reliability index versus depth for the CSA and ACI code is shown in Fig. 5.39.

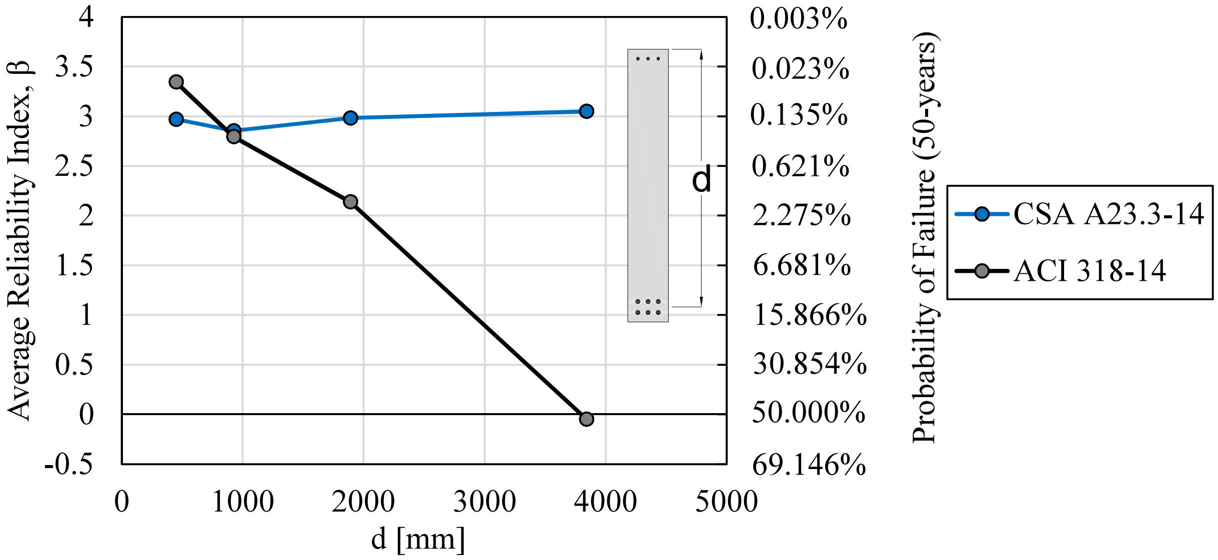

Fig. 5.39: Average reliability index versus depth of specimen for CSA A23.3-14 and ACI 318-14 codes.

As the size of the specimen increases, the reliability decreases rapidly. This is further confirmation that the ACI 318-14 predictions for the shear strength of reinforced concrete members are unconservative.

It should be noted that these reliability results are heavily influenced by the professional factor statistics. The removal of the professional factor results in reliability indices for the CSA code that put the reliability indices at well above the target reliability index. Further research is required, using multiple analytical and computational tools, before a definitive conclusion can be made about the reliability of reinforced concrete beams with no shear reinforcement. This study indicates that the predictions for slender reinforced concrete beams may not be as conservative as preferred.

Lastly it is important to understand when spatial variation is useful in stochastic simulation. The spatial variability of concrete material properties seems to diminish in importance when steel reinforcement is added. The presence of orthogonal reinforcement limits the influence of spatial variability. This is analogous to the fundamental assumptions of the DSFM in which cracks are smeared and a spacing is averaged.

CHAPTER 6: CONCLUSIONS AND RECOMENDATIONS

This section presents conclusions and recommendations for future work based on the research completed for the thesis. The conclusions are arranged such that they mirror the structure of the thesis chapters. The recommendations for future work discuss the inconclusive or ambiguous findings of this thesis and also provides recommendations to advance the state of the art.

6.1 Assessment of Spatial Variability Via Non-destructive Test Methods

The use of ultrasonic pulse velocity to capture the spatial variability of reinforced concrete material properties was accomplished. The ultrasonic pulse velocity was collected for a grid of points on specimen PLS4000 and its associated cylinders. The set of cylinders was used to establish the relation between ultrasonic pulse velocity and concrete compressive strength. For the UPV data collected from PLS4000, kriging maps were developed that allowed for a statistical prediction of the ultrasonic pulse velocity between the measured points. A comparison of the kriging plot and the experimental crack pattern suggest that the spatial distribution of material properties influenced the crack pattern and the failure crack.

The geospatial statistics allowed for a UPV prediction at the centre of each element in the finite element model. This UPV was then converted to compressive strength using the developed relation. Thus a finite element model that incorporated the in-situ material properties was created. This model was compared to a model with uniform material properties. It was found that the inclusion of spatial variability does not have a significant effect on the strength prediction and failure mode for this particular specimen. It is not, however, conclusive that this result generally applies to the analysis of reinforced concrete beams.

6.2 Stochastic Simulation with VecTor2

Several sampling techniques for stochastic simulation were successfully implemented into VecTor2. The software was expanded to perform Monte Carlo simulations, Latin Hypercube simulation, random field generation (both MC and LHS), and correlated sampling (both MC and LHS). All of these methods were implemented and tested in VecTor2.

In addition, several post-processing tools were developed to aid users with post-processing of stochastic simulation results. Multiple MATLAB scripts were created to collect, analyze, and visualize the data.

6.3 Evaluation of VecTor2 Professional Factor for Slender Reinforced Concrete Beams with No Shear Reinforcement

The professional factor for VecTor2, as well as for any other analytical tool, is unique to the structure type being analyzed. The professional factor statistics are obtained by comparing the experimental to predicted ratios for a large number of deterministic tests. The process for creating finite element models in VecTor2 was successfully automated. A mesh generator, a structure file generator, and a load case file generator were all successfully developed. Using the database published by Reineck et al (2014), a total of 371 VecTor2 models were created and run. The database contains a total of 784 tests. This was filtered down to 371 tests by removing tests with missing information and selecting only rectangular specimens. A program was developed to automate the retrieval of the analysis results and identify the peak shear. Of the 371 models, only 318 produced usable results. A total of 53 models contained file generation errors that either didn't run or produced significant numerical errors. The professional factor was found to be normally distributed with a mean value of 1.106 and a coefficient of variation of 17.4 percent. This professional factor was incorporated into the reliability analysis.

6.4 Reliability Analysis with VecTor2

The implemented stochastic simulation tools were used to assess the reliability of shear-critical reinforced concrete beams without transverse reinforcement. Four beams from the 'Toronto Size Effect Series' were selected and a stochastic simulation for each beam was completed. The results of the stochastic simulation were then used in a reliability analysis for the CSA A23.3-14 and ACI 318-14 codes. The analysis results showed that there was no influence of the size effect on the predicted reliability for the CSA A23.3 code. However, the average reliability index for the Canadian code, calculated to be 2.96, is below the target reliability index of 3.5. This suggests that further investigation is required to assess the load factors and safety factors for this class of structure.

The ACI 318-14 code was found to be unconservative with respect to the prediction of deep beams. The average reliability indices for the selected specimens were 3.34, 2.79, 2.14, and -0.05 for BN50, BN100, YB2000, and PLS4000 respectively.

6.5 Recommendations for Future Work

This section outlines the recommendations for future work in the field of stochastic simulation, nondestructive test methods for spatial variability, and needs for new analytical tools.

This thesis has established the viability of using UPV to assess the spatial variability of concrete structures; however, the accuracy of the technique cannot be determined. It is recommended that further testing be conducted wherein existing or new experimental slabs or walls are cast and their UPV measured to assess spatial variability. Additionally, it is recommended that cores be taken at the points of measurement to have a direct correlation between spatial variation predictions from UPV measurements and from concrete cores. Such an experimental program would truly assess the capabilities and usefulness of this test as a method for measuring spatial variability in existing structures.

Additionally, there has not been a Canadian update to the statistical descriptions of concrete strength in approximately 20 years. It is recommended that cylinders be collected from across Ontario (or across Canada) from multiple concrete suppliers to create a database of concrete cylinder strengths. Additionally, tests for the tangent modulus of elasticity and tensile strength of concrete should be included in the study. The statistics for modulus of elasticity and tensile strength have not been updated (or perhaps published) for Canadian concrete in 37 years. Updated statistics for the short-term and long-term properties of Canadian concrete could then be used for better calibration of the Canadian code and more accurate representation of concrete statistics.

From an analytical perspective, the shortcomings in the current implementations need to be addressed. The alternate sampling method for random fields needs to be replaced with two alternatives. First, it is recommended that correlated Latin hypercube sampling be added to the alternate method for simulating random fields. This will lead to improved sampling accuracy for smaller sample sizes. Second, it is recommended that cross-correlated random fields be implemented such that the direct correlation between compressive random fields and tensile random fields is not used.

Additional stochastic properties should be added to the current software formulation. Stochastic variables for the steel reinforcing bar area, the depth of steel reinforcement (d), the thickness of structural elements, and the remaining physical dimensions should be incorporated into stochastic analysis methods. This will help create a more complete picture on the variability of a structural elements in a population of structures.

Currently, the professional factor is only established for slender beams without shear reinforcement. However, it would be useful to identify the statistics for other types of structures as well. Three additional databases exist that include slender beams with shear reinforcement, non-slender beams without shear reinforcement, and non-slender beams with shear reinforcement. Additionally, useful and common structures include shear walls, dapped end beams, beam-column connections, etc. A series of experimental databases for these types of structures should be developed and used to assess the professional factor for VecTor2. In addition to providing statistical descriptions for reliability analysis, this exercise will prove useful in identifying the current strengths and weaknesses of VecTor2 as a deterministic nonlinear finite element analysis program.

To aide in usability, stochastic simulation post-processing should be incorporated with the post-processor Janus. The post-processing of stochastic simulation results still remains a challenge. Currently, separate techniques that are programmatically based are developed and employed. However, expanding Janus to include the stochastic simulation post-processing will improve accessibility for most users.

Lastly, VecTor2 should be expanded to deterministically and stochastically assess deteriorated structures including corrosion of steel reinforcement. The current population of structures in North America are aging and beginning to show signs of deterioration. With fiscal budgets unable to repair or rebuild the majority of deteriorating infrastructure, identification of the structures most at risk is of paramount importance. A tool that can assess the reliability of deteriorated infrastructure could prove invaluable in ensuring the structures most at risk receive appropriate funding. VecTor2 is ideal for such an application; however, it currently lacks the ability to assess deteriorating infrastructure with corroded reinforcement.

References

ACI Committee 318 (2014) Building code requirements for reinforced concrete (ACI 318-14) and commentary ACI 318 R-14. American Concrete Institute. Detroit.

Allen, D. E. (1970). Probabilistic study of reinforced concrete in bending. Technical Paper No. 311. Division of Building Research, National Research Council of Canada, Ottawa, On.

Almusallam, A. A., Al-Gahtani, A. S., Aziz, A. R., & Rasheeduzzafar. (1996). Effect of reinforcement corrosion on bond strength. Construction and Building Materials, 10(2), 123-129.

Al-Sulaimani, G. J., Kaleemullah, M., Basunbul, I. A., & Rasheeduzzafar. (1990). Influence of corrosion and cracking on bond behavior and strength of reinforced concrete members. ACI Structural Journal, 87(2), 220-231.

Amleh, L., & Mirza, S. (1999). Corrosion influence on bond between steel and concrete. ACI Structural Journal, 96(3), 415-423.

Auyeung, Y., Balaguru, P., & Chung, L. (2000). Bond behaviour of corroded reinforcement bars. ACI Materials Journal, 97(2), 214-221.

Bartlett, F. M., & MacGregor, J. G. (1994). Assessment of concrete strength in existing structures. Structural Engineering Report No. 198. University of Alberta.

Bartlett, F. M., & MacGregor, J. G. (1996). Statistical analysis of the compressive strength of concrete in Structures. ACI Materials Journal MJ, 93(2).

Bartlett, F. M. (2007). Canadian Standards Association standard A23.3-04 resistance factor for concrete in compression. Canadian Journal of Civil Engineering Can. J. Civ. Eng., 34(9), 1029-1037.

Bentz. E. C. (2000). Sectional analysis of reinforced concrete members. (Doctoral Thesis). University of Toronto.

Cairns, J., Plizzari, G. A., Du, Y., Law, D. W., & Franzoni, C. (2005). Mechanical properties of corrosion-damaged reinforcement. ACI Materials Journal, 102(4), 256-264.

CSA Committee A23.3 (2014) Design of concrete structures with explanatory notes. Canadian Standards Association. Rexdale.

Chak, I. N. (2013). Janus: A post-processor for VecTor analysis software. (Maters Thesis). University of Toronto.

Choi, B., Scanlon, A., & Johnson, P. A. (2004). Monte Carlo simulation of immediate and time-dependent deflections of reinforced concrete beams and slabs. SJ ACI Structural Journal, 101(5), 633-641.

Choi, S., Canfield, R. A., & Grandhi, R. V. (2006). Estimation of structural reliability for Gaussian random fields. Structure and Infrastructure Engineering, 2(3-4), 161-173.

Collins, M. P., & Mitchell, D. (1997). Prestressed concrete structures. Toronto: Response Publications.

Collins, M. P., Bentz, E. C., & Sherwood, E. G. (2008). Where is shear reinforcement required? Review of research results and design procedures. SJ ACI Structural Journal, 105(5), 590-600.

Collins, M. P., Bentz, E. C., Quach, P. T., & Proestos, G. T. (2015). The challenge of predicting the shear strength of very thick slabs. Concrete International, 37(11), 29-37.

Corder, G. W., & Foreman, D. I. (2014). Nonparametric Statistics: A step-by-step approach, 2nd Edition. John Wiley & Sons.

Coronelli, D. (2002). Corrosion cracking and bond strength modeling for corroded bars in reinforced concrete. SJ ACI Structural Journal, 99(3), 267-276.

Coronelli, D., & Gambarova, P. (2004). Structural assessment of corroded reinforced concrete beams: Modeling guidelines. Journal of Structural Engineering J. Struct. Eng., 130(8), 1214-1224.

Du, Y. G., Clark, L. A., & Chan, A. H. (2005). Residual capacity of corroded reinforcing bars. Magazine of Concrete Research, 57(3), 135-147.

El Maaddawy, T., Soudki, K., & Topper, T. (2005). Analytical model to predict nonlinear flexural behavior of corroded reinforced concrete beams. SJ ACI Structural Journal, 102(4), 550-559.

Ellingwood, B. (1977). Statistical analysis of RC beam-column interaction. Journal of the Structural Division, 103(ST7), 1377-1388.

Ellingwood, B., Galambos, T. V., MacGregor, J. G., & Cornell, C. A. (1980). Development of a probability based load criterion for American National Standard A58. NBS Special Report 577. U.S. Department of Commerce, National Bureau of Standards.

Graham, C., & Talay, D. (2013). Stochastic simulation and Monte Carlo methods: Mathematical foundations of stochastic simulation. New York: Springer.

Hasofer, A. M., & Lind, N. (1974). An exact and invariant first-order reliability format. ASCE Journal of Engineering Mechanics, 100(1), 111-121.

Hunkeler, F. (2000). Corrosion in reinforced concrete: Processes and mechanisms. In H. Böhni (Ed.), Corrosion in reinforced concrete structures (pp. 1-45). Cambridge, England: Woodhead Publishing Limited.

Kemp, E. L., & Wilhelm, W. J. (1979). Investigation of the parameters influencing bond cracking. ACI Journal Proceedings JP, 76(3), 47-71.

L'Ecuyer, P. (2012). Random number generator. In J. E. Gentle, W. K. Härdle, & Y. Mori (Eds.), Handbook of Computational Statistics (2nd ed., pp. 35-72). New York: Springer.

Li, C., Melchers, R. E., & Zheng, J. (2006). Analytical model for corrosion-induced crack width in reinforced concrete structures. SJ ACI Structural Journal, 103(4), 479-487.

Marsaglia, G., & Tsang, W. W. (2000). A simple method for generating gamma variables. ACM Transactions on Mathematical Software ACM Trans. Math. Softw. TOMS, 26(3), 363-372.

Mckay, M. D., Beckman, R. J., & Conover, W. J. (1979). A comparison of three methods for selecting values of input variables in the analysis of output from a computer code. Technometrics, 21(2), 239-245.

Melchers, R. E. (1999). Structural reliability analysis and prediction (2nd ed.). Wiley.

Mirza, S. A., & MacGregor, J. G. (1979a). Variability of mechanical properties of reinforcing bars. Journal of the Structural Division, 105, 921-937

Mirza, S. A., & MacGregor, J. G. (1979b). Variations in dimensions of reinforced concrete members. Journal of the Structural Division, 105, 751-766.

Mirza, S. A., Hatzinikolas, M., & MacGregor, J. G. (1979). Statistical descriptions of strength of concrete. Journal of the Structural Division, 105, 1021-1037.

Mirza, S. A. (1998). Monte Carlo simulation of dispersions in composite steel-concrete column strength interaction. Engineering Structures, 20(1-2), 97-104.

Mirza, S. A., & MacGregor, J. G. (1982). Probabilistic study of strength of reinforced concrete members. Canadian Journal of Civil Engineering Can. J. Civ. Eng., 9(3), 431-448.

Montgomery, D. C., & Runger, G. C. (2014). Applied statistics and probability for engineers. Singapore: Wiley.

Nessim, M. A., Hong, H. P., & Macgregor, J. G. (1993). Verification of the material resistance factors in the CSA-S474 code for offshore concrete structures. Canadian Journal of Civil Engineering Can. J. Civ. Eng., 20(4), 660-671.

Nguyen, N. T., Sbartaï, Z., Lataste, J., Breysse, D., & Bos, F. (2013). Assessing the spatial variability of concrete structures using NDT techniques – Laboratory tests and case study. Construction and Building Materials, 49, 240-250.

Nowak, A. S., & Szerszen, M. M. (2003). Calibration of design code for buildings (ACI 318): Part 1—Statistical models for resistance. SJ ACI Structural Journal, 100(3), 378-382.

Nowak, A. S., & Collins, K. R. (2000). Reliability of structures. Boston: McGraw-Hill.

Olsson, A., Sandberg, G., & Dahlblom, O. (2003). On Latin hypercube sampling for structural reliability analysis. Structural Safety, 25(1), 47-68.

Palsson, R., & Mirza, M. S. (2002). Mechanical response of corroded steel reinforcement of abandoned concrete bridge. ACI Structural Journal, 99(2), 157-162.

Panesar, D. K., & Chidiac, S. E. (2007). Ultrasonic pulse velocity for determining the early age properties of dry-cast concrete containing ground granulated blast-furnace slag. Canadian Journal of Civil Engineering Can. J. Civ. Eng., 34(5), 682-685.

Podgorniak-Stanik, B. A. (1998). The influence of concrete strength, distribution of longitudinal reinforcement, amount of transverse reinforcement, and member size on shear strength of reinforced concrete members (Master's thesis). University of Toronto.

Polizzi, E. (2009). Density-matrix-based algorithm for solving eigenvalue problems. Phys. Rev. B Physical Review B, 79(11), 115112-1-6.

Quach, P. (2016). Understanding and safely predicting the shear response of large-scale reinforced concrete structures (Master's thesis). University of Toronto.

Rakoczy, A., & Nowak, A. (2013). Resistance model of lightweight concrete members. ACI Materials Journal, 110(1), 99-109.

Ramsay, R. J., Mirza, S. A., & MacGregor, J. G. (1979). Monte Carlo study of short time deflections of reinforced concrete beams. ACI Journal Proceedings JP, 76(8), 897-918.

Reineck, K., Bentz, E. C., Fitik, B. F., Kuchma, D. A., & Bayrak, O. (2013). ACI-DAfStb database of shear tests on slender reinforced concrete beams without stirrups. SJ ACI Structural Journal, 110(5), 867-876.

Ripley, B. D. (1987). Stochastic simulation. New York: Wiley.

Rodriguez, J., Ortega, L. M., Casal, J., & Diez, J. M. (1996). Assessing structural conditions of concrete structures with corroded reinforcement. In R. K. Dhir & M. R. Jones (Eds.), Concrete repair, rehabilitation, and protection (pp. 65-78). London, England: Boundary Row.

Sánchez, P., Huespe, A., Oliver, J., & Toro, S. (2010). Mesoscopic model to simulate the mechanical behavior of reinforced concrete members affected by corrosion. International Journal of Solids and Structures, 47(5), 559-570.

Scanlon, A., & Mikhailovsky, L. (1987). Strength evaluation of an existing concrete bridge based on core and non-destructive test data. Canadian Journal of Civil Engineering Can. J. Civ. Eng., 14(2), 145-154.

Stein, M. L. (1999). Interpolation of spatial data: Some theory for kriging. New York: Springer.

Stephens, M. J., Nessim, M. A., & Hong, H. P. (1995). Seismic reliability assessment methodology for CANDU concrete containment structures. Report prepared for Atomic Energy Control Boards. AECB Project No. 2.247.2.

Stewart, M. G., & Mullard, J. A. (2007). Spatial time-dependent reliability analysis of corrosion damage and the timing of first repair for RC structures. Engineering Structures, 29(7), 1457-1464.

Stewart, M. G., & Al-Harthy, A. (2008). Pitting corrosion and structural reliability of corroding RC structures: Experimental data and probabilistic analysis. Reliability Engineering & System Safety, 93(3), 373-382.

Stewart, M. G., & Suo, Q. (2009). Extent of spatially variable corrosion damage as an indicator of strength and time-dependent reliability of RC beams. Engineering Structures, 31(1), 198-207.

Stewart, M. G. (2009). Mechanical behaviour of pitting corrosion of flexural and shear reinforcement and its effect on structural reliability of corroding RC beams. Structural Safety, 31(1), 19-30.

Stewart, M. G. (2012). Spatial and time-dependent reliability modelling of corrosion damage, safety and maintenance for reinforced concrete structures. Structure and Infrastructure Engineering, 8(6), 607-619.

Szerszen, M. M., & Nowak, A. S. (2003). Calibration of design code for buildings (ACI 318): Part 2—Reliability analysis and resistance factors. SJ ACI Structural Journal, 100(3), 383-391.

Teixeira, A. P., Soares, C. G., & Wang, G. (2012). Probabilistic modelling of the ultimate strength of ship plates with non-uniform corrosion. J Mar Sci Technol Journal of Marine Science and Technology, 18(1), 115-132.

Unanwa, C., & Mahan, M. (2014). Statistical analysis of concrete compressive strengths for california highway bridges. J. Perform. Constr. Facil. Journal of Performance of Constructed Facilities, 28(1), 157-167.

Val, D. V., & Chernin, L. (2006). Serviceability reliability of reinforced concrete beams with corroded reinforcement. ASCE Journal of Structural Engineering, 135, 896-905.

Vecchio, F. J. (2000). Disturbed Stress Field Model for reinforced concrete: Formulation. Journal of Structural Engineering J. Struct. Eng., 126(9), 1070-1077.

Vecchio, F. J., Lai, D., Shim, W., & Ng, J. (2001). Disturbed Stress Field Model for reinforced concrete: Validation. Journal of Structural Engineering J. Struct. Eng., 127(4), 350-358.

Vořechovský, M., & Novák, D. (2005). Simulation of random fields for stochastic finite element analysis. In: Augusti, G. Schueller, G. I., & Ciampoli, (Eds). Proceedings from ICOSSAR 2005 (p. 2545-2552), Rotterdam, Netherlands.

Vořechovský, M., & Novák, D. (2009). Correlation control in small-sample Monte Carlo type simulations: A simulated annealing approach. Probabilistic Engineering Mechanics, 24(3), 452-462.

Wang, X., & Liu, X. (2006). Bond strength modeling for corroded reinforcements. Construction and Building Materials, 20, 177-186.

Wiśniewski, D. F., Cruz, P. J., Henriques, A. A., & Simões, R. A. (2012). Probabilistic models for mechanical properties of concrete, reinforcing steel and pre-stressing steel. Structure and Infrastructure Engineering, 8(2), 111-123.

Yoshida, Y. (2000). Shear reinforcement for large lightly reinforced concrete members (Master's thesis). University of Toronto.

APPENDIX A: EXPERIMENTAL DATA

The following appendix contains all of the collected data from the lab test program. All of the destructive testing data were obtained directly from Quach (2015). All of the non-destructive data were obtained by the author. As referenced in Chapter 3, all collected data are in reference to the following two grids. The first grid, in Fig. A.1 covers the entire unreinforced side of the specimen.

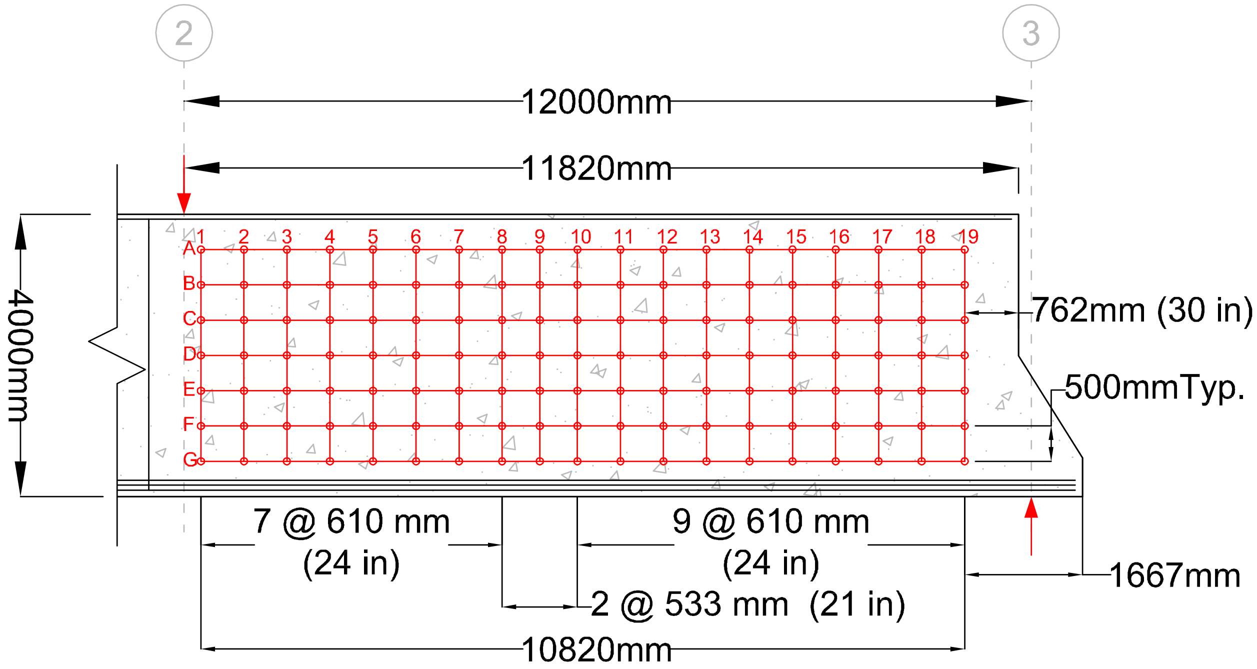

Fig. A.1: Grid layout for ultrasonic pulse velocity measurements.

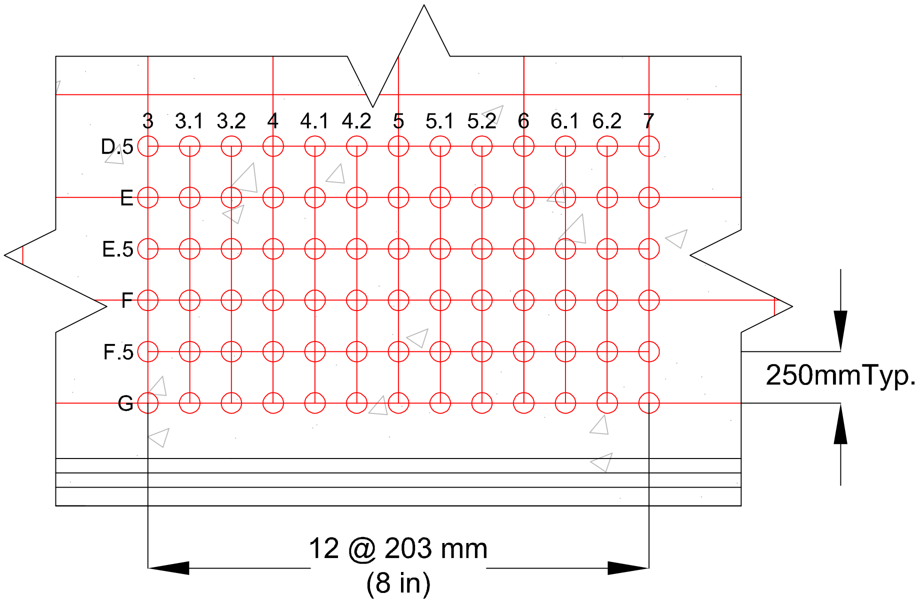

Fig. A.2: Minor grid layout for ultrasonic pulse velocity measurements.

Large Grid UPV Data

Grid Point	Reading 1 [µs]	Reading 2 [µs]	Reading 3 [µs]	Reading 4 [µs]	Reading 5 [µs]	Average [µs]
A1	53.4	52.9	52.9	52.9	52.9	53.00
B1	54.6	54.4	54.2	54.4	54.4	54.40
C1	53.4	53.9	53.4	53.4	53.4	53.50
D1	52.2	52.2	52.1	52.4	53.4	52.46
E1	51.1	51.4	50.4	51.4	51.1	51.08
F1	53.4	52.9	52.9	53.4	52.9	53.10
G1	53.2	52.9	52.9	53.4	53.4	53.16
A2	53.1	52.9	52.6	52.7	52.9	52.84
B2	54.4	53.9	54.4	54.4	54.4	54.30
C2	52.7	52.9	52.7	52.9	52.9	52.82
D2	50.9	51.4	51.4	51.2	51.1	51.20
E2	51.1	50.9	51.1	52.4	52.4	51.58
F2	53.4	52.9	52.7	52.9	53.1	53.00
G2	53.2	52.9	53.2	53.4	52.9	53.12
A3	53.4	53.6	53.4	53.4	53.4	53.44
B3	54.4	54.4	54.4	54.9	54.4	54.50
C3	53.9	53.9	53.6	53.4	53.7	53.70
D3	51.9	51.6	51.9	51.4	51.1	51.58
E3	51.9	51.9	51.4	51.4	51.4	51.60
F3	52.9	52.9	52.4	52.9	52.9	52.80
G3	53.1	52.9	52.9	52.9	52.9	52.94
A4	52.9	52.9	52.9	52.9	52.9	52.90
B4	53.9	53.9	53.9	53.9	53.9	53.90
C4	52.9	52.9	52.9	52.9	52.9	52.90
D4	51.6	51.4	51.4	51.1	50.9	51.28
E4	51.9	51.9	51.9	51.9	51.4	51.80
F4	53.4	53.4	53.4	53.4	53.1	53.34
G4	53.1	52.9	52.9	52.9	52.9	52.94
A5	53.4	53.14	53.4	53.6	53.4	53.39
B5	53.9	53.9	53.4	53.9	53.9	53.80
C5	52.4	52.4	52.4	52.4	52.4	52.40
D5	52.4	51.9	51.9	51.9	51.9	52.00
E5	51.9	51.9	51.4	51.4	51.6	51.64
F5	52.9	53.1	52.9	52.7	52.7	52.86
G5	52.4	52.4	52.4	52.4	52.4	52.40
A6	52.6	52.4	52.4	52.4	52.7	52.50
B6	52.9	53.4	52.9	53.1	53.4	53.14
C6	52.9	52.9	53.1	52.9	52.9	52.94

Grid Point	Reading 1 [μs]	Reading 2 [μs]	Reading 3 [μs]	Reading 4 [μs]	Reading 5 [μs]	Average [μs]
D6	51.9	51.9	51.9	51.7	51.7	51.82
E6	51.9	51.9	51.9	51.6	51.4	51.74
F6	53.6	53.4	53.2	53.2	53.4	53.36
G6	53.4	53.7	53.4	53.4	53.2	53.42
A7	52.9	52.6	52.4	52.6	52.7	52.64
B7	53.4	53.9	53.4	53.4	53.4	53.50
C7	52.9	52.7	52.7	52.4	52.4	52.62
D7	52.1	52.2	52.2	51.9	52.1	52.10
E7	52.2	52.4	52.4	52.2	52.4	52.32
F7	53.6	53.4	53.4	53.4	53.4	53.44
G7	53.4	53.4	53.9	53.7	53.6	53.60
A8	53.1	52.9	52.9	52.9	52.9	52.94
B8	53.9	53.9	53.9	53.9	53.9	53.90
C8	53.4	53.2	52.9	52.9	52.9	53.06
D8	52.4	52.2	52.4	52.4	52.4	52.36
E8	52.1	52.4	51.9	51.9	51.9	52.04
F8	52.9	52.9	52.9	52.9	52.9	52.90
G8	53.9	53.9	53.9	53.6	53.9	53.84
A9	52.7	52.4	52.1	52.2	52.7	52.42
B9	52.4	52.4	52.4	52.4	52.9	52.50
C9	51.52	51.4	51.4	51.1	50.9	51.26
D9	51.4	51.4	51.4	51.4	51.4	51.40
E9	50.9	50.9	50.9	50.9	50.9	50.90
F9	52.4	52.4	52.4	52.4	52.4	52.40
G9	52.9	52.9	52.9	52.9	52.9	52.90
A10	53.1	52.9	52.9	52.9	52.9	52.94
B10	53.4	53.4	53.4	53.4	53.2	53.36
C10	52.4	52.4	52.2	51.9	52.4	52.26
D10	51.9	51.9	51.6	51.9	51.9	51.84
E10	51.9	51.9	51.9	51.6	51.4	51.74
F10	52.9	52.9	52.9	52.9	52.9	52.90
G10	52.9	52.9	52.9	52.7	52.4	52.76
A11	52.4	52.4	52.4	52.4	52.4	52.40
B11	53.6	53.4	53.4	53.4	53.4	53.44
C11	54.1	53.9	53.9	54.2	53.9	54.00
D11	51.9	51.9	51.9	51.9	51.7	51.86
E11	51.9	51.9	51.9	51.9	51.9	51.90
F11	52.2	52.4	52.4	52.4	52.4	52.36
G11	52.4	52.4	52.4	52.4	52.4	52.40

Grid Point	Reading 1 [μs]	Reading 2 [μs]	Reading 3 [μs]	Reading 4 [μs]	Reading 5 [μs]	Average [μs]
A12	52.1	52.4	51.9	52.4	51.9	52.14
B12	53.4	53.4	53.4	53.4	53.4	53.40
C12	52.9	52.9	52.6	52.9	52.4	52.74
D12	50.9	50.9	51.4	51.4	51.1	51.14
E12	51.2	51.6	51.4	51.9	51.9	51.60
F12	52.9	52.9	52.9	52.9	52.9	52.90
G12	52.9	52.9	52.9	52.9	52.9	52.90
A13	52.9	52.9	52.9	52.9	52.4	52.80
B13	53.9	53.6	53.9	53.6	53.4	53.68
C13	52.9	52.9	52.9	53.2	53.1	53.00
D13	51.2	51.2	51.2	51.4	51.1	51.22
E13	51.9	51.9	52.4	51.4	51.9	51.90
F13	52.9	52.9	52.4	52.9	52.4	52.70
G13	53.1	53.4	53.4	53.4	53.9	53.44
A14	52.4	52.6	52.4	52.4	51.9	52.34
B14	53.6	53.4	53.4	53.4	52.9	53.34
C14	52.2	52.2	51.9	52.2	52.1	52.12
D14	51.4	51.4	51.4	51.4	51.4	51.40
E14	51.4	51.4	51.4	51.4	51.4	51.40
F14	52.9	52.9	52.9	52.4	52.7	52.76
G14	53.4	53.2	53.4	52.9	52.9	53.16
A15	53.4	53.4	53.4	53.4	53.4	53.40
B15	52.9	52.9	52.9	52.9	53.4	53.00
C15	51.9	53.9	52.4	52.2	52.2	52.52
D15	51.6	51.4	51.4	51.1	51.4	51.38
E15	51.7	51.4	51.4	51.4	51.4	51.46
F15	52.9	52.9	52.9	52.9	52.9	52.90
G15	53.9	53.9	53.9	53.9	53.9	53.90
A16	53.9	53.9	53.4	53.4	53.4	53.60
B16	53.4	52.9	52.9	53.4	53.1	53.14
C16	52.2	52.4	51.9	52.1	52.4	52.20
D16	51.4	51.4	51.4	51.4	51.4	51.40
E16	51.4	51.4	51.4	51.45	51.4	51.41
F16	53.4	53.4	53.4	53.4	53.4	53.40
G16	53.6	53.9	53.6	53.9	53.9	53.78
A17	53.1	52.9	52.9	53.1	52.9	52.98
B17	53.2	52.9	52.6	52.9	52.9	52.90
C17	52.4	52.4	52.1	51.9	51.9	52.14
D17	50.9	50.9	51.4	50.9	50.9	51.00

Grid Point	Reading 1 [µs]	Reading 2 [µs]	Reading 3 [µs]	Reading 4 [µs]	Reading 5 [µs]	Average [µs]
E17	50.9	51.1	51.1	51.1	50.9	51.02
F17	51.9	52.4	52.04	52.4	52.4	52.23
G17	52.9	52.4	52.4	52.4	52.4	52.50
A18	53.4	53.4	53.4	53.4	53.4	53.40
B18	53.9	52.9	52.9	53.4	53.1	53.24
C18	51.4	52.4	51.6	52.4	51.9	51.94
D18	51.4	51.4	51.4	51.4	51.4	51.40
E18	50.9	51.4	51.2	51.1	50.9	51.10
F18	51.4	51.4	51.9	51.4	51.9	51.60
G18	53.4	53.4	53.9	53.9	53.4	53.60
A19	53.9	53.9	53.9	53.6	53.9	53.84
B19	53.4	53.2	53.1	53.1	52.9	53.14
C19	50.9	51.2	51.4	51.9	51.9	51.46
D19	51.9	51.9	51.4	51.9	51.9	51.80
E19	51.4	51.4	51.4	51.4	51.4	51.40
F19	53.4	52.9	53.2	52.9	52.9	53.06
G19	53.2	52.9	52.9	53.2	53.4	53.12
G - 5.1	52.1	52.2	52.4	52.7	52.4	52.36

Small Grid UPV Data

Grid Point	Reading 1 [µs]	Reading 2 [µs]	Reading 3 [µs]	Reading 4 [µs]	Reading 5 [µs]	Average [µs]
D.5 - 3	51.9	51.6	51.4	51.4	51.4	51.54
D.5 - 3.1	51.4	51.4	51.4	51.4	51.4	51.40
D.5 - 3.2	51.9	51.7	51.4	51.4	51.4	51.56
D.5 - 4	52.1	52.9	52.4	52.4	52.4	52.44
D.5 - 4.1	51.4	51.4	51.4	51.4	51.4	51.40
D.5 - 4.2	51.6	51.4	51.7	51.4	51.4	51.50
D.5 - 5	51.9	51.9	51.9	51.9	51.9	51.90
D.5 - 5.1	51.9	51.6	51.7	51.9	51.9	51.80
D.5 - 5.2	51.9	51.9	51.9	51.9	51.7	51.86
D.5 - 6	52.4	52.4	52.2	52.4	52.6	52.40
D.5 - 6.1	51.9	51.9	51.4	51.6	51.4	51.64
D.5 - 6.2	50.9	51.1	50.9	50.9	50.9	50.94
D.5 - 7	52.4	51.9	51.9	51.9	52.4	52.10
E - 3.1	50.9	51.1	50.9	51.2	51.4	51.10
E - 3.2	50.9	50.6	50.4	50.4	50.4	50.54
E - 4.1	51.4	51.1	50.9	50.9	50.9	51.04
E - 4.2	50.9	50.9	50.9	50.9	50.9	50.90

Grid Point	Reading 1 [μs]	Reading 2 [μs]	Reading 3 [μs]	Reading 4 [μs]	Reading 5 [μs]	Average [μs]
E - 5.1	51.9	51.6	51.4	51.4	51.4	51.54
E - 5.2	50.9	50.9	50.9	50.9	50.9	50.90
E - 6.1	51.4	51.2	51.9	51.4	51.4	51.46
E - 6.2	50.9	50.9	50.9	50.9	50.9	50.90
E.5 - 3	50.9	50.9	50.9	50.9	50.9	50.90
E.5 - 3.1	51.4	51.4	51.4	51.4	51.2	51.36
E.5 - 3.2	50.7	50.9	50.9	51.4	51.2	51.02
E.5 - 4	52.4	51.9	51.9	51.6	51.4	51.84
E.5 - 4.1	50.9	50.9	50.7	50.6	50.6	50.74
E.5 - 4.2	50.7	50.6	50.4	50.4	50.4	50.50
E.5 - 5	51.4	51.4	51.4	51.4	51.4	51.40
E.5 - 5.1	51.4	51.4	51.4	51.4	51.4	51.40
E.5 - 5.2	50.9	50.4	50.4	50.4	50.4	50.50
E.5 - 6	51.4	51.4	51.4	51.4	51.4	51.40
E.5 - 6.1	51.4	51.2	50.9	50.9	50.9	51.06
E.5 - 6.2	50.4	50.4	50.4	50.4	50.4	50.40
E.5 - 7	51.9	51.9	51.9	51.9	51.9	51.90
F - 3.1	52.9	52.4	52.4	52.4	52.4	52.50
F - 3.2	52.6	52.9	52.9	52.7	52.4	52.70
F - 4.1	51.9	51.9	51.7	51.6	51.4	51.70
F - 4.2	52.4	52.4	52.4	52.4	52.4	52.40
F - 5.1	52.4	51.9	52.2	51.9	51.9	52.06
F - 5.2	52.2	52.4	52.4	52.1	51.9	52.20
F - 6.1	52.1	52.2	51.9	51.9	51.9	52.00
F - 6.2	52.4	52.9	52.9	52.9	52.9	52.80
F.5 - 3	52.6	52.4	52.4	52.4	52.4	52.44
F.5 - 3.1	51.9	51.9	52.2	52.1	52.1	52.04
F.5 - 3.2	51.7	52.4	51.9	51.9	51.9	51.96
F.5 - 4	54.1	52.4	52.6	52.4	52.4	52.78
F.5 - 4.1	51.4	51.9	51.9	51.7	51.9	51.76
F.5 - 4.2	51.9	52.4	51.9	52.4	52.4	52.20
F.5 - 5	52.9	52.4	52.4	52.6	52.6	52.58
F.5 - 5.1	51.9	52.1	51.9	51.9	51.9	51.94
F.5 - 5.2	52.4	52.4	52.4	52.4	52.4	52.40
F.5 - 6	53.2	53.4	53.2	52.9	52.9	53.12
F.5 - 6.1	52.4	52.7	52.4	52.4	52.4	52.46
F.5 - 6.2	52.9	52.9	52.7	52.4	52.4	52.66
F.5 - 7	53.4	52.9	53.1	52.9	53.4	53.14
G - 3.1	52.4	52.4	52.6	52.2	52.4	52.40

Grid Point	Reading 1 [µs]	Reading 2 [µs]	Reading 3 [µs]	Reading 4 [µs]	Reading 5 [µs]	Average [µs]
G - 3.2	51.9	51.9	51.9	51.9	51.7	51.86
G - 4.1	51.9	51.9	51.9	51.7	51.9	51.86
G - 4.2	51.4	51.4	51.4	51.4	51.4	51.40
G - 5.1	52.1	52.2	52.4	52.7	52.4	52.36
G - 5.2	51.9	52.9	52.4	52.1	52.1	52.28
G - 6.1	53.4	52.6	52.4	52.7	52.4	52.70
G - 6.2	52.4	52.4	52.4	52.4	52.4	52.40

UPV Cylinder Data

The cylinders were measured as well as the main grid. The following tables are all of the collected data for the cylinders as well as the UPV for each cylinder and the average UPV for each test date.

7-day Cylinders

Cylinder ID	Cylinder Length				UPV Time Measurements					Time Avg [µs]	Velocity Avg [m/s]
	L1 mm	L2 mm	L3 mm	L avg mm	t1 [µs]	t2 [µs]	t3 [µs]	t4 [µs]	t5 [µs]		
PLS4K T1D7A	301	301	301	301	64.9	64.9	64.9	64.9	-	64.9	4638
PLS4k T1D7B	296	295	296	295.6	63.9	63.9	64.4	64.4	-	64.15	4609
PLS4K T2D7A	298	299	298	298.3	62.6	64.4	62.9	62.7	62.4	63.00	4735
PLS4K T2D7B	300	298	300	299.3	63.4	63.1	63.4	63.4	-	63.33	4727
PLS4K T3D7A	294	295	294	294.3	62.9	62.4	62.4	62.9	-	62.65	4698
PLS4k T3D7B	298	297	297	297.3	66.7	64.7	65.4	64.7	64.1	65.12	4566
										Mean	4662
										COV	1.47%

14-day Cylinders

Cylinder ID	Cylinder Length L1 mm	L2 mm	L3 mm	L avg mm	UPV Time Measurements t1 [µs]	t2 [µs]	t3 [µs]	t4 [µs]	t5 [µs]	Time Avg [µs]	Velocity Avg [m/s]
PLS4K T1D14A	299	298	-	298.5	61.9	61.9	61.4	61.4	-	61.65	4842
PLS4k T1D14B	295	296	-	295.5	61.4	61.4	61.9	61.9	-	61.65	4793
PLS4K T2D14A	295	295	-	295	60.9	60.9	60.9	60.9	-	60.90	4844
PLS4K T2D14B	293	293	-	293	60.4	60.4	60.4	60.4	-	60.40	4851
PLS4K T3D14A	299	299	-	299	62.9	62.9	62.9	62.9	-	62.90	4754
PLS4k T3D14B	299	299	-	299	62.4	62.4	62.4	61.9	-	62.28	4801
										Mean	4814
										COV	0.72%

22-day Cylinders

Cylinder ID	Cylinder Length L1 mm	L2 mm	L3 mm	L avg mm	UPV Time Measurements t1 [µs]	t2 [µs]	t3 [µs]	t4 [µs]	t5 [µs]	Time Avg [µs]	Velocity Avg [m/s]
PLS4K T1D22A	304	304	303	303.7	62.1	62.4	61.9	62.1	-	62.13	4888
PLS4k T1D22B	303	304	303	303.3	61.9	61.9	61.9	61.9	-	61.90	4900
PLS4K T2D22A	296	296	296	296.0	60.9	60.9	60.9	60.9	-	60.90	4860
PLS4K T2D22B	296	297	297	296.7	60.9	60.9	60.9	60.7	-	60.85	4875
PLS4K T3D22A	304	304	305	304.3	62.6	62.4	62.1	62.4	-	62.38	4879
PLS4k T3D22B	303	304	304	303.7	62.6	62.9	62.9	62.9	-	62.83	4834
										Mean	4873
										COV	0.44%

28-day Cylinders

Cylinder ID	Cylinder Length				UPV Time Measurements					Time Avg [µs]	Velocity Avg [m/s]
	L1 mm	L2 mm	L3 mm	L avg mm	t1 [µs]	t2 [µs]	t3 [µs]	t4 [µs]	t5 [µs]		
PLS4K T1D28A	300	300	301	300.3	60.9	61.1	60.9	60.9	-	60.95	4928
PLS4k T1D28B	301	301	302	301.3	61.9	61.9	62.1	62.1	-	62.00	4860
PLS4K T2D28A	303	304	302	303.0	61.4	61.4	61.4	61.4	-	61.40	4935
PLS4K T2D28B	300	301	301	300.7	60.1	60.2	60.4	60.2	-	60.23	4992
PLS4K T3D28A	302	303	302	302.3	60.9	60.9	60.7	60.9	-	60.85	4969
PLS4k T3D28B	304	304	303	303.7	61.9	61.9	61.7	61.9	-	61.85	4910
										Mean	4932
										COV	0.85%

42-day Cylinders

Cylinder ID	Cylinder Length				UPV Time Measurements					Time Avg [µs]	Velocity Avg [m/s]
	L1 mm	L2 mm	L3 mm	L avg mm	t1 [µs]	t2 [µs]	t3 [µs]	t4 [µs]	t5 [µs]		
PLS4K T1D42A	302	301	301	301.3	60.9	60.9	60.9	61.1	-	60.95	4944
PLS4k T1D42B	304	303	303	303.3	60.6	60.4	60.4	60.4	-	60.45	5018
PLS4K T2D42A	301	301	301	301.0	60.7	60.4	60.4	60.2	-	60.43	4981
PLS4K T2D42B	303	303	303	303.0	60.4	60.9	60.1	60.4	-	60.45	5012
PLS4K T3D42A	301	301	301	301.0	59.9	59.7	59.7	59.9	-	59.80	5033
PLS4k T3D42B	304	305	305	304.7	60.3	60.9	60.9	60.7	-	60.70	5019
										Mean	5001
										COV	0.60%

APPENDIX B: PROFESSIONAL FACTOR SIMULATION RESULTS

The professional factor simulation results presented below are based on the database vuct-RC-A2A3 published by Reineck et al. (2014). This database represents an exhaustive list of 784 tests for shear-critical reinforced concrete beams with no shear reinforcement. All of the tests with uniform loading and T-shaped beams were removed. Additionally, all tests missing information on the bearing plates were removed. This left a total of 371 tests that were analyzed using VecTor2. Of the 371, 318 tests were successfully modelled. The 53 tests that were excluded contained issues with the automated mesh generator. Fig. B.1 shows the results of the simulation.

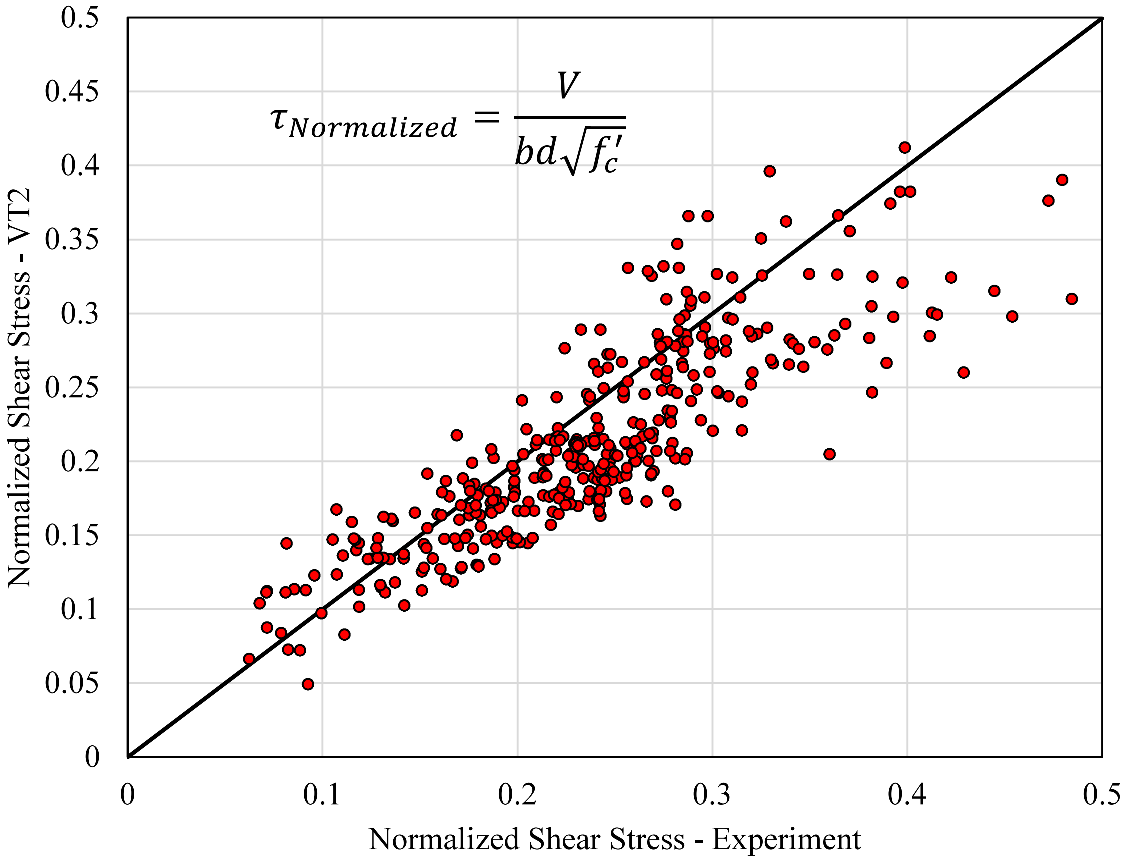

Fig. B.1: Simulation results for VecTor2 professional factor.

Database ID	Original Designation	L [mm]	D [mm]	$V_{Exp.}$ [kN]	V_{VT2} [kN]	$\frac{V_{Exp.}}{V_{VT2}}$
123	DB0530	5400	925	167.9	124.9	1.344
124	DB120	5400	925	181.9	188.1	1.054
125	DB130	5400	925	187.9	218.2	0.927
126	DB140	5400	925	182.9	241.1	0.811
127	DB165	5400	925	187.9	265.1	0.753
128	DB180	5400	925	174.9	290.2	0.637
129	DB230	5400	895	259.9	285.8	0.962
131	2	2500	250	221.6	169.4	1.377
132	3	2500	250	226.1	203.4	1.161
134	11	4750	500	279.7	267.4	1.168
135	12	4750	500	342.5	322.9	1.161
161	AT-1 - East	5400	916	1194.2	1159.2	1.133
162	AT-1 West	5400	916	1287.8	1155.9	1.225
163	AT-2 / 250N	2600	437	116.8	87.2	1.386
164	AT-2/ 250W	2600	439	113.7	87.9	1.339
165	AT-2 /1000W	2600	439	479.3	354.9	1.398
166	AT-2/1000N	2600	438	448.0	348.0	1.333
167	AT-2/3000	2600	439	1308.4	1073.1	1.261
168	AT-3/N1	2080	307	240.2	190.5	1.304
169	AT-3/N2	2080	306	261.3	190.6	1.419
170	AT-3/T1	2080	306	256.4	191.8	1.383
171	AT-3/T2	2080	307	252.3	191.2	1.366
172	A1	2100	168	21.5	16.9	1.311
173	A2	2100	168	24.1	16.1	1.541
174	A3	2100	168	20.2	16.4	1.266
175	A4	2100	168	21.9	16.9	1.335
176	A5	2100	168	21.3	16.1	1.365
177	A6	2100	168	17.6	16.4	1.106
184	B1	1800	300	71.0	72.3	1.008
185	B2	3600	600	119.5	129.2	0.969
186	B3	5400	900	166.4	179.5	0.993
187	B4	7200	1200	187.1	239.9	0.852
188	B5	3600	600	106.9	85.6	1.340
189	B6	3600	600	115.4	103.0	1.188
190	B7	5400	900	140.0	135.5	1.134
191	B8	5400	900	127.6	164.2	0.839
192	0A-1	3658	461	170.7	117.9	1.541
193	0A-2	4572	466	184.4	120.9	1.646
195	H 50/1	2160	360	100.8	103.6	0.991

Database ID	Original Designation	L [mm]	D [mm]	$V_{Exp.}$ [kN]	V_{VT2} [kN]	$\frac{V_{Exp.}}{V_{VT2}}$
196	H 50/5	2160	360	178.7	103.6	1.756
197	H 60/1	2160	360	109.2	108.6	1.023
198	H 75/1	2160	360	101.0	112.5	0.913
199	H 100/1	2160	360	118.9	119.1	1.014
200	H 100/5	2160	360	141.2	119.1	1.204
201	SB 2012/0	10800	1845	418.4	409.9	1.204
202	SB 2003/0	10800	1925	238.9	176.0	0.938
241	IA1	1168	137	20.0	22.1	0.912
243	IB1	762	137	19.6	24.3	0.812
245	IC1	965	137	19.7	23.2	0.855
246	IC2	965	137	17.9	23.2	0.776
249	IIB1	1168	137	16.7	16.3	1.037
251	IIC1	762	137	17.9	21.6	0.831
267	4-21a	1067	137	21.2	22.5	0.949
269	4-22a	1067	137	21.5	21.7	1.000
271	4-23a	1067	137	21.7	21.8	1.004
277	5-21a	1067	137	29.0	24.8	1.176
278	5-21b	1067	137	27.6	24.9	1.116
279	5-22a	1067	137	22.5	24.5	0.926
280	5-22b	1067	137	26.0	24.5	1.070
281	5-23a	1067	137	24.6	24.8	0.999
282	5-23b	1067	137	23.5	24.7	0.956
295	B100	5400	925	227.9	231.7	1.054
296	B100H	5400	925	193.0	317.8	0.639
297	B100B	5400	925	206.9	240.5	0.920
298	B100L	5400	925	225.9	240.3	1.005
299	B100-R	5400	925	251.9	231.7	1.165
300	B100HE	5400	925	219.9	317.8	0.728
301	B100L-R	5400	925	237.9	246.4	1.031
351	L-2	2438	252	76.4	51.4	1.524
352	L-2A	2438	252	80.9	63.4	1.302
353	L-3	2946	252	54.3	47.0	1.195
354	L-4	3454	252	52.0	41.4	1.315
355	L-5	3962	252	52.2	39.2	1.408
358	L2R	1524	252	74.8	53.8	1.411
359	L2aR	1524	252	93.0	68.5	1.372
360	L3R	2032	252	62.4	51.7	1.232
399	N155 (N)	1138	128	112.5	108.5	1.045
400	N155 (S)	1138	128	85.2	84.4	1.020

Database ID	Original Designation	L [mm]	D [mm]	$V_{Exp.}$ [kN]	V_{VT2} [kN]	$\frac{V_{Exp.}}{V_{VT2}}$
401	N220 (N)	1450	190	123.7	132.2	0.946
402	N220 (S)	1450	190	104.6	108.3	0.979
403	N350 (N)	2063	313	180.8	182.3	1.009
404	N350 (S)	2063	313	160.2	147.8	1.108
405	N485 (N)	2700	440	219.1	226.2	0.992
406	N485 (S)	2700	440	191.2	176.4	1.118
409	H90 (N)	825	65	77.7	101.1	0.967
410	H90 (S)	825	65	52.4	76.0	0.826
411	H155 (N)	1138	128	105.6	119.2	0.892
412	H155 (S)	1138	128	77.3	105.5	0.838
413	H220 (N)	1450	190	136.3	152.8	0.900
414	H220 (S)	1450	190	106.9	116.6	0.928
415	H350 (N)	2063	313	191.8	210.9	0.923
416	H350 (S)	2063	313	159.5	153.6	1.060
417	H485 (N)	2700	440	202.7	258.3	0.802
418	H485 (S)	2700	440	202.2	192.1	1.083
421	S 1.1	1540	153	70.9	77.0	0.936
422	S 1.2	1540	152	75.9	86.7	0.888
423	S 1.3	1540	146	99.3	102.8	0.977
424	S 2.2	3260	348	194.0	150.8	1.327
425	S 2.4	3260	328	233.2	193.3	1.236
426	S 3.2	6860	718	270.2	294.9	0.975
428	S 3.4	6860	690	393.1	379.5	1.087
449	B91SC4-2-69	2000	195	74.6	55.9	1.360
451	B91SD2-4-61	2000	195	90.5	63.1	1.461
452	B91SD3-4-66	2000	195	82.1	65.4	1.278
453	B91SD4-4-66	2000	195	79.6	65.2	1.242
463	G1	2560	370	45.0	39.4	1.174
464	G2	2560	372	41.4	30.3	1.418
466	G4a	4440	372	31.0	24.1	1.405
467	G4b	4440	372	38.9	28.2	1.487
468	8A-X	1981	267	81.2	59.5	1.387
469	8A	1981	267	58.4	62.1	0.957
470	8B	1981	267	91.1	68.9	1.342
471	8C	1981	267	128.0	99.3	1.303
472	8D	1981	267	166.2	107.3	1.564
482	M100-S0	2200	203	65.6	59.2	1.135
483	M80-S0	2200	203	58.6	56.0	1.073
484	M60-S0	2200	207	46.1	42.9	1.111

Database ID	Original Designation	L [mm]	D [mm]	$V_{Exp.}$ [kN]	V_{VT2} [kN]	$\frac{V_{Exp.}}{V_{VT2}}$
485	M40-S0	2200	205	55.6	45.2	1.269
486	M25-S0	2200	207	48.1	35.1	1.427
488	40	1952	140	32.0	25.9	1.263
489	41	1137	141	51.4	42.2	1.229
490	43	2083	137	29.1	25.2	1.183
494	47	1814	132	28.2	25.1	1.146
495	48	1814	133	27.1	25.9	1.068
496	52	1544	138	28.9	31.3	0.936
499	55	1270	135	32.6	35.3	0.933
500	56	1409	137	28.0	34.9	0.812
501	57	1952	139	31.6	26.2	1.231
502	58	1409	138	28.9	35.3	0.829
503	59	1203	140	50.2	40.3	1.256
504	60	1271	139	39.3	38.1	1.042
521	63	5356	543	93.2	86.4	1.153
523	65	3734	552	112.3	105.2	1.106
535	3042	7506	1095	236.9	183.7	1.395
536	3043	8585	1092	165.0	171.6	1.063
663	709	3633	279	52.0	43.1	1.264
664	666	2546	277	63.4	62.4	1.038
665	675	2548	277	56.7	59.5	0.975
666	718	3632	280	54.3	43.7	1.298
683	CTL-1	1890	270	71.3	71.1	1.018
684	CTL-2	1890	270	72.3	71.1	1.032
685	P1.0-1	1904	272	58.9	54.3	1.107
686	P1.0-2	1904	272	57.1	54.3	1.072
687	P3.4-1	1869	267	78.7	88.1	0.904
688	P3.4-2	1869	267	79.2	88.1	0.909
689	P4.6-1	1785	255	90.4	95.9	0.952
690	P4.6-2	1785	255	96.0	95.9	1.011
693	A4.5-1	2700	270	67.5	55.4	1.253
694	A4.5-2	2700	270	64.7	55.4	1.201
695	A6.0-1	3510	270	60.4	50.4	1.248
696	A6.0-2	3510	270	62.2	50.4	1.286
697	D142-1	994	142	41.2	49.5	0.839
698	D142-2	994	142	39.5	49.5	0.805
699	D550-1	3850	550	231.0	215.1	1.110
700	D550-2	3850	550	219.4	215.1	1.055
701	D915-1	6405	915	284.9	337.7	0.892

Database ID	Original Designation	L [mm]	D [mm]	$V_{Exp.}$ [kN]	V_{VT2} [kN]	$\frac{V_{Exp.}}{V_{VT2}}$
702	D915-2	6405	915	345.3	337.7	1.081
713	11A2	1829	314	74.4	73.3	1.036
714	12A2	1829	238	64.7	55.1	1.203
715	III-18A2	1829	316	64.0	58.2	1.129
716	18B2	1829	316	73.0	58.9	1.272
717	18C2	1829	316	73.9	62.1	1.220
718	18D2	1829	316	60.9	61.5	1.015
719	IV-13A2	1829	319	49.2	35.4	1.453
720	14A2	1829	243	35.8	29.0	1.291
721	15A2	1829	316	46.5	44.5	1.081
722	15B2	1829	316	52.7	45.1	1.210
723	16A2	1829	240	42.5	34.5	1.280
724	17A2	1829	243	44.6	38.6	1.196
725	18E2	1829	316	82.6	58.7	1.445
726	19A2	1829	240	46.8	44.3	1.088
727	20A2	1829	238	51.3	46.7	1.130
728	21A2	1829	238	77.2	63.4	1.252
730	2AC	2438	254	38.3	30.8	1.314
731	3AC	2438	256	45.1	33.9	1.397
732	4AC	2438	254	38.4	33.1	1.218
733	5AC	2438	252	42.7	37.0	1.208
734	6AC	2438	250	54.4	43.1	1.310
737	3CC	3048	256	36.5	31.5	1.236
738	4CC	3048	254	41.0	32.9	1.323
739	5CC	3048	252	45.8	34.9	1.391
753	VII-6C	1829	252	51.9	47.4	1.125
754	VIII- 3AAC	1829	256	56.4	48.3	1.199
755	4AAC	1829	254	58.5	51.1	1.174
756	5AAC	1829	252	57.6	56.2	1.048
757	6AAC	1829	250	60.7	61.3	1.011
758	3AC	2438	256	54.1	38.5	1.468
759	4AC	2438	254	54.8	42.7	1.334
760	5AC	2438	252	55.3	47.0	1.218
761	6AC	2438	250	59.9	50.3	1.231
762	4CC	3048	254	53.7	41.4	1.361
763	5CC	3048	252	58.1	42.6	1.431
764	6CC	3048	250	63.8	49.4	1.344
766	5EC	3658	252	53.9	42.0	1.357
767	6EC	3658	250	50.0	42.6	1.240

Database ID	Original Designation	L [mm]	D [mm]	$V_{Exp.}$ [kN]	V_{VT2} [kN]	$\frac{V_{Exp.}}{V_{VT2}}$
769	4AAC	1829	254	43.2	35.9	1.247
770	5AAC	1829	252	51.0	41.9	1.256
772	3AC	2438	256	37.5	28.0	1.420
777	4CC	3048	254	35.8	29.8	1.285
782	X-C	3048	483	86.8	77.4	1.183
783	XI-PCA	3658	250	53.9	42.3	1.348
784	PCB	3658	250	53.9	42.4	1.345
785	s-I-OCa	3048	254	49.1	41.5	1.241
786	OCb	3048	254	53.1	43.9	1.265
787	s-II- Oca	3658	456	150.0	127.9	1.228
788	OCb	3658	456	137.3	127.9	1.125
820	S2	2743	269	43.2	39.8	1.125
821	S3	2743	265	53.8	43.1	1.292
822	S4	2743	263	56.3	46.1	1.260
823	S5	2743	262	50.5	48.0	1.085
826	S11	2743	267	34.5	29.0	1.252
827	S13	2743	262	50.5	45.5	1.146
845	4l	1700	270	81.2	77.3	1.068
846	4r	1700	270	86.6	79.5	1.107
847	5l	1950	270	59.8	67.6	0.904
848	5r	1950	270	75.8	68.9	1.125
849	6l	2350	270	59.7	58.0	1.061
850	6r	2350	270	67.2	58.4	1.186
851	7-1	3100	278	60.9	51.6	1.233
852	7-2	3100	278	67.0	50.7	1.383
853	8-1	3600	278	64.0	48.9	1.383
854	8-2	3600	274	64.2	50.4	1.345
859	EA1	2000	270	59.2	64.1	0.951
860	EA2	2000	270	75.5	59.3	1.313
861	D1/1	520	70	7.3	7.0	1.050
862	D1/2	520	70	7.2	7.0	1.036
863	D2/1	1040	140	21.3	22.5	0.957
864	D2/2	1040	140	23.4	22.5	1.049
865	D3/1	1560	210	46.8	44.1	1.080
866	D3/2l	1560	210	41.6	44.1	0.960
867	D3/2r	1560	210	44.9	44.1	1.037
868	D4/1	2080	280	75.1	69.7	1.106
869	D4/2l	2080	280	75.0	69.7	1.105
870	D4/2r	2080	280	69.6	69.7	1.026

Database ID	Original Designation	L [mm]	D [mm]	$V_{Exp.}$ [kN]	V_{VT2} [kN]	$\frac{V_{Exp.}}{V_{VT2}}$
871	C1	1000	150	21.7	23.7	0.926
872	C2	2000	300	65.5	53.6	1.248
873	C3	3000	450	100.5	96.0	1.083
874	C4	4000	600	150.8	141.1	1.118
875	E6	2000	270	92.0	75.1	1.256
907	IIIa- 17	3658	403	90.4	84.7	1.115
908	IIIa-18	3658	403	83.1	82.3	1.056
909	Va-19	3658	403	65.7	60.2	1.160
910	Va-20	3658	403	68.3	62.0	1.170
911	VIb-21	2896	403	73.3	61.5	1.249
912	VIb-22	2896	403	64.3	61.2	1.101
913	VIb-23	2896	403	77.0	64.0	1.258
914	VIa-24	3658	403	56.9	44.7	1.384
915	VIa-25	3658	403	52.3	47.7	1.186
929	A1	1600	262	60.6	65.7	0.935
930	A2	1600	267	67.3	68.7	0.992
931	A3	1600	268	76.2	70.5	1.095
932	A4	1600	270	71.7	73.7	0.985
933	B1	1600	267	56.8	53.5	1.080
934	B2	1600	268	60.6	54.8	1.125
935	B3	1600	270	56.1	52.9	1.080
936	B4	1600	272	56.1	51.1	1.119
941	1	2743	268	58.8	50.5	1.199
942	2	2743	268	36.6	38.7	0.982
943	3	2743	268	53.3	44.8	1.229
944	4	2743	268	41.5	37.7	1.144
945	5	2743	268	53.1	48.2	1.135
946	6	2743	268	35.5	37.9	0.973
947	7	2743	268	52.2	48.5	1.108
949	9	2743	268	54.4	52.4	1.067
950	10	2743	268	49.9	44.1	1.171
951	11	2743	268	61.1	51.4	1.222
952	12	2743	268	48.2	41.8	1.193
953	13	2743	268	56.6	50.5	1.154
954	14	2743	268	44.2	43.5	1.050
955	15	2743	268	52.2	50.1	1.072
956	16	2743	268	38.8	38.6	1.045
983	B40 B4	2388	368	157.6	138.2	1.170
984	B56 B2	3200	368	102.6	83.0	1.302

Database ID	Original Designation	L [mm]	D [mm]	$V_{Exp.}$ [kN]	V_{VT2} [kN]	$\frac{V_{Exp.}}{V_{VT2}}$
986	B56 A4	3200	375	140.4	115.8	1.258
987	B56 B4	3200	368	124.8	106.1	1.225
988	B56 E4	3200	368	111.5	91.5	1.277
989	B56 A6	3200	356	180.5	148.9	1.248
990	B56 B6	3200	372	139.3	127.5	1.130
991	B70 B2	3912	365	92.0	78.5	1.264
992	B70 A4	3912	368	135.4	103.3	1.387
993	B70 A6	3912	356	181.0	140.5	1.343
994	B84 B4	4623	363	114.8	88.6	1.403
997	AO-3-3b	2134	298	65.3	54.3	1.229
998	AO-3-3c	2134	298	67.5	53.4	1.292
999	AO-7-3a	2134	298	82.8	68.9	1.223
1000	AO-7-3b	2134	298	83.5	70.7	1.200
1001	AO-11-3a	2134	298	90.4	84.8	1.080
1002	AO-11-3b	2134	298	90.0	84.1	1.086
1003	AO-15-3a	2134	298	94.1	86.8	1.099
1004	AO-15-3b	2134	298	100.7	90.6	1.126
1005	AO-15-3c	2134	298	98.5	89.9	1.110
1006	AO-3-2	1492	298	78.2	64.3	1.239
1007	AO-7-2	1492	298	118.4	90.9	1.319
1008	AO-11-2	1492	298	111.8	106.7	1.059
1009	AO-15-2a	1492	298	178.3	109.3	1.649
1010	AO-15-2b	1492	298	206.2	102.7	2.031
1025	BRL100	5400	925	165.6	192.1	0.938
1026	BRH100	5400	895	690.4	508.4	1.402
1027	BN100	5400	925	193.6	200.1	1.049
1028	BH100	5400	925	195.0	254.4	0.817
1029	BN50	2700	450	132.4	98.3	1.403
1030	BH50	2700	450	132.0	133.1	1.022
1031	BN25	1352	225	73.0	73.1	1.012
1032	BH25	1352	225	85.2	90.4	0.953
1044	R1	1828	272	46.5	43.2	1.104
1046	R3	1828	272	46.5	42.6	1.120
1050	R7	1828	272	56.5	44.2	1.311
1051	R29	1828	272	54.5	45.3	1.233
1054	P 1	3000	313	333.1	264.5	1.311
1069	1.2 / 1	1800	260	91.2	90.7	1.018
1071	2.3 / 1	2300	262	79.7	63.3	1.292
1072	2.4 / 1	2250	260	121.1	79.8	1.548

Database ID	Original Designation	L [mm]	D [mm]	$V_{Exp.}$ [kN]	V_{VT2} [kN]	$\frac{V_{Exp.}}{V_{VT2}}$
1073	2.6 / 1	2250	260	75.9	59.1	1.319
1074	X	1250	111	14.7	16.1	0.926
1075	Y	2240	199	30.6	32.0	0.980
1076	Z	2960	262	56.0	56.5	1.028
1086	A-2	3500	372	85.3	79.9	1.115
1089	B-2	3500	368	127.3	115.9	1.132
1090	B-3	3500	368	111.9	102.0	1.135
1092	C-2	3500	366	123.3	141.0	0.896
1093	C-3	3500	366	108.0	126.8	0.875
1095	D-2	3500	362	123.3	132.5	0.955
1096	D-3	3500	362	123.0	121.8	1.039
1226	NNN-3	1295	216	36.9	45.4	0.811
1229	NHN-3	1295	216	46.0	59.1	0.776
1233	YB2000/0	10800	1890	289.4	333.0	0.809
1234	AW1	3700	538	604.3	437.0	1.358
1235	AW4	3700	506	744.6	617.0	1.192
1236	AW8	3700	507	819.3	609.1	1.329
1237	AX6	2080	288	282.5	232.6	1.207
1238	AX7	2080	287	250.5	183.9	1.352
1239	AX8	2080	289	272.0	239.2	1.130
1241	L-10N1	8100	1400	270.6	297.8	0.869
1242	L-10N2	8100	1400	247.9	304.0	0.780
1243	L-10H	8100	1400	240.4	355.3	0.651
1244	L-20N1	8100	1400	268.4	313.5	0.820
1245	L-20N2	8100	1400	272.5	328.7	0.796
1246	L-40N1	8100	1400	245.0	324.9	0.723
1247	L-40N2	8100	1400	290.7	332.0	0.841
1248	L-50N1	8100	1400	274.3	369.9	0.715
1249	L-50N2	8100	1400	299.1	367.6	0.784
1250	L-50N2R	8100	1400	331.2	367.7	0.868
1251	S-10N1	1620	280	36.7	36.3	1.005
1252	S-10N2	1620	280	38.3	36.3	1.049
1253	S-10H	1620	280	37.7	41.6	0.902
1254	S-20N1	1620	280	39.2	35.8	1.086
1255	S-20N2	1620	280	38.3	35.2	1.079
1256	S-40N1	1620	280	41.7	34.5	1.201
1257	S-40N2	1620	280	34.9	34.5	1.003
1258	S-50N1	1620	280	38.5	39.2	0.976
1259	S-50N2	1620	280	40.6	39.2	1.029

Database ID	Original Designation	L [mm]	D [mm]	$V_{Exp.}$ [kN]	V_{VT2} [kN]	$\frac{V_{Exp.}}{V_{VT2}}$
1262	T1_ohne	2100	248	107.4	80.8	1.319
1263	T7_70_oben	2100	297	130.9	111.9	1.160
1264	T9_ohne	1700	167	112.2	91.4	1.224
1265	T13_ohne	1700	217	127.8	115.6	1.101
1266	T10_40_oben	1700	167	102.4	82.8	1.231
1270	SB 2	1601	200	42.0	31.9	1.310
1271	SB 3	2400	300	52.4	42.5	1.224
1272	SB 4	3600	450	93.4	102.6	0.900
1273	SB 5	4800	600	165.7	165.9	0.984
1274	SB 6	7200	900	304.2	368.0	0.808
1281	1.1-1	1800	260	50.6	42.3	1.188
1282	2.1-1	1800	260	91.1	92.2	0.984
1286	SBB1.1	495	84	14.5	18.4	0.786
1287	SBB1.2	495	84	18.5	18.6	0.995
1288	SBB1.3	495	84	15.0	18.4	0.813
1289	SBB2.1	990	168	28.9	28.2	1.022
1290	SBB2.2	990	168	30.6	28.0	1.089
1291	SBB2.3	990	166	29.8	27.8	1.071
1292	SBB3.1	1980	333	42.5	42.6	0.991
1293	SBB3.2	1980	333	41.0	41.6	0.980
1294	SBB3.3	1980	333	43.3	41.6	1.034
1358	1-1	1397	233	131.1	93.0	1.096
1359	1-2	3162	532	139.3	215.5	0.640
1364	2-3	4064	684	260.8	133.0	1.880
1365	2-4	4928	820	344.2	600.3	0.564

APPENDIX C: SOFTWARE VERIFICATION

Random Variable Generator Testing

To test each random variable generator, a single element mesh was created with applied nodal displacements of zero. A total of 500 simulations were performed for each distribution type. Each implementation was tested using the chi-squared goodness of fit test and the Kolmogorov-Smirnov (KS) test. For the normal and lognormal distributions, a mean of 30 MPa and a standard deviation of 6 MPa was assumed. To test the beta distribution, the alpha and beta parameters were selected equal to 2.0. To test the gamma distribution, alpha was taken as 1.0 and beta was taken as 2.0. The beta and gamma distributions were deliberately taken as simple cases so that they could be readily compared with their respective theoretical distributions. For the beta and gamma distributions, a chi-squared goodness of fit value could not be calculated easily and thus the KS test was considered sufficient.

a) Normal Distribution: n = 500
$\mu = 30 \quad \sigma = 6.0$

Chi-squared: p-value = 0.793
KS test: p-value = 0.923

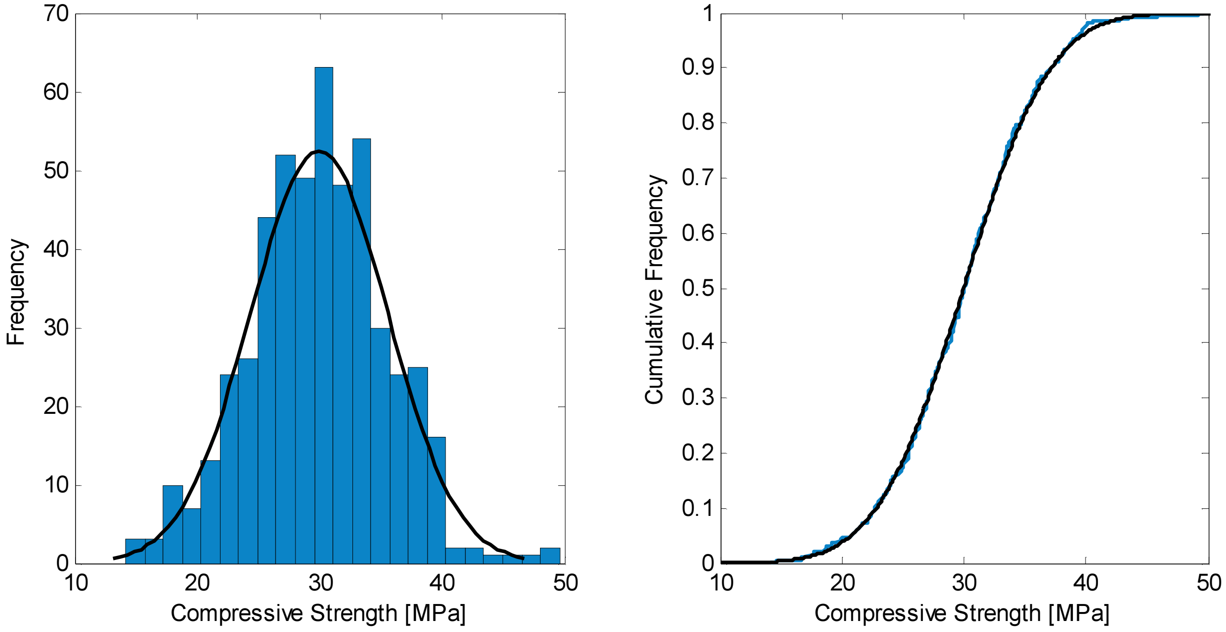

b) Lognormal Distribution: n = 500
$\mu = 30 \quad \sigma = 6.0$

Chi-squared: p-value = 0.190
KS test: p-value = 0.937

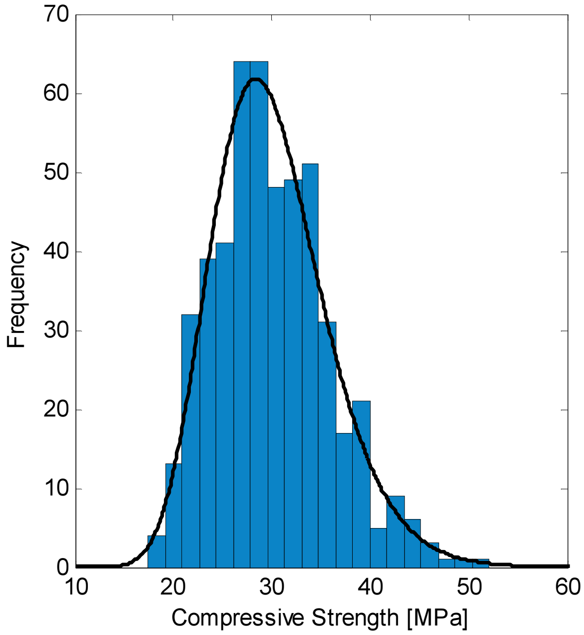

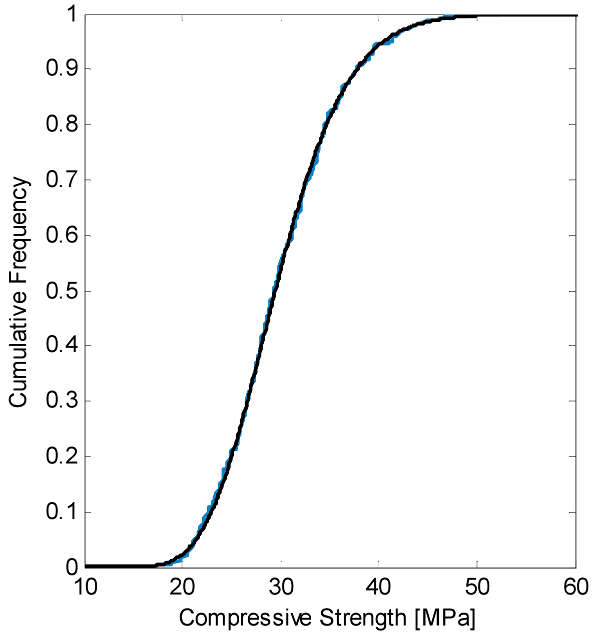

c) Beta Distribution: n = 500
$\alpha = 2.0 \quad \beta = 2.0$

Chi-squared: p-value = N/A
KS test: p-value = 0.423

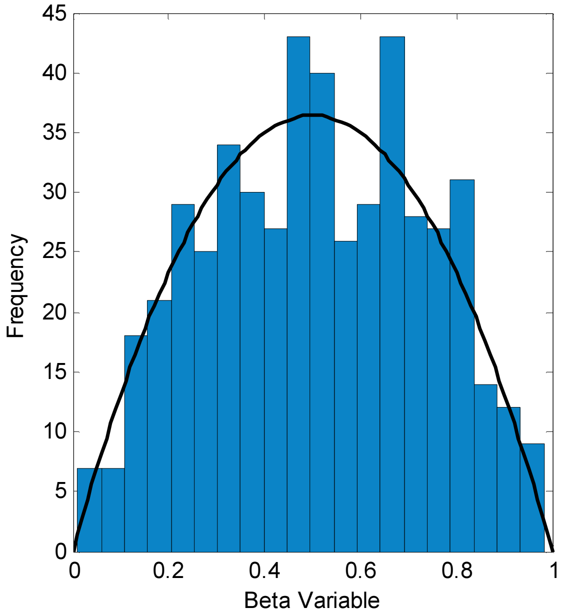

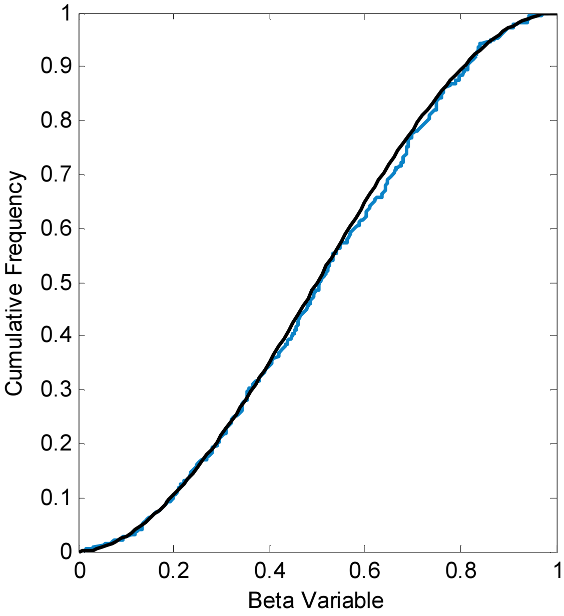

d) Gamma Distribution: n = 500
$\alpha = 1.0 \quad \beta = 2.0$

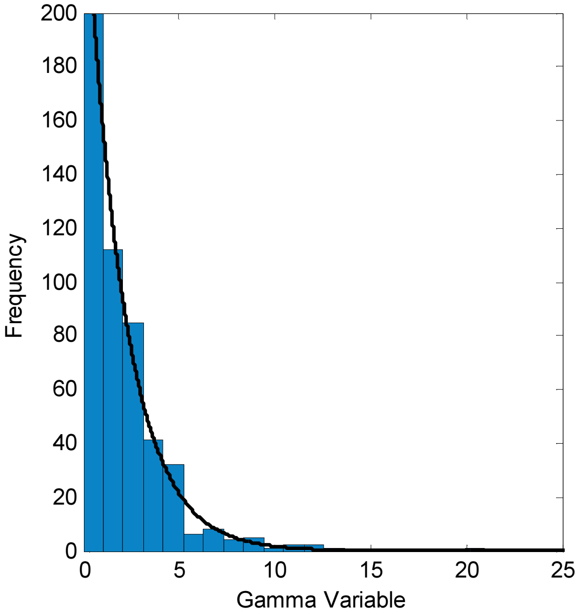

Chi-squared: p-value = N/A
KS test: p-value = 1.000

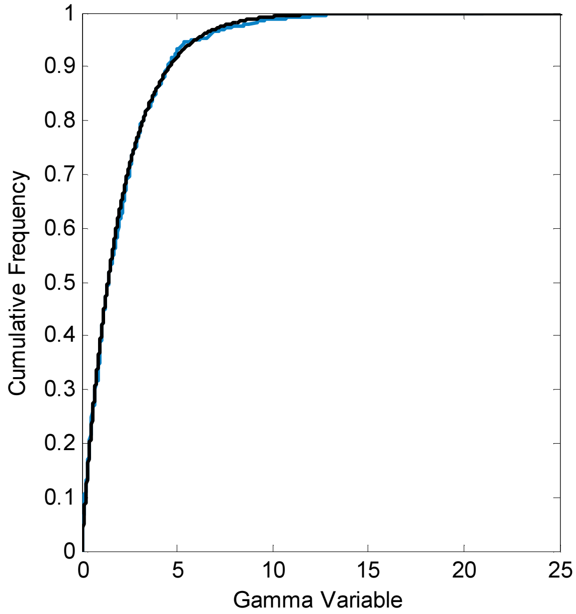

APPENDIX D: USER’S MANUAL

D.1 Introduction

This appendix serves as a guide for users who want to conduct stochastic simulations using VecTor2. As part of this thesis, a range functionality was implemented into the VecTor2 source code to allow users to conduct stochastic simulations. The current implementation includes: the input of user specified material property factors; Monte Carlo sampling with uniform, correlated, nugget-effect, and spatially correlated (random field) random variables; and Latin hypercube sampling with uniform, correlated, and spatially correlated random variables. For more information on the theory behind each implementation, the reader is referred to Chapter 4.

Stochastic simulation in the context of this thesis involves the randomization of the concrete and steel material properties within VecTor2. The user specifies the material properties, which are then modified for each simulation based on their respective statistical distributions. The material properties can be assumed to be independent, or correlated (both globally and spatially). As a user, the goal of the stochastic simulation may be to: assess the probabilistic deflection of a critical structural component; to assess the reliability of a structural element; or to understand the sensitivity to failure mode that the structural element has relative to material property inputs. The stochastic simulation derives information on these random outputs by repeated simulation with randomly generated inputs. This user's manual focuses on the implemented options for stochastic simulation with VecTor2.

In Formworks, the dedicated pre-processor for VecTor2, the stochastic simulation options are found under the *Define Job* menu in the *Special* tab. The default menu is shown in Fig. D.1.

By default, the stochastic analysis type is set to *Not Considered*. This means that VecTor2 will bypass the stochastic simulation subroutines and run as a deterministic simulation. The dropdown menu for stochastic simulation type is highlighted in Fig. D.1. The *stochastic analysis types* are listed as follows:

1. User Input Modification Factors	(SFD Option: -1)
2. Not Considered	(SFD Option: 0)
3. Monte Carlo Simulation MCS	(SFD Option: 1)
4. Uncorrelated Spatial Variation MCS	(SFD Option: 2)

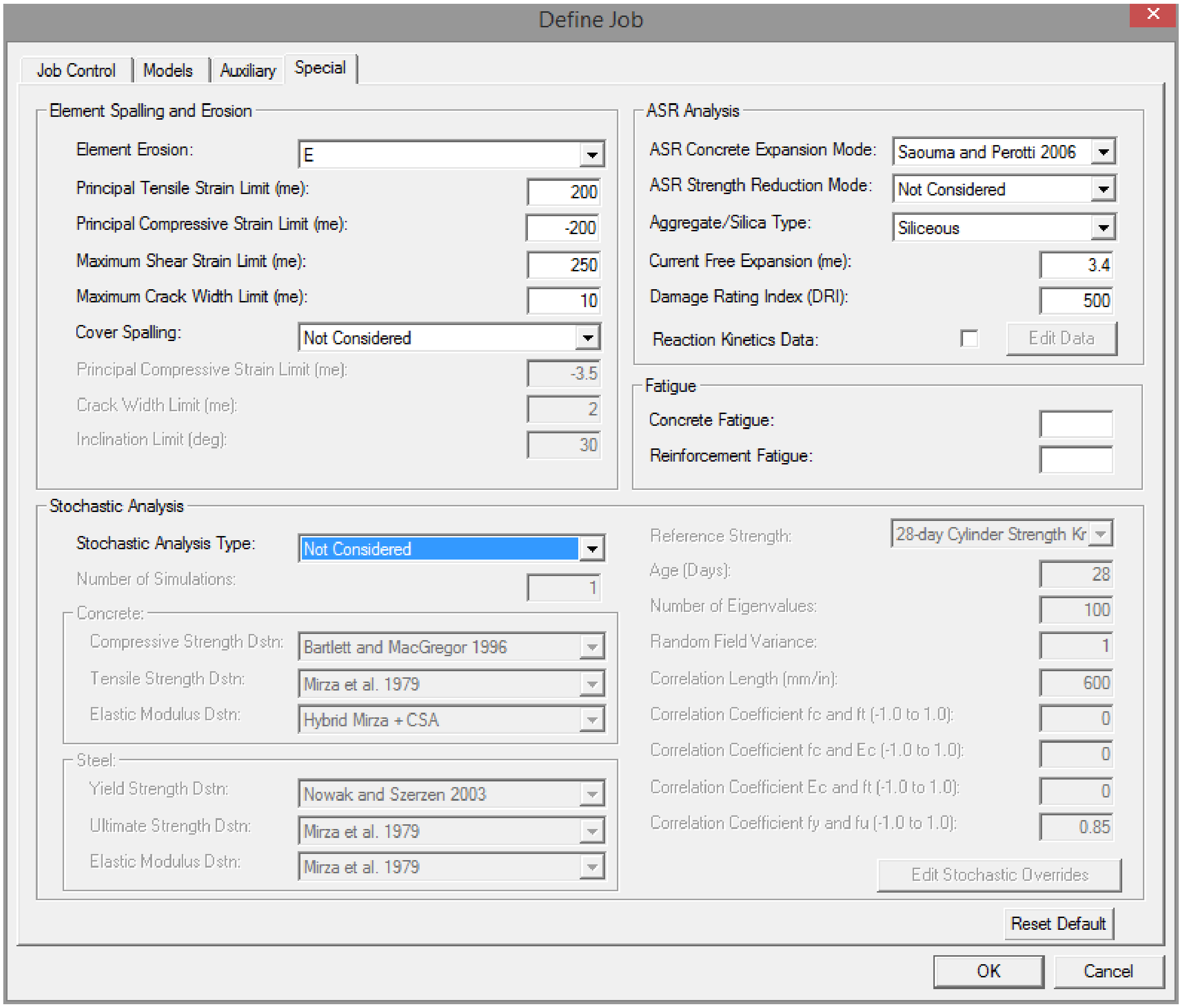

Element Spalling and Erosion

Element Erosion: E
Principal Tensile Strain Limit (me): 200
Principal Compressive Strain Limit (me): -200
Maximum Shear Strain Limit (me): 250
Maximum Crack Width Limit (me): 10
Cover Spalling: Not Considered
Principal Compressive Strain Limit (me): -3.5
Crack Width Limit (me): 2
Inclination Limit (deg): 30

ASR Analysis

ASR Concrete Expansion Mode: Saouma and Perotti 2006
ASR Strength Reduction Mode: Not Considered
Aggregate/Silica Type: Siliceous
Current Free Expansion (me): 3.4
Damage Rating Index (DRI): 500
Reaction Kinetics Data: ☐

Fatigue

Concrete Fatigue:
Reinforcement Fatigue:

Stochastic Analysis

Stochastic Analysis Type: Not Considered
Number of Simulations: 1

Concrete:
Compressive Strength Dstn: Bartlett and MacGregor 1996
Tensile Strength Dstn: Mirza et al. 1979
Elastic Modulus Dstn: Hybrid Mirza + CSA

Steel:
Yield Strength Dstn: Nowak and Szerzen 2003
Ultimate Strength Dstn: Mirza et al. 1979
Elastic Modulus Dstn: Mirza et al. 1979

Reference Strength: 28-day Cylinder Strength Kr
Age (Days): 28
Number of Eigenvalues: 100
Random Field Variance: 1
Correlation Length (mm/in): 600
Correlation Coefficient fc and ft (-1.0 to 1.0): 0
Correlation Coefficient fc and Ec (-1.0 to 1.0): 0
Correlation Coefficient Ec and ft (-1.0 to 1.0): 0
Correlation Coefficient fy and fu (-1.0 to 1.0): 0.85

Fig. D.1: Stochastic simulation input options in *Define Job* menu.

5. Random Field Spatial Variation MCS (SFD Option: 3)
6. Latin Hypercube Sampling LHS (SFD Option: 4)
7. Correlated Sampling MCS (SFD Option: 5)
8. Correlated Sampling LHS (SFD Option: 6)
9. Random Field Generation LHS (SFD Option: 7)

Each of these options are detailed in the following sections. Note that any option that ends with MCS uses Monte Carlo sampling and that any option ending in LHS uses Latin hypercube sampling.

The number of simulations to be undertaken is specified in the input box below the *stochastic analysis type* dropdown menu. The user can currently select a maximum of 999 simulations. If more simulations are desired for any Monte Carlo sampling, another analysis can be run and produce independent results. This cannot be done for Latin hypercube sampling, as the stratification for both simulations is identical. However, the purpose of Latin hypercube sampling is to reduce the required number of simulations and thus it is unlikely that a user will require Latin hypercube samples in excess of the maximum.

D.2 Monte Carlo Sampling

Monte Carlo sampling involves the basic random number generation to any of the selected distributions. The user is able to select a distribution for the concrete compressive strength, the concrete tensile strength, the concrete elastic modulus, the steel yield strength, the steel ultimate strength, and the steel elastic modulus. If the material properties in the model represent the assumed material properties (the specified strength for example) then the following models are recommended and set as the default distributions.

Parameter	**Models from Literature**
Compressive Strength	Bartlett and MacGregor 1996
Tensile Strength	Mirza et al. 1979
Elastic Modulus (Concrete)	Hybrid Mirza + CSA
Yield Strength	Nowak and Szerzen 2003
Ultimate Strength	Mirza et al. 1979
Elastic Modulus	Mirza et al. 1979

These selected models are not specific to Monte Carlo sampling; they are recommended for all stochastic simulations. Note that for the concrete tensile strength and elastic modulus, the CSA A23.3 predictions for the modulus of elasticity and tensile strength are substituted. This was considered more representative of modern day concrete than the original statistics proposed by Mirza et al. (1979). The selection of Mirza et al. (1979) for the tensile strength and modulus of elasticity reflect that a contemporary database of those parameters has not recently been compiled for Canadian concrete.

When SFD Option 1: *Monte Carlo Simulation MCS* is selected, all of the parameters on the right of the *Special* tab can be ignored except the specified age of the concrete. Some of the models (Bartlett and MacGregor, 1996; Unanwa and Mahan, 2014) scale the specified strength up to the current age of the concrete. Thus, if a specific structure is being analyzed where the age and specified strength are known, these models are preferred.

The required number of simulations for Monte Carlo sampling can vary widely. It is recommended that the number of simulations be greater than 200; however, this is contingent on model simplicity, variation in failure mode, computation time, etc. If the sampling of the tails is paramount, then the number of simulation should be increased significantly. The parameters employed when SFD Option 1: *Monte Carlo Simulation MCS* is selected are highlighted in Fig. D.2.

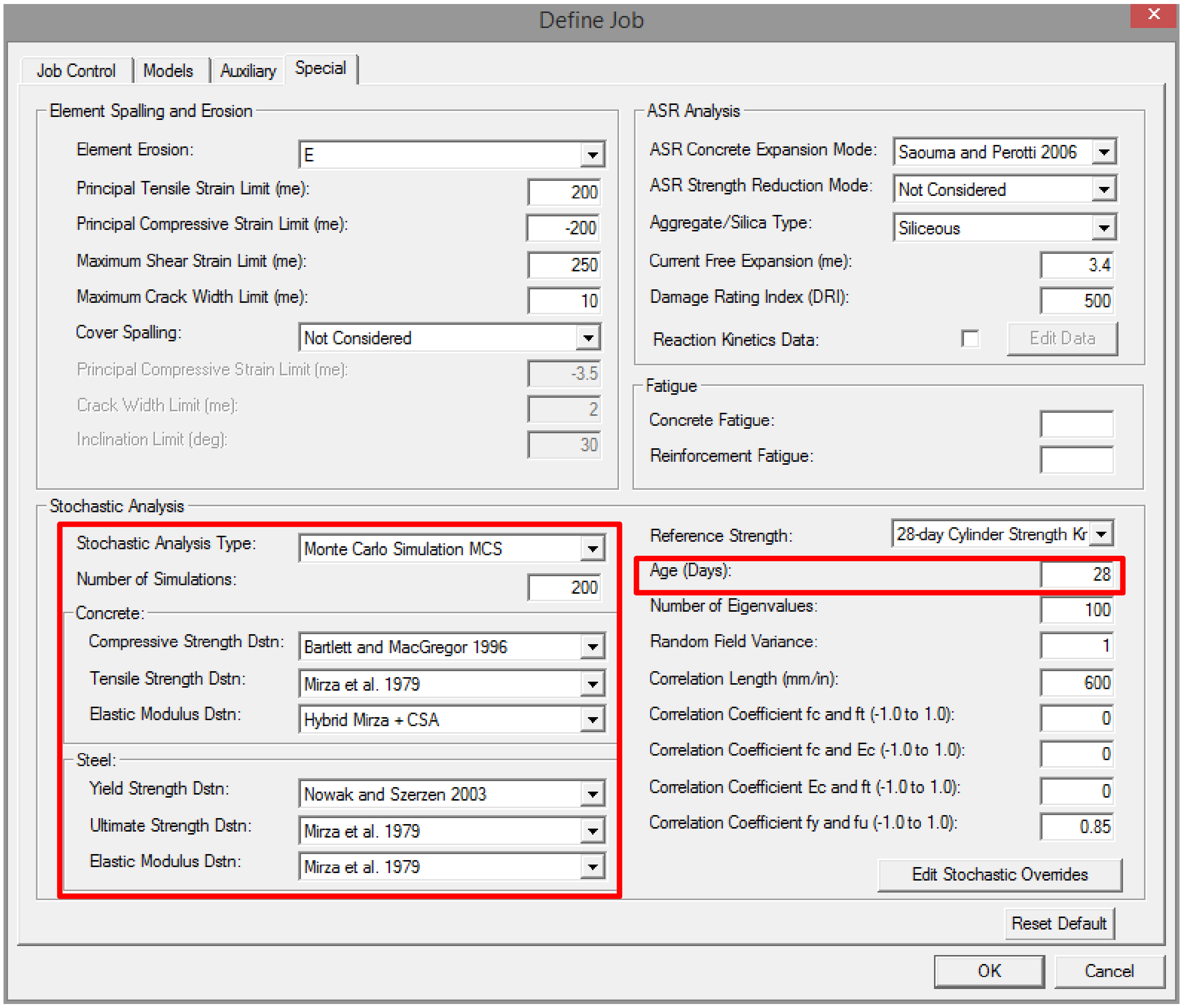

Element Spalling and Erosion

Element Erosion: E
Principal Tensile Strain Limit (me): 200
Principal Compressive Strain Limit (me): -200
Maximum Shear Strain Limit (me): 250
Maximum Crack Width Limit (me): 10
Cover Spalling: Not Considered
Principal Compressive Strain Limit (me): -3.5
Crack Width Limit (me): 2
Inclination Limit (deg): 30

ASR Analysis

ASR Concrete Expansion Mode: Saouma and Perotti 2006
ASR Strength Reduction Mode: Not Considered
Aggregate/Silica Type: Siliceous
Current Free Expansion (me): 3.4
Damage Rating Index (DRI): 500
Reaction Kinetics Data: ☐

Fatigue

Concrete Fatigue:
Reinforcement Fatigue:

Stochastic Analysis

Stochastic Analysis Type: Monte Carlo Simulation MCS
Number of Simulations: 200

Concrete:
Compressive Strength Dstn: Bartlett and MacGregor 1996
Tensile Strength Dstn: Mirza et al. 1979
Elastic Modulus Dstn: Hybrid Mirza + CSA

Steel:
Yield Strength Dstn: Nowak and Szerzen 2003
Ultimate Strength Dstn: Mirza et al. 1979
Elastic Modulus Dstn: Mirza et al. 1979

Reference Strength: 28-day Cylinder Strength Kr
Age (Days): 28
Number of Eigenvalues: 100
Random Field Variance: 1
Correlation Length (mm/in): 600
Correlation Coefficient fc and ft (-1.0 to 1.0): 0
Correlation Coefficient fc and Ec (-1.0 to 1.0): 0
Correlation Coefficient Ec and ft (-1.0 to 1.0): 0
Correlation Coefficient fy and fu (-1.0 to 1.0): 0.85

Fig. D.2: Relevant parameters for the *Monte Carlo Simulation MCS* option.

The simulation options that employ Monte Carlo sampling are SFD Options 1, 2, 3, and 5 (in reference to the list supplied above). The parameters for SFD Options 3 and 5 are detailed in Section D.4. The parameters for SFD Option 2 are the same as SFD Option 1.

D.3 Latin Hypercube Sampling

Latin hypercube sampling is a stratified simulation technique that has been shown to reduce the required number of simulations. This technique is advantageous when the computation time for each simulation is long. For example, it is not uncommon for a VecTor2 analysis to take between 3 and 10 minutes to run a set of load stages that capture the behaviour of the specimen. Thus if 300 simulations were desired, the total running time would range between approximately 15 to 50 hours of computation time. If Latin hypercube sampling is employed, this number can drop significantly and thus the simulation time can drop significantly. Some researchers estimate that satisfactory results can be obtained with less than 50 simulations (Vorechovsky and Novak, 2005). Nevertheless, it is recommended that between 50 and 100 simulations are selected when Latin Hypercube sampling is employed.

The required parameters for SFD Option 4: *Latin Hypercube Sampling LHS* are the same as those described for SFD Option 1 and are highlighted in Fig. D.2. The simulation options that employ Latin hypercube sampling are SFD Options 4, 6, and 7. The parameters for SFD Options 6 and 7 are detailed in Section D.4.

Option 9 has limited functionality in the current implementation. The sampling method described in Section 4.5.6 is currently set to default. Thus it is not entirely a Latin Hypercube sample as the local random field is a Latin Hypercube sample but the RF mean is still a Monte Carlo sample. This represents one of the biggest limitations and thus the recommended number of simulations for Option 9 should exceed 200.

D.4 Random Field Generation and Correlated Sampling

Random field generation and correlated sampling represent the majority of the remaining stochastic simulation options not addressed in Section D.1 through Section D.3. A random field requires three parameter: the number of included eigenvalues, the random field variance, and the correlation length. The eigenvalues are calculated in VecTor2 using the FEAST algorithm and, as such, eigenvalues are computed in descending order (largest to smallest). Thus the user can specify the number of eigenvalues to be calculated. VecTor2 will display the computed eigenvalues in ascending order. The maximum number of eigenvalues is equal to the maximum number of elements. However, Vorechovsky and Novak (2005) noted that a majority of the eigenvalues when using the Karhunen-Louve Transform (see Section 4.5.2) are zero. As a result, it is useful to reduce the number of calculated eigenvalues, and thus the number of random variables required for simulation. The recommended number of eigenvalues varies depending on the correlation length. For a large correlation length, the number of significant (non-zero) eigenvalues is small. For a nugget-effect model, each eigenvalue is significant. It has been found that selecting 80 eigenvalues results is adequate in generating of random fields for correlations lengths observed in concrete. The computed eigenvalues are displayed when VecTor2 is running and can be inspected to ensure that the lowest computed eigenvalue is significantly smaller than the largest eigenvalue. An example of this printout is shown in Fig. D.3. Note that the 80th eigenvalue is 0.18 and the largest is 97.40. Thus, 80 eigenvalues are sufficient for the generation for this random field.

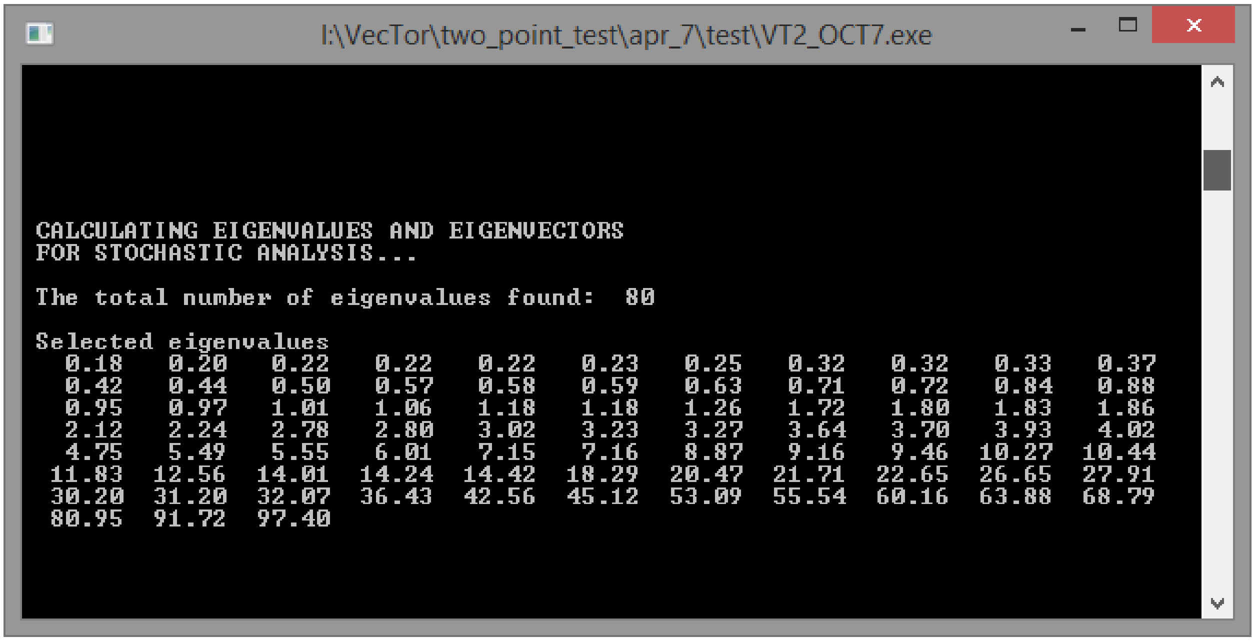

```
CALCULATING EIGENVALUES AND EIGENVECTORS
FOR STOCHASTIC ANALYSIS...

The total number of eigenvalues found:  80

Selected eigenvalues
  0.18   0.20   0.22   0.22   0.22   0.23   0.25   0.32   0.32   0.33   0.37
  0.42   0.44   0.50   0.57   0.58   0.59   0.63   0.71   0.72   0.84   0.88
  0.95   0.97   1.01   1.06   1.18   1.18   1.26   1.72   1.80   1.83   1.86
  2.12   2.24   2.78   2.80   3.02   3.23   3.27   3.64   3.70   3.93   4.02
  4.75   5.49   5.55   6.01   7.15   7.16   8.87   9.16   9.46  10.27  10.44
 11.83  12.56  14.01  14.24  14.42  18.29  20.47  21.71  22.65  26.65  27.91
 30.20  31.20  32.07  36.43  42.56  45.12  53.09  55.54  60.16  63.88  68.79
 80.95  91.72  97.40
```

Fig. D.3: VecTo2 eigenvalue printout.

The correlation length describes the distance in which two element become completely uncorrelated. The current implementation is limited to a Gaussian correlation function. Based on a review of the literature and the experimental program in this thesis, a correlation length of 800 – 1200 mm is recommended for stochastic simulations.

The random field variance should always remain at 1.0 with the current implementation. The current implementation produces a random field with a mean of zero and a variance equal to the specified variance, however this random field is then scaled to meet the global distribution for concrete. As a result, until the random field data implementations are expanded to include non-Gaussian random fields, this parameter should always be specified as 1.0. A summary of the relevant parameters for random field generation is presented in Fig. D.4.

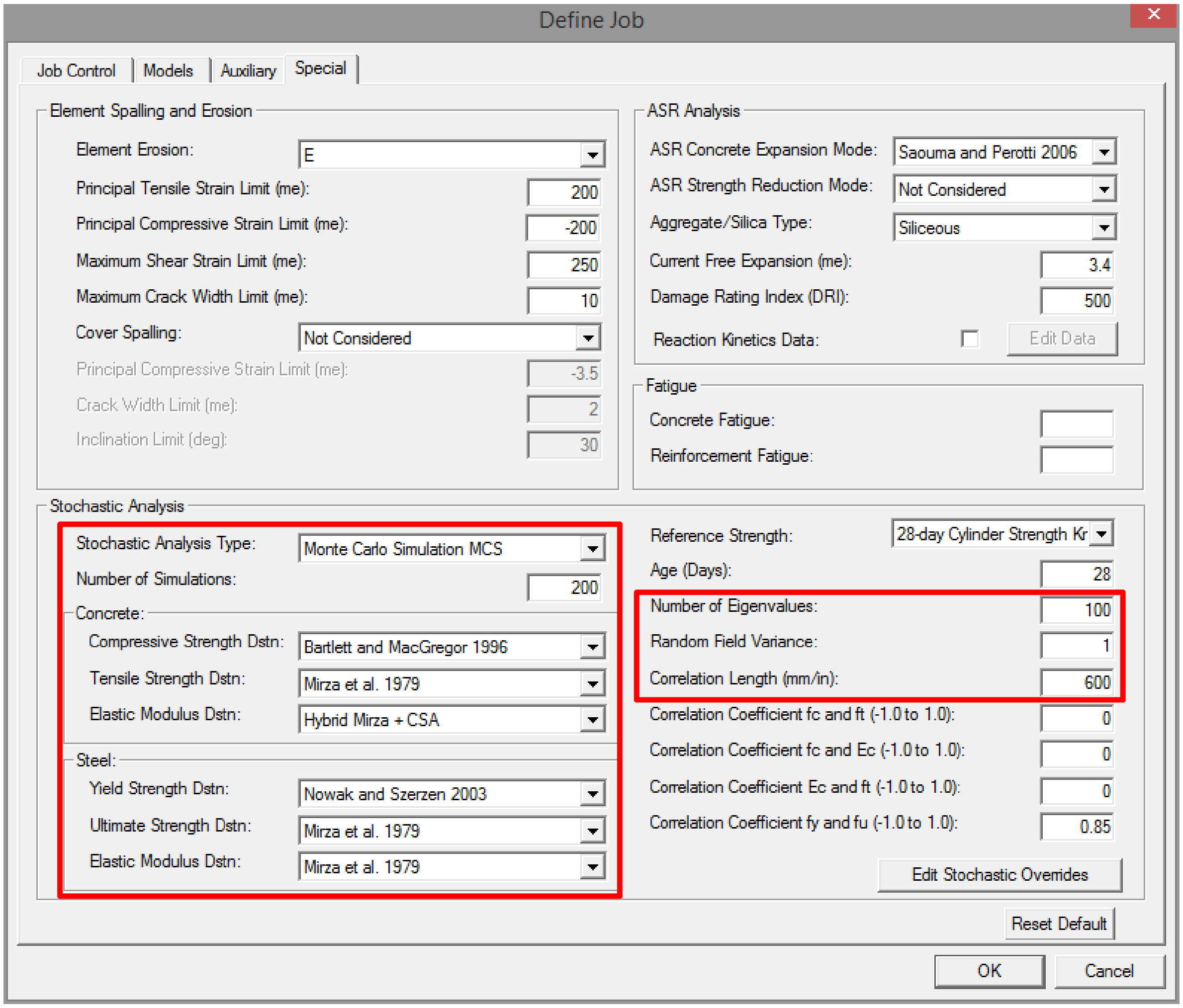

Element Spalling and Erosion
Element Erosion: E
Principal Tensile Strain Limit (me): 200
Principal Compressive Strain Limit (me): -200
Maximum Shear Strain Limit (me): 250
Maximum Crack Width Limit (me): 10
Cover Spalling: Not Considered
Principal Compressive Strain Limit (me): -3.5
Crack Width Limit (me): 2
Inclination Limit (deg): 30

ASR Analysis
ASR Concrete Expansion Mode: Saouma and Perotti 2006
ASR Strength Reduction Mode: Not Considered
Aggregate/Silica Type: Siliceous
Current Free Expansion (me): 3.4
Damage Rating Index (DRI): 500
Reaction Kinetics Data: ☐

Fatigue
Concrete Fatigue:
Reinforcement Fatigue:

Stochastic Analysis
Stochastic Analysis Type: Monte Carlo Simulation MCS
Number of Simulations: 200
Concrete:
Compressive Strength Dstn: Bartlett and MacGregor 1996
Tensile Strength Dstn: Mirza et al. 1979
Elastic Modulus Dstn: Hybrid Mirza + CSA
Steel:
Yield Strength Dstn: Nowak and Szerzen 2003
Ultimate Strength Dstn: Mirza et al. 1979
Elastic Modulus Dstn: Mirza et al. 1979
Reference Strength: 28-day Cylinder Strength Kr
Age (Days): 28
Number of Eigenvalues: 100
Random Field Variance: 1
Correlation Length (mm/in): 600
Correlation Coefficient fc and ft (-1.0 to 1.0): 0
Correlation Coefficient fc and Ec (-1.0 to 1.0): 0
Correlation Coefficient Ec and ft (-1.0 to 1.0): 0
Correlation Coefficient fy and fu (-1.0 to 1.0): 0.85

Fig. D.4: Relevant parameters for random field generation.

Correlated sampling allows users to induce correlations into their simulation of random variables. In reality, there are well established trends that show that the concrete compressive, tensile, and elastic modulus are correlated random variables. These correlations are established usually based on a range of concrete strengths and their resulting tensile strength or modulus of elasticity. Thus, when simulating a structure with a population of concrete strengths, it may be useful to induce correlation in the simulation. It should be noted, however, that assuming the variables are uncorrelated does not necessarily result in a reduction in simulation accuracy. The dispersion matrix for concrete is represented as follows:

$$C = \begin{bmatrix} 1.0 & C_1 & C_2 \\ C_1 & 1.0 & C_3 \\ C_2 & C_3 & 1.0 \end{bmatrix}$$

where C_1 represents the correlation coefficient between the compressive strength and the tensile strength, C_2 represent the correlation coefficient between the compressive strength and the modulus of elasticity, and C_3 represents the correlation coefficient between the tensile strength and the modulus of elasticity. It should be noted that the current implementation requires that the dispersion matrix be positive definite. This means that conflicting correlations cannot exist. For example, if concrete compressive strength is positive and strongly correlated (>0.8) with both the tensile strength and the elastic modulus, then the C_3 coefficient cannot be weakly correlated (~<0.5). This will cause the current generation method to produce numerical errors. It is noted that techniques like simulated annealing (Vořechovský & Novák, 2009) circumvent this problem; however, that is outside the scope of the current implementation. There is little literature on the correlation coefficients for concrete material properties for a distribution based on a specified strength, and thus no correlation coefficients are suggested as defaults.

Another important correlation coefficient is the relationship between the yield strength and the ultimate strength of steel reinforcement. This was included in the implementation and a default value of 0.85 (Wisniewski et al., 2012) is recommended. Fig. D.5 summarizes the input parameters relevant to correlated sampling.

D.5 Stochastic Overrides

In addition to the implemented distributions, the user may elect to use an alternate distribution or exclude certain material properties from stochastic simulation. This can be accomplished using the stochastic overrides. A menu that is used for the input of stochastic override parameters is opened by clicking the *Edit Stochastic Overrides* button on the bottom right hand corner.

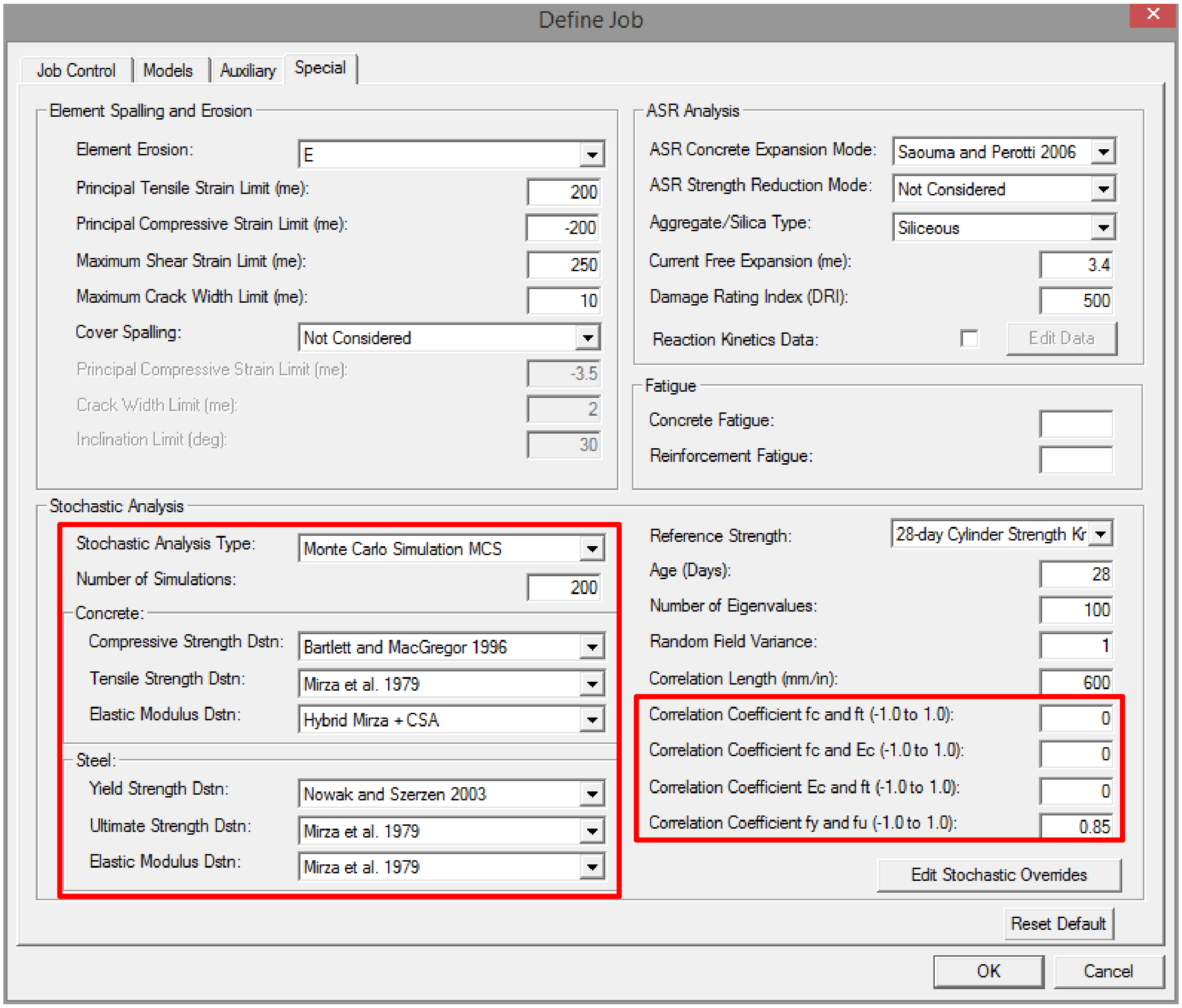

Element Spalling and Erosion
Element Erosion: E
Principal Tensile Strain Limit (me): 200
Principal Compressive Strain Limit (me): -200
Maximum Shear Strain Limit (me): 250
Maximum Crack Width Limit (me): 10
Cover Spalling: Not Considered
Principal Compressive Strain Limit (me): -3.5
Crack Width Limit (me): 2
Inclination Limit (deg): 30

ASR Analysis
ASR Concrete Expansion Mode: Saouma and Perotti 2006
ASR Strength Reduction Mode: Not Considered
Aggregate/Silica Type: Siliceous
Current Free Expansion (me): 3.4
Damage Rating Index (DRI): 500
Reaction Kinetics Data: ☐

Fatigue
Concrete Fatigue:
Reinforcement Fatigue:

Stochastic Analysis
Stochastic Analysis Type: Monte Carlo Simulation MCS
Number of Simulations: 200
Concrete:
Compressive Strength Dstn: Bartlett and MacGregor 1996
Tensile Strength Dstn: Mirza et al. 1979
Elastic Modulus Dstn: Hybrid Mirza + CSA
Steel:
Yield Strength Dstn: Nowak and Szerzen 2003
Ultimate Strength Dstn: Mirza et al. 1979
Elastic Modulus Dstn: Mirza et al. 1979

Reference Strength: 28-day Cylinder Strength Kr
Age (Days): 28
Number of Eigenvalues: 100
Random Field Variance: 1
Correlation Length (mm/in): 600
Correlation Coefficient fc and ft (-1.0 to 1.0): 0
Correlation Coefficient fc and Ec (-1.0 to 1.0): 0
Correlation Coefficient Ec and ft (-1.0 to 1.0): 0
Correlation Coefficient fy and fu (-1.0 to 1.0): 0.85

Fig. D.5: Relevant parameters for correlated sampling.

The edit stochastic override menu allows the user to selected a specific variable from a specific material property and control its distribution. The stochastic override menu is shown in Fig. D.6.

From the stochastic override menu, the user can select one of the following options for random variables:

1. Not a random variable.

2. Normally distributed random variable.

3. Lognromally distributed random variable.

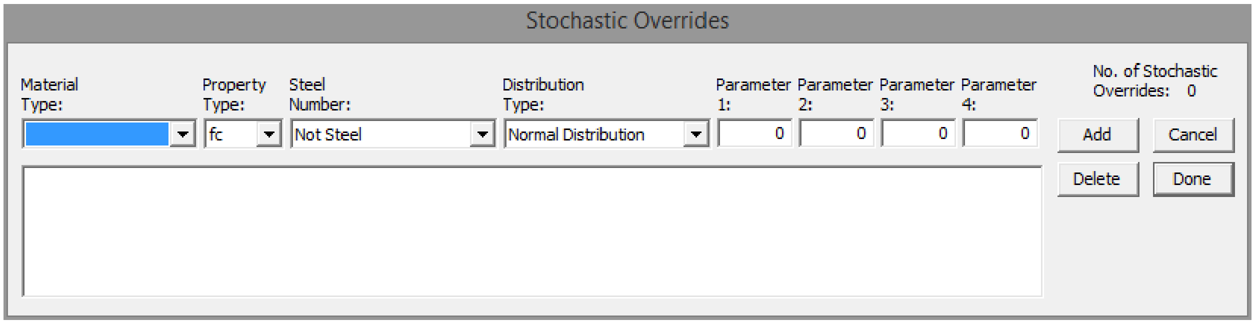

Material Type:
Property Type: fc
Steel Number: Not Steel
Distribution Type: Normal Distribution
Parameter 1: 0
Parameter 2: 0
Parameter 3: 0
Parameter 4: 0
No. of Stochastic Overrides: 0

Fig. D.6: Stochastic override menu.

4. Beta distribution random variable.

5. Gamma distribution random variable.

In order to alter the properties of smeared reinforcement, the Steel number dropdown menu allows the user to select the steel layer, or indicate that the material is a truss bar. The user will then select the appropriate distribution and input the distribution parameters manually. The parameters for each distribution type are summarized below.

Distribution Type	Parameter 1	Parameter 2	Parameter 3	Parameter 4
Normal	Mean	Standard Deviation	N/A	N/A
Lognormal	Mean	Standard Deviation	N/A	N/A
Beta	Alpha	Beta	Lower Bound	Upper Bound
Gamma	Alpha	Beta	N/A	N/A

Once the override properties for a material type are input, the user selects the *Add* button and the stochastic override appears. These overrides can be deleted at any time.

D.6 User Input Modification Files

In addition to the options provided within VecTor2 for stochastic simulation, the user may elect to construct separate input modification factors for the simulation. This was done in Chapter 3 in order to include the kriging predictions for concrete properties in a VecTor2 analysis. The user input file is currently created manually, and formatted according to the VT2.STOC file format. The VT2.STOC file can be generated with any text editor and a template is available. Currently the user input modification files must include a factor for every property and every element.

In order for VecTor2 to read the input file, Option 1 must be selected in the *Special* tab. An example of the manual input file is shown in Fig. D.7.

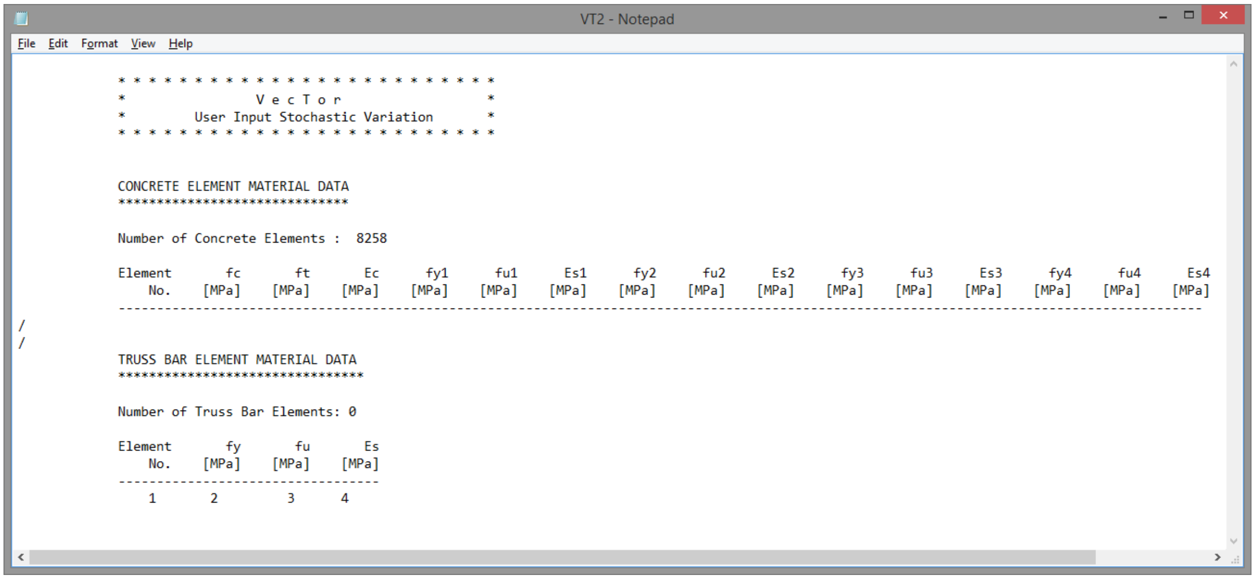

```
             * * * * * * * * * * * * * * * * * * * * * * * * *
             *                 V e c T o r                    *
             *          User Input Stochastic Variation       *
             * * * * * * * * * * * * * * * * * * * * * * * * *


             CONCRETE ELEMENT MATERIAL DATA
             ******************************

             Number of Concrete Elements :  8258

             Element       fc       ft       Ec      fy1      fu1      Es1      fy2      fu2      Es2      fy3      fu3      Es3      fy4      fu4      Es4
                 No.    [MPa]    [MPa]    [MPa]    [MPa]    [MPa]    [MPa]    [MPa]    [MPa]    [MPa]    [MPa]    [MPa]    [MPa]    [MPa]    [MPa]    [MPa]
             ---------------------------------------------------------------------------------------------------------------------------------------------
/
/
             TRUSS BAR ELEMENT MATERIAL DATA
             ********************************

             Number of Truss Bar Elements: 0

             Element       fy       fu       Es
                 No.    [MPa]    [MPa]    [MPa]
             ----------------------------------
                 1       2         3      4
```

Fig. D.7: 'VT2.STOC' file template in a text editor.

D.7 Disaggregated Variability Options

All of the implemented models for concrete strength represent the relationship between the specified strength and the actual statistical distribution for concrete material properties. However, an analyst may have access to the actual cylinder strength of the concrete, or even the current strength of the concrete. Thus an attempt is made to disaggregate the variability in the selected statistical models to allow the user to perform stochastic simulation on a specific structure, with more information than the specified material properties. To incorporate this into the stochastic simulation framework, an additional variable, denoted 'Reference Strength', is added to the simulation options. This section outlines the possible disaggregation for a few selected concrete compressive strength models.

D.7.1 Mirza et al. 1979

Mirza et al. 1979 offers limited information on the source of variability that makes up their concrete compressive strength. It is simply noted that the coefficient of variation due to spatial and batch-to-batch variation can be taken as 0.13. Thus if the analyst knows the concrete strength matching the actual age of the structure the coefficient of variation may be taken as 0.13.

D.7.2 Bartlett and MacGregor 1996

Bartlett and MacGregor (1996) constructed a model that is based on two parameters:

$$\overline{f_c'} = f_1 f_2 f_c'$$

where f_1 relates the cylinder strength to the specified strength and f_2 relates the cylinder strength to the actual strength of the structure. Thus if the 28-day cylinder strength is known, the parameter f_1 can be removed from the prediction of the distribution parameters and the coefficient of variation becomes 0.14. Note that this only applies to the 28-day strength as the f_2 parameter implicitly includes the variation of strength with time.

D.7.3 Unanwa and Mahan 2014

Unanwa and Mahan (2014) proposed a model for the compressive strength of concrete that incorporated three parameters:

$$\overline{f_c'} = f_1 f_2 f_3 f_c'$$

where f_1 relates the cylinder strength to the specified strength, f_2 relates the cylinder strength to the actual strength of the structure, and f_3 scales the strength of the concrete to any specified age. The statistics of these parameters are summarized below.

Parameter	Bias factor	Coefficient of Variation
f_1	1.45	0.15
f_2	0.81	0.11
f_3	$e^{\left(0.3\sqrt{\frac{a}{28}}\right)}$	0.07

D.7.4 Implementation in VecTor2

These three models are currently implemented in VecTo2. The Reference Strength can be selected as one of the following three options:

A. Specified strength is known.

B. 28-day cylinder strength is known.

C. Current cylinder strength is known.

Option A represents the default option. It assumes that the strength in VecTor2 is a specified strength and thus all models can be used. Option B assumes that the 28-day cylinder strength is known. Thus the variability relating the cylinder strength to the specified strength can be removed. For Mirza et al. (1979) a coefficient of variation of 0.13 can be used for Option B. For Bartlett and MacGregor (1996) the first parameter can be removed and thus the coefficient of variation is reduced to 0.14. For Unanwa and Mahan (2014) the coefficient of variation is approximated as

$$V = \sqrt{(0.11)^2 + (0.07)^2} = 0.1304$$

For Option C, the cylinder strength at the current age of the structure is known, and thus the variability associated with the age is eliminated. If the Unanwa and Mahan (2014) model is selected, then the coefficient of variation is further reduced to 0.11. A summary of which models are compatible with each reference strength is shown below.

Model	Option A: Specified Strength is known (Default)	Option B: 28-day cylinder strength is known	Option C: Current/test-day cylinder strength is known
Mirza et al. 1979	Compatible [1]	Compatible Use for older concrete	Not Compatible
Bartlett and MacGregor 1996	Compatible [2]	Compatible[5]	Not Compatible
Nowak and Szerszen 2003	Compatible [3]	Not Compatible	Not Compatible
Unanwa and Mahan 2014	Compatible [4]	Compatible	Compatible

[1] Recommended for older concrete [2] Developed from Canadian concrete [3] Developed from American Concrete
[4] Developed from California Concrete [5] Preferred for Option B

The reported data from the disaggregation are taken or calculated from the published works only. These statistics should be verified via an independent database before they can be used with confidence. It is worth noting that the coefficients of variation for Option B for all three models were essentially equal. This suggests that the reduction in variability may be representative of the actual data. Additionally, the influence of reduced concrete strength variability on the tensile strength and modulus of elasticity statistics is unclear.

The user should employ these modifications with caution, and whenever possible, use the unaltered distributions presented in the literature.

D.8 Stochastic Simulation Output Files

The modifications factors generated in stochastic simulations are output to a series of text files. Each file is referenced to a specific trial with the name and extension 'TRIAL_X.C2E', where X represents the trial number. The stochastic output files identify the default distribution models, trial number, and override distribution parameters. Additionally, they report all of the stochastic modification factors generated in VecTor2 for concrete, smeared steel, and truss bar steel. An example of a stochastic output file is shown in Fig. D.8.

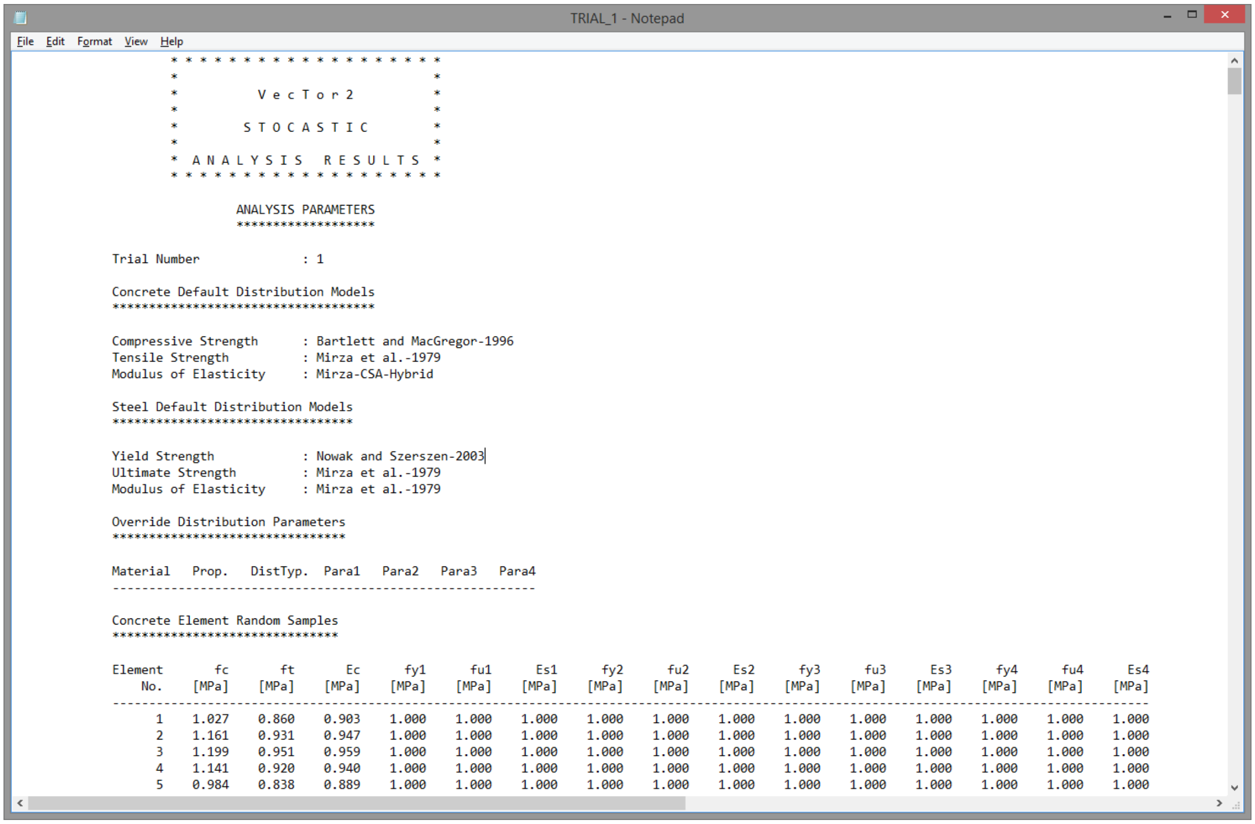

```
        * * * * * * * * * * * * * * * * * * *
        *                                   *
        *           V e c T o r 2           *
        *                                   *
        *         S T O C A S T I C         *
        *                                   *
        *  A N A L Y S I S   R E S U L T S  *
        * * * * * * * * * * * * * * * * * * *

                 ANALYSIS PARAMETERS
                 ******************

Trial Number              : 1

Concrete Default Distribution Models
************************************

Compressive Strength      : Bartlett and MacGregor-1996
Tensile Strength          : Mirza et al.-1979
Modulus of Elasticity     : Mirza-CSA-Hybrid

Steel Default Distribution Models
*********************************

Yield Strength            : Nowak and Szerszen-2003
Ultimate Strength         : Mirza et al.-1979
Modulus of Elasticity     : Mirza et al.-1979

Override Distribution Parameters
********************************

Material   Prop.   DistTyp.  Para1   Para2   Para3   Para4
----------------------------------------------------------

Concrete Element Random Samples
*******************************

Element       fc       ft       Ec      fy1      fu1      Es1      fy2      fu2      Es2      fy3      fu3      Es3      fy4      fu4      Es4
    No.    [MPa]    [MPa]    [MPa]    [MPa]    [MPa]    [MPa]    [MPa]    [MPa]    [MPa]    [MPa]    [MPa]    [MPa]    [MPa]    [MPa]    [MPa]
----------------------------------------------------------------------------------------------------------------------------------------------
      1    1.027    0.860    0.903    1.000    1.000    1.000    1.000    1.000    1.000    1.000    1.000    1.000    1.000    1.000    1.000
      2    1.161    0.931    0.947    1.000    1.000    1.000    1.000    1.000    1.000    1.000    1.000    1.000    1.000    1.000    1.000
      3    1.199    0.951    0.959    1.000    1.000    1.000    1.000    1.000    1.000    1.000    1.000    1.000    1.000    1.000    1.000
      4    1.141    0.920    0.940    1.000    1.000    1.000    1.000    1.000    1.000    1.000    1.000    1.000    1.000    1.000    1.000
      5    0.984    0.838    0.889    1.000    1.000    1.000    1.000    1.000    1.000    1.000    1.000    1.000    1.000    1.000    1.000
```

Fig. D.8: Stochastic simulation output file.